

# **Multifunctional Nanomaterials for Theranostic Applications**

A dissertation submitted by

**Deepanjalee Dutta**

to

**Indian Institute of Technology Guwahati**

For the award of the degree of

**Doctor of Philosophy**



**Centre for Nanotechnology**

**Indian Institute of Technology Guwahati**

**Guwahati – 781039, Assam, India**

**May 2018**



# DECLARATION

---

The thesis “**Multifunctional Nanomaterials for Theranostic Applications**” is an original work carried out by me under the supervision of Prof. Siddhartha Sankar Ghosh, Department of Biosciences and Bioengineering, Indian Institute of Technology Guwahati and Prof. Arun Chattopadhyay, Department of Chemistry, Indian Institute of Technology Guwahati for the award of the degree of Doctor of Philosophy.

I declare that this thesis has not been previously submitted or concurrently being submitted in substance for the award of any degree or diploma.

**Deepanjalee Dutta**

Centre for Nanotechnology  
Indian Institute of Technology Guwahati  
Guwahati – 781039  
Assam, India

May, 2018  
Guwahati



# CERTIFICATE

---

This is to certify that the research work embodied in the thesis entitled “**Multifunctional Nanomaterials for Theranostic Applications**” submitted to Centre for Nanotechnology Indian Institute of Technology Guwahati for the award of the degree of Doctor of Philosophy is a bonafide record of research work carried out by Deepanjalee Dutta. The content of the thesis reported by her are solely the results of her original findings. This work has not been submitted elsewhere for any degree or diploma.

**Prof. Siddhartha Sankar Ghosh**

Professor  
Department of Biosciences and  
Bioengineering  
Indian Institute of Technology Guwahati  
Guwahati - 781039, Assam, India

**Arun Chattopadhyay**

Professor  
Department of Chemistry  
Indian Institute of Technology Guwahati  
Guwahati - 781039, Assam, India





***Dedicated to....***

***My Parents and Teachers***



# ACKNOWLEDGEMENT

---

Before we get into the thick of things, I will try my best to express what I sincerely feel for each one of you who have created an impact throughout my PhD in the most beautiful way possible.

I extend my heartfelt gratitude to Prof. Siddhartha Sankar Ghosh and Prof. Arun Chattopadhyay my thesis supervisors, for giving me the opportunity to be a part of an esteemed institution as a PhD student. I will be always grateful to you for understanding my choice as well as value my opinion and for providing your able guidance to better my endeavours. Your words, lessons and valued suggestions will always be my inspiration in future ventures.

I would like to thank my doctoral committee members Dr. Tapas Kumar Mandal, Dr. Sunanda Chatterjee, Dr. Partho Sarathi Gooh Pattader for evaluating my work from time to time and for providing their valuable suggestions.

I would like to express my sincere regards to Dr. Sunil Kumar Sailapu, Dr. Rumi Khandelia and Dr. Amaresh Kumar Sahoo for training me in conducting experiments, planning and execution. Most importantly for teaching me not to let go and fight back.

My present and previous lab members for giving me wonderful memories that I would cherish forever and also for making me learn team work. I thank my collaborators for their help and support. My juniors Anitha, Kasturi, Tamanna who gave me an opportunity to teach as well as learn along with them.

I thank my friends from Disneyland, K.V Khanapara and Sathyabama University for being my second family and giving me the hope that life is still beautiful even when the world around has turned upside down.

My teachers from K.V Khanapara, Chandan Sir and Pranamita Mam for introducing me to the interesting world of research and making biology my favourite subject. Debangshu Sir for making physics interesting inspite of my dislike for maths.

Ma and papa for gifting me with this life and making me the way I am. Papa for believing in me at times when I refused to believe myself and for always being the first one to cheer for my happiness. Ma for putting all the efforts starting from teaching me alphabets, ensuring everything was on my fingertip even before I realised what I wanted and the list goes on.

I sincerely apologize if I have missed mentioning a few names. I wholeheartedly acknowledge everyone who was a part of this eventful journey of my life called ...PhD.

Deepanjalee



# ABSTRACT

---

Multifunctional nanomaterials have been a point of attraction in cancer research due to its breadth of applications in imaging, therapeutics and targeting. Apart from imparting targeted diagnosis and therapy, these systems render the advantages of combinatorial therapeutic regime in alleviation of cancer. Particularly, biopolymer based nanoparticle delivery systems have been developed for anticancer treatments, wound healing and hydrogel based injection modules. They can achieve efficient conjugation, entrapment, absorption and encapsulation of drugs or imaging probes and enable the delivery of the same to the desired regions. In addition, small chemical molecules also have been modified towards development of theranostic agents for enhancing therapeutic potential and cell permeability. Imaging techniques involved in field of theranostic is mostly dependent on various types of contrast agents out of which luminescence probes acquire special attention. Such luminescence based imaging probes can be used to monitor the accumulation of nanomaterials in tissues and to track their multivalent interactions in intracellular domain. This dissertation focusses on biopolymer as well as small molecule based multifunctional nanomaterials in achieving the combined goal of *in vitro* therapy and diagnostics in a single module. The **chapter 1** begins with an insight into the fascinating world of multifunctional nanomaterials. It traces back to the developmental junctures of theranostic nano-medicine and discusses the most recent progresses in the field. Some of the landmark findings have been highlighted to convey the importance of multifunctional nanomaterials in different arenas. **Chapter 2** deals with chitosan biopolymer mediated formation of bimetallic silver nanoparticle based luminescent gold nanocluster composite nanoparticles for *in vitro* cancer theranostics. Herein, the composite nanoparticles deliver the combinatorial properties of both the metals present in different nanoscale domains and deliver both anticancer therapy and bioimaging of cervical cancer (HeLa) cells. The uptake of the composite nanoparticles was studied by time dependent sample analysis using TEM. The molecular events of cell death have been studied in detail by flow-cytometry based assays. Subsequently, **chapter 3** demonstrates cationic serum albumin based formation of composite nanoparticles embedded with luminescent bimetallic Au-Ag nanoclusters, which were applied for suicide gene therapy in HeLa cells followed by bioimaging. The combination therapy is achieved with cationic albumin based Au-Ag nanoclusters embedded composite nanoparticles loaded with a suicide gene (CD-UPRT). The suicide gene when successfully delivered into cells by the composite nanoparticles initiates a therapeutic response cascade by converting prodrug 5-FC to toxic 5-FU along with its metabolites. Additionally, the Au-Ag nanoclusters owing to their ultrasmall size generate reactive oxygen species, which further trigger apoptosis mediated cell death. Further, luminescence of Au-Ag nanoclusters serves to track the gene delivery into cells. The detailed mechanism of uptake and manner of cell death have been demonstrated to understand the combinatorial therapeutic efficacy of the composite system. In the **chapter 4**, a varied aspect of generation of reactive oxygen species for initiating apoptosis mediated cell death in HeLa cells was explored by implementing photodynamic

therapy. Herein, a mucin protein based luminescent gold nanocluster embedded composite nanoparticle has been developed for the delivery of photosensitizer drug methylene blue with subsequent monitoring of drug delivery with the aid of luminescent Au nanoclusters in HeLa cancer cells. The mechanism of cell death and uptake was analysed by flow cytometry as well as confocal microscopy. The **chapter 5** reports phenylboronic acid mediated development of targeted luminescent gold nanoclusters for *in vitro* cancer theranostics. The gold nanocluster probe was applied for *in vitro* targeted bioimaging of HeLa and Hep G2 cancer cells. It successfully demonstrated specific therapeutic effects toward cancer cells as well as multicellular tumor spheroids. They exhibited pronounced effect toward HeLa cells as compared to other cell lines, and a pathway of cell death was established using flow-cytometry-based assays. The targeted phenylboronic acid gold nanoclusters were also applied for specific detection of a biomarker mucin *in vitro*, using a smartphone based device. In **chapter 6**, a rapid and easy method of synthesis of protein based gold nanoclusters have been reported for diagnostic applications. The gold nanoclusters were successfully applied towards protein expression studies of recombinant proteins GST and GST-hGMCSF using a custom developed bench top device.

In brief, this dissertation explores the various forms of cancer theranostic solutions employing multifunctional nanomaterials. Rapid and facile synthetic procedures for multifunctional nanomaterials using biopolymers as well as small molecules were developed. Applications for delivery of metal nanoparticles, suicide gene, photosensitizer as well as smartphone based diagnostics were reported.

# Contents

---

|  |    |
|--|----|
| <b>Chapter 1: Introduction</b> .....   | 1  |
| 1.1 Fabrication of Nanomaterials .....   | 2  |
| 1.2 Characterization of Nanomaterials .....  | 3  |
| 1.3 Types of Nanomaterials .....   | 5  |
| 1.4 Multifunctional Nanomaterials and their Applications .....   | 9  |
| 1.5 Scope and Challenges .....   | 16 |
| 1.6 References .....   | 18 |
| <b>Chapter 2: Bimetallic Silver Nanoparticle–Gold Nanocluster Embedded Composite Nanoparticles for Cancer Theranostics</b> .....         | 25 |
| 2.1. Introduction .....  | 25 |
| 2.2. Synthesis and Characterisation of AgNP–AuNCs .....  | 28 |
| 2.3. Synthesis and Characterisation of Composite NPs (AgNP–AuNC–CSNPs) .....   | 30 |
| 2.4. Uptake and Bio-imaging Application of Composite NPs .....   | 32 |
| 2.5. Cell Viability Assay and Mechanism of Cell Death .....  | 33 |
| 2.6. Conclusions .....   | 36 |
| 2.7. References .....  | 36 |
| <b>Appendix A</b> .....  | 40 |
| A.1 Experimental Section .....   | 40 |
| A.2 Figures .....  | 45 |
| <b>Chapter 3: Cationic BSA Templated Au–Ag Bimetallic Nanoclusters as a Theranostic Gene Delivery Vector for HeLa Cancer Cells</b> ..... | 53 |
| 3.1. Introduction .....  | 53 |
| 3.2. Synthesis and Characterisation of Au–Ag NCs, Au–Ag NC-Embedded Cationic BSA .....   | 56 |
| 3.3. Synthesis and Characterisation of Au–Ag NCs Embedded Cationic BSA Composite Nanoparticles and pDNA Loading .....                    | 57 |
| 3.4. Uptake and Bio-imaging Application of pDNA Loaded Composite NPs .....   | 59 |
| 3.5. Cell Viability and Mechanism of Cell Death .....  | 61 |
| 3.6. Conclusions .....   | 63 |
| 3.7. References .....  | 64 |
| <b>Appendix B</b> .....  | 68 |
| B.1 Experimental Section .....   | 68 |
| B.2 Figures and Tables .....   | 72 |
| <b>Chapter 4: Gold Nanoclusters Embedded Mucin Nanoparticles for Photodynamic Therapy and Bioimaging</b> .....                           | 83 |
| 4.1. Introduction .....  | 83 |
| 4.2. Synthesis and Characterisation .....  | 87 |
| 4.3. Detection of Singlet Oxygen Generation .....  | 88 |

|  |     |
|--|-----|
| 4.4. Uptake and Delivery of MB Loaded Au NC-mucin NPs .....  | 89  |
| 4.5. Photodynamic Therapy and Mechanism of Cell Death .....  | 90  |
| 4.6. Conclusions .....   | 93  |
| 4.7. References .....  | 93  |
| <b>Appendix C</b> .....  | 96  |
| C.1 Experimental Section.....  | 96  |
| C.2 Figures .....  | 99  |
| <b>Chapter 5: Phenylboronic Acid Templated Gold Nanoclusters for Mucin Detection Using a Smartphone-Based Device and Targeted Cancer Cell Theranostics</b> ..... | 105 |
| 5.1. Introduction .....  | 105 |
| 5.2. Synthesis and Characterisation of PB-Au NCs .....   | 108 |
| 5.3. Uptake and Targeting of Cancer Cells by PB-Au NCs .....   | 109 |
| 5.4. Cell Viability and Mechanism of Cell Death .....  | 110 |
| 5.5. 3D Multicellular Spheroids Culture and Anticancer Activity .....  | 112 |
| 5.6. Antibacterial Activity .....  | 113 |
| 5.7. Detection of Mucin using Smartphone Based Platform .....  | 113 |
| 5.8. Conclusions .....   | 117 |
| 5.9. References .....  | 118 |
| <b>Appendix D</b> .....  | 121 |
| D.1 Experimental Section.....  | 121 |
| D.2 Figures .....  | 126 |
| <b>Chapter 6: Protein Expression Analyses Using Luminescent Gold Nanoclusters</b> .....  | 137 |
| 6.1. Introduction .....  | 137 |
| 6.2. Rapid Synthesis of Au Nanoclusters with Proteins .....  | 140 |
| 6.3. Application of Au Nanoclusters for Protein Expression Studies.....  | 143 |
| 6.4. Enhancement of Sensitivity with Zinc Ions.....  | 145 |
| 6.5. Conclusions .....   | 145 |
| 6.6. References .....  | 146 |
| <b>Appendix E</b> .....  | 149 |
| E.1 Experimental Section .....   | 149 |
| E.2 Figures.....   | 152 |
| <b>Conclusions and Future Perspectives</b> .....   | 157 |
| <b>Publication and Patents</b> .....   | 159 |
| <b>Conference and Workshop attended</b> .....  | 161 |
| <b>Permissions</b> .....   | 162 |

# Abbreviations

---

**AFM:** Atomic force microscopy

**AAS:** Atomic absorption spectroscopy

**BSA:** Bovine serum albumin

**CT:** Computed tomography

**CD:** Circular dichroism

**CD-UPRT:** Cytosine deaminase uracil phosphoribosyltransferase

**CDNB:** 1-Chloro-2,4-dinitrobenzene

**DPBF:** 1, 3 – diphenylisobenzofuran

**DLS:** Dynamic light scattering

**DCFHDA:** Dichloro-dihydro-fluorescein diacetate

**EMF:** Electromotive force

**EDX:** Energy dispersive X-ray

**FTIR:** Fourier transform infrared spectroscopy

**FESEM:** Field emission scanning electron microscope

**FITC:** Fluorescein isothiocyanate

**FACS:** Fluorescence activated cell sorter

**GUI:** Graphical user interface

**GSH:** Glutathione

**GST:** Glutathione-S-Transferase

**HRTEM:** High resolution transmission electron microscope

**SAED:** Selected area electron diffraction

**SDS:** Sodium dodecyl sulphate

**SERS:** Surface enhanced raman scattering

**TEM:** Transmission electron microscope

**TPP: Trisodium polyphosphate**

**LDH: Lactate dehydrogenase**

**LED: Light emitting diode**

**MALDI-TOF: Matrix Assisted Laser Desorption/Ionization-Time of flight**

**MB: Methylene blue**

**MEMS: Micro electro mechanical systems**

**MPA: Mercaptopropionic acid**

**MUA: Mercaptoundecanoic acid**

**MRI: Magnetic resonance imaging**

**MTT:[3-(4,5-dimethylthiazol-2-yl)-2,5-diphenyltetrazolium bromide]**

**MIC: Minimum inhibitory concentration**

**MBC: Minimum bactericidal concentration**

**NEMS: Nano-electro-mechanical systems**

**NPs: Nanoparticles**

**NCs: Nanoclusters**

**PDT: Photodynamic therapy**

**PET: Positron emission tomography**

**pDNA: Plasmid DNA**

**PEI: Polyethyleneimine**

**PAMAM: polyamidoamine**

**PI: Propidium iodide**

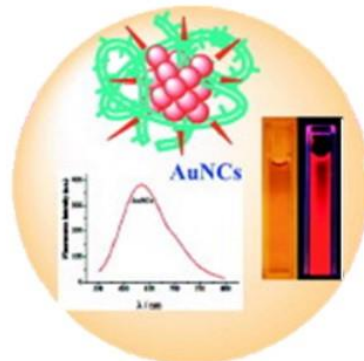
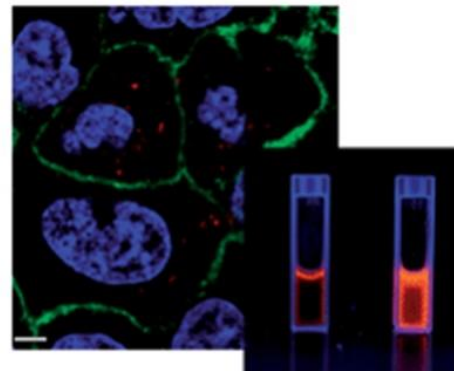
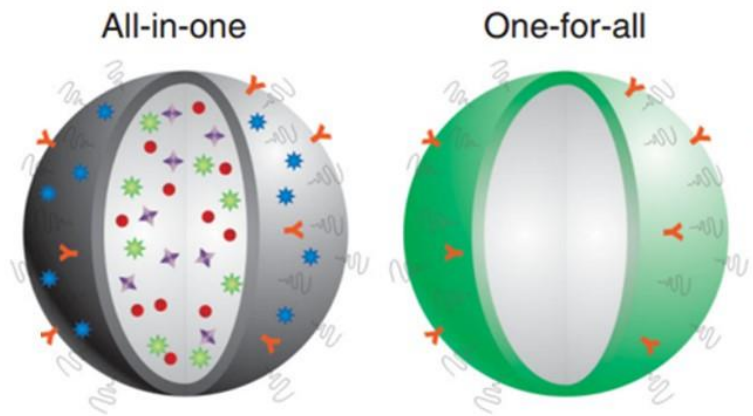
**PVDF: Polyvinylidene difluoride**

**TNBS: 2,4,6-Trinitrobenzene Sulfonic Acid**

**XRD: X-ray diffraction**

**XPS: X-ray photoelectron spectroscopy**

# Chapter 1



## Introduction



## Chapter 1

# Introduction

---

The incessant efforts towards identification and advancement of first-hand drug development and diagnostics have led to a considerable decline in mortality rates for most of the life-threatening diseases, such as cancer, which is one of the leading causes of death across the globe. However, out of the administered drugs, a small portion is conveyed to the diseased site. Moreover, multidrug resistance <sup>(1)</sup> is a key factor contributing to the failure of several chemotherapeutic drugs affecting the treatment regime of different types of cancers including cervical, liver, breast, ovarian, lung, and colon cancer. Nanoparticles offer to improve the pharmacokinetic profile of drugs, reduce off-target interactions, and increase therapeutic index as well as circulation time in blood.<sup>(2)</sup> The strategic approach towards development of multifunctional nanoparticles is intended to advance the early diagnosis, delivery, therapeutic efficacy, prognosis and outcome of treatment in due course. Also, to deliver the therapeutic payload selectively to cancer cells it demands functionalization of nanoparticles with targeting molecules that can bind to their kindred counterparts overexpressed on the target cells. Multifunctional nanoparticles also exhibit synergistic action when actively targeted with therapeutic antibodies, genes, peptides etc.<sup>(3)</sup> Apart from this, the approach of nano-packaging the therapeutic moieties hold several other advantages like enhanced solubility, increased oral bioavailability, increased surface area, decreased dosage, to name a few.<sup>(4)</sup> Together with recent methodologies implemented for improving the therapeutic accomplishments, nanoparticles are being explored for various novel and improved methods of disease detection. This has been realised with the innovative development of image contrast agents along with their conjugation with targeting molecules. Quantum dots, metal nanoclusters, paramagnetic nanoparticles, SERS active nanoparticles are widely employed for diagnostic resolutions.<sup>(5-8)</sup> The integration of therapeutic and diagnostic properties in a single entity had of late emerged as a recent trend, more commonly referred to as ‘theranostics’. Theranostic agents can simultaneously convey both imaging and therapeutic payloads to the desired locations enabling two in one action. This is deemed with the advantage of having similar biodistribution of both imaging and therapeutic molecules, which in turn assists in tracking the real time localisation as well as therapeutic outcome of the molecules *in vitro* or *in vivo*. As a result, there is a better prognosis, allowing development of personalized medicine to improve the quality of treatment and survival chances.

The word Nano was coined from the Latin word ‘nanus’ meaning dwarf. The size domain of nanotechnology denotes to one thousand millionth of a meter (i.e. 1 nm = 10<sup>-9</sup> m). Nanotechnology is a widely applied interdisciplinary science in fields like electronics, chemistry, physics, biology

and engineering since many decades. It is termed as science of materials and the devices based on them expressing novel and reformed physical, chemical and biological properties attributed to their nanoscale size. In particular nanotechnology has fashioned a special impression in various arenas of medicine including oncology, immunology, endocrinology, radiology, ophthalmology, and importantly, specialized areas like delivery of therapeutic gene, drug delivery across blood-brain barrier etc. Nanotechnology offers noteworthy systems, materials and devices for enhancement of pharmaceutical applications. Thus, through the manipulation of matter in molecular and nanoscale levels, nanotechnology provides novel technological advances mainly in the field of medicine leading to the rise of an independent branch, referred to as nanomedicine. There are five sub-disciplines of nanomedicine specified according to European Science Foundation, which includes nanoimaging tools, analytical tools, clinical and toxicological issues, nanomaterials and nanodevices, drug delivery systems and novel therapeutics.<sup>(9)</sup>

## 1.1 Fabrication of Nanomaterials

The fabrication of nanomaterials, are broadly classified into two main classes top-down approach and bottom-up approach.<sup>(10)</sup>

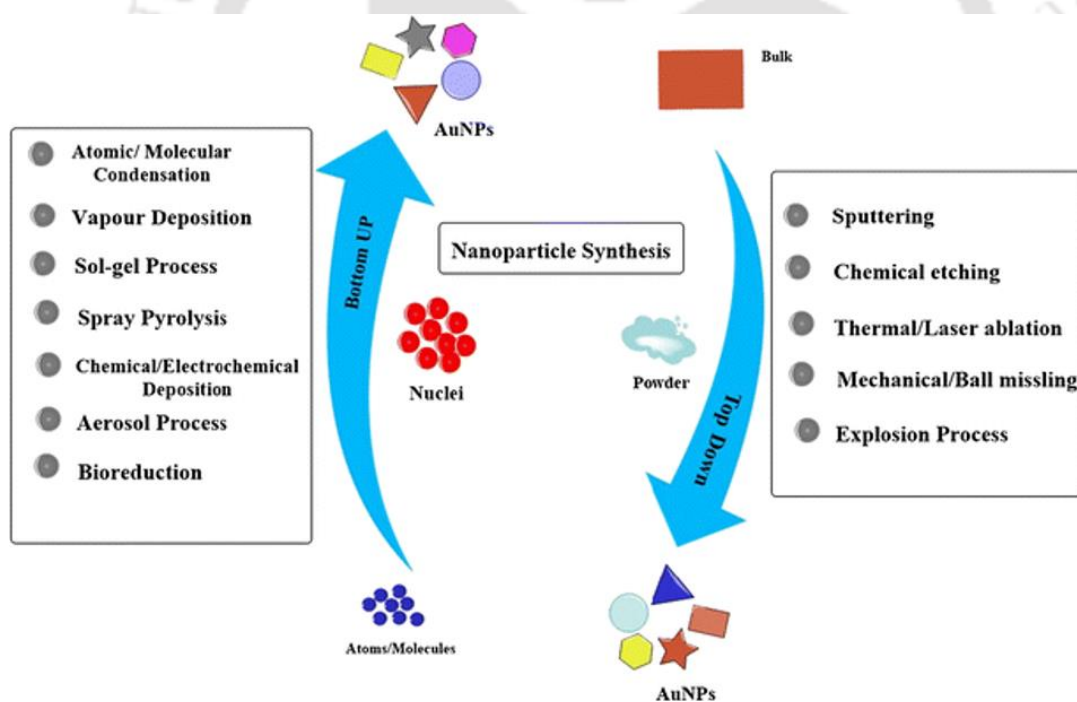


**Figure 1.1.** Top-down and bottom-up methods for the synthesis of nanoparticles. (Reprinted with permission from reference (10) Copyright 2017, Springer-Verlag Berlin Heidelberg)

### Top-down synthesis

In this method, the bulk material is disintegrated into particles via physical processes like milling or grinding, crushing, and lithography. The larger materials after being decomposed into smaller units are then converted into suitable nanoparticles. Top down approaches are extensively employed in the

development of MEMS (micro electro mechanical systems) technology in micro-electronics industry.

However, this process usually does not yield homogenous shaped materials, and the process of acquisition of very small particles at the cost of high energy is complicated.<sup>(11)</sup> Also, the materials synthesised by this route are bestowed with imperfections in the surface structure, crystallographic damage which have a profound impact on their physical properties and surface chemistry.

### **Bottom-up synthesis**

This is the general synthetic route implemented for preparing most of the nanoscale materials. Precursor atoms/molecules via reduction and sedimentation techniques or chemical vapour deposition (CVD), physical vapour deposition (PVD) and other decomposition techniques build up (block by block) to form nanoparticles with desired properties. Such build up finally gives rise to nanoparticles of uniform size, shape and distributions. It is generally governed by chemical synthesis and has precise control over the reaction to inhibit further particle growth thereby giving rise to nanoparticles of desired size. Green synthesis of nanoparticles using biomolecules as precursors has invited attention due to their ease in synthesis, eco friendliness and non-toxic nature.<sup>(12)</sup> Proteins, biopolymers, phytogetic extracts, bacterial cells, and even mammalian cells are widely explored for the synthesis of nanoparticles.

## **1.2 Characterization of Nanomaterials**

### **Morphological characterization**

The morphology of the nanoparticles influences its properties in a significant manner and thereby plays a decisive role in demarcating its applications. This makes the study of morphology an important aspect to understand properties of nanomaterials in detail. There are varied characterization procedures for morphological examination of which techniques such as SEM and TEM are the foremost ones. SEM is based on scanning the sample with an electron beam, wherein a fine electron beam focuses on a sample and after interaction with the sample produce signals in the form of secondary electrons which in turn are detected through secondary electron detectors. The emission of secondary electrons near to the surface of the sample leads to high-resolution image formation of the surface. Similarly, TEM is based on electron transmittance principle, wherein an electron beam is transmitted through a sample. Upon interacting with the sample the passage of the electrons through it results into formation of an image which is then magnified and captured by focussing onto a detection device which then processes the information about the sample at various magnifications starting from low to high.

**Structural characterization**

The information about structural properties is essential for revealing the composition and nature of the nanomaterials. Techniques such as XRD, EDX, Raman, XPS, IR, BET and Zeta/size analyser are commonly implemented to unknot the structural features of nanoparticles.

**Particle size and surface area characterization**

The size of the nanoparticles is one of the major factors which influences its applicability in different procedures. For particle size measurement sophisticated techniques like SEM, TEM, AFM, and DLS are implemented. SEM, TEM, and AFM provides the dry diameter of the particles, whereas DLS can measure the hydrodynamic diameter of the nanoparticles. The Brownian motion displayed by nanoparticles in suspension is measured by DLS, which then relates its translational diffusion coefficient (velocity), to the size of nanoparticles based on the Stokes–Einstein equation. In case of agglomeration however, DLS may offer inaccurate measurements, wherein a high resolution technique named differential sedimentation centrifugation comes into play. The relation between Brownian motion rate to particle size is utilized in nanoparticle tracking analysis (NTA) which can be applied to visualize and analyse nanoparticles in media. For surface area characterisation of the nanoparticles, a technique named BET is implemented wherein nitrogen gas is used for the purpose of elucidating the principle of adsorption, desorption using Brunauer–Emmett–Teller (BET) theorem. Four different types of isotherm namely Type-I, Type-II, Type-III and Type-IV are produced in BET.

**Optical characterization**

It is important to acquire a fair knowledge of optical properties of the nanoparticles as they are keenly regarded in photocatalytic, electronics as well as biological applications. The optical properties of nanoparticles can be illustrated by UV-visible spectroscopy wherein quantitative formation and size measurement of nanoparticles can be monitored through tracking their different responses corresponding to the electromagnetic waves, ranging from 190.0 nm to 700.0 nm. FTIR is implemented to gather information about capping and stabilization of nanoparticles by elucidating functional groups from the spectrum. The crystal properties and information regarding lattice spacing of nanoparticles can be verified by XRD. Nanoparticles such as quantum dots, metal nanoclusters exhibit size dependent luminescence properties which are of major interest for photo-related application of these luminescent particles. The fluorescence (photoluminescence) spectroscopy provide the information regarding the excitation and emission profile of luminescent nanoparticles. This technique sells information about the important optical properties such as absorption, luminescence, reflectance, and phosphorescence of nanoparticles.

### 1.3 Types of Nanomaterials

On the basis of the physiochemical properties, nanoparticles are broadly categorised into various classes as given below.

#### **Carbon-based nanomaterials**

Carbon nanotubes, discovered in 1991 are tubular structures that contain hexagonal networks of carbon atoms having diameter of one nanometre and length ranging from 1 to 100 nm. Layers of graphite are arranged and rolled up into a cylindrical form creating this carbon network. They exhibit unique electrical properties and are well noted for their strength. They are classified into two different types single-walled nanotubes (SWNTs) and multiwalled nanotubes (MWNTs). Additionally, C60 fullerenes which are hollow, carbon-based, cage-like architectures, also known as bucky balls, have made significant advances in the field of carbon based nanomaterials. The morphology, surface and size characteristics of these materials make them attractive candidates for drug delivery applications. Also, they can be functionalized to enhance solubility, penetration into cell cytoplasm as well as nucleus and finds application in photodynamic therapy, photothermal therapy, gene delivery, peptide delivery.<sup>(13,14)</sup> Additionally, they are recognised as efficient gas adsorbents for environmental remediation, and as support medium for catalysts. Fullerenes have also shown drug targeting capability to a greater extent. Carbon dots (CDs), as well as graphene quantum dots (GQDs), are emerging class of fluorescent carbon based nanomaterials <sup>(15)</sup>, discovered by scientists (Xu et al.) in 2004. Such a finding was accomplished during the electrophoretic purification of single walled carbon nanotubes (SWCNTs) via arc-discharge methods. They have exceptional merits in terms of their luminescence, chemical stability, excellent biocompatibility and have been explored in a wide range of applications.

#### **Lipid-based nanomaterials**

Lipid based vesicles known as liposomes are comprehensively explored and extensively developed nanocarriers for drug delivery.<sup>(16)</sup> These vesicles synthesized by hydration of dry phospholipids can entrap drug molecules in aqueous space or get intercalated into the lipid bilayer of liposomes. Liposomes with versatile properties such as distinct composition, size, options for multiple surface modification can be developed making them as intelligent nanocarriers for both active and passive delivery of theranostic molecules. They have been successfully exploited in drug therapy, immunotherapy, gene delivery etc.<sup>(16)</sup> An alternative nanocarrier system for liposomes are the solid-lipid nanoparticles which were developed for controlled drug delivery. They have distinct advantages in terms of presence of a solid lipid matrix with an average diameter below 1  $\mu\text{m}$  where the drug is generally incorporated. They are nanoparticles produced by high pressure homogenization in presence of surfactants to avoid aggregation and to promote stabilization of the dispersion.

**Polymeric nanomaterials**

Natural polymer based nanoparticles bestow substantial enhancement over traditional drug delivery systems in terms of biocompatibility, biodegradability and efficacy for potential application in drug and gene delivery, tissue engineering, and immunotherapy.<sup>(17)</sup> The various natural polymers like chitosan, gelatin, albumin and alginate are used to prepare the nanoparticles. Modified forms of natural polymers consisting of synthetic polyesters like poly(D, L-lactide) and related polymers like poly(lactic acid) or poly(lactide-co-glycolide) PLGA have also been explored widely. Although they suffer from some inherent drawbacks like immunogenicity, poor reproducibility and susceptibility to degradation, there are several notable advantages enlisted such as improvement in stability of pharmaceutical molecules, easier bulk production, feasibility in being engineered to deliver theranostic agents to a desired target. Polymer drug conjugates<sup>(18)</sup> can also be formulated by the conjugation of low molecular weight drugs with polymers. This, in fact, improves the pharmacokinetic profile of drug throughout the body and various intracellular locations. They are specifically designed to have high molecular weight with appropriate size so that after being passively targeted, the nanoformulation facilitate their retention in cancer cells through enhanced permeation and retention effect. Drug loaded onto polymeric nanoparticles is limited into a cavity fenced by polymeric membrane and matrix type in which the drug is dispersed or attached throughout the polymer matrix. The release kinetics of the drug incorporated into the polymer can be modulated depending on the properties demonstrated by the polymer in intracellular environment. Polymeric nanoparticle systems are attractive modules for intracellular and site specific delivery. From the polymer chemistry viewpoint, it will be a challenge to create new polymers matching hydrophilic and lipophilic properties of upcoming drugs for smart formulation in the nearby future. Polymers carrying functional groups have also been explored as stabilizers for synthesis of nanoparticles.<sup>(19)</sup> Due to hydrophobicity and high surface-to-volume ratio, nanoparticles tend to agglomerate which can be avoided in presence of a suitable stabilizer. Various kinds of stabilizers like surfactants, polymers like poly(vinyl alcohol) (PVA), poly(vinyl pyrrolidone), poly(l-lactide) and poly( $\epsilon$ -caprolactone) etc. have been utilised to provide steric protection and to prevent aggregation of nanoparticles along with size control.

**Metal nanoparticles**

The term metal nanoparticle is used to describe metal particles with dimensions (length, width or thickness) within the nanoscale domain having a size range of 1-100 nm and possesses captivating properties markedly distinct from their bulk metal counterparts. The existence of metallic nanoparticles in solution was first recognized by Faraday in 1857. The quantitative explanation of their colour was further defined by Mie in 1908. The dynamic display of visible colours by noble metal nanoparticles is the outcome of collective oscillations of conduction band electrons resulted by excitation using the light of suitable frequency. The collective oscillation of the conduction

electrons induced by the incident electric field results in light scattering exhibiting the phenomenon of localized surface plasmon resonance (LSPR). LSPR are surface electromagnetic waves propagating in a parallel direction to the metal/dielectric (or metal/vacuum) interface. The position of the plasmon band can be ascertained using a UV-visible spectrophotometer which generally appears with an extremely high extinction coefficient. Due to the high surface area to volume ratio, the surface plasmon resonance frequency in case of nanoparticles is highly sensitive to the shape, size of nanoparticle and dielectric environment. These properties are favourably put together for the purpose of innovative development of biosensors, optoelectronic devices, memory devices, chemical sensors, photosensitizers, photothermal agents and enhanced Raman spectroscopy substrates.<sup>(20)</sup> Metallic nanoparticles have captivated the attention of scientific community in the recent past and have been extensively applied in biomedical and engineering solutions. These materials can be synthesised and functionalised with molecules such as antibodies, ligands, sugars, peptides and drugs as per the requirement allowing them to be qualified for multiple applications in pharmaceutical biotechnology, biosensor development, bioassays, targeted drug, protein, peptide and gene delivery combined with diagnostic imaging. With the advancement of time, metal nanoparticles (iron, gold, copper, silver) have been developed to act as agent with contrasting property in imaging modalities like MRI, CT, PET, ultrasound, SERS, and optical imaging, which makes them an important tool for medical diagnostics.<sup>(21)</sup> Additionally, metal nanoparticles of varied morphologies have been explored for therapeutic action via ROS mediated cell death, photothermal, photodynamic effects. They are also used in combination with chemotherapeutic drugs to fight against multidrug resistance, enabling administration at minimal dosage and enhanced activity.

### **Semiconductor nanoparticles**

In case of bulk inorganic semiconductors, the charge carriers are represented by electrons and holes. The electron hole pair, loosely bounded is generally delocalised over a larger area in comparison to the lattice constant. This distance which is few nanometers is known as the Bohr radius. The minimum energy that is mandatory for separation of charge carriers is known as band gap energy. As the size of semiconductor material becomes equal to or smaller than the Bohr radius, such that the space where the charge carriers move decreases, it results in quantum confinement. This results in increase of band gap energy, along with the increase in the kinetic energy of the electron and hole and increased density of the charge carriers. Excitons are generated in such nanomaterials upon the absorption of light, and electron-hole recombination finally leading to luminescence. QDs are colloidal semiconductor nanocrystals with dimensions ranging from 2 to 10 nm. They are crystalline materials with facets and a lattice structure analogous to bulk semiconductor material. Semiconducting quantum dots, having particle sizes in nano domain, possess striking features in contrast to bulk semiconductors. Depending on their sizes, quantum states and confinement of their excitons, semiconducting quantum dots may shift their optical absorption and emission energies.

The capping procedure of quantum dots improves their solubility in water or buffers. The outer shell of the quantum dots is available for biomolecular conjugation and targeting. Owing to their size dependent tunable emission, high quantum yield, photostability and broad excitation range, QDs have been adopted for *in vitro* bioimaging and real time intracellular tracking.<sup>(22)</sup> QDs have been applied as a fluorescence probe in *in vitro* and *in vivo* diagnostic assays, genomics, proteomics, MRI contrast agents, single particle tracking, vehicles for drugs, recombinant protein, gene therapy, biolabeling of cells and particularly for cancer theranostic.<sup>(23)</sup>

### **Metal nanoclusters**

Metal nanoclusters of noble metals (e.g., Au, Cu, Ag) are comprised of sizes less than 2-3 nm and has attracted attention owing to their excellent features, such as luminescence, biocompatibility, large Stokes shift, photostability, and ease of synthesis.<sup>(24)</sup> They bridge the gap “missing link” between metal atoms and metal nanoparticle by displaying molecule like behaviour. In case of bulk metals, the absence of energy gap between valence band and conduction band restrict the motion of electrons unlike in metal NPs. In metal nanoparticles, size constrains limits the motion of electrons leading to occurrence of interactions of the electron on its surface giving rise to the phenomenon of surface plasmon resonance. In case of metal NCs, the size is further scaled down to less than 2-3 nm, due to which the continuous band becomes discretised into different levels making them neither conductive nor plasmonic. On irradiating with an incident light of suitable wavelength, electrons transitions occur between the energy levels leading to excitation which is followed by the consecutive event of emission. This dominant optical property allows metal nanoclusters to qualify as luminescent probes in biosensor development and bio-imaging applications. Fluorescent metal NCs are considered as good alternatives to organic dyes and QDs due to its minimum cytotoxicity, high photostability, large Stokes shift, higher aqueous solubility. Also, wide varieties of chemical as well as biological materials can act as stabilizers for their synthesis. In fact, they can be readily functionalized with targeting agents for site specific activities finally equipping the entire moiety to be suitable for both *in vitro* and *in vivo* applications. These nanoclusters due to their ultrasmall size have been reported to have ROS generation capability which can be exploited in cancer therapeutics. Good renal clearance and biodistribution has been observed for metal nanoclusters in *in vivo* investigations.<sup>(25)</sup>

## 1.4 Multifunctional Nanomaterials and their Applications

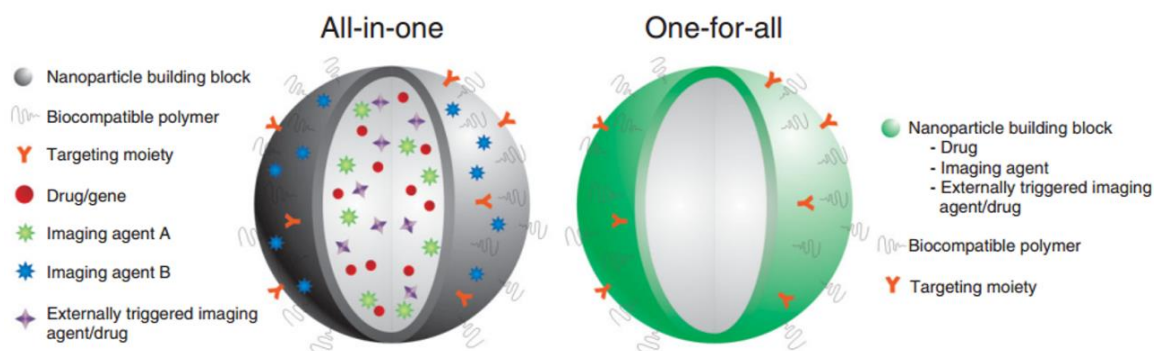


**Figure 1.2.** Design approaches for multifunctional nanoparticles. All-in-one design involves combination of different entities into a single nanoparticle. One-for-all design incorporates multifunctional properties possessed inherently in single nanoparticle. (Reproduced with permission from reference (26). Copyright 2013, Wiley Periodicals, Inc.)

Amongst the emerging branches of life sciences biomedical nanotechnology requires special mention. It has extended the applications of nanotechnology towards biomedical applications in the form of materials and devices for drug delivery, diagnostic, imaging and biosensing. This provides for accurate diagnostics and dedicated treatment of a disease at cellular and molecular levels. It helps in improvement of detection of biomarkers associated with diseases such as cancer, autoimmune diseases, genetic disorders, diabetes mellitus, neurodegenerative diseases, infectious diseases as well as it can detect whole cells (pathogenic microorganisms and viruses) associated with infections. Applications of nanotechnology to therapeutics providing smart delivery systems is expected to surface as an alternate to form of treatment along with conventional therapeutic solutions. Biomedical nanotechnology is profoundly influenced by two most important elements namely nanomaterials and nanodevices. Orthopedic and dental implants, prosthetics, drug encapsulation matrices together with scaffolds for tissue-engineered constitutes the nanomaterials for biological applications. Nanodevices mostly constitute of nanoscale miniaturised devices including nanoelectromechanical systems and microelectromechanical systems (NEMS/ MEMS), microarrays and microfluidics. They are applied for detection of biomolecules/chemical moieties or real time tracking of the same for development of healthcare devices/detection systems.

### Cancer theranostics

Theranostics is a rapidly growing discipline that has shown significant advancement in different sectors like pharmaceuticals, molecular biology, medicine, nanotechnology, physics and chemistry. With the amalgamation of nanotechnology a new arena called “nanotheranostics” have evolved which comprises of nano based formulations for pursuing combined diagnostics and therapeutics for simultaneous detection as well as imaging mediated therapeutic delivery and concomitant release.

Cancer theranostics similarly goals for combinatorial diagnosis and therapeutics to alleviate cancer as well as for detection of cancer at nascent stages thereby diminishing delays in treatment and improved personalized treatment. Developments in material science have provided for a leap in the field of cancer theranostics which includes characterisation and discovery of novel cancer biomarkers, methods for early cancer detection and development of contrast agents for imaging, image guided cancer therapy, nanomaterials based platforms embedding both cancer imaging and therapeutic agents. It is anticipated that with the recent developments it will be possible to identify cancer early, analyse the pharmacokinetics and pharmacodynamics profile of newly developed therapeutics, monitor success of the therapy and therapeutic response. The procedures that are adopted for imaging purposes are optical imaging (OI), magnetic resonance imaging (MRI), photoacoustic imaging (PAI), positron emission tomography (PET) and ultrasound (US). Among these techniques optical imaging (fluorescence based) is economically feasible, easily adaptable and has become one of the commonly used approaches for *in vitro* and *in vivo* applications. In fluorescence based imaging the probe is excited by a light source and the emitted light is collected at desired wavelengths. The obtained optical signals provide information regarding the underlying molecular and cellular processes that contribute towards cancer development and its clinical presentation.

#### **Biomolecule based bimetallic nanomaterials for cancer theranostics**

The ultimate aim of majority of nanomaterial based biomedical technologies is cancer diagnostics and development of anticancer agents for therapy. Nanotheranostics have been implemented by amalgamating unique inherent properties of nanomaterials of different nanoscale levels into a multifunctional platform.<sup>(26)</sup> Several nanoparticles like silver, copper, zinc etc. have been reported to have anticancer applications by virtue of its potential in ROS generation and succeeding DNA damage. However, there lacks a mechanism to track these nanoparticles inside cancer cells alongside bioimaging. To fulfil this requirement organic dyes, quantum dots and carbon dots have been extensively experimented as a diagnostic entity. Ortega and co-workers reported a study of antitumor activity in breast cell lines using silver nanoparticles (Ag NPs) conjugated with FITC.<sup>(27)</sup> Pietro et al reported FITC-RGD peptide functionalized silver nanoparticles as a targeted platform for cells and bacteria.<sup>(28)</sup> ZnO quantum dots labelled Au nanoparticles were designed for targeted camptothecin delivery in cancer cells.<sup>(29)</sup> Another investigation on carbon dots embedded into composites alongwith silver/zinc have been carried out for cancer theranostics.<sup>(30)</sup> However, these compounds suffer from drawbacks like narrow Stokes shift, photoblinking, low stability, heavy metal toxicity and poor water solubility. Their synthesis also requires multistep processing, high temperature reactions as well as time consuming methods. Also, blue emission of most of the carbon dots makes them susceptible to interference from cellular autofluorescence. Therefore, novel luminescent metal nanoclusters (Au, Ag, Cu) synthesized using biomolecular templates like chitosan, protein, DNA,

dendrimers etc. have been preferred to act as diagnostic probes. These metal clusters exhibit extraordinary properties in terms of luminescence, photo stability, longer luminescence lifetime, large Stokes shift.<sup>(31)</sup> They render possibilities for functionalisation and exhibit less toxicity thereby enabling their use as in vitro as well as in vivo probes. Hence, therapeutic nanoparticles conjugated with luminescent nanoclusters becomes an ideal candidate towards developing a multifunctional theranostic system. Bimetallic systems moreover offer combined properties of two metals and have proved to be more efficient in comparison to their monometallic counterparts. A luminescent Au-Ag alloy quantum clusters (QCs) in bovine serum albumin (BSA), was reported with combined properties of both metals.<sup>(31)</sup>

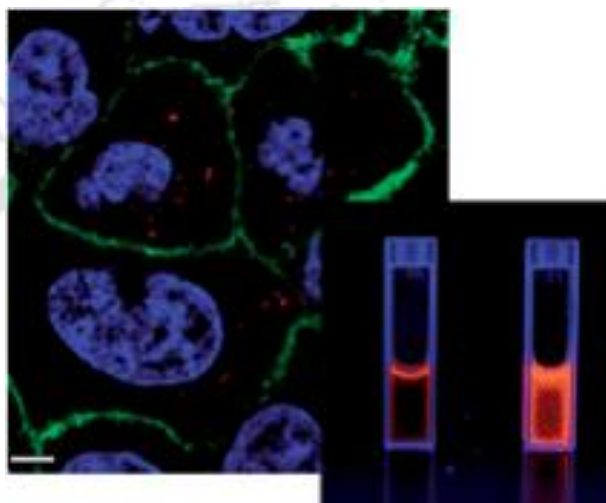


**Figure 1.3.** Photostable silver doped gold nanoclusters having enhanced fluorescence applied for bioimaging. (Reproduced with permission from reference (32), The Royal Society of Chemistry. Copyright 2012, Royal Society of Chemistry.)

Xavier and co-workers reported a highly photostable silver doped gold nanoclusters having enhanced fluorescence and applied for bioimaging.<sup>(32)</sup> Also, bimetallic systems have been applied as efficient catalyst compared to monometallic ones in oxidation reactions. Nevertheless, there are only a few reports on therapeutic applications of bimetallic nanocluster systems. In order to achieve sustained delivery and protection from degradation, these metal nanoparticles need to be embedded into a suitable nanocarrier. The potential of nanocarriers based on dendrimers, liposomes, hydrogels, and polymeric NPs in drug delivery has been well established, whereas their implementation in delivery of metal NPs for theranostics is less explored. Some of the similar reports include a targeted gold nanocluster-conjugated amphiphilic block copolymer for camptothecin delivery in cancer cells designed by Chen and co-workers.<sup>(33)</sup> Another report demonstrated carbon dot embedded chitosan nanoparticle for cell imaging and telmisartan hydrophobic drug delivery.<sup>(34)</sup>

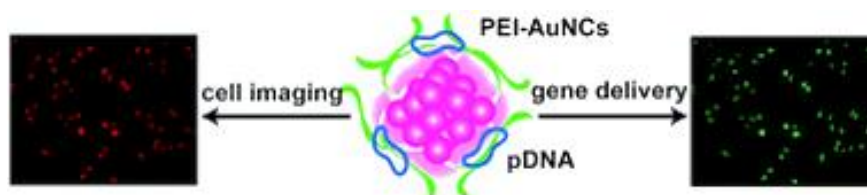


**Figure 1.4.** PEI- functionalized gold nanoclusters for therapeutic gene delivery.(Reproduced with permission from reference (39), The Royal Society of Chemistry. Copyright 2013, Royal Society of Chemistry.)

Gene therapy has attained a distinctive position amongst the advanced forms of treatment in current era. It is related to the transfer of nucleic acids to the diseased cells in order to correct the genetic anomalies thereby restoring normal function. Suicide gene therapy is one of the prominent forms of gene therapy executed in clinical trials. In this technique, genes of interest are inserted into diseased cells via vectors and the delivered gene in presence of a suitable prodrug converts the non-toxic prodrug into a toxic drug and its metabolites, further triggering the destruction of cancer cells. One of the widely applied suicide gene therapy system consists of *E. coli cytosine deaminase uracil phosphoribosyltransferase* (CD-UPRT) encoded suicide gene which converts nontoxic prodrug 5-fluorocytosine (5-FC) to 5-fluorouracil (5-FU) and other toxic metabolites. An important aspect, which provides the scope to explore the versatility in a gene therapy procedure lies in the design of a suitable delivery vector. It must ensure the delivery of the loaded gene to its destined location along with assured protection from nuclease degradation and better stability in both intracellular and extracellular environments. Hitherto, there are different types of gene delivery vehicles developed including viral vectors which have proved to be much more efficient but are less preferred due to its highly immunogenic nature and economically unfeasible procedures involved. Thereby with the advancement in nanomedicine, researches have been streamlined towards developing nanomaterials based gene delivery carriers. Cationic polymers like PEI, chitosan, DEAE dextran, poly-lysine, etc. have been applied for the synthesis of non-viral vectors.<sup>(35)</sup> Serum albumin which had been a good choice of material for drug delivery has also been explored for delivery of siRNA after converting it into cationic albumin. Yet, there lies a lot of opportunities in using serum albumin as a gene carrier. Gene therapy guided via molecular imaging is essentially required for tracking the delivery process and analysing its ultimate fate. Variety of fluorescent based probes like organic dyes and semiconductor quantum dots have been applied in this regard. PEI-FITC functionalized single shell calcium phosphate nanoparticles were reported as gene delivery agents with comparative study conducted in different cell lines.<sup>(36)</sup> Also, another approach on synthesis of cationic carbon quantum dots from alginate was carried out for gene delivery applications.<sup>(37)</sup> An efficient gene delivery vehicle was designed using CdSe quantum dot coated electrostatically with polyethyleneimine for application in human colon cancer cell lines.<sup>(38)</sup> However, as discussed above, these materials suffer from setbacks with respect to their inherent properties hindering their use in such processes. Few atomic metal nanoclusters have been widely applied for bioimaging recently. Metal nanoclusters can

be synthesised on polymers like chitosan, DNA, protein, peptides, PAMAM, PEI which act as stabilizers. Hence, such nanoclusters can be easily incorporated into a polymers based gene delivery vehicle. PEI- functionalized gold nanoclusters<sup>(39)</sup> and PEI-capped silver nanoclusters<sup>(40)</sup> were developed for gene delivery applications and microRNA delivery respectively. Gold nanoclusters were successfully implemented as a carrier of NGF siRNA for treatment of pancreatic cancer.<sup>(41)</sup> Further, TAT peptide based nucleus-targeting gold nanoclusters were applied for gene delivery along with other multifunctional applications.<sup>(42)</sup>

### Biomolecule based photodynamic drug delivery for cancer theranostics

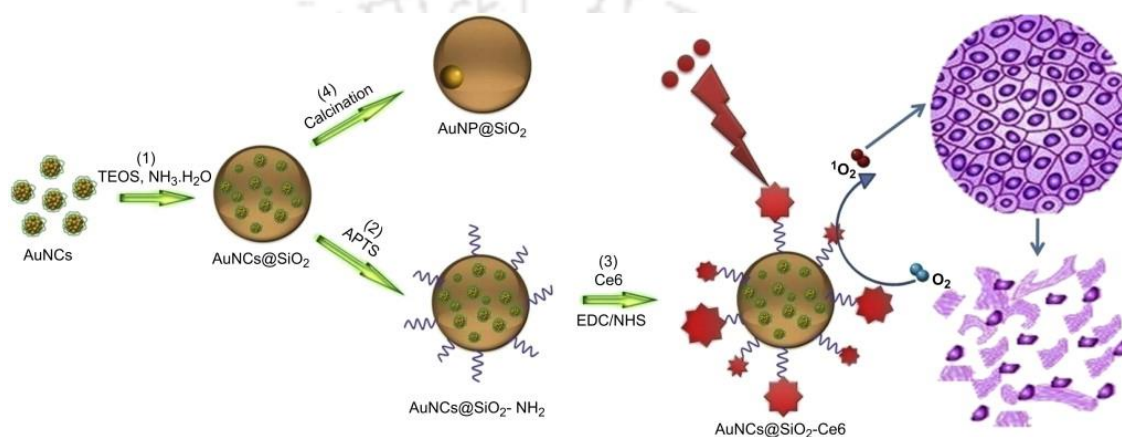


**Figure 1.5.** Ce6-conjugated silica-coated gold nanoclusters (AuNCs@SiO<sub>2</sub>-Ce6) for photodynamic therapy and the calcination of AuNCs@SiO<sub>2</sub> into AuNP@SiO<sub>2</sub>. (Reproduced with permission from reference (47) Copyright 2013, Elsevier Ltd.)

Photodynamic therapy (PDT) is an imminent alternative, non-invasive form of treatment for diseases such as dental plaques, acne vulgaris, dermatological disorders and most notably cancers. In this form of therapy, photosensitizers (PS) when activated by a suitable light irradiation, undergo photochemical reactions resulting in generation of singlet oxygen that triggers apoptosis mediated cell death. However, some of the notable limitations of most of the current PSs include poor accumulation in tumor sites, degradation of photophysical characteristics, low solubility in physiological fluids and self-aggregation.<sup>(43)</sup> To combat these issues several types of nanocarriers are developed such as liposomes, polymeric nanoparticles, carbon based nanomaterials, metal nanoparticles, quantum dots (QDs), and upconversion nanoparticles (UCNPs). Such nanocarriers are synthesized with the basis to encapsulate the photosensitizers to provide stability and prevent their unwanted interactions with the surrounding environment. Also in the process of developing a nanocarrier, the biocompatibility, biodegradability and its penetration ability are some of the important factors to be taken into account. In conventional photodynamic therapy, there are no significant means to trace the photosensitizers that obstruct tracking of outcomes in such therapies.

With the development of biomedical nanoscience, image-guided photosensitizer delivery is gaining popularity which not only aids in tracking but also enables follow up of the therapeutic regime. Such an advancement leads to better management of the disease and effective cure.<sup>(44)</sup> A wide variety of luminescent materials including QDs, nanoparticles conjugated organic molecules and metal nanoclusters have been developed as multifunctional platform for both optical imaging and photosensitizer delivery. Wu and his co-worker developed a targeted FITC conjugated folic acid chitosan functionalised carbon nanotubes for pyropheophorbide mediated photodynamic therapy.<sup>(45)</sup> Another study was performed where CdTe quantum dot/ photosensitizer hybrid system was applied for photodynamic therapy in HeLa and HepG2 cancer cells.<sup>(46)</sup> Researchers have developed photosensitizer conjugated silica-coated gold nanoclusters for fluorescence imaging-guided photodynamic therapy.<sup>(47)</sup> In one of the studies, fluorescence imaging assisted photodynamic therapy was achieved using photosensitizer linked to gold nanoclusters.<sup>(48)</sup>

### Luminescent nanomaterials for rapid detection of biomolecules

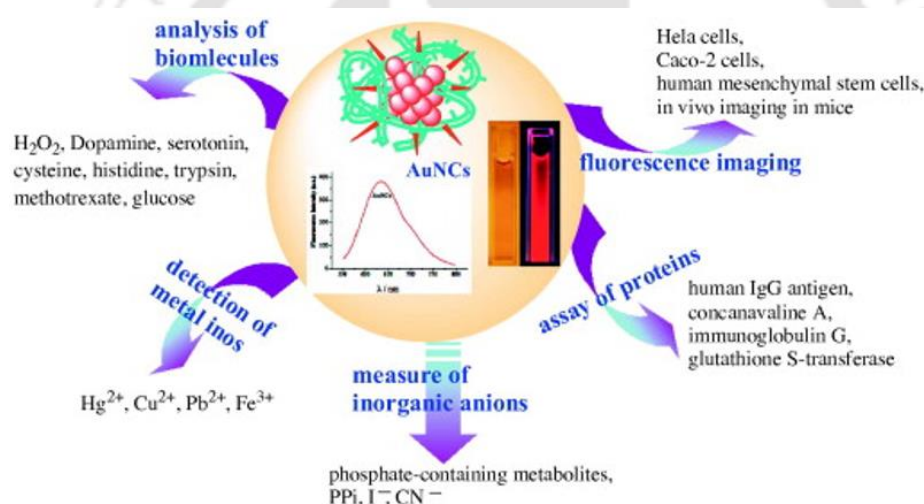


**Figure 1.6.** Applications of Au NCs in biomolecular detection. All rights reserved. (Reproduced with permission from reference (49). Copyright 2014, Elsevier Ltd.)

Ultra-small gold nanoclusters (Au NCs) with sizes less than 3 nm constitutes a special class of optically active nanomaterials extensively applied in sensing and imaging. Such luminescent nanomaterials possess several advantages in terms of photostability, large Stokes shift, and biocompatibility.<sup>(49)</sup> Researchers have developed glucose oxidase-functionalized Au NCs based glucose sensing system with a LOD of 0.7  $\mu\text{M}$ .<sup>(50)</sup> The quenching of the luminescence of Au NCs in the presence of glucose is a result of oxidation of the Au core by the enzymatic product of  $\text{H}_2\text{O}_2$  to form  $\text{Au}^+$ . Aggregation of the nanoclusters is another factor that induces quenching of Au NCs luminescence. Urease-stabilized Au NCs<sup>(51)</sup> were employed for sensitive detection of urea with a detection limit of 1.0 mM in blood samples. Upon addition of urea, the urease enzyme catalyses the conversion of urea into  $\text{NH}_3$  and  $\text{CO}_2$  which causes  $\text{NH}_4^+$  generation. This  $\text{NH}_4^+$  in turn reacts with

the negative surface charge of the Au NCs leading to its aggregation and subsequent fluorescence quenching. The detection of biomolecules containing phosphate groups such as adenosine-5'-triphosphate (ATP) has been carried out by GSH stabilized Au NCs.<sup>(52)</sup> The interaction of folic acid with BSA and succeeding changes in the surrounding environment around the BSA–Au NCs quenches the fluorescence. Based on this mechanism, a rapid method was devised for determination of folic acid concentration in a sample, with a 41 nM detection limit.<sup>(53)</sup> Au NCs decorated multifunctional boron nitride (BN) sheet was used as fluorescent as well as electrochemical sensor for interleukin-6 detection.<sup>(54)</sup> Post-translational modification enzymes and peptidase, (histone deacetylase 1, protein kinase A, elastase), at subpicomolar levels were tracked based on a real time label free sensing method using peptide template Au NCs.<sup>(55,56)</sup> Another approach based on detection of proteins, such as haemoglobin, cytochrome c, and myoglobin have been reported that have the potency to quench the luminescence of 11-MUA stabilized Au NCs. This change occurs through redox reactions between the Fe(II) atoms of hemin units and 11-MUA stabilised Au NCs.<sup>(57)</sup> Luminescence based methods for the detection of DNA and microRNA have been developed using Au NCs as probes.<sup>(58,59)</sup> Further, BSA stabilised AuNCs have been also applied towards detection of important drug molecules such as methotrexate, cobalamin and organophosphorus pesticides. Protein receptors, antibodies, antigens, aptamers, peptides etc. are certain biological molecules that have been applied towards development of sensitive detection methods. However, they suffer from drawbacks which include loss of stability when subjected to fluctuations in local environment and loss of function upon surface modifications. Such limitations have accelerated research strategies towards development of detection assays based on small synthetic molecules having property to bind a respective analyte with decent selectivity and sensitivity. Boronic acid is one of such molecules that have been applied in development of various sensing systems. In addition to its execution in sensing applications, boronic acids have also gained interest in anticancer therapy as potential proteasome inhibitors, enzyme inhibitors, boron neutron therapy agents, etc. Boron-containing drugs have emerged as a new class of chemicals wherein drug testing trials are being carried out for various diseases including cancer. Many fluorescent sensors have been also designed based on boronic acid functionalised fluorescent probes. Shen and co-worker reported a boronic acid functionalized carbon dots for fluorescent blood sugar sensing with 1.5  $\mu\text{M}$  detection limit.<sup>(60)</sup> Their study has signified that glucose can selectively lead to the assembly of the C-dots based on the covalent binding between the cis-diols of glucose and boronic acid of the C-dot surface. Selective sensing of dopamine with 0.1  $\mu\text{M}$  detection limit was achieved using boronic acid functionalized gold nanoclusters.<sup>(61)</sup> In this technique, DNA molecules (in basic pH) were found to self-polymerize with one another forming polydopamine with increased cis-diol groups, interacting with boronic acid on AuNC surface. This results in quenching of the luminescence of the AuNCs via electron transfer.

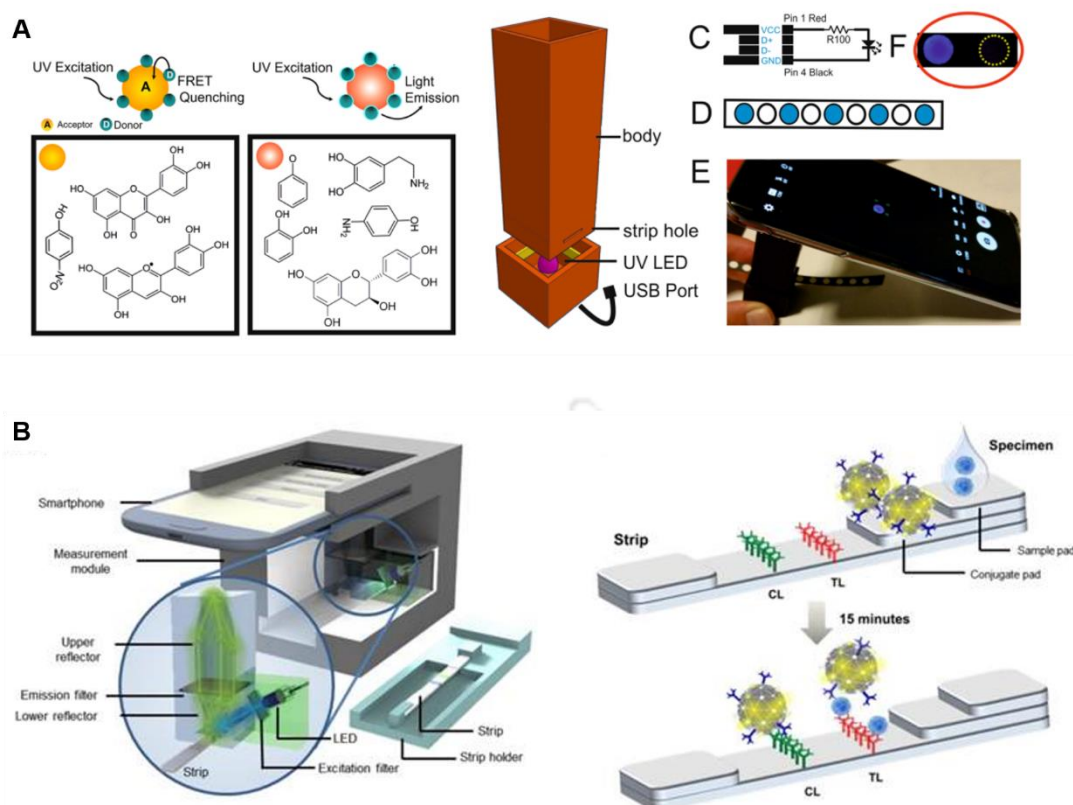


**Figure 1.7.** Smartphone based diagnostic devices. (Reproduced with permission from reference (62), (63). Copyright 2017, 2016, Springer Nature, Ivyspring International Publisher)

Recently for development of diagnostic medical devices, the smartphone camera mediated detection procedures are being widely implemented. In this regard, portable spectrophotometers, fluorescence spectrophotometers, and microscopes have been developed for point of care diagnostics. The availability of smartphones in nook and corner of the globe has evolved more than a billion smartphone users which makes an attractive tool for designing point-of-care diagnostic devices. They also promote wireless transmission and data management facilities. Such devices however are required to be tested in real clinical samples in different field studies with reproducible measurements. The assurance of the reproducible data would equip these devices to be used for clinical detection purposes in future. Recently, accurate and sensitive smartphone-based diagnostics have been implemented for enzyme-linked immunosorbent assay (ELISA), ion sensing, environmental monitoring etc.<sup>(62-65)</sup>

## 1.5 Scope and Challenges

The incredible development accomplished in nanotechnology inspired biomedical research envisions substantial opportunities in the arena of nanomedicine. The developments toward fabricating therapeutic delivery vehicles and multimodal imaging techniques open up a new paradigm in this respect. With this idea the scope of the present dissertation is summarised below:

- The application of multifunctional platforms to better the indigenous properties of individual elements in designing application oriented nanocarriers and imaging agents based on their responsive physiognomies.
- The encouraging consequences of application of knowledge of nanosystems in life science and biomedical electronics can very well lead to development of novel systems with amplified proficiencies in theranostics.
- Synthesis and development of biocompatible and sustainable systems with committed acumen for theranostic applications that needs to be realized by identifying key areas amalgamating the fields of medical sciences and biomedical devices.
- The development of sensitive and rapid nanomaterial based detection systems applicable in diverse environments.

**Salient features of the current dissertation:**

- A bimetallic module consisting of Au NCs (gold nanoclusters) and Ag NPs (silver nanoparticles) was synthesized and characterized to be effective in theranostic application. Time dependent TEM sample analysis showed clear evidence of uptake and activity of the bimetallic module and pathway of cell death was established using flow cytometry analysis.
- A stable cationic BSA Au-Ag NCs composite NPs loaded with suicide gene (CD-UPRT) was developed and characterization of the composite system was carried out. Bioimaging and combinatorial activity of gene therapy and ROS mediated cell death initiated by bimetallic nanoclusters was evaluated on HeLa cells and combined module was found to be more effective. The possible pathway of uptake and mechanism of cell death was substantiated.
- A mucin based nanocarrier embedded with Au NCs was developed and characterised for photosensitizer drug delivery. Bioimaging and photodynamic therapy mediated cell death was evaluated on HeLa cells. The mechanism of cell death was elucidated by flow cytometry.
- Phenylboronic acid templated Au NCs was synthesized following a rapid synthesis protocol. Characterization of the synthesized Au NCs was carried out. A smartphone based platform was designed for biomarker mucin detection. The synthesized Au NCs were also applied for targeted bioimaging and therapy of cancer cells and was found to be more effective towards HeLa cells. The pathway and mechanism of cell death initiated was studied using flow-cytometry-based assays. The response of the Au NCs was evaluated in multicellular HeLa cell spheroids. Also, the potential antibacterial nature of the Au NCs was studied which expands its application in combating possible secondary bacterial infections in some cancers.

- A stable protein templated Au NC was synthesized using minimum precursors and time. Characterization of the synthesized Au NCs was carried out. The synthesized Au NCs were applied for detection of GST and GST tagged recombinant proteins.

## 1.6 References

1. Persidis, A. Cancer Multidrug Resistance. *Nature Biotechnology* **1999**, *17* (1), 94–95.
2. Rocas, P.; Fernández, Y.; García-Aranda, N.; Foradada, L.; Calvo, P.; Avilés, P.; Guillén, M. J.; Schwartz, S.; Rocas, J.; Albericio, F.; et al. Improved Pharmacokinetic Profile of Lipophilic Anti-Cancer Drugs Using Av $\beta$ 3-Targeted Polyurethane-Polyurea Nanoparticles. *Nanomedicine: Nanotechnology, Biology and Medicine* **2018**, *14* (2), 257–267.
3. Jia, F.; Liu, X.; Li, L.; Mallapragada, S.; Narasimhan, B.; Wang, Q. Multifunctional Nanoparticles for Targeted Delivery of Immune Activating and Cancer Therapeutic Agents. *Journal of Controlled Release* **2013**, *172* (3), 1020–1034.
4. Biswas, A. K.; Islam, M. R.; Choudhury, Z. S.; Mostafa, A.; Kadir, M. F. Nanotechnology Based Approaches in Cancer Therapeutics. *Adv. Nat. Sci. Nanosci. Nanotechnol.* **2014**, *5* (4), 043001.
5. Kong, K.; Kendall, C.; Stone, N.; Notingher, I. Raman Spectroscopy for Medical Diagnostics — From In-Vitro Biofluid Assays to in-Vivo Cancer Detection. *Advanced Drug Delivery Reviews* **2015**, *89*, 121–134.
6. Jin, S.; Hu, Y.; Gu, Z.; Liu, L.; Wu, H.-C. Application of Quantum Dots in Biological Imaging. *Journal of Nanomaterials* **2011**, Article ID 834139.
7. Palmal Sharbari; Jana Nikhil R. Gold Nanoclusters with Enhanced Tunable Fluorescence as Bioimaging Probes. *Wiley Interdisciplinary Reviews: Nanomedicine and Nanobiotechnology* **2013**, *6* (1), 102–110.
8. Lee Soo Hong; Kim Byung Hyo; Na Hyon Bin; Hyeon Taeghwan. Paramagnetic Inorganic Nanoparticles as T1 MRI Contrast Agents. *Wiley Interdisciplinary Reviews: Nanomedicine and Nanobiotechnology* **2013**, *6* (2), 196–209.
9. Gad, S. C. *Pharmaceutical Manufacturing Handbook: Production and Processes*; John Wiley & Sons, 2008 Nanotechnology in pharmaceutical manufacturing, Yiguang Jin, Page 1278.
10. Ovais, M.; Raza, A.; Naz, S.; Islam, N. U.; Khalil, A. T.; Ali, S.; Khan, M. A.; Shinwari, Z. K. Current State and Prospects of the Phytosynthesized Colloidal Gold Nanoparticles and

- Their Applications in Cancer Theranostics. *Appl. Microbiol. Biotechnol.* **2017**, *101* (9), 3551–3565.
11. Biswas, A.; Bayer, I. S.; Biris, A. S.; Wang, T.; Dervishi, E.; Faupel, F. Advances in Top–down and Bottom–up Surface Nanofabrication: Techniques, Applications & Future Prospects. *Advances in Colloid and Interface Science* **2012**, *170* (1), 2–27.
  12. Saif, S.; Tahir, A.; Chen, Y. Green Synthesis of Iron Nanoparticles and Their Environmental Applications and Implications. *Nanomaterials* **2016**, *6* (11), 209.
  13. Yang, W.; Thordarson, P.; Gooding, J. J.; Ringer, S. P.; Braet, F. Carbon Nanotubes for Biological and Biomedical Applications. *Nanotechnology* **2007**, *18* (41), 412001.
  14. Wang, G.; Zhang, F.; Tian, R.; Zhang, L.; Fu, G.; Yang, L.; Zhu, L. Nanotubes-Embedded Indocyanine Green–Hyaluronic Acid Nanoparticles for Photoacoustic-Imaging-Guided Phototherapy. *ACS Appl. Mater. Interfaces* **2016**, *8* (8), 5608–5617.
  15. Wang Dan; Chen Jian-Feng; Dai Liming. Recent Advances in Graphene Quantum Dots for Fluorescence Bioimaging from Cells through Tissues to Animals. *Particle & Particle Systems Characterization* **2014**, *32* (5), 515–523.
  16. Puri, A.; Loomis, K.; Smith, B.; Lee, J.-H.; Yavlovich, A.; Heldman, E.; Blumenthal, R. Lipid-Based Nanoparticles as Pharmaceutical Drug Carriers: From Concepts to Clinic. *Crit Rev Ther Drug Carrier Syst* **2009**, *26* (6), 523–580.
  17. Han, J.; Zhao, D.; Li, D.; Wang, X.; Jin, Z.; Zhao, K. Polymer-Based Nanomaterials and Applications for Vaccines and Drugs. *Polymers* **2018**, *10* (1), 31.
  18. Khandare, J.; Minko, T. Polymer–drug Conjugates: Progress in Polymeric Prodrugs. *Progress in Polymer Science* **2006**, *31* (4), 359–397.
  19. Bajpai, S. K.; Mohan, Y. M.; Bajpai, M.; Tankhiwale, R.; Thomas, V. Synthesis of Polymer Stabilized Silver and Gold Nanostructures. *J Nanosci Nanotechnol* **2007**, *7* (9), 2994–3010.
  20. Conde, J.; Doria, G.; Baptista, P. Noble Metal Nanoparticles Applications in Cancer. *Journal of Drug Delivery* **2012**, Article ID 751075.
  21. Mody, V. V.; Siwale, R.; Singh, A.; Mody, H. R. Introduction to Metallic Nanoparticles. *J Pharm Bioallied Sci* **2010**, *2* (4), 282–289.
  22. Brichkin, S. B.; Razumov, V. F. Colloidal Quantum Dots: Synthesis, Properties and Applications. *Russ. Chem. Rev.* **2016**, *85* (12), 1297.

23. Petryayeva, E.; Algar, W. R.; Medintz, I. L. Quantum Dots in Bioanalysis: A Review of Applications Across Various Platforms for Fluorescence Spectroscopy and Imaging. *Appl. Spectrosc., AS* **2013**, *67* (3), 215–252.
24. Xie, J.; Zheng, Y.; Ying, J. Y. Protein-Directed Synthesis of Highly Fluorescent Gold Nanoclusters. *J. Am. Chem. Soc.* **2009**, *131* (3), 888–889.
25. Guével, X. L. Recent Advances on the Synthesis of Metal Quantum Nanoclusters and Their Application for Bioimaging. *IEEE Journal of Selected Topics in Quantum Electronics* **2014**, *20* (3), 45–56.
26. Huynh Elizabeth; Zheng Gang. Engineering Multifunctional Nanoparticles: All-in-one versus One-for-all. *Wiley Interdisciplinary Reviews: Nanomedicine and Nanobiotechnology* **2013**, *5* (3), 250–265.
27. Ortega, F. G.; Fernández-Baldo, M. A.; Fernández, J. G.; Serrano, M. J.; Sanz, M. I.; Diaz-Mochón, J. J.; Lorente, J. A.; Raba, J. Study of Antitumor Activity in Breast Cell Lines Using Silver Nanoparticles Produced by Yeast. *Int J Nanomedicine* **2015**, *10*, 2021–2031.
28. Pietro, P. D.; Zaccaro, L.; Comegna, D.; Gatto, A. D.; Saviano, M.; Snyders, R.; Cossement, D.; Satriano, C.; Rizzarelli, E. Silver Nanoparticles Functionalized with a Fluorescent Cyclic RGD Peptide: A Versatile Integrin Targeting Platform for Cells and Bacteria. *RSC Adv.* **2016**, *6* (113), 112381–112392.
29. Chen, T.; Zhao, T.; Wei, D.; Wei, Y.; Li, Y.; Zhang, H. Core-shell Nanocarriers with ZnO Quantum Dots-Conjugated Au Nanoparticle for Tumor-Targeted Drug Delivery. *Carbohydrate Polymers* **2013**, *92* (2), 1124–1132.
30. Sachdev, A.; Matai, I.; Gopinath, P. Dual-Functional Carbon Dots-silver@zinc Oxide Nanocomposite: In Vitro Evaluation of Cellular Uptake and Induction of Apoptosis. *J. Mater. Chem. B* **2015**, *3* (7), 1217–1229.
31. Mohanty, J. S.; Xavier, P. L.; Chaudhari, K.; Bootharaju, M. S.; Goswami, N.; Pal, S. K.; Pradeep, T. Luminescent, Bimetallic AuAg Alloy Quantum Clusters in Protein Templates. *Nanoscale* **2012**, *4* (14), 4255–4262.
32. Guével, X. L.; Trouillet, V.; Spies, C.; Li, K.; Laaksonen, T.; Auerbach, D.; Jung, G.; Schneider, M. High Photostability and Enhanced Fluorescence of Gold Nanoclusters by Silver Doping. *Nanoscale* **2012**, *4* (24), 7624–7631.
33. Chen, T.; Xu, S.; Zhao, T.; Zhu, L.; Wei, D.; Li, Y.; Zhang, H.; Zhao, C. Gold Nanocluster-Conjugated Amphiphilic Block Copolymer for Tumor-Targeted Drug Delivery. *ACS Appl Mater Interfaces* **2012**, *4* (11), 5766–5774.

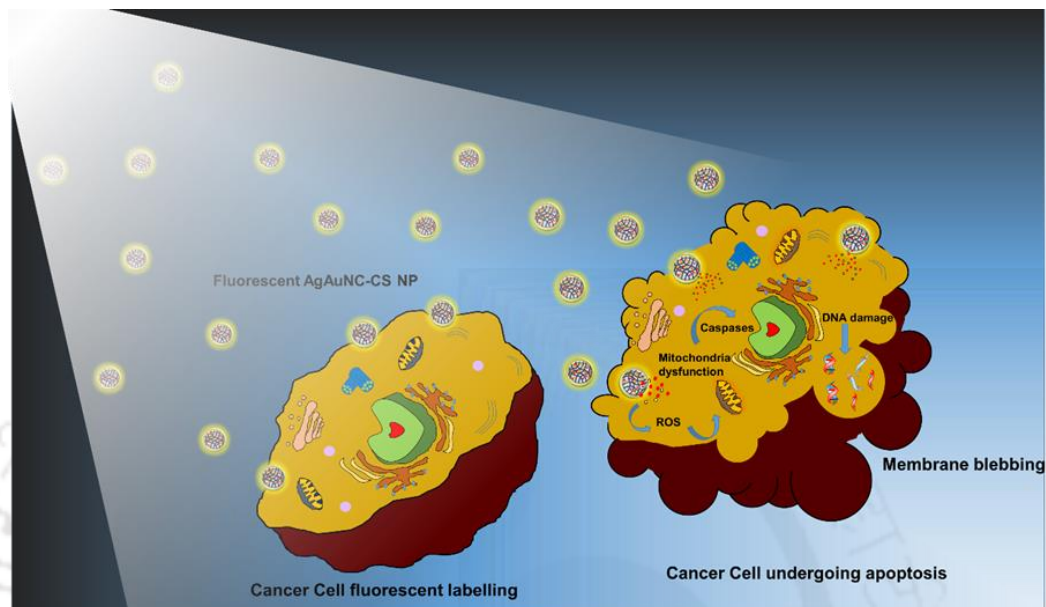
34. Chowdhuri, A. R.; Tripathy, S.; Haldar, C.; Roy, S.; Sahu, S. K. Single Step Synthesis of Carbon Dot Embedded Chitosan Nanoparticles for Cell Imaging and Hydrophobic Drug Delivery. *J. Mater. Chem. B* **2015**, *3* (47), 9122–9131.
35. Ishii, T.; Okahata, Y.; Sato, T. Mechanism of Cell Transfection with Plasmid/Chitosan Complexes. *Biochimica et Biophysica Acta (BBA) - Biomembranes* **2001**, *1514* (1), 51–64.
36. Neuhaus, B.; Tosun, B.; Rotan, O.; Frede, A.; Westendorf, A. M.; Epple, M. Nanoparticles as Transfection Agents: A Comprehensive Study with Ten Different Cell Lines. *RSC Adv.* **2016**, *6* (22), 18102–18112.
37. Zhou, J.; Deng, W.; Wang, Y.; Cao, X.; Chen, J.; Wang, Q.; Xu, W.; Du, P.; Yu, Q.; Chen, J.; et al. Cationic Carbon Quantum Dots Derived from Alginate for Gene Delivery: One-Step Synthesis and Cellular Uptake. *Acta Biomater* **2016**, *42*, 209–219.
38. Au, G. H. T.; Shih, W. Y.; Shih, W.-H. Efficient Intranuclear Gene Delivery by CdSe Aqueous Quantum Dots Electrostatically-Coated with Polyethyleneimine. *Mater. Res. Express* **2015**, *2* (1), 015401.
39. Tao, Y.; Li, Z.; Ju, E.; Ren, J.; Qu, X. Polycations-Functionalized Water-Soluble Gold Nanoclusters: A Potential Platform for Simultaneous Enhanced Gene Delivery and Cell Imaging. *Nanoscale* **2013**, *5* (13), 6154–6160.
40. Du, C.; Yan, H.; Liang, J.; Luo, A.; Wang, L.; Zhu, J.; Xiong, H.; Chen, Y. Polyethyleneimine-Capped Silver Nanoclusters for MicroRNA Oligonucleotide Delivery and Bacterial Inhibition. *Int J Nanomedicine* **2017**, *12*, 8599–8613.
41. Lei, Y.; Tang, L.; Xie, Y.; Xianyu, Y.; Zhang, L.; Wang, P.; Hamada, Y.; Jiang, K.; Zheng, W.; Jiang, X. Gold Nanoclusters-Assisted Delivery of NGF SiRNA for Effective Treatment of Pancreatic Cancer. *Nat Commun* **2017**, *8*, 15130.
42. Vankayala Raviraj; Kuo Chien-Lin; Nuthalapati Karthik; Chiang Chi-Shiun; Hwang Kuo Chu. Nucleus-Targeting Gold Nanoclusters for Simultaneous In Vivo Fluorescence Imaging, Gene Delivery, and NIR-Light Activated Photodynamic Therapy. *Advanced Functional Materials* **2015**, *25* (37), 5934–5945.
43. Lismont Marjorie; Dreesen Laurent; Wuttke Stefan. Metal-Organic Framework Nanoparticles in Photodynamic Therapy: Current Status and Perspectives. *Advanced Functional Materials* **2017**, *27* (14), 1606314.
44. Mallidi, S.; Spring, B. Q.; Hasan, T. Optical Imaging, Photodynamic Therapy and Optically-Triggered Combination Treatments. *Cancer J* **2015**, *21* (3), 194–205.

45. Wu, B.; Zhao, N. A Targeted Nanoprobe Based on Carbon Nanotubes-Natural Biopolymer Chitosan Composites. *Nanomaterials (Basel)* **2016**, *6* (11).
46. Rakovich, A.; Savateeva, D.; Rakovich, T.; Donegan, J. F.; Rakovich, Y. P.; Kelly, V.; Lesnyak, V.; Eychmüller, A. CdTe Quantum Dot/Dye Hybrid System as Photosensitizer for Photodynamic Therapy. *Nanoscale Res Lett* **2010**, *5* (4), 753–760.
47. Huang, P.; Lin, J.; Wang, S.; Zhou, Z.; Li, Z.; Wang, Z.; Zhang, C.; Yue, X.; Niu, G.; Yang, M.; et al. Photosensitizer-Conjugated Silica-Coated Gold Nanoclusters for Fluorescence Imaging-Guided Photodynamic Therapy. *Biomaterials* **2013**, *34* (19), 4643–4654.
48. Nair, L. V.; Nazeer, S. S.; Jayasree, R. S.; Ajayaghosh, A. Fluorescence Imaging Assisted Photodynamic Therapy Using Photosensitizer-Linked Gold Quantum Clusters. *ACS Nano* **2015**, *9* (6), 5825–5832.
49. Cui, M.; Zhao, Y.; Song, Q. Synthesis, Optical Properties and Applications of Ultra-Small Luminescent Gold Nanoclusters. *TrAC Trends in Analytical Chemistry* **2014**, *57*, 73–82.
50. Xia, X.; Long, Y.; Wang, J. Glucose Oxidase-Functionalized Fluorescent Gold Nanoclusters as Probes for Glucose. *Anal. Chim. Acta* **2013**, *772*, 81–86.
51. Nair Lakshmi V.; Philips Divya S.; Jayasree Ramapurath S.; Ajayaghosh Ayyappanpillai. A Near-Infrared Fluorescent Nanosensor (AuC@Urease) for the Selective Detection of Blood Urea. *Small* **2013**, *9* (16), 2673–2677.
52. Li, P.-H.; Lin, J.-Y.; Chen, C.-T.; Ciou, W.-R.; Chan, P.-H.; Luo, L.; Hsu, H.-Y.; Diau, E. W.-G.; Chen, Y.-C. Using Gold Nanoclusters As Selective Luminescent Probes for Phosphate-Containing Metabolites. *Anal. Chem.* **2012**, *84* (13), 5484–5488.
53. Hemmateenejad, B.; Shakerizadeh-shirazi, F.; Samari, F. BSA-Modified Gold Nanoclusters for Sensing of Folic Acid. *Sensors and Actuators B: Chemical* **2014**, *199*, 42–46.
54. Yang, G.-H.; Shi, J.-J.; Wang, S.; Xiong, W.-W.; Jiang, L.-P.; Burda, C.; Zhu, J.-J. Fabrication of a Boron Nitride–gold Nanocluster Composite and Its Versatile Application for Immunoassays. *Chem. Commun.* **2013**, *49* (91), 10757–10759.
55. Wen, Q.; Gu, Y.; Tang, L.-J.; Yu, R.-Q.; Jiang, J.-H. Peptide-Templated Gold Nanocluster Beacon as a Sensitive, Label-Free Sensor for Protein Post-Translational Modification Enzymes. *Anal. Chem.* **2013**, *85* (24), 11681–11685.
56. Gu, Y.; Wen, Q.; Kuang, Y.; Tang, L.; Jiang, J. Peptide-Templated Gold Nanoclusters as a Novel Label-Free Biosensor for the Detection of Protease Activity. *RSC Adv.* **2014**, *4* (27), 13753–13756.

57. Chen, L.-Y.; Huang, C.-C.; Chen, W.-Y.; Lin, H.-J.; Chang, H.-T. Using Photoluminescent Gold Nanodots to Detect Hemoglobin in Diluted Blood Samples. *Biosensors and Bioelectronics* **2013**, *43*, 38–44.
58. Sahoo, A. K.; Sailapu, S. K.; Dutta, D.; Banerjee, S.; Ghosh, S. S.; Chattopadhyay, A. DNA-Templated Single Thermal Cycle Based Synthesis of Highly Luminescent Au Nanoclusters for Probing Gene Expression. *ACS Sustainable Chem. Eng.* **2018**, *6* (2), 2142–2151.
59. Hosseini, M.; Ahmadi, E.; Borghei, Y.-S.; Ganjali, M. R. A New Fluorescence Turn-on Nanobiosensor for the Detection of Micro-RNA-21 Based on a DNA – Gold Nanocluster. *Methods Appl. Fluoresc.* **2017**, *5* (1), 015005.
60. Shen, P.; Xia, Y. Synthesis-Modification Integration: One-Step Fabrication of Boronic Acid Functionalized Carbon Dots for Fluorescent Blood Sugar Sensing. *Anal. Chem.* **2014**, *86* (11), 5323–5329.
61. Chen, H.; Liu, C.; Xia, Y. One-Step Synthesis of Boronic Acid Functionalized Gold Nanoclusters for Photoluminescence Sensing of Dopamine. *Methods Appl. Fluoresc.* **2017**, *5* (1), 014006.
62. Álvarez-Diduk, R.; Orozco, J.; Merkoçi, A. Paper Strip-Embedded Graphene Quantum Dots: A Screening Device with a Smartphone Readout. *Scientific Reports* **2017**, *7* (1), 976.
63. Yeo, S.-J.; Choi, K.; Cuc, B. T.; Hong, N. N.; Bao, D. T.; Ngoc, N. M.; Le, M. Q.; Hang, N. L. K.; Thach, N. C.; Mallik, S. K.; et al. Smartphone-Based Fluorescent Diagnostic System for Highly Pathogenic H5N1 Viruses. *Theranostics* **2016**, *6* (2), 231–242.
64. Ogirala, T.; Eapen, A.; Salvante, K. G.; Rapaport, T.; Nepomnaschy, P. A.; Parameswaran, A. M. Smartphone-Based Colorimetric ELISA Implementation for Determination of Women's Reproductive Steroid Hormone Profiles. *Med Biol Eng Comput* **2017**, *55* (10), 1735–1741.
65. Zhang, C.; Kim, J. P.; Creer, M.; Yang, J.; Liu, Z. A Smartphone-Based Chloridometer for Point-of-Care Diagnostics of Cystic Fibrosis. *Biosens Bioelectron* **2017**, *97*, 164–168.



## Chapter 2



### Bimetallic Silver Nanoparticle - Gold Nanocluster Embedded Composite Nanoparticles For Cancer Theranostics

D. Dutta, A. K. Sahoo, A. Chattopadhyay and S. S. Ghosh, *J. Mater. Chem. B*, 2016, 4, 793 - 800



## Chapter 2

# Bimetallic Silver Nanoparticle–Gold Nanocluster Embedded Composite Nanoparticles for Cancer Theranostics

### Abstract

A bimetallic silver nanoparticle based gold nanocluster module has been developed for theranostic cellular application by a rapid and simple galvanic exchange method. The use of chitosan as a template has helped to convert the bimetallic system into composite nanoparticles, which can be easily delivered into cancer cells. The synthesized composite nanoparticles offer the advantage of combinatorial properties of the metals present in two different nanoscale levels enabling both killing and bioimaging of cancer cells. Detailed molecular events of cell death were illustrated for this combined module to decipher apoptotic mediated cell death.

### 2.1. Introduction

Possibilities to create nanoscale materials with desired properties have been in focus to address several issues in the field of cancer medicine.<sup>(1,2)</sup> The ultimate target of these nanomaterial based techniques is to diagnose cancer at nascent stages and to fabricate effective anti-cancer agents targeting signalling pathway for effective drug delivery or gene silencing. Presently much effort has been made in nanomedicine to embed both therapy and diagnosis in a single entity *i.e.*, ‘nanotheranostics’.<sup>(3,4)</sup> By exploring size dependent physicochemical properties, the noble metal nanoparticles had emerged as promising materials for therapy as well as diagnosis. Silver nanoparticles (Ag NPs) are known to induce apoptosis by ROS generation and subsequent DNA damage.<sup>(5)</sup> Also nanoparticles conjugated to different organic dyes have been in use for cancer imaging and diagnostic applications.<sup>(6–8)</sup> However these organic dyes suffer from several disadvantages like narrow Stokes shift, photoblinking, low stability, and shorter lifetime.<sup>(9)</sup> Further, decrease in the length scale of the metal NPs, in the range of <2 nm, led to ultra-small nanoparticles known as nanoclusters, which are fascinating in the field of nanophotonics. Numerous methods have been developed for the synthesis of these metal clusters using proteins, DNA, and polymers as templates in the presence of thiols, some requiring the use of additional reducing agents, further functionalization have been achieved by using capping agents.<sup>(10–12)</sup> These metal clusters owe some extraordinary properties like inherent luminescence attributing to their small size, enhanced photo stability, longer lifetime, large Stokes shift, and lower toxicity, making them excellent candidates to

be used as imaging agents and catalysts in biological applications.<sup>(13,14)</sup> For instance AuNCs have been used for bioimaging due to their excellent stability, biocompatibility, and emission in the red region allowing differentiation of cellular autofluorescence. Further, to maximise the use of metal NCs as *in vitro* as well as *in vivo* probes special characteristics such as specificity, cell penetration ability, intracellular environment monitoring, toxicity, and clearance have been explored.<sup>(15–19)</sup> Hence, conjugation of nanoclusters with nanoparticles would be an ideal candidate for developing an efficient and advanced smart theranostic vehicle. Bimetallic systems are preferred rather than single metal systems as it gives an opportunity to combine the properties of two metals in a single entity making it a smartly architected nanostructure.<sup>(20)</sup> There are various methods reported by which bimetallic nanoparticles and nanoclusters can be synthesized. It can be broadly classified into co-reduction methods involving addition of both metal ion salt precursors followed by reduction and post treatment methods like core etching, galvanic replacement etc.<sup>(21,22)</sup> Also, the synthesis of bimetallic hollow NPs have been reported by the galvanic replacement method.<sup>(23)</sup> Silver and gold are one of the most widely used bimetallic systems due to the ease in synthesis.<sup>(24)</sup> The so far studied bimetallic nanocluster systems focused mainly on enhanced luminescence intensity and the catalytic properties of bimetallic systems over monoatomic ones.<sup>(25–27)</sup> However, less reports are available on evaluation of the therapeutic potential of bimetallic nanocluster systems. Recently, the effect of luminescent Au NCs on various cancer cell lines have been studied alongside bioimaging.<sup>(28)</sup> Also, another work which employed bimetallic AgAuNCs for cellular applications reported non-cytotoxicity towards cancer cells except at a very high silver concentration.<sup>(29)</sup> Hence, it is anticipated that a combined system including both Ag NPs and luminescent Au NCs would serve the purpose of anticancer activity and bioimaging better than a monoatomic system. Also, the importance of biocompatible composite nanoparticles as carriers for effective and sustained delivery of these metal NPs into cancer cells is a demand of the situation. The potential of nanocarriers based on dendrimers, liposomes, hydrogels, and polymeric NPs in drug delivery has been well established but the use of these in delivery of metal NPs is less explored.<sup>(30,31)</sup> Keeping all these elements in mind, herein this chapter reports an easy aqueous synthesis of the AuNCs [standard reduction potential of  $\text{AuCl}_4^- + 3\text{e}^- = \text{Au}(0) + 4\text{Cl}^-$  is  $1.00\text{E}^\circ$  (V)] by Galvanic replacement of AgNPs [standard reduction potential of  $\text{Ag}^+ + \text{e}^- = \text{Ag}(0)$  is  $0.80\text{E}^\circ$  (V)] with biocompatible chitosan polymer as a template harbouring both the AgNPs and AuNCs, which was further converted into theranostic composite nanoparticles (AgNP–AuNC–CSNPs) by crosslinking of the polymer using sodium tripolyphosphate,<sup>(32)</sup> which acted as a carrier to deliver the AgNPs and AuNCs inside cancer cells (**Figure 2.1**). The synthesis procedure involves initial preparation of AgNPs on chitosan by reduction under basic conditions. Then AuNCs were prepared alongside AgNPs by treating with mercaptopropionic acid (MPA). Generally, the formation of bimetallic nanoclusters or coreshell nanoparticles takes longer time, harsh reaction conditions, and extensive purification steps. The present method of water soluble bimetallic nanoparticle–nanocluster synthesis can be marked as a simple and rapid method. The effect of these theranostic composite nanoparticles was studied in human cervical cancer (HeLa) cell

line. The disadvantages of using chitosan along with gold nanoclusters is the poor solubility of native chitosan at pH above 6.5, which is generally resolved by the use of modified chitosan<sup>(33,34)</sup> and the excitation of gold nanoclusters, which is in the UV region making it difficult to be used in *in vivo* applications,<sup>(35)</sup> although there are reports of use of UV excitation dependent materials in *in vivo* bioimaging applications also.<sup>(36,37)</sup> Furthermore, considering numerous advantages like low toxicity, high photo stability, water solubility, ultrasmall size enabling deeper tissue penetration of gold nanoclusters compared to quantum dots and organic dyes as biological probes and use of a natural polymer chitosan as a stabilizer makes the system more biocompatible and biodegradable rather than those involving the use of organic moieties,<sup>(38)</sup> with enhanced permeation and mucoadhesive properties suitable for systemic nanocarrier based applications. In addition, the possibility of using gold nanoclusters for two photon imaging *in vitro*, with both excitation and emission wavelengths in the NIR region, has been demonstrated.<sup>(17)</sup> This also makes the use of gold nanoclusters appealing. On a promising note, a reduction of cell viability was observed in the bimetallic system, and a comparative study was done with AgNPs only. Along with cytotoxic nature, the system facilitated bio-imaging of the cancer cells. The detailed mechanism of cell death established apoptosis mediated cell death. Thus, these theranostic composite nanoparticles killed cancer cells and provided an option for concomitant cellular imaging.

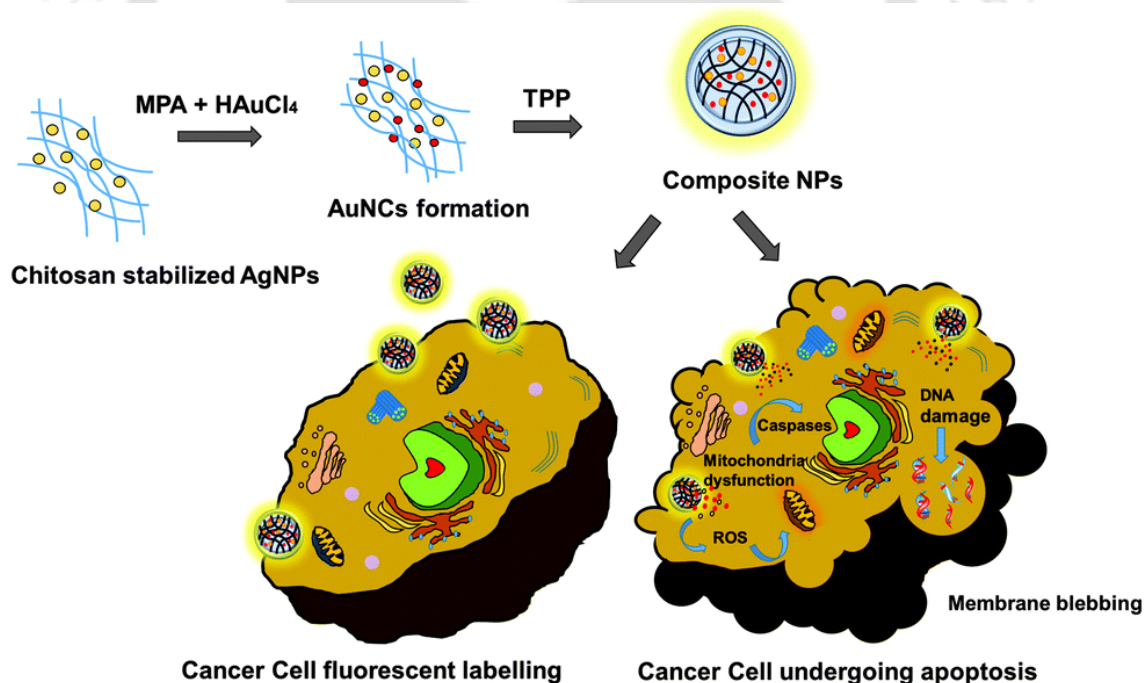


**Figure 2.1** The synthesis and delivery of bimetallic composite nanoparticles for bioimaging and induction of apoptosis in cancer cells.

## 2.2. Synthesis and Characterisation of AgNP–AuNCs

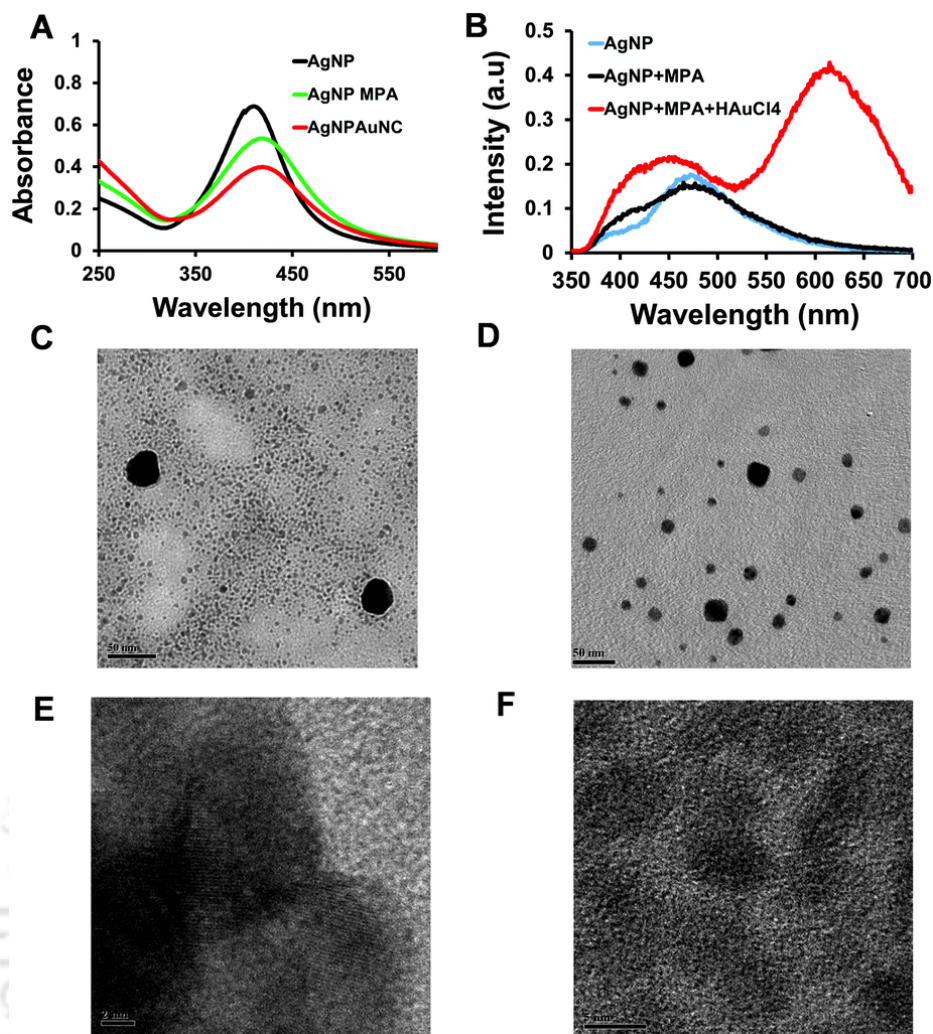


**Figure 2.2.** (A) The UV-Vis absorption spectra of Ag NPs, AgNPs after reacting with MPA and AgNP–AuNCs. (B) Emission spectra of AgNP–AuNCs showing the emission peak at 620 nm when excited at 300 nm. (C) TEM images of AgNP–AuNCs at 50 nm scale bar. (D) TEM images of initial Ag NPs at 50 nm scale bar. (E) HRTEM images of Ag NPs and (F) Au NCs present in AgNP–AuNCs.

AgNP–AuNCs appeared as brown color dispersion with UV-Vis absorbance at 425 nm indicating the presence of silver nanoparticles (**Figure 2.2A**). In case of control silver nanoparticles, the UV-Vis peak found at 410 nm was slightly red shifted after addition of MPA, which may be attributed to the change in dielectric constant<sup>(41)</sup> of the stabilizing layer (of the AgNPs) in addition to some aggregation in the presence of a thiol group containing molecules.<sup>(42)</sup> The surface plasmon property was still persistent after treating AgNPs with MPA and subsequent formation of AuNCs, unlike in previously reported cases where complete disappearance of plasmonic properties was observed.<sup>(43,44)</sup> In certain cases for gold nanoclusters absorption at around 300–400 nm due to “d–sp, sp–sp” transitions or the formation of thiolate complexes has been reported.<sup>(45)</sup> Nevertheless, there are reports supporting complete disappearance of UV absorbance after the formation of

nanoclusters.<sup>(46)</sup> Here, the galvanic replacement yielded metal nanoclusters, possibly due to the reaction of the as-formed Au–thiolate complexes by the reaction of HAuCl<sub>4</sub> in the presence of MPA with AgNPs<sup>(46)</sup> within the biopolymer chitosan, which acted as a template for directed synthesis of metal clusters. Possibly, along with Ag NPs, the presence of the thiol (in MPA) as the stabilizing ligand and appropriate amount of template (chitosan) provided protection due to its bulk nature, facilitating the formation of AgNP–AuNCs. The plasmonic absorption peak for Au NPs was missing (as inferred from the absorption spectrum) whereas that for AgNPs it was prominent at 425 nm. Thus in the composite, possibly AuNCs and AgNPs were present and larger particles of AuNPs were absent. The time dependent UV-Vis spectra remained unaltered, indicating that stable products were formed (**Appendix A, Figure A2.1a**). The same sample upon excitation by UV light (300 nm) exhibited a strong emission peak at 620 nm, which indicated the formation of AuNCs (**Figure 2.2B**) and a comparatively weaker peak in the region of 400–500 nm possibly due to chitosan<sup>(47)</sup> (**Appendix A, Figure A2.1b**). The luminescence intensity of AgNP–AuNCs could be tuned when synthesized in different ratios of the precursors. Keeping the concentration of AgNO<sub>3</sub> constant, with increasing concentrations of HAuCl<sub>4</sub> a gradual increase in luminescence intensity was observed alongside the loss of SPR peak due to etching of silver nanoparticles by gold salts (**Appendix A, Figure A2.1c and d**). But, when the reverse process was performed, that is, with increasing concentration of silver, keeping gold concentration constant an interesting observation was made. The luminescence of gold clusters was optimised with increasing silver content, and a luminescence enhancement (red) effect was seen at higher silver concentrations<sup>(48–50)</sup> (**Appendix A, Figure A2.2a and b**). However, for the cellular studies, optimum concentrations of Au and Ag were standardized where both the SPR peak of AgNPs and luminescence of AuNCs prevailed. TEM investigation showed the formation of AgNP–AuNCs when compared to initial AgNPs (**Figure 2.2C and D**). The HRTEM image of bigger particles which are likely to be Ag nanoparticles (as inferred from the absorption spectrum of **Figure 2.2A**) showed a lattice spacing of 0.22 nm which corresponds to Ag. However, the HRTEM image of small size particles possibly due to Au NCs did not show any distinct lattice spacing (**Figure 2.2E and F**). The SAED pattern corresponded to AgNPs, but did not show any distinctive signature for AuNCs (**Appendix A, Figure A2.3a**). The EDX spectrum of the particles confirmed the presence of both Ag and Au (**Appendix A, Figure A2.3b**) which was supported by the HAADF-STEM(BF) image of AgNP–AuNCs and corresponding EDX mapping of Ag and Au which signified that the AgNPs and the AuNCs were present as individual entities in chitosan matrix (**Appendix A, Figure A2.4a-c**). The average diameter of the particles revealed two different size distributions of  $1.41 \pm 0.41$  nm corresponding to AuNCs and the size distribution of AgNPs showing majority of the particles in the 3–10 nm range along with few particles of bigger size (**Appendix A, Figure A2.5**). Also MALDI-TOF analysis of the sample (**Appendix A, Figure A2.6**) showed a peak at  $m/z = 5390$ , which was justified by the formation of  $[\text{Au}_{20}(\text{MPA})_{13} + 4\text{Na}^+ - 4\text{H}^+]^{4-}$ ; hence we may conclude that there are 20 Au atoms in the metal cluster core. The presence of additional peaks could be due to fragmentation of the sample or the formation of other NCs in small numbers. The photostability

studies of emission intensity of the NCs revealed that the NCs were stable compared to standard rhodamine 6G. The luminescence intensity decrease rate ( $F/F_0$ ) of the NCs was 0.0025% per sec, whereas in the case of commonly used fluorescent dye, such as rhodamine 6G, the rate was found to be 0.095% per sec. The quantum yield of AgNP–AuNCs was measured to be 2.3% using quinine sulfate as standard (Appendix A, Figure A2.7a and b) and was deemed suitable for imaging applications.<sup>(51)</sup> The FTIR spectra of the AgNPs when compared to control chitosan showed prominent shift in the peak of –NH bending from  $1609\text{ cm}^{-1}$  to  $1570\text{ cm}^{-1}$ , suggesting interaction of the as-formed AgNPs with the –NH group of chitosan. Also, the –SH stretching of MPA, which occurred at  $2580\text{ cm}^{-1}$  for free MPA disappeared after the formation of AuNCs, possibly due to –S–Au bond formation<sup>(52,53)</sup> (Appendix A, Figure A2.8a-d).

### 2.3. Synthesis and Characterisation of Composite NPs (AgNP–AuNC–CSNPs)

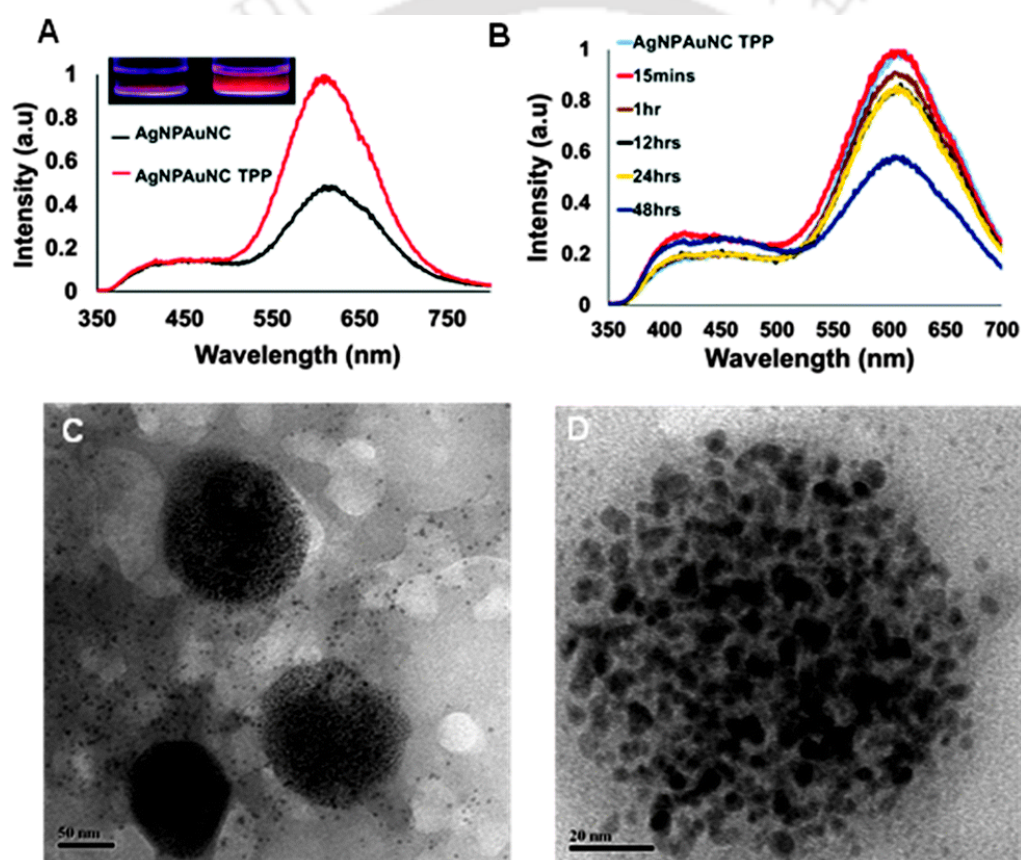


**Figure 2.3.** (A) Luminescence spectra of AgNP–AuNCs before and after addition of TPP (the inset contains images of AgNP–AuNCs before and after addition of TPP under UV transillumination). (B) Time dependent emission spectra of composite NPs. (C) TEM image of composite NPs. (D) Magnified TEM image of composite NPs.

An important application of this bimetallic system with dual nature of SPR and luminescence is as a theranostic agent. The luminescence of AuNCs can be used for imaging and further cytotoxicity is provided by the presence of AgNPs. With the help of the ionic gelation method, the chitosan biopolymer composite can easily be converted into nanoparticles with its intact luminescent property

of the NCs for delivery into cancer cells as a smart theranostic vehicle (**Figure 2.3A and B**). The luminescence enhancement observed after addition of TPP is probably due to aggregation of nanoclusters during chitosan nanoparticle formation. Similar observation has been made in the presence of  $Zn^{2+}$  ions.<sup>(54)</sup> The mean hydrodynamic diameter of the hence prepared composite NPs (AgNP–AuNC–CSNPs) was 155.5 nm, with a zeta potential of +19.3 mV, which are generally considered favourable for cellular delivery applications<sup>(55)</sup> (**Appendix A, Figure A2.9a and b**). Additionally, TEM images revealed that the average size of the composite NPs was  $120 \pm 20$  nm (**Figure 2.3C and D**) and FESEM images too exhibited the size to be  $120 \pm 30$  nm (**Appendix A, Figure A2.9c**). Further, the presence of both gold and silver was confirmed by atomic absorption spectroscopy (AAS). The presence of unreacted ions was eliminated by repeated washing of the sample after centrifugation. The concentrations of Ag and Au in the as-synthesized composite used were found to be  $0.68 \mu\text{g mL}^{-1}$  and  $0.0017 \mu\text{g mL}^{-1}$ , respectively. Thereby, an easy rapid fabrication of smart bimetallic theranostic vehicle was achieved with the conjugation of gold nanoclusters and silver nanoparticles.



## 2.4. Uptake and Bio-imaging Application of Composite NPs

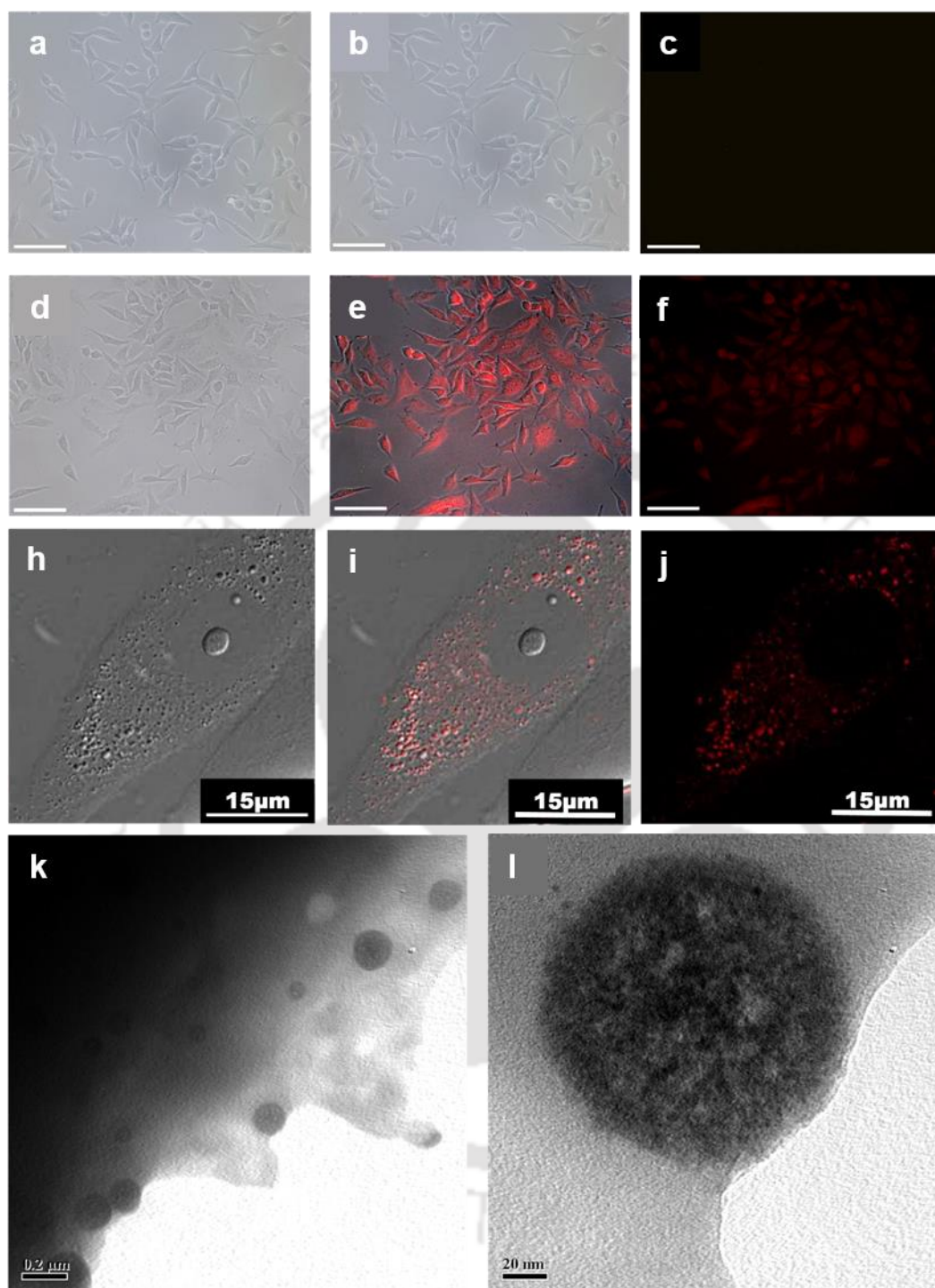


**Figure 2.4.** Epi fluorescence microscopic images of control HeLa cells; (A) bright field image; (B) the merged fluorescent image. (C) Fluorescence image and HeLa cells treated with composite NPs for 3 h; (D) bright field image, and (E) the merged fluorescent image. (F) Fluorescence image at scale bar 100  $\mu\text{m}$ . Deconvolution fluorescence microscopic image showing the magnified image of the HeLa cells treated with composite NPs for 3 h; (H) bright field image, and (I) the merged fluorescent image. (J) Fluorescence image. (K) TEM image of HeLa cell treated with composite NPs for 3 h at 0.2  $\mu\text{m}$  scale. (L) Magnified TEM image of composite NP of the same cell at 20 nm scale bar shows the uptake of the composite NPs inside the cell.

To analyse the capability of these bimetallic chitosan composite NPs for possible use as intracellular probes, human cervical cancer (HeLa) cells were incubated with  $80 \mu\text{g mL}^{-1}$  of the NPs in cell culture medium for 3 h and then the cells were imaged under a fluorescence microscope. The control cells showed no fluorescence (**Figure 2.4A-C**) and the presence of the fluorescent nanoclusters was seen inside the treated cells as shown in **Figure 2.4D-F**, which was supported by a high resolution deconvolution fluorescence microscopy image (**Figure 2.4H-J**). Here, it is to be mentioned that these composite NPs (AgNPs–AuNC embedded) should be non-cytotoxic for fluorescent probing. Hence, a lower concentration ( $80 \mu\text{g mL}^{-1}$ ) than toxic dose for short duration was applied for imaging applications. The uptake of composite NPs was evident from the TEM analysis. The incorporation of the composite (Ag NPs with Au NCs) inside the cell was clearly observed, and the extension of the plasma membrane suggests possible endocytosis mediated uptake of composite NPs<sup>(56)</sup> (**Figure 2.4K and L**). The average size of composite NPs was similar to the as-synthesized ones, confirming overall stability of the particles after uptake, which is essential for optimal activity. The time dependent TEM analysis provides an idea of how the cell progresses towards apoptosis by visualizing the changes in the plasma membrane at different time points (**Appendix A, Figure A2.10a-e**). In addition to the conventional methods, this approach provides a new insight to monitor the uptake of composite NPs by cancer cells where alteration of the cell membrane was also seen in TEM images. The uptake was further confirmed by exploiting the composite nanoparticle's luminescence property using fluorescence activated cells sorter (FACS) without addition of any conventional dye. A dose dependent study was done which revealed the maximum shift in FL3-H (**Figure 2.5A**) corresponding to the red emission compared to FL2-H and FL1-H where it was least (**Appendix A, Figure A2.10f and g**).

## 2.5. Cell Viability Assay and Mechanism of Cell Death

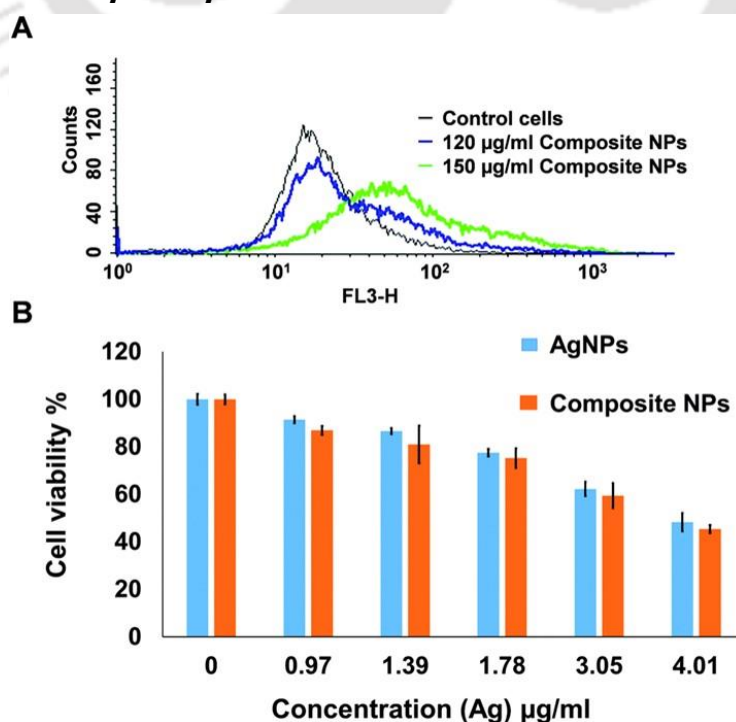


**Figure 2.5.** (A) Uptake study of the composite NPs by FACS in HeLa cells, probing the luminescence of Au NCs without using any additional dye, was carried out (5 h) after treatment with different amounts of the composite. (B) The MTT assay of control and treated cells depicting cell viability. The values are represented as mean  $\pm$  SD of three individual experiments.

For establishing the role of cytotoxic activity, MTT assay was done. The results (**Figure 2.5B**) indicated that the  $IC_{50}$  value of the composite NPs was at Ag concentration of  $3.6 \mu\text{g mL}^{-1}$ . Also simultaneously AgNPs only were tested for cytotoxicity, which showed around 40% cell death at around  $3.6 \mu\text{g mL}^{-1}$ . The amount of Au present in the composite at  $IC_{50}$  was found to be  $0.068 \mu\text{g mL}^{-1}$ . The as-synthesized composite NPs were concentrated prior to use in cell viability studies. Here it may be noted that in the case of the presence of gold nanoclusters along with silver nanoparticles, the activity of the composite had increased as compared to the monoatomic gold nanocluster system reported earlier,<sup>47</sup> possibly due to the synergistic effect of the bimetallic system. Here in this case, we have optimized the ratio of AgNPs and AuNCs in such a way that the cytotoxicity is retained (due to Ag) alongside with the ability to image the cells. Only 2.1 : 1 ratio of Ag to Au was found to satisfy both the criteria. The FESEM analysis of HeLa cells treated for 24 h at  $IC_{50}$  dose revealed membrane blebbing and disoriented morphology characterizing that the cells have possibly undergone programmed cell death (**Appendix A, Figure A2.11a and b**). Ethidium bromide/acridine orange double staining confirmed that significant percentage of cells were dead at  $IC_{50}$  when compared to the control cells (**Appendix A, Figure A2.12a -c**).

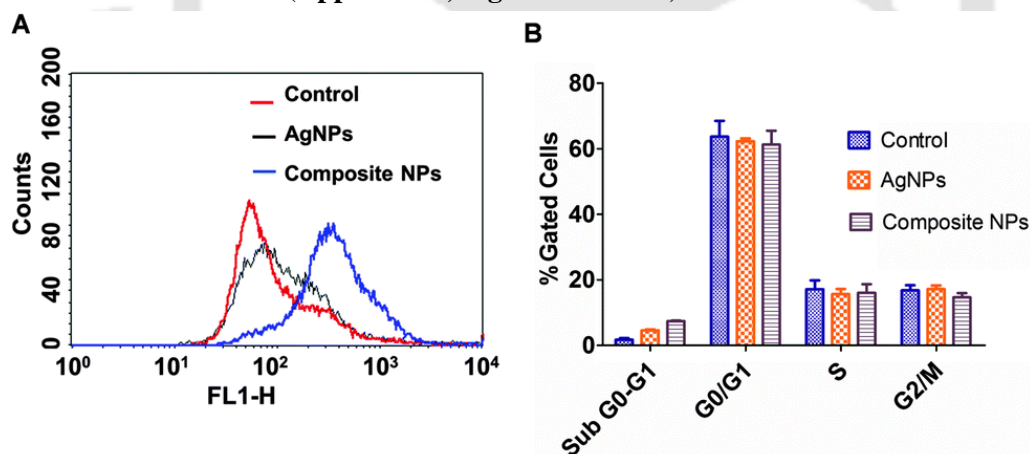


**Figure 2.6.** (A) ROS generation in case of composite NPs with respect to control and AgNPs treated cells. (B) Cell cycle analysis by FACS of the control, AgNPs treated, and the composite NPs treated cells. The data are represented as mean  $\pm$  SD of three individual experiments.

In order to have a clear picture of the mechanism of cell death involved, DCFHDA staining was performed to confirm the generation of reactive oxygen species, which is the most common established mechanism of rendering a cell towards apoptosis by AgNPs. A slightly higher amount of ROS was seen to be generated in the case of composite NPs compared to AgNPs only, possibly due

to the presence of AuNCs along with AgNPs. Also, cell cycle analysis was carried out by propidium iodide (PI) staining, which showed significant increase in sub  $G_0/G_1$  cell population along with slight changes in other phases of cell cycle ( $G_0/G_1$ , S, and  $G_2/M$ ) as shown in **Figure 2.6A and B**. After treatment with composite NPs as compared to AgNPs only, which too showed increase in sub  $G_0-G_1$ , but at a lower percentage than composite NPs. Herein, the significant increase in sub- $G_0/G_1$  population gives the indication of apoptosis mode of cell death (further details are available in **Appendix A, Figure A2.13**).

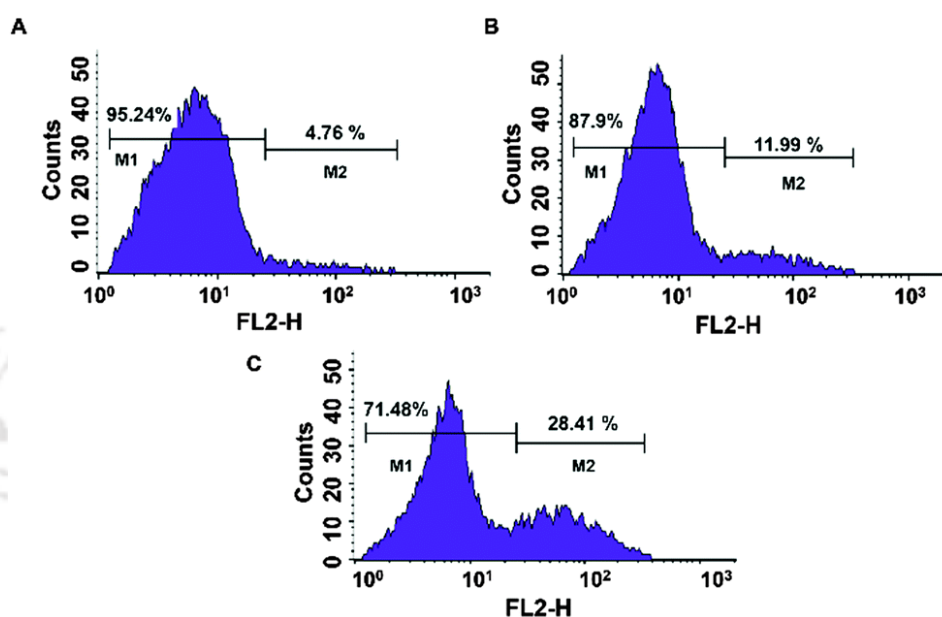


**Figure 2.7.** (A) Caspase-3 assay showing percentage of apoptosis in control and (B) AgNPs and (C) composite NPs treated cells.

It was further confirmed by the caspase-3 assay, which exhibited a marked increase in the percentage of apoptotic population of cells in the case of composite NP treatment as compared to AgNP treatment only and the control cells (**Figure 2.7A-C**). Relative expression level of caspase-3 was confirmed by reverse transcription polymerase chain reaction (RT-PCR). For that the total RNA was extracted from the control untreated as well as composite NP treated HeLa cells and was subsequently transformed into cDNA by (RT-PCR). The cDNA was used to find out the expression level of the caspase-3 by semi-quantitative polymerase chain reaction (PCR) analysis followed by the agarose gel electrophoresis. The results demonstrated that caspase-3 expression was significantly high in case of treated HeLa cells as compared to the control; while  $\beta$ -actin a house keeping gene, served as an endogenous control showed the similar expression level in both cases. From this, we could infer that cells started to undergo apoptosis *via* activation of caspases (**Appendix A, Figure A2.14a and b**). Hence, it is clear that the bimetallic composite NPs were effective in killing cancer cells by apoptosis with having the advantage of detection of cancer cells using photoluminescence under proper excitation.

## 2.6. Conclusions

In brief, bimetallic NP–NC based theranostic composite NP nanoparticles were synthesized using an easy and fast method involving minimal amount of the precursors. The prepared composite NPs were successfully internalized by HeLa cells due to the favourable size and surface charge. The uptake and subsequent morphological changes of the cell upon treatment with the composite NPs were evident. This current module enables cellular imaging due to the presence of luminescent AuNCs without the use of any organic dye. Also the composite NPs when incubated with HeLa cells offered anticancer properties due to the presence of AgNPs, resulting in successful killing of cancer cells through apoptosis.

## 2.7. References

1. Chow, E. K.-H.; Ho, D. Cancer nanomedicine: from drug delivery to imaging. *Sci Transl Med* **2013**, *5* (216), 216rv4.
2. Langer, R.; Peppas, N. A. Advances in Biomaterials, Drug Delivery, and Bionanotechnology. *AIChE J.* **2003**, *49* (12), 2990–3006.
3. Lammers, T.; Aime, S.; Hennink, W. E.; Storm, G.; Kiessling, F. Theranostic Nanomedicine. *Acc. Chem. Res.* **2011**, *44* (10), 1029–1038.
4. Barros, A. L. B. de; Soares, D. C. F. Theranostic Nanoparticles: Imaging and Therapy Combined. *Journal of Molecular Pharmaceutics & Organic Process Research* **2014**, *2* (1), 1–2.
5. AshaRani, P. V.; Low Kah Mun, G.; Hande, M. P.; Valiyaveetil, S. Cytotoxicity and Genotoxicity of Silver Nanoparticles in Human Cells. *ACS Nano* **2009**, *3* (2), 279–290.
6. Liu, H.; Chen, F.; Xi, P.; Chen, B.; Huang, L.; Cheng, J.; Shao, C.; Wang, J.; Bai, D.; Zeng, Z. Biocompatible Fluorescent Hydroxyapatite: Synthesis and Live Cell Imaging Applications. *J. Phys. Chem. C* **2011**, *115* (38), 18538–18544.
7. Li, S.; Shen, X.; Li, L.; Yuan, P.; Guan, Z.; Yao, S. Q.; Xu, Q.-H. Conjugated-Polymer-Based Red-Emitting Nanoparticles for Two-Photon Excitation Cell Imaging with High Contrast. *Langmuir* **2014**, *30* (26), 7623–7627.
8. Bhattacharyya, K.; Goldschmidt, B. S.; Hannink, M.; Alexander, S.; Jurkevic, A.; Viator, J. A. Gold Nanoparticle-Mediated Detection of Circulating Cancer Cells. *Clin. Lab. Med.* **2012**, *32* (1), 89–101.
9. Resch-Genger, U.; Grabolle, M.; Cavaliere-Jaricot, S.; Nitschke, R.; Nann, T. Quantum Dots versus Organic Dyes as Fluorescent Labels. *Nat. Methods* **2008**, *5* (9), 763–775.
10. Shang, L.; Dong, S.; Nienhaus, G. U. Ultra-Small Fluorescent Metal Nanoclusters: Synthesis and Biological Applications. *Nano Today* **2011**, *6* (4), 401–418.
11. X. Qu, Y. Li, L. Li, Y. Wang, J. Liang and J. Liang, *J. Nanomater.*, 2015, 784097, DOI: 10.1155/2015/784097.

12. Zheng, J.; Zhang, C.; Dickson, R. M. Highly Fluorescent, Water-Soluble, Size-Tunable Gold Quantum Dots. *Phys. Rev. Lett.* **2004**, *93* (7), 077402.
13. Xie, J.; Zheng, Y.; Ying, J. Y. Protein-Directed Synthesis of Highly Fluorescent Gold Nanoclusters. *J. Am. Chem. Soc.* **2009**, *131* (3), 888–889.
14. Li, G.; Jin, R. Atomically Precise Gold Nanoclusters as New Model Catalysts. *Acc. Chem. Res.* **2013**, *46* (8), 1749–1758.
15. Chen, L.-Y.; Wang, C.-W.; Yuan, Z.; Chang, H.-T. Fluorescent Gold Nanoclusters: Recent Advances in Sensing and Imaging. *Anal. Chem.* **2015**, *87* (1), 216–229.
16. Huang, X.; Luo, Y.; Li, Z.; Li, B.; Zhang, H.; Li, L.; Majeed, I.; Zou, P.; Tan, B. Biolabeling Hematopoietic System Cells Using Near-Infrared Fluorescent Gold Nanoclusters. *J. Phys. Chem. C* **2011**, *115* (34), 16753–16763.
17. Khandelia, R.; Bhandari, S.; Pan, U. N.; Ghosh, S. S.; Chattopadhyay, A. Gold Nanocluster Embedded Albumin Nanoparticles for Two-Photon Imaging of Cancer Cells Accompanying Drug Delivery. *Small* **2015**, *11* (33), 4075–4081.
18. Guével, X. L. Recent Advances on the Synthesis of Metal Quantum Nanoclusters and Their Application for Bioimaging. *IEEE Journal of Selected Topics in Quantum Electronics* **2014**, *20* (3), 45–56.
19. Shang, L.; M. Dörlich, R.; Brandholt, S.; Schneider, R.; Trouillet, V.; Bruns, M.; Gerthsen, D.; Ulrich Nienhaus, G. Facile Preparation of Water-Soluble Fluorescent Gold Nanoclusters for Cellular Imaging Applications. *Nanoscale* **2011**, *3* (5), 2009–2014.
20. Banerjee, M.; Sharma, S.; Chattopadhyay, A.; Ghosh, S. S. Enhanced Antibacterial Activity of Bimetallic Gold-Silver Core-shell Nanoparticles at Low Silver Concentration. *Nanoscale* **2011**, *3* (12), 5120–5125.
21. Yuan, X.; Dou, X.; Zheng, K.; Xie, J. Recent Advances in the Synthesis and Applications of Ultrasmall Bimetallic Nanoclusters. *Part. Part. Syst. Charact.* **2015**, *32* (6), 613–629.
22. Ortac, I.; Simberg, D.; Yeh, Y.; Yang, J.; Messmer, B.; Trogler, W. C.; Tsien, R. Y.; Esener, S. Dual-Porosity Hollow Nanoparticles for the Immunoprotection and Delivery of Nonhuman Enzymes. *Nano Lett.* **2014**, *14* (6), 3023–3032.
23. González, E.; Arbiol, J.; Puntès, V. F. Carving at the Nanoscale: Sequential Galvanic Exchange and Kirkendall Growth at Room Temperature. *Science* **2011**, *334* (6061), 1377–1380.
24. Link, S.; Wang, Z. L.; El-Sayed, M. A. Alloy Formation of Gold–Silver Nanoparticles and the Dependence of the Plasmon Absorption on Their Composition. *J. Phys. Chem. B* **1999**, *103* (18), 3529–3533.
25. Wang, D.; Li, Y. Bimetallic Nanocrystals: Liquid-Phase Synthesis and Catalytic Applications. *Adv. Mater. Weinheim* **2011**, *23* (9), 1044–1060.

26. Chen, P.-C.; Ma, J.-Y.; Chen, L.-Y.; Lin, G.-L.; Shih, C.-C.; Lin, T.-Y.; Chang, H.-T. Photoluminescent AuCu Bimetallic Nanoclusters as PH Sensors and Catalysts. *Nanoscale* **2014**, *6* (7), 3503–3507.
27. Le Guével, X.; Trouillet, V.; Spies, C.; Li, K.; Laaksonen, T.; Auerbach, D.; Jung, G.; Schneider, M. High Photostability and Enhanced Fluorescence of Gold Nanoclusters by Silver Doping. *Nanoscale* **2012**, *4* (24), 7624–7631.
28. Dong, L.; Li, M.; Zhang, S.; Li, J.; Shen, G.; Tu, Y.; Zhu, J.; Tao, J. Cytotoxicity of BSA-Stabilized Gold Nanoclusters: In Vitro and In Vivo Study. *Small* **2015**, *11* (21), 2571–2581.
29. Ristig, S.; Kozlova, D.; Meyer-Zaika, W.; Epple, M. An Easy Synthesis of Autofluorescent Alloyed Silver–gold Nanoparticles. *J. Mater. Chem. B* **2014**, *2* (45), 7887–7895.
30. Ganta, S.; Devalapally, H.; Shahiwala, A.; Amiji, M. A Review of Stimuli-Responsive Nanocarriers for Drug and Gene Delivery. *J Control Release* **2008**, *126* (3), 187–204.
31. Chen, J.; Ding, J.; Xiao, C.; Zhuang, X.; Chen, X. Emerging Antitumor Applications of Extracellularly Reengineered Polymeric Nanocarriers. *Biomater Sci* **2015**, *3* (7), 988–1001.
32. López-León, T.; Carvalho, E. L. S.; Seijo, B.; Ortega-Vinuesa, J. L.; Bastos-González, D. Physicochemical Characterization of Chitosan Nanoparticles: Electrokinetic and Stability Behavior. *J Colloid Interface Sci* **2005**, *283* (2), 344–351.
33. Rodrigues, S.; Dionísio, M.; López, C. R.; Grenha, A. Biocompatibility of Chitosan Carriers with Application in Drug Delivery. *Journal of Functional Biomaterials* **2012**, *3* (3), 615–641.
34. Sonone, S. B.; Kokane, S. P.; Shirote, P. J.; Naikawade, N. S. Controlled Release Matrix Tablet Formulation Using Synthesized N-Acyl Thiolated Chitosan Derivatives. *Arabian Journal of Chemistry* **2015**, DOI: 10.1016/j.arabjc.2014.12.036.
35. Wang, J.; Zhang, G.; Li, Q.; Jiang, H.; Liu, C.; Amatore, C.; Wang, X. In Vivo Self-Bio-Imaging of Tumors through in Situ Biosynthesized Fluorescent Gold Nanoclusters. *Sci Rep* **2013**, *3*, 1157.
36. Goh, E. J.; Kim, K. S.; Kim, Y. R.; Jung, H. S.; Beack, S.; Kong, W. H.; Scarcelli, G.; Yun, S. H.; Hahn, S. K. Bioimaging of Hyaluronic Acid Derivatives Using Nanosized Carbon Dots. *Biomacromolecules* **2012**, *13* (8), 2554–2561.
37. He, H.; Wang, X.; Feng, Z.; Cheng, T.; Sun, X.; Sun, Y.; Xia, Y.; Wang, S.; Wang, J.; Zhang, X. Rapid Microwave-Assisted Synthesis of Ultra-Bright Fluorescent Carbon Dots for Live Cell Staining, Cell-Specific Targeting and in Vivo Imaging. *J. Mater. Chem. B* **2015**, *3* (24), 4786–4789.
38. Phuoc, T. X. Complete Green Synthesis of Gold Nanoparticles Using Laser Ablation in Deionized Water Containing Chitosan and Starch. *Journal of Materials Science and Nanotechnology* **2014**, DOI: 10.15744/2348-9812.1.401.

39. Murugadoss, A.; Chattopadhyay, A. A “green” Chitosan-Silver Nanoparticle Composite as a Heterogeneous as Well as Micro-Heterogeneous Catalyst. *Nanotechnology* **2008**, *19* (1), 015603.
40. Calvo, P.; Remuñán-López, C.; Vila-Jato, J. L.; Alonso, M. J. Novel Hydrophilic Chitosan-Polyethylene Oxide Nanoparticles as Protein Carriers. *J. Appl. Polym. Sci.* **1997**, *63* (1), 125–132.
41. Underwood, S.; Mulvaney, P. Effect of the Solution Refractive Index on the Color of Gold Colloids. *Langmuir* **1994**, *10* (10), 3427–3430.
42. Ravindran, A.; Chandrasekaran, N.; Mukherjee, A. Studies on Differential Behavior of Silver Nanoparticles Towards Thiol Containing Amino Acids. *Current Nanoscience* **2012**, *8* (1), 141–149.
43. Zhou, T.; Lin, L.; Rong, M.; Jiang, Y.; Chen, X. Silver–Gold Alloy Nanoclusters as a Fluorescence-Enhanced Probe for Aluminum Ion Sensing. *Anal. Chem.* **2013**, *85* (20), 9839–9844.
44. Krishnadas, K. R.; Udayabhaskararao, T.; Choudhury, S.; Goswami, N.; Pal, S. K.; Pradeep, T. Luminescent AgAu Alloy Clusters Derived from Ag Nanoparticles – Manifestations of Tunable AuI–CuI Metallophilic Interactions. *Eur. J. Inorg. Chem.* **2014**, *2014* (5), 908–916.
45. Paramanik, B.; Patra, A. Fluorescent AuAg Alloy Clusters: Synthesis and SERS Applications. *J. Mater. Chem. C* **2014**, *2* (16), 3005–3012 ; Negishi, Y.; Tsukuda, T. Visible Photoluminescence from Nearly Monodispersed Au<sub>12</sub> Clusters Protected by Meso-2,3-Dimercaptosuccinic Acid. *Chemical Physics Letters* **2004**, *383* (1), 161–165.
46. Udayabhaskararao, T.; Sun, Y.; Goswami, N.; Pal, S. K.; Balasubramanian, K.; Pradeep, T. Ag<sub>7</sub>Au<sub>6</sub>: A 13-Atom Alloy Quantum Cluster. *Angew. Chem.* **2012**, *124* (9), 2197–2201.
47. Sahoo, A. K.; Banerjee, S.; Ghosh, S. S.; Chattopadhyay, A. Simultaneous RGB Emitting Au Nanoclusters in Chitosan Nanoparticles for Anticancer Gene Theranostics. *ACS Appl. Mater. Interfaces* **2014**, *6* (1), 712–724.
48. Guével, X. L.; Trouillet, V.; Spies, C.; Li, K.; Laaksonen, T.; Auerbach, D.; Jung, G.; Schneider, M. High Photostability and Enhanced Fluorescence of Gold Nanoclusters by Silver Doping. *Nanoscale* **2012**, *4* (24), 7624–7631.
49. Sun, J.; Wu, H.; Jin, Y. Synthesis of Thiolated Ag/Au Bimetallic Nanoclusters Exhibiting an Anti-Galvanic Reduction Mechanism and Composition-Dependent Fluorescence. *Nanoscale* **2014**, *6* (10), 5449–5457.
50. Zhang, N.; Si, Y.; Sun, Z.; Chen, L.; Li, R.; Qiao, Y.; Wang, H. Rapid, Selective, and Ultrasensitive Fluorimetric Analysis of Mercury and Copper Levels in Blood Using Bimetallic Gold-Silver Nanoclusters with “Silver Effect”-Enhanced Red Fluorescence. *Anal. Chem.* **2014**, *86* (23), 11714–11721.
51. Lin, C.-A. J.; Yang, T.-Y.; Lee, C.-H.; Huang, S. H.; Sperling, R. A.; Zanella, M.; Li, J. K.; Shen, J.-L.; Wang, H.-H.; Yeh, H.-I.; Parak, W. J.; Chang, W. H. Synthesis,

- Characterization, and Bioconjugation of Fluorescent Gold Nanoclusters toward Biological Labeling Applications. *ACS Nano* **2009**, *3* (2), 395–401.
52. Qi, L.; Xu, Z.; Jiang, X.; Hu, C.; Zou, X. Preparation and Antibacterial Activity of Chitosan Nanoparticles. *Carbohydr. Res.* **2004**, *339* (16), 2693–2700.
53. Wei, D.; Sun, W.; Qian, W.; Ye, Y.; Ma, X. The Synthesis of Chitosan-Based Silver Nanoparticles and Their Antibacterial Activity. *Carbohydr. Res.* **2009**, *344* (17), 2375–2382.
54. Yao, Q.; Luo, Z.; Yuan, X.; Yu, Y.; Zhang, C.; Xie, J.; Lee, J. Y. Assembly of Nanoions via Electrostatic Interactions: Ion-like Behavior of Charged Noble Metal Nanoclusters. *Sci Rep* **2014**, *4*, 3848.
55. Sahay, G.; Alakhova, D. Y.; Kabanov, A. V. Endocytosis of Nanomedicines. *J Control Release* **2010**, *145* (3), 182–195.
56. Peer, D.; Karp, J. M.; Hong, S.; Farokhzad, O. C.; Margalit, R.; Langer, R. Nanocarriers as an Emerging Platform for Cancer Therapy. *Nat Nanotechnol* **2007**, *2* (12), 751–760.

Content of the chapter has been reproduced with permission from Royal Society of Chemistry (D. Dutta, A. K. Sahoo, A. Chattopadhyay and S. S. Ghosh, *J. Mater. Chem. B*, 2016, *4*, 793–800).

## Appendix A

### A.1 Experimental Section

#### Materials and methods

**Chemicals.** For the synthesis mentioned below,  $\text{HAuCl}_4$  (Au, 17 wt% in dilute HCl; 99.99%, Sigma Aldrich),  $\text{AgNO}_3$  (Merck), chitosan ( $M_w$  672 KDa, Sigma Aldrich), sodium hydroxide (Merck), mercaptopropionic acid (Sigma Aldrich), sodium tripolyphosphate (TPP, Sigma Aldrich), and Milli-Q grade water ( $>18 \text{ M}\Omega \text{ cm}^{-1}$ , Millipore) were used without any alterations.

#### Synthesis of AgNP–AuNCs

For the synthesis of luminescent AgNP–AuNCs, a 0.5% (w/v) chitosan solution was initially prepared by dissolving 500 mg per 100 mL in Milli Q water containing 0.1% (v/v) acetic acid. After filtering out the undissolved residues, pH of the resultant solution was adjusted to 6.4 using 5 M NaOH. Then, a solution was prepared by successive addition of 10 mL of Milli Q water, 1 mL of the filtered chitosan, 400  $\mu\text{L}$  of 10 mM  $\text{AgNO}_3$  and then heated to 90 °C. As soon as it started to boil, 400  $\mu\text{L}$  of 0.3 M NaOH was added drop wise. The colour of the solution turned light brown which indicated the formation of silver nanoparticles.<sup>(39)</sup> The reaction was allowed to proceed for 10 min and then cooled to room temperature. The hence formed AgNPs were centrifuged (10 000 rpm, 10 min) and the supernatant was discarded. The pellet containing AgNPs was redispersed in 10 mL water with pH adjusted to 6.4. Then 2 mL of this AgNPs solution was taken and subsequently 1 mL

of water, 8  $\mu\text{L}$  of 0.11 M mercapto propionic acid (MPA, Sigma Aldrich) and 20  $\mu\text{L}$  of 10 mM  $\text{HAuCl}_4$  were added and the mixture was stirred for 5 min. The final solution contained both AuNCs and AgNPs and was characterized for confirmation.

### **Synthesis of AgNP–AuNC chitosan composite nanoparticles**

Chitosan nanoparticle synthesis was done by a slightly modified method from that developed by Calvo *et al.*<sup>(40)</sup> With the rest of the traditional methods followed, herein, 0.2 mg  $\text{mL}^{-1}$  sodium tripolyphosphate (TPP, Sigma Aldrich) was added drop-wise to 3 mL solution of above synthesized AgNP–AuNCs under constant stirring conditions at room temperature to prepare chitosan composite nanoparticles. AgNP–chitosan NPs (without AuNCs) were synthesized by the same method, keeping the concentration of chitosan and  $\text{AgNO}_3$  constant.

### **Characterization studies**

#### **UV visible spectroscopy.**

The absorbance characteristics in the UV-Vis region of the as-synthesized AgNPs and AgNP–AuNCs were examined using an UV-visible spectrophotometer JASCO V-630.

#### **Transmission electron microscopy (TEM)**

The sample preparation for the TEM analysis was done by diluting 500  $\mu\text{L}$  of the composite solution in 500  $\mu\text{L}$  water and out of which 7  $\mu\text{L}$  was drop-cast onto the TEM grids. The dried TEM grid was examined under a transmission electron microscope (TEM; JEM 2100; Jeol, Peabody, MA, USA), operating at a maximum accelerating voltage of 200 keV.

#### **Luminescence measurements**

All luminescence measurements were performed using a fluorescence spectrophotometer LS55, Perkin Elmer and Horiba Fluorolog3.

#### **Quantum yield measurements**

For quantum yield (QY) measurements of the AgNP–AuNCs a conventional method was followed by using quinine sulfate in a 0.10 M  $\text{H}_2\text{SO}_4$  solution as standard. The calculation of the absolute value of QY was done on the basis of the following equation

$$\text{QY} = \text{QY}_r \frac{m}{m_r} \frac{n^2}{n_r^2}$$

Here,  $m$  is the slope of integrated luminescence intensity vs. absorbance plot,  $n$  is the refractive index and suffix  $r$  refers to reference quinine sulphate solution. The absorbance and the luminescence intensity were measured simultaneously using the same solution. The refractive index of solvent (water) is 1.33 and the quantum yield of the standard ( $\text{QY}_r$ ) is 0.54.

### **Dynamic light scattering study**

For the measurement of hydrodynamic diameter and the zeta potential, AgNP–AuNCs (composite NPs) were assessed using a Malvern Zetasizer Nano ZS.

### **Matrix-assisted laser desorption ionization time-of-flight mass spectrometry (MALDI-TOF MS) analysis**

MALDI-TOF (Applied Biosystems 4800 Plus MALDI TOF/TOF Analyzer) analysis was performed using an R-cyano-4-hydroxycinnamic acid (CHCA) matrix.

### **Fourier transform infrared (FTIR) spectroscopy**

To carry out FTIR analysis, samples were initially lyophilized and then pellets were prepared after mixing with KBr. The pellets were characterized by a Perkin-Elmer Spectrum One machine in the range of 4000–400  $\text{cm}^{-1}$ .

### **Atomic absorption spectroscopy (AAS)**

The amounts of silver and gold present in AgNPs and AgNP–AuNCs (composite NPs) were determined using an Atomic absorption spectrophotometer AA240-Varian Inc.

### **Cellular activity studies**

#### **Cell culture**

For cell culture studies, HeLa cells (human cervical carcinoma) were procured from National Center for Cell Sciences (NCCS), Pune, India. These cells were cultured in Dulbecco's Modified Eagle's Medium supplemented with L-glutamine (4 mM), penicillin (50 units per mL), streptomycin (50 mg  $\text{mL}^{-1}$ , Sigma-Aldrich) and 10% (v/v) fetal bovine serum (PAA Laboratories, Austria) in a 5%  $\text{CO}_2$  humidified incubator at 37 °C.

#### **Epi-fluorescence microscopy**

The cells were treated with composite NPs and imaged under an epi-fluorescence microscope (Nikon ECLIPSE, TS100, Tokyo) under UV (340–380 nm) excitation. Briefly, the sample preparation for imaging involves incubation of  $1 \times 10^6$  HeLa cells (seeded into a cover slip contained in a 35 mm culture plate) for 24 h. The hence incubated cells were treated with composite NPs for 6 h. Following which, the medium was discarded and the cells were washed with 1X PBS for visualization under a microscope.

#### **Deconvolution fluorescence microscopy**

The cells were treated with composite NPs and imaged under a Delta Vision deconvolution microscope (GE Healthcare). Herein, the sample preparation for imaging involves incubation of  $1 \times 10^6$  HeLa cells (seeded into a cover slip contained in a 35 mm culture plate) for 24 h. The hence incubated cells were treated with composite NPs for 6 h. The medium was then discarded and the cells were washed with 1× PBS for visualization under a microscope.

**MTT assay**

For cell viability studies,  $1 \times 10^5$  HeLa cells per well were (seeded in a 96-well microtiter plate) grown overnight in a 5% CO<sub>2</sub> humidified incubator (37 °C for 24 h). These cells were subsequently treated with composite NPs. MTT [3-(4,5-dimethylthiazol-2-yl)-2,5 diphenyltetrazolium bromide] assay was carried after 24 h to obtain the number of viable cells. Mitochondria reduces MTT into color formazan in living cells. Thus, absorbance at 550 nm reveals the amount of formazan product, which is directly proportional to the number of living cells. However, there is a background interference due to absorbance at 690 nm which is to be addressed. The % of cell viability was calculated as

$$\text{Cell Viability (\%)} = \frac{(\text{Abs}_{570} - \text{Abs}_{690}) \text{ of treated cells}}{(\text{Abs}_{570} - \text{Abs}_{690}) \text{ of control cells}} \times 100$$

**Acridine orange/ethidium bromide staining**

Also for AO/EB staining,  $1 \times 10^5$  HeLa cells per well were (seeded in a 96-well microtiter plate) grown overnight in a 5% CO<sub>2</sub> humidified incubator (37 °C for 24 h) and were subsequently treated with composite NPs. The treated cells were stained with AO/EB (Sigma-Aldrich) dual dyes. After removing the culture media, cells were washed twice with PBS and stained by adding 5  $\mu\text{L}$  of 1 mg mL<sup>-1</sup> EtBr and 2  $\mu\text{L}$  of 1 mg mL<sup>-1</sup> AO. The cells were then incubated for 10 min and were washed again with PBS for visualization under a fluorescence microscope (Nikon ECLIPSE, TS100, Tokyo) with an excitation filter of 480/30 nm.

**Field emission scanning electron microscopy (FESEM)**

FESEM analysis was carried out to reveal the cell morphology prior to and after the treatment with composite NPs. Briefly, the sample preparation involves the growth of cells ( $1 \times 10^5$  cells per well, 6-well tissue culture plates) and then treatment with composite NPs. These cells were fixed in 0.1% formaldehyde after being washed with PBS. Centrifugation of this cell suspension is done and the pellet is redispersed in PBS. Following this, the cells were drop-cast on an aluminium foil covered glass slide and were allowed to dry for analysis.

**Uptake studies of composite NPs in HeLa cells by TEM**

The uptake of composite NPs by cells was examined under a transmission electron microscope. The sample preparation involved the initial growth of HeLa ( $1 \times 10^5$  cells, 35 mm culture dishes) cells and then they were treated with composite NPs for 1 h, 3 h, 6 h, 12 h and 24 h. These cells were then harvested by trypsinisation followed by centrifugation (650 rcf, 6 min) and finally were fixed in (or with) 70% chilled ethanol. For the TEM analysis, 7  $\mu\text{L}$  of this sample was drop-cast onto copper TEM grids.

### **Determination of reactive oxygen species (ROS)**

For ROS determination, HeLa cells ( $1 \times 10^5$  cells per well, seeded in a 6-well plate) were grown for 24 h and then treated with composite NPs for 3 h. These cells were incubated for 10 min after adding 1 mM 2,7-dichlorofluorescein diacetate (5  $\mu$ L per well, DCFH-DA, Sigma-Aldrich). After discarding the media, the cells were harvested and redispersed in fresh media. DCFH-DA (non-fluorescent dye) can readily diffuse inside the cell where it is converted to DCFH through hydrolysis. Thus formed DCFH will be ultimately transformed to dichlorofluorescein (DCF, green fluorescent) upon oxidation. Hence, samples were analyzed for DCF fluorescence in –a FL1-H channel in a flow cytometer (FacsCalibur, BD Biosciences, NJ) at an excitation wavelength of 488 nm and an emission wavelength of 530 nm. The fluorescence data were recorded using the Cell Quest program (BD Biosciences) for 15000 cells in each sample.

### **Cell cycle analysis**

The propidium iodide staining method was adopted for cell cycle analysis. Initially, HeLa cells ( $1 \times 10^5$  cells, 6 well plates) were grown and then were treated with composite NPs for 24 h. Here, for both treated and control cells, the media and PBS were collected separately. These cells were then harvested by trypsinization. After harvesting, the cells along with the media and collected PBS were centrifuged (650 rcf, 6 min). Following this, the cells were fixed by slowly adding 1 mL of cold 70% ethanol under vortexing and were stored at 4 °C. The cells were then centrifuged and washed in ice-cold PBS. Upon washing, these cells were treated with RNase for 1 h at 55 °C. To this, 10  $\mu$ L of 1 mg mL<sup>-1</sup> PI was added and incubated (37 °C, 30 min) in the dark. The samples were then analyzed in a FACSCalibur (BD Biosciences, NJ). PI fluorescence data were recorded using the CellQuest program (BD Biosciences) for 15000 cells in each sample and subsequently analyzed.

### **Caspase-3 assay**

Sample preparation for the Caspase-3 assay involved the growth of HeLa cells ( $1 \times 10^5$  cells per well, 6 well plates) followed by treatment with composite NPs for 24 h. These treated cells were then harvested by trypsinisation and fixed in 0.1% formaldehyde for 15 min. After fixing, the samples were centrifuged (650 rcf, 6 min) and the pellet was redispersed in PBS. 0.5% of Tween 20 was added to this and was incubated in the dark for 20 min. Following this, the cells were washed with PBS thrice and then 10  $\mu$ L of PE conjugated anticaspase-3 antibody was added. Finally, these cells were incubated for half an hour at 37 °C and were analysed for PE fluorescence in a FACSCalibur (BD Biosciences, NJ).

### **RT-PCR for caspase expression.**

Total RNA was extracted from HeLa cells and the cDNA was prepared using a Verso cDNA kit (Thermo Scientific). Then, cDNA was amplified by polymerase chain reaction (PCR) using 2 $\times$  BiomixRed (Bioline) and IDT (Integrated DNA technologies) forward primer 5'-TTTGGTTTGTGTGCTTCTGAGCC-3' and the reverse primer 5'-ATTCTGTTGCCACCTTTCGG-

3' which is specific for the gene Caspase-3 and  $\beta$ -actin served as control with forward primer 5'-CTGTCTGGCGGCACCACCAT-3' and reverse primer 5'-GCAACTAAGTCATAGTCCGC-3'. The PCR amplification condition was maintained as denaturation at 94 °C for 60 s, annealing at 55 °C for 60 s and extension at 72 °C for 60 s.

## A.2 Figures

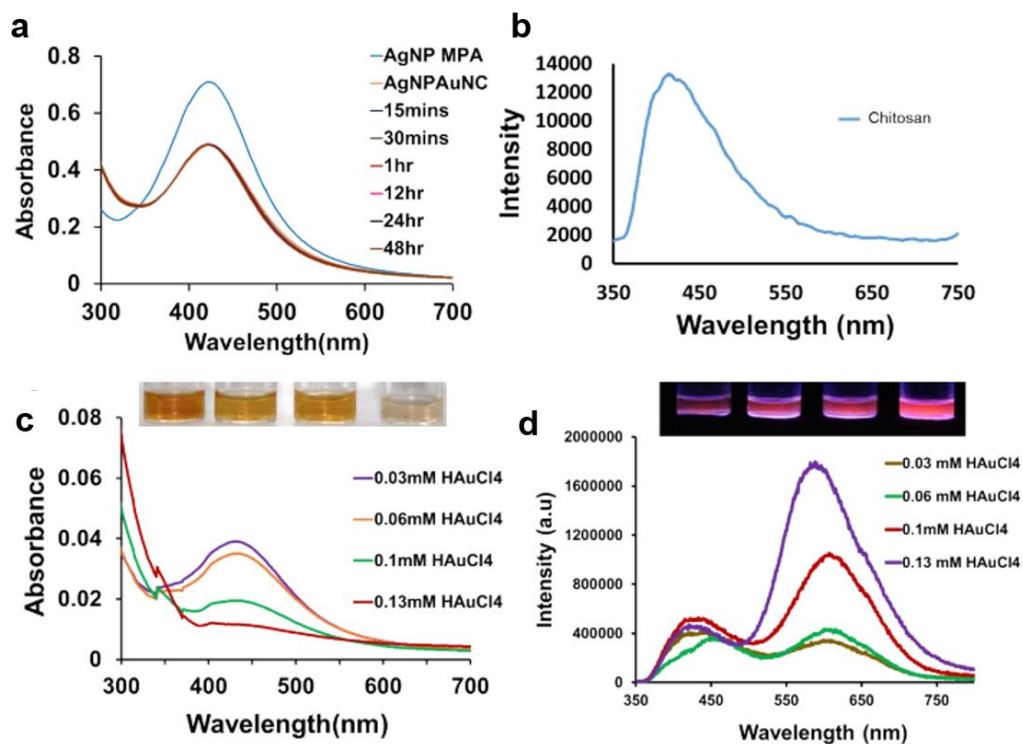


**Figure A2.1.** (a) Time dependent UV – Vis absorption spectra of the AgNP-AuNCs, (b) Emission spectra of control chitosan. ( $\lambda_{\text{ex}} = 300 \text{ nm}$ ), (c) UV-Vis absorption spectra of the AgNP-AuNCs with increasing concentration of HAuCl<sub>4</sub>, corresponding images are given in the inset, (d) Emission spectra of the AgNP-AuNCs with increasing concentration of HAuCl<sub>4</sub>, corresponding images are given in the inset. ( $\lambda_{\text{ex}} = 300 \text{ nm}$ ).

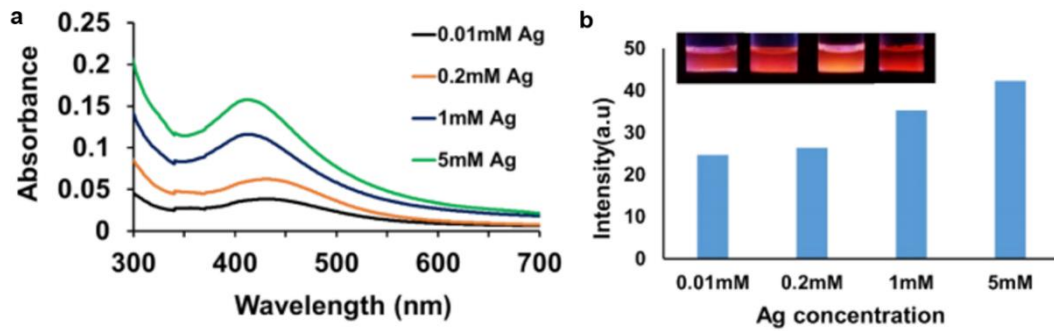


**Figure A2.2.** (a) UV-Vis absorption spectra of the AgNP-AuNCs with increasing amount of Ag. (b) Emission intensity of the AgNP-AuNCs with increasing concentration of Ag, corresponding images are given in the inset.

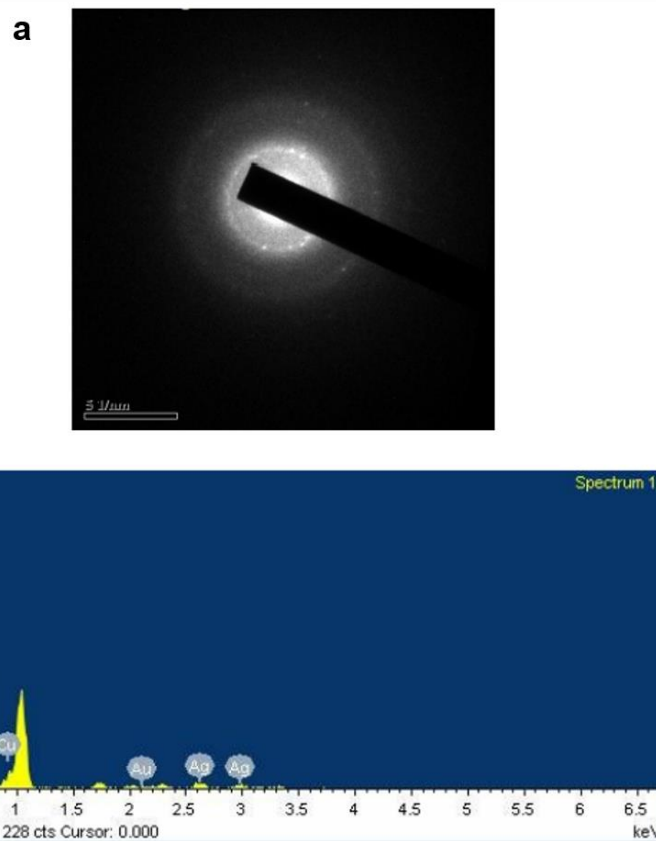


**Figure A2.3.** (a) SAED of AgNP-AuNCs, (b) EDX spectrum of the AgNP-AuNCs.

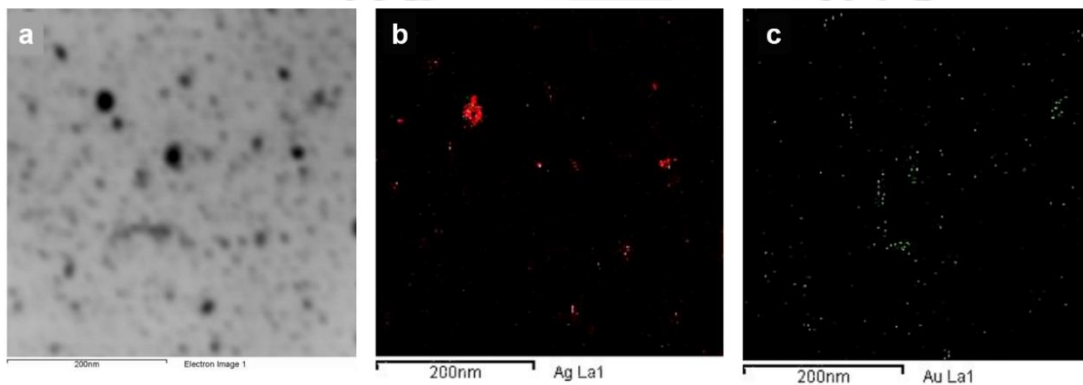


**Figure A2.4.** HAADF-STEM (BF) image of AgNP-AuNCs synthesized in chitosan matrix (a); EDX mapping image corresponding to Ag (b) and EDX mapping image corresponding to Au(c).

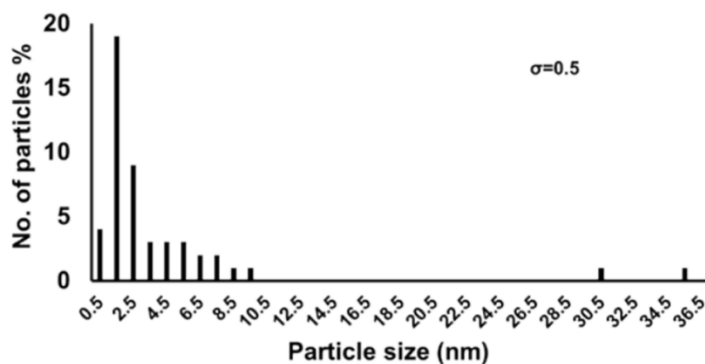


**Figure A2.5.** Particle size distribution of the AgNP-AuNCs as obtained from the TEM image in Figure 2.2(C).

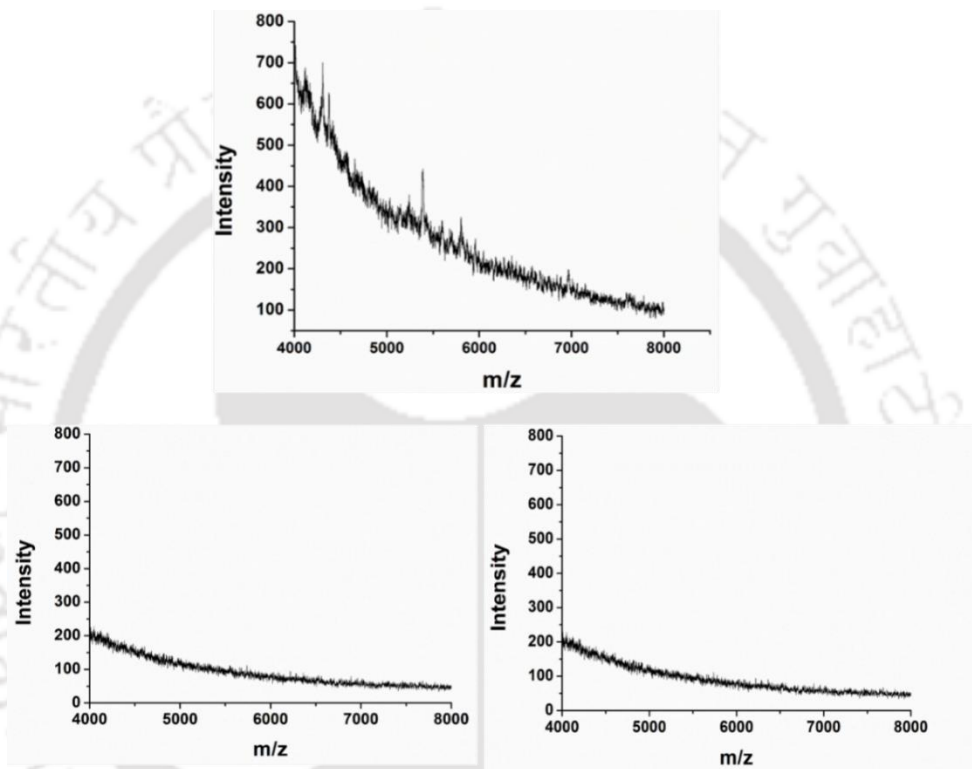


**Figure A2.6:** MALDI-TOF analysis of (a) AgNP-AuNCs, (b) control AgNPs and (c) control chitosan.

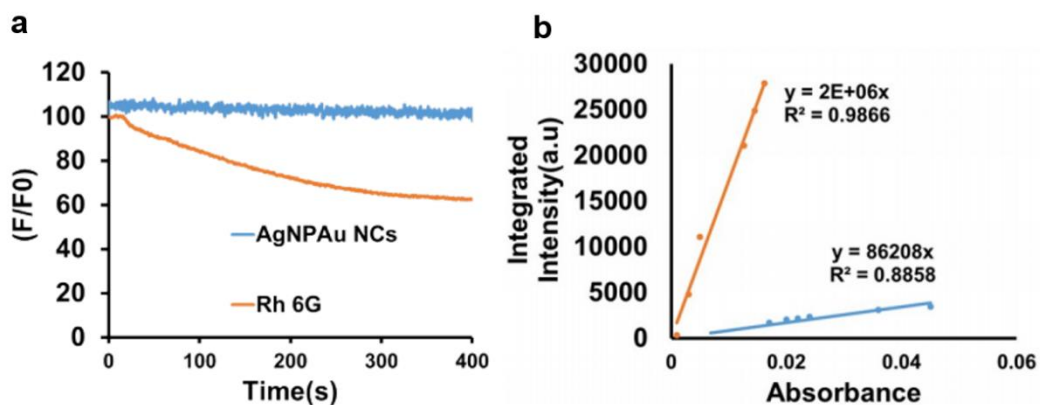


**Figure A2.7.** (a) Photostability of AgNP-AuNCs with respect to rhodamine 6G. (b) Quantum yield of AgNP-AuNCs with respect to quinine sulphate.

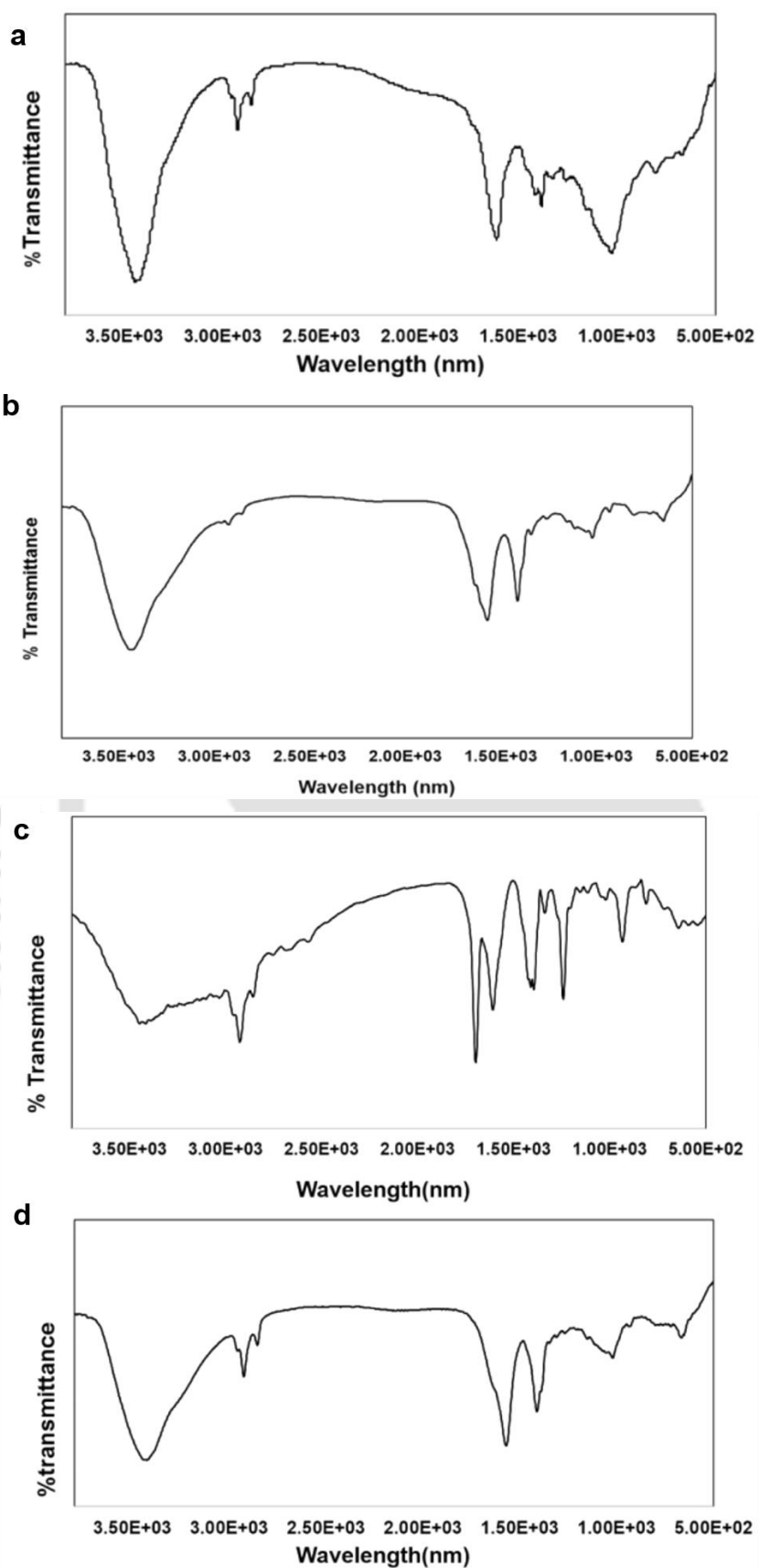


**Figure A2.8.** (a) FTIR spectrum of control chitosan (b) FTIR spectrum of AgNPs (chitosan stabilized), (c) FTIR spectrum of free MPA, (d) FTIR spectrum of AgNP-AuNCs (chitosan stabilized).

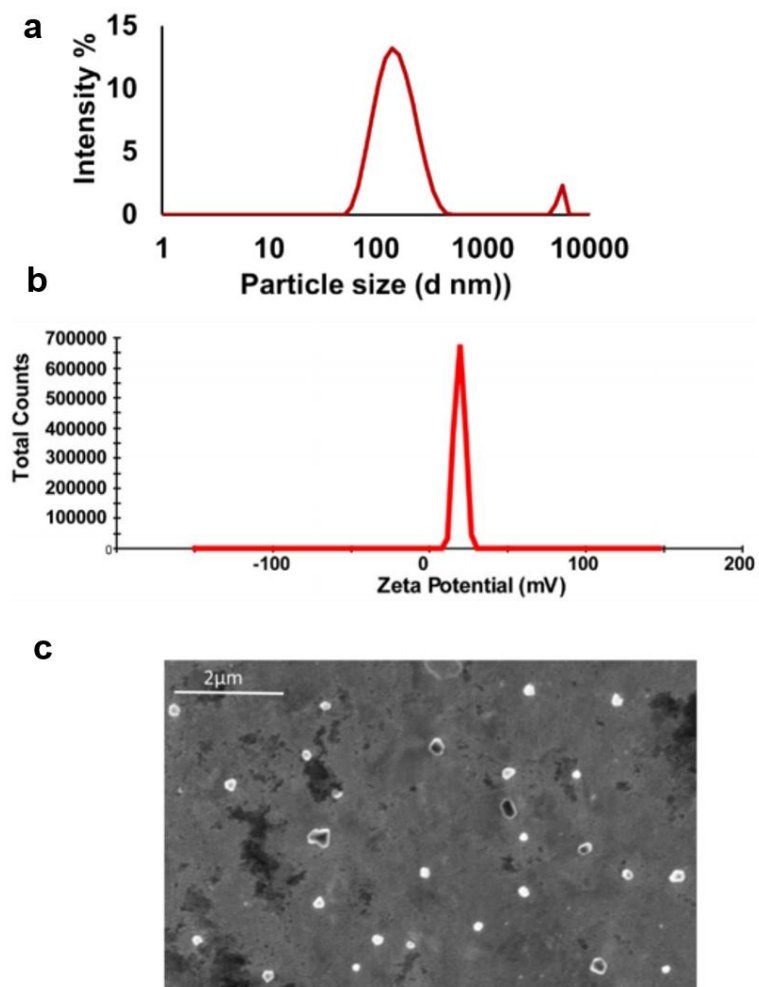


**Figure A2.9.** (a) Hydrodynamic particle size of composite NPs (AgNP-AuNC-CS NP). (b) Zeta potential distribution of composite NPs. (c) FESEM image of the composite NPs.

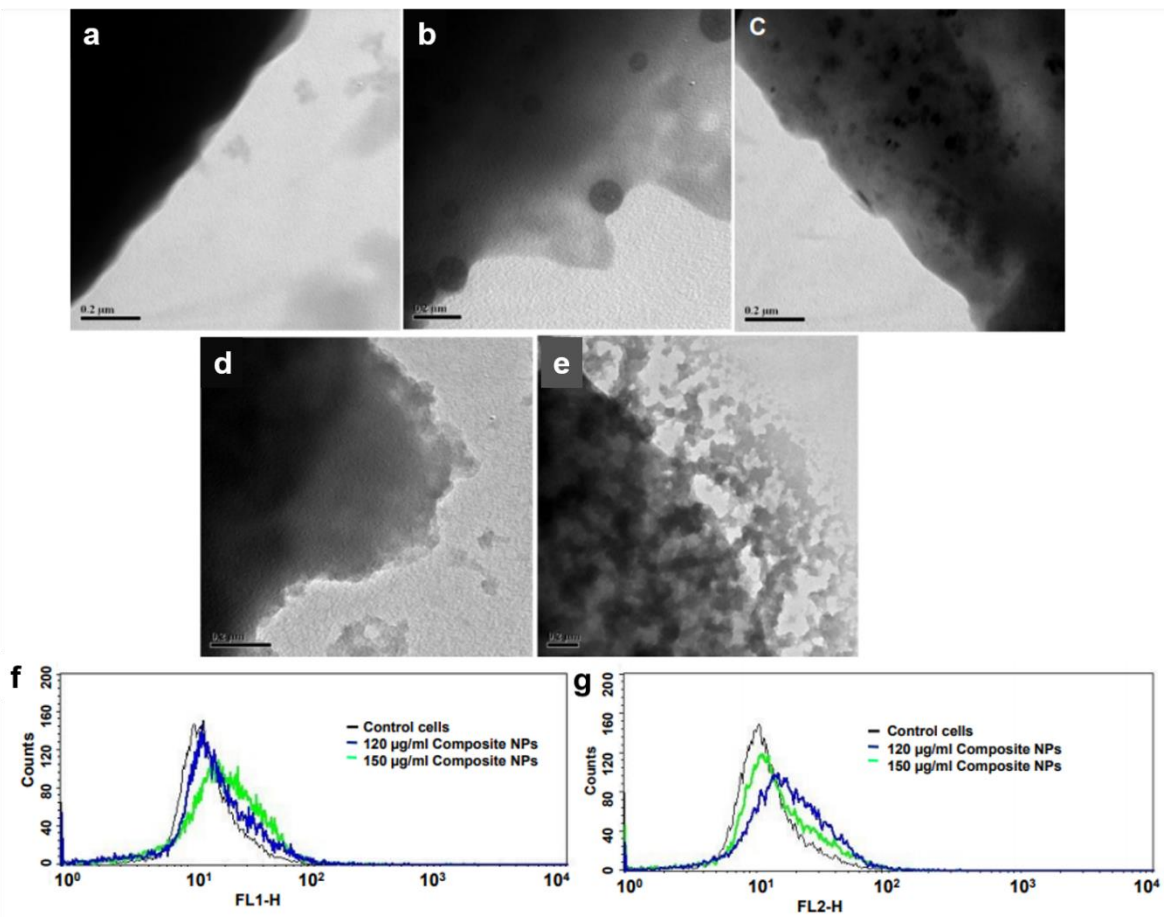


**Figure A2.10.** (a-e) Time dependent TEM analysis of HeLa cells treated with IC50 dose of composite NPs for 1 h, 3 h, 6 h, 12 h, 24 h, respectively, at 0.2 μm scale. Extensions of plasma membrane at 3 h suggests endocytosis mediated uptake of composite NPs; membrane disruption at 24 h is visible. (f,g) FACS analysis of uptake of composite NPs in FL1-H and FL2-H, respectively.

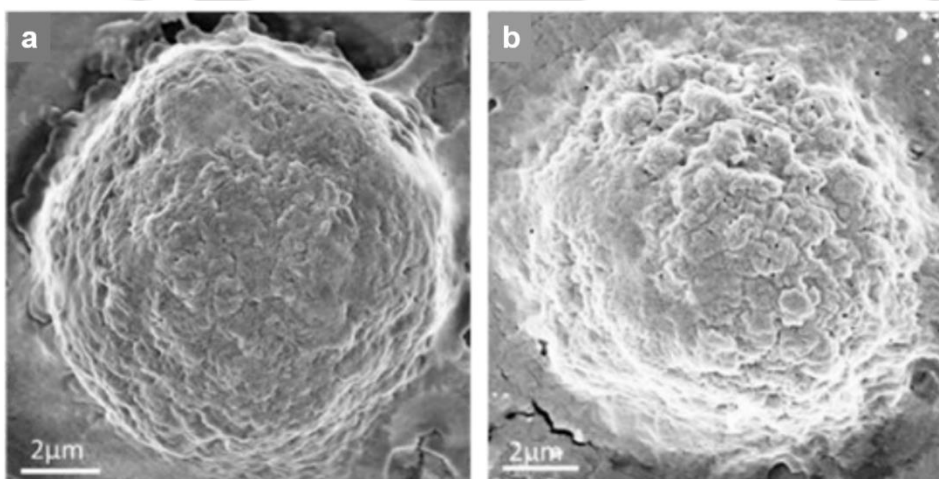


**Figure A2.11.** (a-b) FESEM images of control and composite NPs treated HeLa cells. Scale bar is 2 μm.

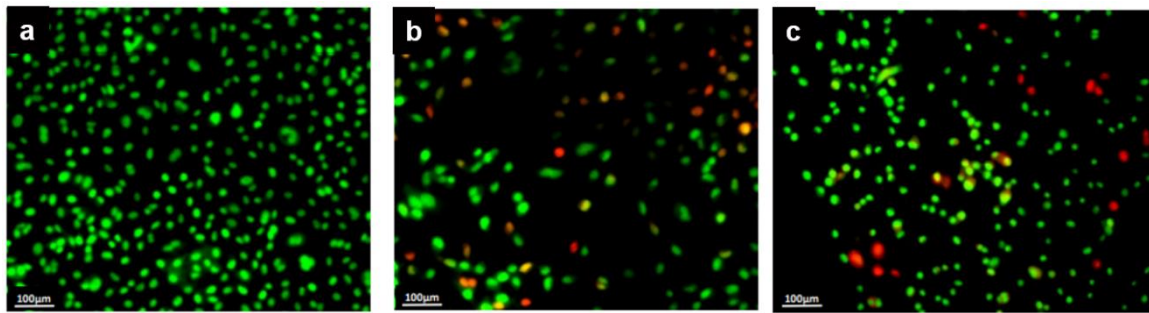


**Figure A2.12.** (a) EtBr/AO double staining of control HeLa cells, (b) composite NPs treated (for 24 h at IC5) HeLa cells, (c) AgNPs only treated HeLa cells for 24 hrs at IC50.

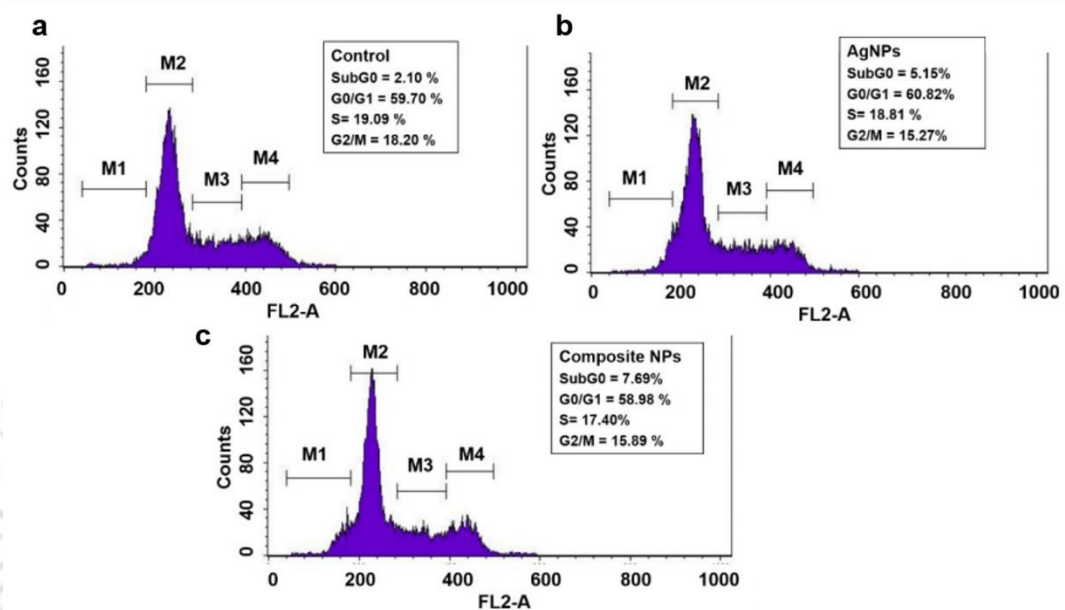


**Figure A2.13.** (a-c) Cell cycle analysis of control HeLa cells, AgNPs treated HeLa Cells, composite NPs treated HeLa cells, respectively, for 24 h at IC50.

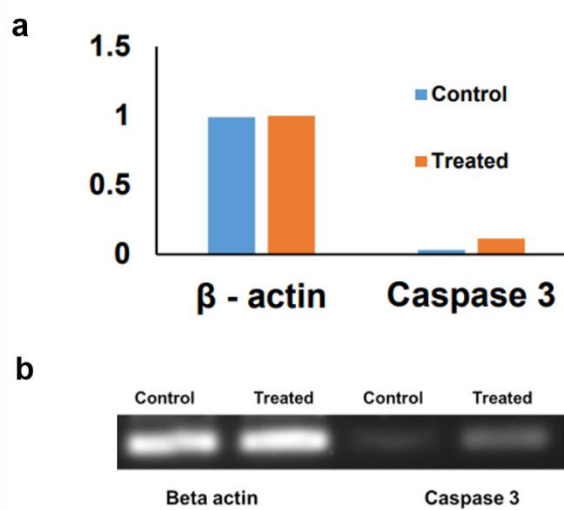
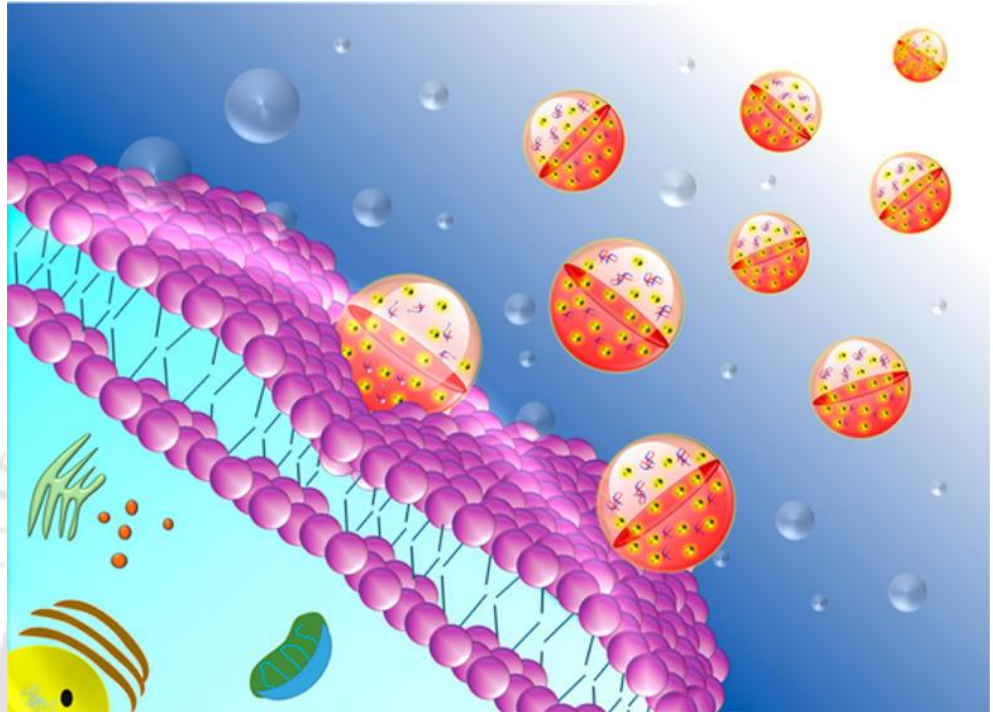


**Figure A2.14.** (a-b) Overexpression of Caspase-3 was observed from gene expression analysis of composite NPs treated and control cells, taking  $\beta$ -actin as endogenous control.



## Chapter 3



**Cationic BSA Templated Au - Ag Bimetallic  
Nanoclusters as a Theranostic Gene Delivery  
Vector for HeLa Cancer Cells**

D. Dutta, A. Chattopadhyay And S. S. Ghosh, *ACS Biomater. Sci. Eng.* 2,  
11, 2090-2098



## Chapter 3

# Cationic BSA Templated Au–Ag Bimetallic Nanoclusters as a Theranostic Gene Delivery Vector for HeLa Cancer Cells

## Abstract

A cationic BSA nanoparticle system incorporating bimetallic Au–Ag luminescent nanoclusters (NCs) was developed for the delivery of therapeutic suicide gene in HeLa cancer cells. Combinatorial therapy is achieved with cationic BSA Au–Ag NCs composite NPs loaded with pDNA, which binds efficiently with pDNA due to its positive nature. While successful delivery of a suicide gene (CD-UPRT) into cells by pDNA loaded composite NPs initiates a therapeutic response cascade by converting prodrug 5-FC to 5-FU, Au–Ag NCs results in ROS (reactive oxygen species) triggered apoptosis mediated cell death. Further, luminescence of Au–Ag NCs serves to track the gene delivery into cells. The detailed mechanism of uptake and manner of cell death have been demonstrated to comprehend the combinatorial therapeutic efficacy of the composite system.

## 3.1. Introduction

In this current era of personalized genomic medicine, the ability to cure diseases at the genetic origins makes gene therapy a significant practice in clinical treatment of several diseases like cancer, autoimmune and mutation induced metabolic syndromes. The strategical transfer of appropriate genetic material within desired cells to achieve alteration of the diseased phenotype and thereby induce normal biological behaviour formulates the core aspects of this treatment.<sup>(1-3)</sup> Here, it is to be mentioned that out of all gene therapy techniques, suicide gene therapy is the first of its kind to have clinical implications. One of the most widely used systems in this respect is the *E. coli cytosine deaminase uracil phosphoribosyltransferase* (CD-UPRT) encoded suicide gene which converts nontoxic prodrug 5- fluorocytosine (5-FC) to 5-fluorouracil (5-FU) and other toxic metabolites, resulting in killing of transfected cancer cells.<sup>(4-6)</sup> In cancer gene therapy, a variety of delivery vehicles to transfer the naked DNA molecule into the cell have been developed. However, most of them suffered from hurdles arising in terms of nuclease susceptibility, immune response, reduced uptake, and selectivity. Above all, non-viral vectors had proved to be more advantageous than their viral contemporaries due to immunogenicity, safety concerns, and the high cost involved in the practice of the latter.<sup>(7-9)</sup> Particularly through advances in nanomedicine, several nanomaterials have progressed as efficient gene carriers.<sup>(10, 11)</sup> Nanocarriers based on cationic polymers offers salient features like efficient electrostatic interactions with anionic nucleic acids, encapsulation to protect gene from degradation, and specific accumulation in tumor cells. Cationic polymers such as chitosan, poly-lysine, etc. have been used to synthesize non-viral gene carriers with superior uptake and mucoadhesive properties attributed to their electrostatic interactions with the cell membrane.<sup>(12-</sup>

<sup>15)</sup> Serum albumin had been an important choice of material in various drug delivery systems due to its non-toxic nature, biodegradability, biocompatibility, and cost effectiveness. For instance, Abraxane, an FDA-approved albumin-based nanoparticle system has been successfully applied for breast cancer. Additionally, albumin also extends an advantage via numerous important functional moieties present on its surface for favorable interactions to occur.<sup>(16-18)</sup> But nevertheless, the use of serum albumin as a carrier of genetic material has always remained a challenge due to its negative surface charge at physiological pH. One possible way for application of serum albumin as a gene delivery vehicle is through modification of the carboxylic group, thereby transforming the negatively charged albumin into cationic albumin. This cationic albumin can then interact with a negatively charged DNA molecule more efficiently and importantly results in preferential uptake into cells.<sup>(19-21)</sup>

Luminophores are often tagged to the non-viral vectors with the motive of tracking the gene delivery. Several organic fluorophores, quantum dots, etc. have been put to use in this regard.<sup>(22, 23)</sup> With many of these having issues related to biocompatibility, stability, and environmental friendliness, the lookout for alternatives is a subject of intense research.<sup>(24)</sup> In this regard, noble metal nanoclusters have become a viable alternative as a result of their excellent luminescent properties, high photostability, environmental friendliness, and suitable quantum yield for imaging applications.<sup>(25-27)</sup> Metal nanoclusters of gold, silver, and copper have been well established as imaging agents in both *in vitro* and *in vivo* systems. Also, in the synthesis of these metal nanoclusters, several polymers like DNA, protein, chitosan, PAMAM, etc. have been successfully applied as a template or stabilizer.<sup>(28-32)</sup> Moreover, bimetallic nanoclusters have been found to be more advantageous in comparison to the monometallic ones in various aspects like enhanced fluorescence, better catalytic activity, and improved sensitivity in the case of sensing applications.<sup>(33-36)</sup> Though metal nanoclusters are generally regarded as noncytotoxic,<sup>(37)</sup> there are several reports stating the cytotoxic nature of these metal nanoclusters attributed to their small sizes which effectively contributes towards ROS generation in cells.<sup>(38,39)</sup> Hence, by embedding these metal nanoclusters into a suitable positive charge nanocarrier as a delivery vehicle, loaded with a therapeutic suicide gene, could enhance the apoptosis mediated death induced by gene therapy in cancer cells alongside imaging. Such a non-viral vector-based combinatorial treatment would deliver efficient tracking of gene delivery with augmented cancer therapy.<sup>(40)</sup>

Herein, the synthesis of a cationic BSA embedded Au–Ag bimetallic nanocluster system molded into a composite nanoparticle as a carrier for the pDNA encoding CD-UPRT enzyme is reported. Native BSA was used for the synthesis of bimetallic Au–Ag nanoclusters. Subsequently, ethylenediamine was used to modify the anionic BSA into cationic BSA bearing a positive charge at pH 7. The cationic BSA embedded with bimetallic nanoclusters were then converted into composite nanoparticles via desolvation in the presence of acetone followed by heat cross-linking. Finally, the negative charged pDNA was bound to these composite nanoparticles. These composite nanoparticles were effectively

uptaken by cancer cells, and the luminescence of bimetallic nanoclusters allowed tracking the delivery of pDNA into cells. It was observed that the cytotoxicity of the bimetallic nanocluster system augmented the therapeutic effects of suicide gene mediated killing of cancer cells. Hence, the incorporation of a bimetallic system in a biocompatible cationic polymer with a loaded suicide gene bestowed the advantage of combinatorial therapeutic ability along with bioimaging, giving a theranostic angle to the composite nanoparticle system. The schematic description of the overall work illustrating Au–Ag NC-embedded cationic BSA composite nanoparticle application in elucidating combined therapeutic response via metal nanoclusters and suicide gene delivery alongside bioimaging is demonstrated in **Figure 3.1**.

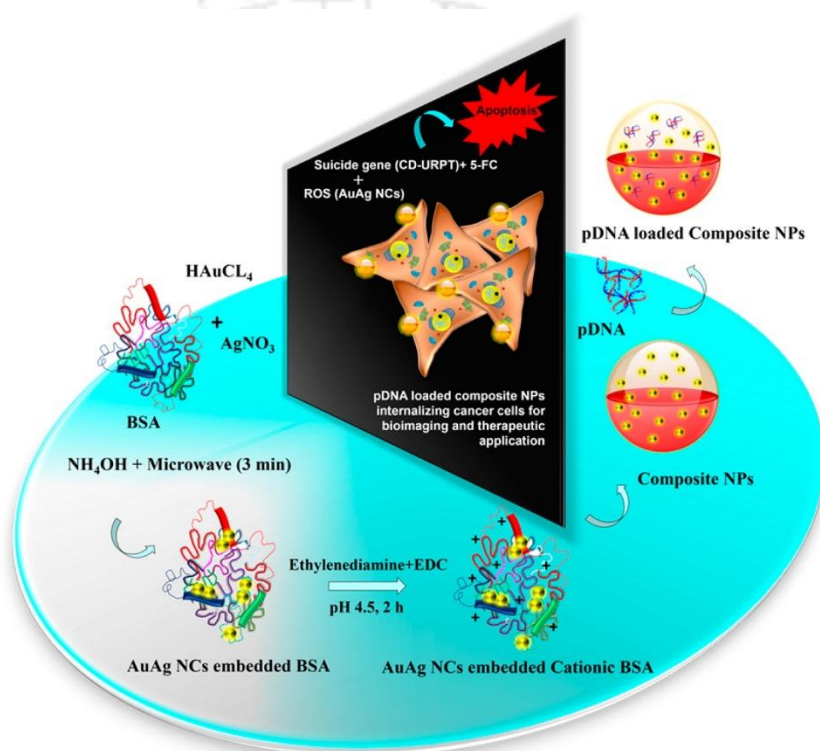


**Figure 3.1.** Synthesis of cationic BSA Au–Ag NCs composite NPs to achieve bioimaging alongside combinatorial therapy as a result of suicide gene delivery and Au–Ag NC induced ROS generation in cancer cells.

### 3.2. Synthesis and Characterisation of Au–Ag NCs, Au–Ag NC-Embedded Cationic BSA

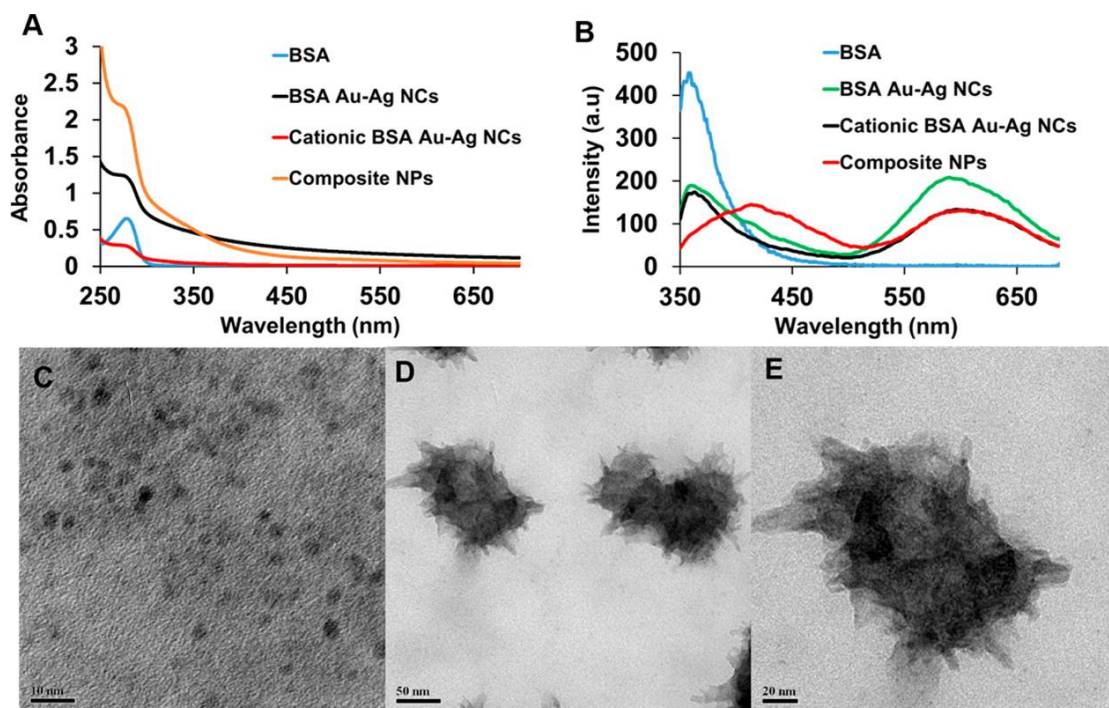


**Figure 3.2.** (A) UV–vis absorption spectra of BSA, BSA Au–Ag NCs, cationic BSA Au–Ag NCs, and composite NPs. (B) Emission spectra of BSA ( $\lambda_{em} = 359$  nm), BSA Au–Ag NCs ( $\lambda_{em} = 590$  nm), cationic BSA Au–Ag NCs ( $\lambda_{em} = 596$  nm), and composite NPs ( $\lambda_{em} = 600$  nm) when excited at 300 nm. (C) TEM images of Au–Ag NCs with 50 nm scale bar. (D) TEM images of pDNA loaded composite NPs with 50 nm scale bar. (E) Magnified TEM image of pDNA loaded composite NPs with 20 nm scale bar.

The as synthesized BSA templated Au–Ag NC suspension was deep yellow in color and did not show any SPR (surface plasmon resonance) peak in the UV–vis region negating the presence of large sized nanoparticles (**Figure 3.2A**). It exhibited a sharp emission peak at around 590 nm when excited at 300 nm, indicating the formation of metal nanoclusters. The second peak at around 360 nm can be attributed to the native fluorescence of tryptophan residues of BSA (**Figure 3.2B**).<sup>(41)</sup> TEM image revealed the formation of NCs (**Figure 3.2C**) with an average size of  $2.0 \pm 0.49$  nm as inferred from the particle size distribution (**Appendix B, Figure B3.1a**). The size distribution was obtained by calculating particle size from the TEM image in ImageJ software. Energy-dispersive X-ray spectroscopy (EDX) analysis confirmed the presence of both Au and Ag in the nanoclusters as shown in **Appendix B, Figure B3.1b**. The formation of bimetallic BSA Au–Ag NCs (as alloys) was supported and confirmed by the previously reported method via structural analysis.<sup>(34)</sup> Hence the synthesized Au–Ag NC embedded BSA was subjected to cationization by ethylenediamine according to a well-established process for formation of cationic BSA. The formation of positive charge BSA was confirmed by a change in zeta potential across different pH values. The cationic BSA (embedded with Au–Ag NCs) in contrast to native BSA (embedded with Au–Ag NCs) was found to be positively

charged at physiological pH around 7, as confirmed by zeta potential analysis (**Appendix B, Figure B3.1c**). Also, the presence of amine groups were analyzed using standard TNBS assay for primary amines.<sup>(42)</sup> It was revealed that the cationic BSA (embedded with Au–Ag NCs) had increased amine group content indicated by increased absorbance at 420 nm for cationic BSA (embedded with Au–Ag NCs) at all concentrations (20, 75, 100, 200 µg/mL) as compared to native BSA (embedded with Au–Ag NCs; **Appendix B, Figure B3.1d**). Also, FTIR analysis showed shifting in amide I (from 1651 to 1637 cm<sup>-1</sup>) and amide II (1540 cm<sup>-1</sup> to 1601 cm<sup>-1</sup>) in the case of cationic BSA in comparison to native BSA and BSA Au–Ag NCs (amide I at 1642 cm<sup>-1</sup>, amide II at 1606 cm<sup>-1</sup>), which suggests changes in the secondary structure of protein; also for native BSA the peak at 1398 cm<sup>-1</sup> due to the side chain carboxyl group (COO<sup>-</sup>) has a prominent shift to 1511 cm<sup>-1</sup> in the case of cationic BSA, suggesting possible modification<sup>(43,44)</sup> (**Appendix B, Figure B3.2a-c**) CD spectra revealed that there was a considerable change in the secondary structure of the protein after the formation of BSA Au–Ag NCs and cationic BSA Au–Ag NCs (**Appendix B, Figure B3.3a-c**).

### **3.3. Synthesis and Characterisation of Au–Ag NCs Embedded Cationic BSA Composite Nanoparticles and pDNA Loading**

For efficient application of these metal nanoclusters in imaging and therapy along with suicide gene transfection into cancer cells, the formation of a composite nanoparticle is essential for its success as a delivery vehicle. Hence, composite nanoparticles of Au–Ag NC embedded cationic BSA were formed in a similar way with slight modifications as in the synthesis of BSA nanoparticles.<sup>(45, 46)</sup> In brief, desolvation in the presence of acetone was carried out at an acetone addition rate of 1 mL per minute at pH 7. The appearance of turbidity indicated formation of coacervates, which were allowed to stabilize and then heat cross-linked at 80 °C for 1 h. The obtained product after centrifugation at 10 000 rpm for 5 min contained positively charged composite nanoparticles (referred as composite NPs from now on). Similarly, sets of negatively charged BSA nanoparticles embedded with Au–Ag NCs and cationic BSA nanoparticles without Au–Ag NCs were prepared. Now, to appraise the performance of these composite NPs in bioimaging and gene delivery, a suicide gene (referred to as pDNA) expressing CD-UPRT enzyme was loaded onto the composite nanoparticles, and DNA binding studies were carried out. CD-UPRT enzyme converts the non-toxic prodrug 5-FC into 5-FU and other toxic metabolites, leading to cancer cell death. The pDNA binding studies with increasing amounts of composite NPs indicated that the pDNA (0.5 µg/mL) was bound to composite NPs. Agarose gel electrophoresis revealed that at a 0.7 mg/mL concentration of composite NPs, the pDNA was immobilized into the wells, and its migration was retarded (compared to free pDNA), indicating the formation of a polyplex with the composite NPs (**Appendix B, Figure B3.4a**). Also, a DNase protection assay was carried out to ensure the integrity of the loaded pDNA during delivery, which is a key element for successful development of a non-viral vector in the form of composite NPs. It was observed that the unbound pDNA was cleaved by DNase when compared to pDNA loaded into

composite NPs, which remained intact and retained in the wells, demonstrating the ability of composite NPs in protecting the pDNA from DNases (**Appendix B, Figure B3.4b**). TEM investigation revealed that pDNA loaded composite nanoparticles with an average size of  $145 \pm 28$  nm were formed (**Figure 3.2D and E**). The mean hydrodynamic diameter was found to be 267 nm with a positive zeta potential of  $20.9 \pm 5.78$  mV, which is essential for its use as a DNA carrier and in cellular uptake. The particle size was found to be increased in both pH 5 and pH 11 with respect to pH 7. A pronounced increase in particle size was observed in the presence of pDNA at all pH values (**Appendix B, Table B3.1**). The zeta potential was found to be positive at pH 5, pH 7, and negative at pH 11. In the presence of pDNA, there was a reduction of positive charge at all pH values (**Appendix B, Table B3.2**). FESEM analysis also indicated the formation of particles with an average size of  $154 \pm 29$  nm (**Appendix B, Figure B3.4c-e**). Time dependent luminescence spectra revealed that the pDNA loaded composite nanoparticles were stable in nature. Also, photostability of the cationic BSA Au–Ag NCs, pDNA loaded composite and NPs indicated by a luminescence decrease rate of 0.093% per min and 0.069% per min respectively when compared to standard organic dye, rhodamine 6G with a luminescence decrease rate of 0.279% per min. The quantum yield of the cationic BSA Au–Ag NCs have been found to be 11.7% and that of pDNA loaded composite NPs was found to be 8.8%, which is well suited for bioimaging purposes (**Appendix B, Figure B3.5a-c**). The photoluminescence intensity was found to be almost similar for pH 7 and pH 11 with a slight decrease in intensity at pH 5. In the presence of pDNA there was an increase in the intensity initially, which gets saturated at higher pDNA concentration (**Appendix B, Figure B3.6a and b**). The presence of both Au and Ag was confirmed using atomic absorption spectroscopy. The concentration of Au and Ag was found to be 13.25  $\mu\text{g/mL}$  and 3.11  $\mu\text{g/mL}$ , respectively, in the prepared pDNA loaded composite NPs (**Appendix B, Figure B3.6c and d**). The above results indicated the formation of a non-viral vector carrying pDNA (encoding CD-UPRT) in conjunction with luminescent metal nanoclusters for potential use as a safe, biocompatible combinatorial delivery system to achieve therapy as well as imaging of cancer cells.

### 3.4. Uptake and Bio-imaging Application of pDNA Loaded Composite NPs

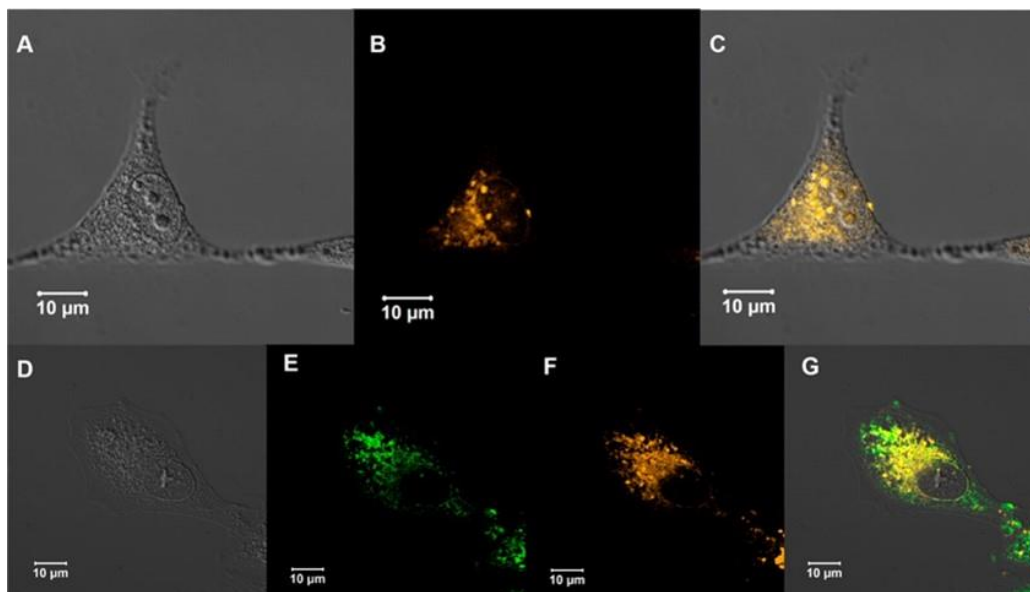


**Figure 3.3.** Confocal microscopic images. (A) Bright field image, (B) fluorescence image, and (C) merged fluorescence image of HeLa cells treated with pDNA loaded composite NPs for 4 h. (D) Bright field image of HeLa cells treated with pDNA loaded composite NPs and cytopainter green lysosomal staining kit, (E) fluorescence image showing green fluorescence from stained lysosomes of HeLa cells treated with pDNA loaded composite NPs and cytopainter green lysosomal staining kit, (F) fluorescence image showing fluorescent pDNA loaded composite from NPs inside HeLa cells treated with pDNA loaded composite NPs and cytopainter green lysosomal staining kit, and (G) merged fluorescence image of HeLa cells treated with pDNA loaded composite NPs and cytopainter green lysosome staining kit showing localization of pDNA loaded composite in the lysosomes. Scale bar, 10  $\mu\text{m}$ .

For the application of the composite system in bioimaging through the luminescence attributed to Au–Ag NCs, HeLa cancer cells were kept under treatment with pDNA loaded composite NPs for 4 h and then were visualized under a confocal microscope. The confocal microscopic images showed the uptake of pDNA loaded composite NPs into cancer cells (**Figure 3.3A–C**) as indicated by the luminescence arising due to Au–Ag NCs. The images of control cells without treatment have been incorporated in the **Appendix B, Figure B3.7a–c**. This showed the potential use of luminescent Au–Ag NCs in pDNA loaded composite NPs in imaging cancer cells. To analyze whether the pDNA loaded composite NPs were localized in the lysosomal compartments, lysosomes were stained with a cytopainter green lysosome staining kit (Abcam) for 2 h, after incubating the cells with pDNA loaded composite NPs for 4 h. The merged images revealed that the pDNA loaded composite NPs were homed into the lysosomal compartments, which is essential for their activity as shown in **Figure 3.3D–G**. The images of control cells without treatment are shown in **Appendix B, Figure B3.7d–g**. The depth projection of the confocal microscopy image of pDNA loaded composite NP treated cells revealed the intake of composite NPs inside cells (**Appendix B, Figure B3.7h**). Also, the uptake of the cationic BSA Au–Ag NCs was analyzed, and a lower uptake compared to the composite NPs

(Figure 3.3A-C) was observed (Appendix B, Figure B3.8a-d). Hence, the composite NPs were able to bind pDNA and were more efficiently uptaken by the cells due to their favorable size and positive surface charge. The time dependent confocal microscopy studies gave a better insight into the uptake of pDNA loaded composite NPs. The results showed that the luminescence of the pDNA loaded composite NPs inside the cells increased with respect to time (Appendix B, Figure B3.9a-d), indicating the gradual uptake of pDNA loaded composite NPs inside the cells. To confirm the pathway of uptake of these pDNA loaded composite NPs, the cells were treated with 0.1% sodium azide (Sigma-Aldrich) for 10 min prior to the treatment with pDNA loaded composite NPs in order to block the energy dependent uptake processes. There was a visible difference in uptake of the pDNA loaded composite NPs in case of sodium azide treated cells (Appendix B, Figure B3.10a-f) after 4 h of treatment. From the above confocal microscopy results, it can be concluded that the composite NPs were possibly uptaken by the cells via endocytosis mediated uptake pathway.<sup>(47, 48)</sup> To study the effects of delivery of these ultrasmall metal nanoclusters and the suicide gene in cancer cells, the uptake of the pDNA loaded composite nanoparticles was evaluated by fluorescence-activated cell sorting (FACS) in the FL3-H channel exploiting the luminescence property of the composite NPs. The studies revealed that pDNA loaded composite NPs were more efficiently uptaken having around 93% of the cell population positive for fluorescence recorded in the FL3-H channel, with respect to control cells where it is only 10% and 47% in the case of cells treated with pDNA loaded negative charged composite NPs as shown in Figure 3.4A-C.

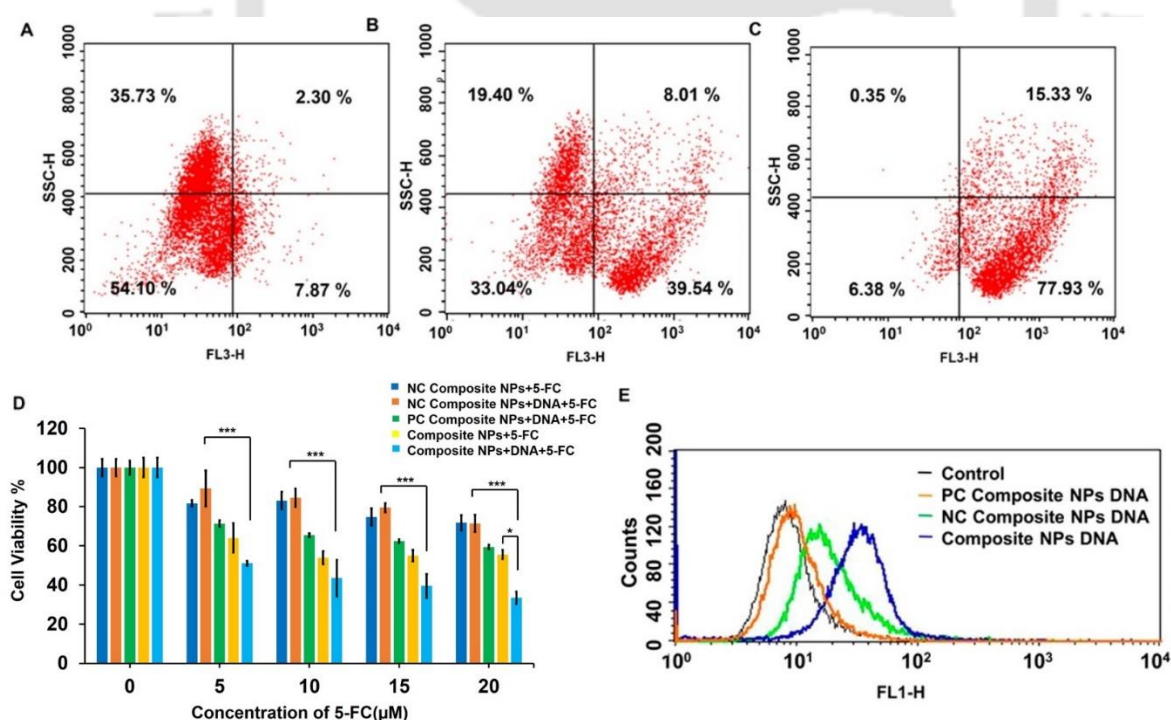


**Figure 3.4** (A–C) Uptake of the composite NPs loaded with DNA and negatively charged composite NPs loaded with DNA in HeLa cells after 5 h of treatment was studied by FACS in the FL3-H channel by tracing the luminescence of Au–Ag NCs without using any organic fluorophore. (D) The MTT assay representing cell viability of HeLa cells treated with negatively charged composite NPs, negatively charged composite NPs+DNA, composite NPs, composite NPs+DNA, and positively charged

composite NPs+DNA without Au–Ag NCs in the presence of 5-FC with respect to control cells. (E) ROS generation profile of HeLa cells treated with composite NPs+DNA, negatively charged composite NPs+DNA, and positively charged composite NPs+DNA without Au–Ag NCs with respect to control cells. The values are represented as mean  $\pm$  SD of three individual experiments.

### 3.5. Cell Viability and Mechanism of Cell Death

Now, the challenge is to study the cytotoxic potential of the Au–Ag NCs in pDNA loaded composite nanoparticles in addition to suicide gene therapy mediated cell death. MTT assay of cells treated with the composite NPs and negative charge composite NPs (without pDNA, for 36 h) was carried out. It was observed that the composite NPs effectively induced cell death with an  $IC_{50}$  at 2.20  $\mu\text{g/mL}$  and 0.51  $\mu\text{g/mL}$  of Au and Ag concentrations, respectively, in comparison to negative charged composite NPs where more cells were found to be viable at the above-mentioned  $IC_{50}$  dose (**Appendix B, Figure B3.11a**). The results inferred that Au–Ag NCs contributed to cytotoxicity as indicated in previous reports.<sup>(49)</sup> Also, as speculated, the positive nature of the composite NPs may possibly have resulted in efficient interaction with the negatively charged cell membrane leading to increased activity. The MTT assay of BSA Au–Ag NCs and cationic BSA Au–Ag NCs (before forming composite NPs) indicated more percentage of viable cells at the  $IC_{50}$  dose (2.20  $\mu\text{g/mL}$  of Au, 0.51  $\mu\text{g/mL}$  of Ag) of composite NPs, signifying better uptake of composite NPs which corroborated with the confocal microscopy analysis (**Appendix B, Figure B3.11b**). The biocompatibility of the composite NPs was evaluated with HEK 293 cells, and 78% of the cells were found to be viable at the  $IC_{50}$  dose (2.20  $\mu\text{g/mL}$  of Au, 0.51  $\mu\text{g/mL}$  of Ag) of composite NPs (**Appendix B, Figure B3.11c**). Thereafter, to elucidate the effects of suicide gene transfection in combination with cytotoxicity of metal nanoclusters, a concentration (1.72  $\mu\text{g/mL}$  of Au, 0.40  $\mu\text{g/mL}$  of Ag) slightly lower than the above-mentioned  $IC_{50}$  was chosen. The cells were treated with pDNA loaded composite NPs, composite NPs, pDNA loaded negatively charged composite NPs, and negatively charged composite NPs in the presence of 5-FC for 36 h. An MTT assay showed that at a 5  $\mu\text{M}$  concentration of 5-FC, about 50% cell death was observed in the case of pDNA loaded composite NPs, i.e., in the combined system, which is more with respect to composite NPs, pDNA loaded negatively charged composite NPs, and negatively charged composite NPs. This indicated a possible combinatorial effect of the metal nanoclusters (Au–Ag NCs) as well as pDNA encoding CD-UPRT in rendering the cancer cells towards death. Further, pDNA loaded positive charged composite NPs without Au–Ag NCs evaluated simultaneously in similar conditions exhibited a much lower cytotoxicity than the combined system in the presence of Au–Ag NCs (**Figure 3.4D**). A FACS based DCFH-DA (dichloro-dihydro-fluorescein diacetate) assay was carried out to ascertain ROS generating potential of Au–Ag NCs embedded in pDNA loaded composite NPs. It was revealed that the pDNA loaded composite NPs generated a maximum amount of ROS with respect to control cells,

pDNA loaded negative charged composite NPs, and pDNA loaded positive charged composite NPs without Au–Ag NCs as shown in **Figure 3.4E**.

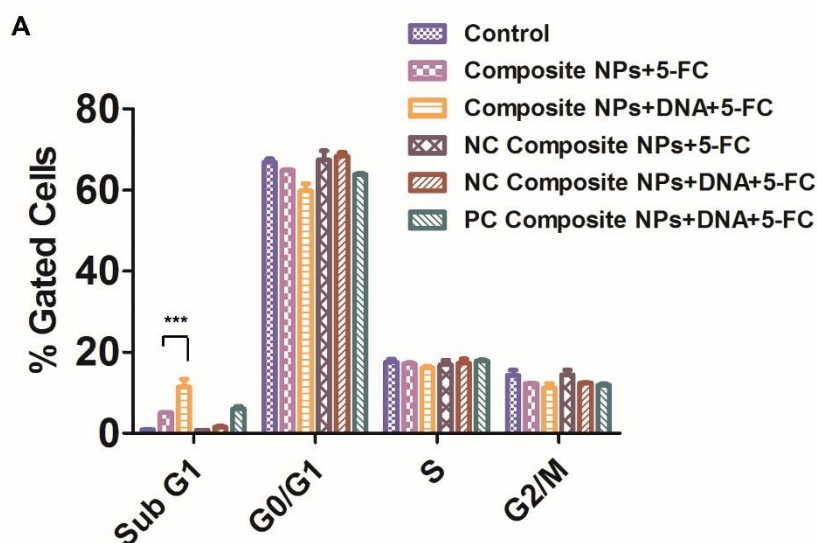


**Figure 3.5.** (A) Cell cycle analysis of control HeLa cells, HeLa cells treated with composite NPs, composite NPs+DNA, negatively charged composite NPs, negatively charged composite NPs+DNA, and positively charged composite NPs+DNA without Au–Ag NCs in the presence of 5-FU. The values are represented as mean  $\pm$  SD of three individual experiments.

Further, to evaluate the mode of cell death by pDNA composite NPs, cell cycle analysis was carried out by propidium iodide staining (**Figure 3.5A**). A significant increase of the sub G<sub>1</sub> population was observed in the case of pDNA loaded composite NPs compared to control cells and pDNA loaded negative charged composite. Also, in the absence of pDNA, both composite NPs and the negative charged composite NPs exhibited less accumulation of cells in sub G<sub>1</sub>. Further results include the simultaneous cell cycle analysis of pDNA loaded positive charged composite NPs without Au–Ag NCs, where a lesser percentage of cells in sub G<sub>1</sub> was observed. Hence, the increase in sub G<sub>1</sub> population indicated significant apoptosis mediated cell death in the case of the combined system, i.e., pDNA loaded composite NPs as shown in **Figure 3.5A** and **Appendix B, Figure B3.12**.

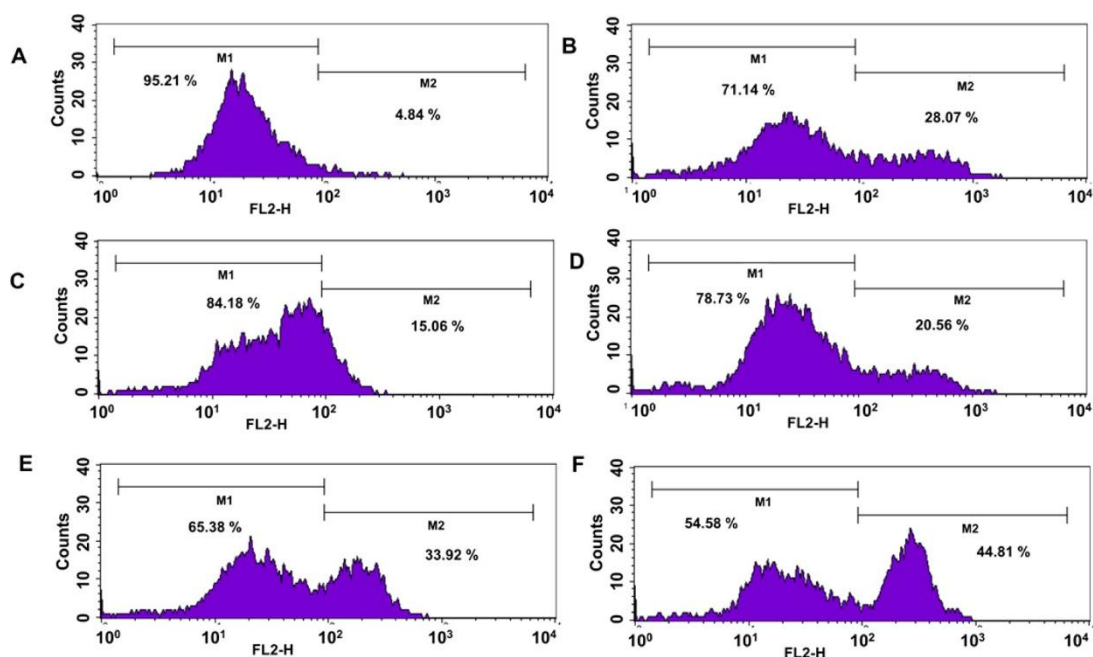


**Figure 3.6.** Caspase-3 assay of HeLa cells showing percentage of apoptosis in (A) control, treated with (B) positively charged composite NPs+DNA without Au–Ag NCs, (C) negatively charged composite NPs, (D) negatively charged composite NPs+DNA, (E) composite NPs, and (F) composite NPs+DNA in the presence of 5-FC.

The caspase-3 assay further strengthened the observed apoptosis mediated cell death. It revealed that pDNA loaded composite NPs treated cells showed a considerable increase in the apoptotic population in comparison to control cells and pDNA loaded negative charged composite NPs. Both composite NPs and negative charged composite NPs in the absence of pDNA exhibited a lesser percentage of apoptotic signature. Also, pDNA loaded positive charged composite NPs without Au–Ag NCs were simultaneously evaluated for their caspase-3 activity, which again showed a nominal increase in the apoptotic population (**Figure 3.6A-F**). The FESEM images of control cells and pDNA loaded composite NP treated cells revealed morphological distortions, like membrane blebbing in the case of pDNA loaded composite NP treated cells when compared to control cells (**Appendix B, Figure B3.13**). Hence from all the above findings, it can be concluded that the pDNA loaded composite NPs effectively killed the cancer cells by virtue of suicide gene therapy alongside cytotoxicity imparted by the Au–Ag bimetallic nanoclusters. Also, the luminescence property of the composite NPs conferred biolabeling properties, thereby helping in tracking the delivery process.

### 3.6. Conclusions

In a nutshell, cationic BSA embedded Au–Ag NC composite nanoparticles were synthesized for effectively carrying a suicide gene payload into the cancer cells. The pDNA binding and uptake of the composite NPs was favoured due to its positive nature. The pDNA loaded composite NPs delivered combinatorial therapeutic activity conferred due to the cytotoxicity attributed by bimetallic

Au–Ag NCs through ROS generation, and the suicide gene through conversion of prodrug 5-FC into 5-FU. Also, the luminescent nature of the bimetallic NCs gave an opportunity for tracking the delivery of the gene inside the cells without the need for organic fluorophores. The mechanism of uptake and mode of cell death have been established via confocal microscopy and flow cytometry based assays. Thus, the present biocompatible cationic composite NPs have potential for bioimaging in combinatorial cancer therapy.

### 3.7. References

1. Amer, M. H. Gene therapy for cancer: present status and future perspective *Mol. Cell. Ther.* **2014**, 2, 27.
2. Maeder, M. L.; Gersbach, C. A. Genome-editing Technologies for Gene and Cell Therapy *Mol. Ther.* **2016**, 24, 430–446.
3. Seroogy, C. M.; Fathman, C. G. The application of gene therapy in autoimmune diseases *Gene Ther.* **2000**, 7, 9–13.
4. Morgan, R. A. Live and Let Die: A New Suicide Gene Therapy Moves to the Clinic *Mol. Ther.* **2012**, 20, 11–13.
5. Miyagi, T.; Koshida, K.; Hori, O.; Konaka, H.; Katoh, H.; Kitagawa, Y.; Mizokami, A.; Egawa, M.; Ogawa, S.; Hamada, H.; Namiki, M. Gene therapy for prostate cancer using the cytosine deaminase/uracil phosphoribosyltransferase suicide system *J. Gene Med.* **2003**, 5, 30–37.
6. Christensen, C. L.; Gjetting, T.; Poulsen, T. T.; Cramer, F.; Roth, J. A.; Poulsen, H. S. Targeted cytosine deaminase-uracil phosphoribosyl transferase suicide gene therapy induces small cell lung cancer specific cytotoxicity and tumor growth delay *Clin. Cancer Res.* **2010**, 16, 2308–2319.
7. Zhang, Y.; Satterlee, A.; Huang, L. In Vivo Gene Delivery by Nonviral Vectors: Overcoming Hurdles? *Mol. Ther.* **2012**, 20, 1298–1304.
8. Mairhofer, J.; Grabherr, R. Rational Vector Design for Efficient Non-viral Gene Delivery: Challenges Facing the Use of Plasmid DNA *Mol. Biotechnol.* **2008**, 39, 97–104.
9. Yin, H.; Kanasty, R. L.; Eltoukhy, A. A.; Vegas, A. J.; Dorkin, J. R.; Anderson, D. G. Non-viral vectors for gene-based therapy *Nat. Rev. Genet.* **2014**, 15, 541–555.
10. Chen, J.; Guo, Z.; Tian, H.; Chen, X. Production and clinical development of nanoparticles for gene delivery *Mol. Ther.--Methods Clin. Dev.* **2016**, 3, 16023.
11. Lin, G.; Zhang, H.; Huang, L. Smart Polymeric Nanoparticles for Cancer Gene Delivery *Mol. Pharmaceutics* **2015**, 12, 314–321.

12. Kirtane, A. R.; Panyam, J. Polymer nanoparticles: Weighing up gene delivery *Nat. Nanotechnol.* **2013**, 8, 805– 806.
13. Pack, D. W.; Hoffman, A. S.; Pun, S.; Stayton, P. S. Design and development of polymers for gene delivery *Nat. Rev. Drug Discovery* **2005**, 4, 581– 593.
14. Shmueli, R. B.; Anderson, D. G.; Green, J. J. Electrostatic Surface Modifications to Improve Gene Delivery *Expert Opin. Drug Delivery* **2010**, 7, 535– 550.
15. Dai, S. In *Cationic Polymers in Regenerative Medicine*; The Royal Society of Chemistry, **2014**; Chapter 21, pp 557– 582.
16. Larsen, M. T.; Kuhlmann, M.; Hvam, M. L.; Howard, K. A. Albumin-based drug delivery: harnessing nature to cure disease. *Mol. Cell. Ther.* **2016**, 4.
17. Elsadek, B.; Kratz, F. Impact of albumin on drug delivery — New applications on the horizon *J. Controlled Release* **2012**, 157, 4– 28.
18. Chen, Q.; Liu, Z. Albumin Carriers for Cancer Theranostics: A Conventional Platform with New Promise. *Adv. Mater.* **2016**, DOI: 10.1002/adma.201600038.
19. Zhang, T.; Song, X.; Kang, D.; Zhang, L.; Zhang, C.; Jin, S.; Wang, C.; Tian, J.; Xing, J.; Liang, X.-J. Modified bovine serum albumin as an effective charge-reversal platform for simultaneously improving the transfection efficiency and biocompatibility of polyplexes *J. Mater. Chem. B* **2015**, 3, 4698– 4706.
20. Han, J.; Wang, Q.; Zhang, Z.; Gong, T.; Sun, X. Cationic Bovine Serum Albumin Based Self-Assembled Nanoparticles as siRNA Delivery Vector for Treating Lung Metastatic Cancer *Small* **2014**, 10, 524– 535.
21. Fischer, D.; Bieber, T.; Brüsselbach, S.; Elsässer, H.-P.; Kissel, T. Cationized human serum albumin as a non-viral vector system for gene delivery? Characterization of complex formation with plasmid DNA and transfection efficiency *Int. J. Pharm.* **2001**, 225, 97– 111.
22. Srinivasan, C.; Lee, J.; Papadimitrakopoulos, F.; Silbart, L.K.; Zhao, M.; Burgess, D.J. Labeling and Intracellular Tracking of Functionally Active Plasmid DNA with Semiconductor Quantum Dots *Mol. Ther.* **2006**, 14, 192– 201.
23. Liu, G.; Swierczewska, M.; Lee, S.; Chen, X. Functional nanoparticles for molecular imaging guided gene delivery *Nano Today* **2010**, 5, 524– 539.
24. Hardman, R. A Toxicologic Review of Quantum Dots: Toxicity Depends on Physicochemical and Environmental Factors *Environ. Health Perspect.* **2006**, 114, 165– 172.

25. Tao, Y.; Li, Z.; Ju, E.; Ren, J.; Qu, X. Polycations-functionalized water-soluble gold nanoclusters: a potential platform for simultaneous enhanced gene delivery and cell imaging *Nanoscale* **2013**, 5, 6154– 6160.
26. Vankayala, R.; Kuo, C.-L.; Nuthalapati, K.; Chiang, C.-S.; Hwang, K. C. Cancer Therapy: Nucleus-Targeting Gold Nanoclusters for Simultaneous In Vivo Fluorescence Imaging, Gene Delivery, and NIR-Light Activated Photodynamic Therapy *Adv. Funct. Mater.* **2015**, 25, 5934– 5945.
27. Sahoo, A. K.; Banerjee, S.; Ghosh, S. S.; Chattopadhyay, A. Simultaneous RGB Emitting Au Nanoclusters in Chitosan Nanoparticles for Anticancer Gene Theranostics *ACS Appl. Mater. Interfaces* **2014**, 6, 712– 724.
28. Palmal, S.; Jana, N. R. Gold nanoclusters with enhanced tunable fluorescence as bioimaging probes *Wiley Interdiscip. Rev. Nanomed. Nanobiotechnol.* **2014**, 6, 102– 110.
29. Wang, C.; Yao, Y.; Song, Q. Interfacial synthesis of polyethyleneimine-protected copper nanoclusters: Size-dependent tunable photoluminescence, pH sensor and bioimaging *Colloids Surf., B* **2016**, 140, 373– 381.
30. Zhao, T.; He, X.-W.; Li, W.-Y.; Zhang, Y.-K. Transferrin-directed preparation of red-emitting copper nanoclusters for targeted imaging of transferrin receptor over-expressed cancer cells *J. Mater. Chem. B* **2015**, 3, 2388– 2394.
31. Ai, J.; Guo, W.; Li, B.; Li, T.; Li, D.; Wang, E. DNA G-quadruplex-templated formation of the fluorescent silver nanocluster and its application to bioimaging *Talanta* **2012**, 88, 450– 455.
32. Qu, X.; Li, Y.; Li, L.; Wang, Y.; Liang, J.; Liang, J. Fluorescent Gold Nanoclusters: Synthesis and Recent Biological Application *J. Nanomater.* **2015**, 2015, 1 DOI: 10.1155/2015/784097.
33. Chen, P.-C.; Ma, J.-Y.; Chen, L.-Y.; Lin, G.-L.; Shih, C.-C.; Lin, T.-Y.; Chang, H.-T. Photoluminescent AuCu bimetallic nanoclusters as pH sensors and catalysts *Nanoscale* **2014**, 6, 3503– 3507.
34. Zheng, B.; Zheng, J.; Yu, T.; Sang, A.; Du, J.; Guo, Y.; Xiao, D.; Choi, M. M. F. Fast microwave-assisted synthesis of AuAg bimetallic nanoclusters with strong yellow emission and their response to mercury(II) ions *Sens. Actuators, B* **2015**, 221, 386– 392.
35. Yuan, X.; Dou, X.; Zheng, K.; Xie, J. Recent Advances in the Synthesis and Applications of Ultrasmall Bimetallic Nanoclusters *Part. Part. Syst. Char.* **2015**, 32, 613– 629.

36. Zhou, Q.; Lin, Y.; Xu, M.; Gao, Z.; Yang, H.; Tang, D. Facile Synthesis of Enhanced Fluorescent Gold–Silver Bimetallic Nanocluster and Its Application for Highly Sensitive Detection of Inorganic Pyrophosphatase Activity *Anal. Chem.* **2016**, 88, 8886– 8892.
37. Ristig, S.; Kozlova, D.; Meyer-Zaika, W.; Epple, M. An easy synthesis of autofluorescent alloyed silver–gold nanoparticles *J. Mater. Chem. B* **2014**, 2, 7887– 7895.
38. Dong, L.; Li, M.; Zhang, S.; Li, J.; Shen, G.; Tu, Y.; Zhu, J.; Tao, J. Cytotoxicity of BSA-Stabilized Gold Nanoclusters: In Vitro and In Vivo Study *Small* **2015**, 11, 2571– 2581.
39. Yang, Y.; Nan, J.; Hou, J.; Yu, B.; Zhao, T.; Xu, S.; Lv, S.; Zhang, H. Cytotoxicity of gold nanoclusters in human liver cancer cells *Int. J. Nanomed.* **2014**, 9, 5441– 5448.
40. Gopinath, P.; Gogoi, S. K.; Chattopadhyay, A.; Ghosh, S. S. Implications of silver nanoparticle induced cell apoptosis for in vitro gene therapy *Nanotechnology* **2008**, 19, 075104.
41. Moriyama, Y.; Ohta, D.; Hachiya, K.; Mitsui, Y.; Takeda, K. Fluorescence behavior of tryptophan residues of bovine and human serum albumins in ionic surfactant solutions: A comparative study of the two and one tryptophan(s) of bovine and human albumins *J. Protein Chem.* **1996**, 15, 265– 272.
42. Goh, E. J.; Kim, K. S.; Kim, Y. R.; Jung, H. S.; Beack, S.; Kong, W. H.; Scarcelli, G.; Yun, S. H.; Hahn, S. K. Bioimaging of Hyaluronic Acid Derivatives Using Nanosized Carbon Dots *Biomacromolecules* **2012**, 13, 2554– 2561.
43. Grdadolnik, J.; Maréchal, Y. Bovine serum albumin observed by infrared spectrometry. I. Methodology, structural investigation, and water uptake *Biopolymers* **2001**, 62, 40– 53.
44. Schmidt, M. P.; Martínez, C. E. Kinetic and Conformational Insights of Protein Adsorption onto Montmorillonite Revealed Using in Situ ATR-FTIR/2D-COS *Langmuir* **2016**, 32, 7719– 7729.
45. Yu, Z.; Yu, M.; Zhang, Z.; Hong, G.; Xiong, Q. Bovine serum albumin nanoparticles as controlled release carrier for local drug delivery to the inner ear. *Nanoscale Res. Lett.* **2014**, 9.
46. Khandelia, R.; Bhandari, S.; Pan, U. N.; Ghosh, S. S.; Chattopadhyay, A. Gold Nanocluster Embedded Albumin Nanoparticles for Two-Photon Imaging of Cancer Cells Accompanying Drug Delivery *Small* **2015**, 11, 4075– 4081.
47. Pooja, S.; Pushpanathan, M.; Gunasekaran, P.; Rajendhran, J. Endocytosis-Mediated Invasion and Pathogenicity of *Streptococcus agalactiae* in Rat Cardiomyocyte (H9C2). *PLoS One* **2015**, 10.

48. Nesti, E.; Everill, B.; Morielli, A. D. Endocytosis as a Mechanism for Tyrosine Kinase-dependent Suppression of a Voltage-gated Potassium Channel *Mol. Biol. Cell* **2004**, 15, 4073–4088.
49. Zhang, C.; Zhou, Z.; Zhi, X.; Ma, Y.; Wang, K.; Wang, Y.; Zhang, Y.; Fu, H.; Jin, W.; Pan, F.; Cui, D. Insights into the Distinguishing Stress-induced Cytotoxicity of Chiral Gold Nanoclusters and the Relationship with GSTP1 *Theranostics* **2015**, 5, 134–149.

Content of the chapter has been reproduced with permission from American Chemical Society (D. Dutta, A. Chattopadhyay and S. S. Ghosh, *ACS Biomater. Sci. Eng.* 2, 11, 2090-2098).

## Appendix B

### B.1 Experimental Section

#### Materials and Methods

##### Chemicals

In the synthesis procedure detailed below,  $\text{HAuCl}_4$  (Au, 17 wt % in dilute HCl; 99.99%, Sigma-Aldrich),  $\text{AgNO}_3$  (Merck), BSA (Mw 66 kDa, Himedia), ammonia (25%, Emparta), ethylenediamine (Merck), 1-ethyl-3-(3-(dimethylamino)propyl) carbodiimide hydrochloride (Sigma-Aldrich), sodium acetate (Ranbaxy Chemicals), glacial acetic acid (Merck), and Milli-Q grade water ( $>18 \text{ M}\Omega \text{ cm}^{-1}$ , Millipore) were used without further alterations.

##### Synthesis of Au–Ag NCs, Au–Ag NC-embedded cationic BSA, and Au–Ag NC-embedded cationic BSA composite nanoparticles

For the synthesis of luminescent Au–Ag NCs, 1 mL of 65 mg/mL BSA solution was taken and 100  $\mu\text{L}$  of 10 mM  $\text{AgNO}_3$  and 600  $\mu\text{L}$  of 10 mM  $\text{HAuCl}_4$  were added. After stirring for 5 min, 200  $\mu\text{L}$  of 25% ammonium hydroxide was added dropwise to the mixture and heated in a microwave oven at 180 W for 3 min. The color of the solution turned to deep yellow from the initial light yellow color.<sup>(34)</sup> To the hence prepared Au–Ag NCs, 1.4 M ethylenediamine was added, and the pH of the solution was adjusted to 4.5. Then, 15 mg of EDC (1-ethyl-3-(3-(dimethylamino) propyl) carbodiimide hydrochloride) was added, and the pH was further adjusted to 4.5. After 2 h of stirring, 100  $\mu\text{L}$  of acetate buffer (4 M, pH 4.5) was added to stop the reaction.<sup>(20)</sup> The above prepared cationic BSA solution was adjusted to pH 7, and acetone was added dropwise until slight turbidity appeared. Thereafter, the temperature of the solution was raised to 80 °C and kept for an hour under constant stirring. The hence formed composite nanoparticles (composite NPs) solution was centrifuged at

10 000 rpm for 5 min and thoroughly washed before further use. Another set of negatively charged BSA nanoparticles embedded with Au–Ag NCs (NC composite NPs) and cationic BSA nanoparticles without Au–Ag NCs (PC composite NPs) were prepared by the same process.

#### **DNA binding and gel retardation assay, DNase protection assay**

For DNA binding experiments, various amounts (0, 0.7, 1.4, 3.0 mg/mL) of composite NPs and 0.5 µg/mL of pDNA were added and incubated for half an hour at 37 °C. After centrifugation, the samples were analyzed by gel electrophoresis at 80 V in 0.8% agarose gel. For the DNase protection assay, the unbound pDNA and pDNA loaded into composite NPs were treated in the presence of 1 U/mL and 2 U/mL DNase I (Promega, USA) for 10 min at 37 °C and were compared with control pDNA (without any treatment) and composite NPs alone. The gel electrophoresis was carried out in 0.8% agarose gel at 80 V and visualized in the gel documentation system.

#### **UV visible spectroscopy and luminescence measurements**

The absorbance profile in the UV–vis region of the synthesized samples was recorded on a UV–visible spectrophotometer (JASCO V-630). A fluorescence spectrophotometer (LS55, PerkinElmer) was used to record all luminescence measurements.

#### **Transmission electron microscopy (TEM)**

Sample preparation for TEM analysis requires 7 µL of the synthesized composite to be drop cast onto the TEM grids. The TEM grid was air-dried and observed under a transmission electron microscope operating at a maximum accelerating voltage of 200 keV (TEM; JEM 2100; Jeol, Peabody, MA, USA).

#### **Quantum yield measurements**

For the calculation of quantum yield (QY) of the composite NPs, a standard method was followed using reference quinine sulfate in 0.10 M H<sub>2</sub>SO<sub>4</sub> solution. The calculation of QY (absolute value) was done according to the following equation: Here,  $n$  is the refractive index,  $m$  is the slope of integrated luminescence intensity vs absorbance plot, and the  $r$  subscript indicates reference quinine sulfate solution. The measurement of the absorbance and luminescence intensity was done simultaneously one after the other using the same solution. The standard (QY<sub>r</sub>) has a quantum yield of 0.54 and the refractive index of solvent (water) is 1.33.

$$QY = QY_r \frac{m n^2}{m_r n_r^2}$$

#### **Dynamic light scattering study**

For the measurement of hydrodynamic diameter and zeta potential, of composite NPs, a Malvern Zetasizer Nano ZS was used.

**Fourier transform infrared (FTIR) spectroscopy and atomic absorption spectroscopy (AAS)**

For FTIR analysis, pellets were prepared by mixing with KBr after the samples were lyophilized initially. A PerkinElmer Spectrum One machine in the range of 4000–400  $\text{cm}^{-1}$  was used to characterize the pellets. An atomic absorption spectrophotometer (AA240 - Varian Inc.) was used to determine the amounts of silver and gold present in composite NPs.

**Cell culture**

HeLa cells (human cervical carcinoma) were acquired from the National Center for Cell Sciences (NCCS), Pune, India for cell culture experiments. Dulbecco's Modified Eagle's Medium supplemented with l-glutamine (4 mM), penicillin (50 units/mL), streptomycin (50 mg/mL, Sigma-Aldrich), and 10% (v/v) fetal bovine serum (PAA Laboratories, Austria) was used for culturing cells in a 5%  $\text{CO}_2$  humidified incubator at 37 °C.

**Confocal microscopy**

For confocal microscopy studies,  $1 \times 10^5$  HeLa cells were seeded on a coverslip in a 35 mm culture dish and grown in a 5%  $\text{CO}_2$  humidified incubator (37 °C for 24 h). Thereafter, the cells were treated with pDNA loaded composite NPs for the required time intervals. Then, they were fixed using 0.1% formaldehyde and 70% chilled ethanol. The coverslips were mounted onto glass slides, and the ends were sealed. Control samples without treatment with pDNA loaded composite NPs were prepared in a similar manner. The samples were then observed under a Zeiss LSM 880 microscope (excitation at 405 nm). For the lysosomal staining experiment, a Cytopainter green lysosomal staining kit (Abcam) was used according to the manufacturer's instructions after treatment with pDNA loaded composite NPs for 4 h. For the endocytosis inhibition experiment, 0.1% sodium azide was used to treat the cells for 10 min prior to treatment with the pDNA loaded composite NPs, and subsequently the same steps were followed as described above.

**MTT Assay**

For the cell viability assay,  $1 \times 10^4$  HeLa cells/well were (seeded in 96-well microtiter plate) cultured overnight in a 5%  $\text{CO}_2$  humidified incubator (37 °C for 24 h). For the gene transfection, the cells were treated with the composite NPs, pDNA loaded composite NPs, negative charged composite NPs, pDNA loaded negative charged composite NPs, and pDNA loaded positive charged composite NPs without Au–Ag NCs for 6 h; subsequently, different concentrations of the pro-drug 5-FC were added. MTT [3-(4,5-dimethylthiazol-2-yl)-2,5-diphenyltetrazolium bromide] assay was carried after 36 h. MTT is reduced into colored formazan by mitochondria in living cells. Thus, absorbance at 570 nm reveals the amount of formazan product, which is directly proportional to the number of living cells, and background interference due to absorbance at 690 nm is subtracted. The % of cell viability was calculated as

$$\text{Cell Viability (\%)} = \frac{(\text{Abs}_{570} - \text{Abs}_{690}) \text{ of treated cells}}{(\text{Abs}_{570} - \text{Abs}_{690}) \text{ of control cells}} \times 100$$

### Field emission scanning electron microscopy (FESEM)

FESEM was carried out to reveal the morphological changes in the cell prior to and after the treatment with composite NPs. Cells were grown overnight in a 5% CO<sub>2</sub> incubator (1 × 10<sup>5</sup> cells, in 35 mm culture dish). For sample preparation, the grown cells were treated with composite NPs for 6 h followed by 5-FC for 36 h, washed with PBS, and harvested by trypsinisation. Thereafter, it was fixed in 70% chilled ethanol. Following this, the cells were drop-casted on an aluminum foil covered glass slide and were allowed to dry for analysis.

### Determination of Reactive Oxygen Species (ROS)

For ROS generation studies, HeLa cells (1 × 10<sup>5</sup> cells/well, seeded in 6-well plate) were grown for 24 h and then treated for 3 h with pDNA loaded composite NPs, pDNA loaded negatively charged composite NPs, and pDNA loaded positive charged composite NPs without Au–Ag NCs. These cells were incubated for 10 min after adding 1 mM 2,7-dichlorofluoresceindiacetate (5 μL/well, DCFH-DA, Sigma-Aldrich). The cells were harvested after discarding the media and redispersed in fresh media. DCFH-DA (nonfluorescent dye) is converted to DCFH through hydrolysis inside living cells. Upon oxidation, the hence formed DCFH will be converted to dichlorofluorescein (DCF, green fluorescent). The samples were analyzed in the FL1-H channel in a flow cytometer (FacsCalibur, BD Biosciences, NJ) at an excitation wavelength of 488 nm and emission wavelength of 530 nm for DCF fluorescence. The fluorescence data for 15 000 cells in each sample were recorded with the Cell Quest program (BD Biosciences).

### Cell cycle analysis

For cell cycle analysis, the propidium iodide staining method was employed. HeLa cells (1 × 10<sup>5</sup> cells, 6 well plates) were grown and then treated with composite NPs, pDNA loaded composite NPs, negative charged composite NPs, pDNA loaded negative charged composite NPs, and pDNA loaded positive charged composite NPs without Au–Ag NCs for 6 h, and subsequently different concentrations of the pro-drug 5-FC were added and kept for 36 h. For both treated and control cells, the media and PBS were collected separately. After harvesting the cells by trypsinization, the cells and the collected PBS both were centrifuged (650 rcf, 6 min). Subsequently under constant vortexing, the cells were fixed by slowly adding 1 mL of cold 70% ethanol and were stored at 4 °C. Thereafter, centrifugation of the cells was carried out, and they were washed in ice-cold PBS. These cells were treated with RNase for 1 h at 55 °C. A total of 10 μL of PI (1 mg/mL) was added to this and incubated in the dark (37 °C, 30 min). The samples were then analyzed in a FACSCalibur (BD Biosciences, NJ), and PI fluorescence data were recorded with the CellQuest program (BD Biosciences) for 15 000 cells in each sample for subsequent analysis.

### Caspase-3 assay

Caspase-3 assay sample preparation involves initial growth of HeLa cells ( $1 \times 10^5$  cells/well, 6 well plates) followed by treatment with composite NPs, pDNA loaded composite NPs, negative charged composite NPs, pDNA loaded negative charged composite NPs, and pDNA loaded positive charged composite NPs without Au-Ag NCs for 6 h with the subsequent addition of different concentrations of the pro-drug 5-FC, followed by being kept for 36 h. The treated and control cells were then trypsinized and fixed in 0.1% formaldehyde for 15 min. The samples were centrifuged (650 rcf, 6 min), and the pellet was redispersed in PBS. After the addition of 0.5% Tween 20 to the samples, they were incubated in the dark for 20 min. A total of 10  $\mu$ L of PE conjugated anticaspase-3 antibody was added, after the cells were washed with PBS thrice. Finally, these cells were incubated for half an hour at 37 °C and were analyzed for PE fluorescence in FACSCalibur (BD Biosciences, NJ). Fluorescence data were recorded with the CellQuest program (BD Biosciences) for 15 000 cells in each sample for subsequent analysis.

## B.2 Figures and Tables

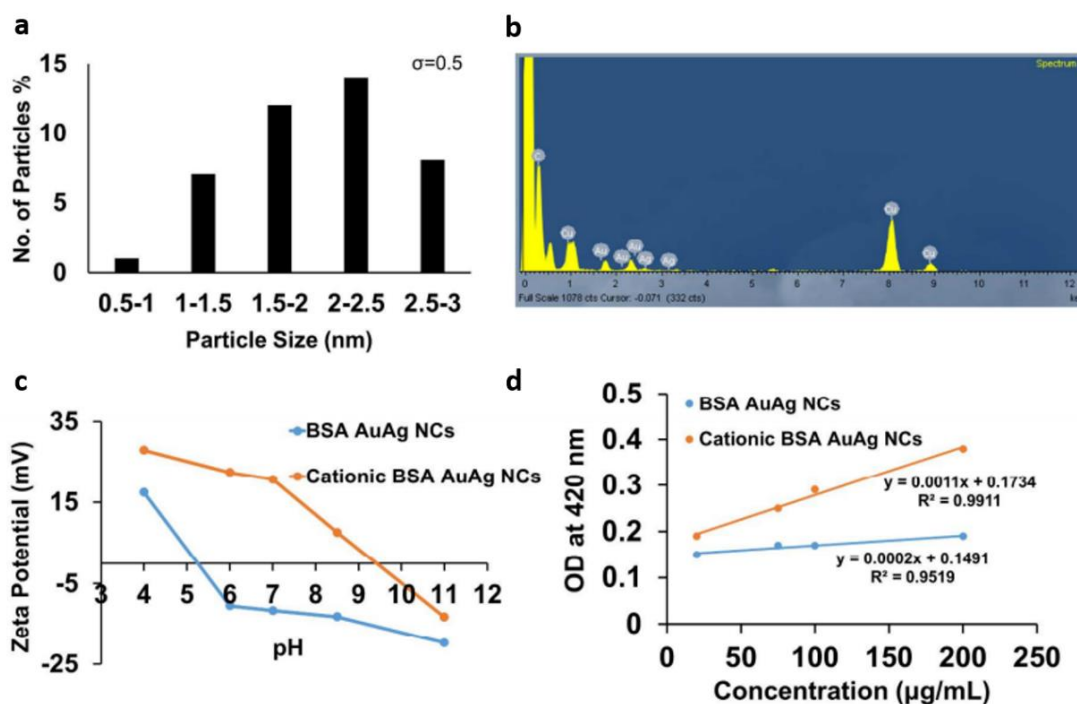


**Figure B3.1.** (a) Particle size distribution of BSA Au-Ag NCs. (b) EDX analysis of BSA AuAg NCs. (c) Zeta potential of BSA Au-Ag NCs and cationic BSA Au-Ag NCs. (d) TNBS assay of BSA Au-Ag NCs and cationic BSA Au-Ag NCs.

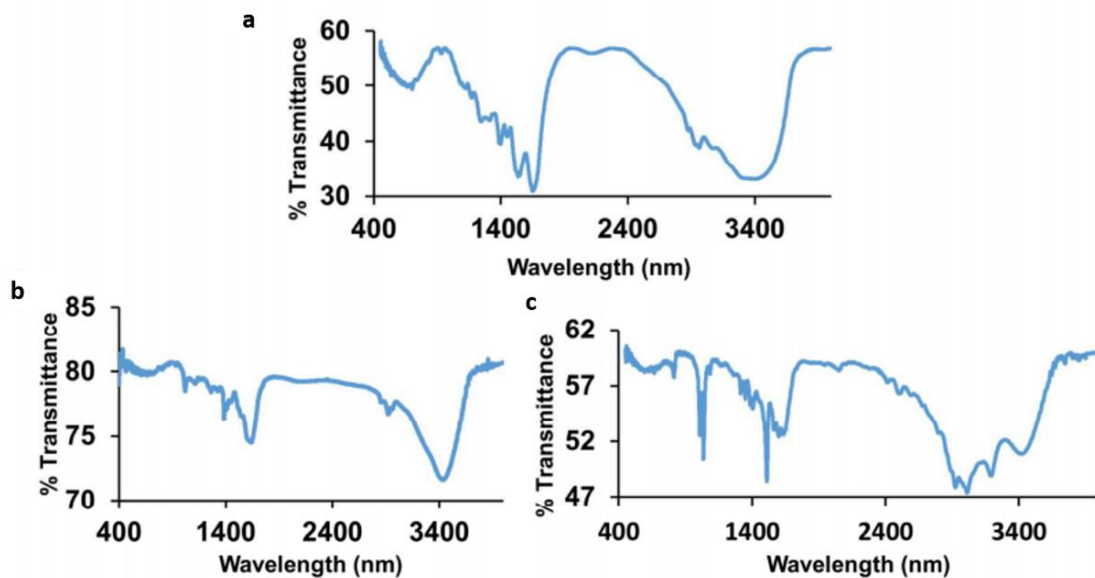


**Figure B3.2.** FTIR spectra of (a) BSA, (b) BSA Au-Ag NCs and (c) cationic BSA Au-Ag NCs.

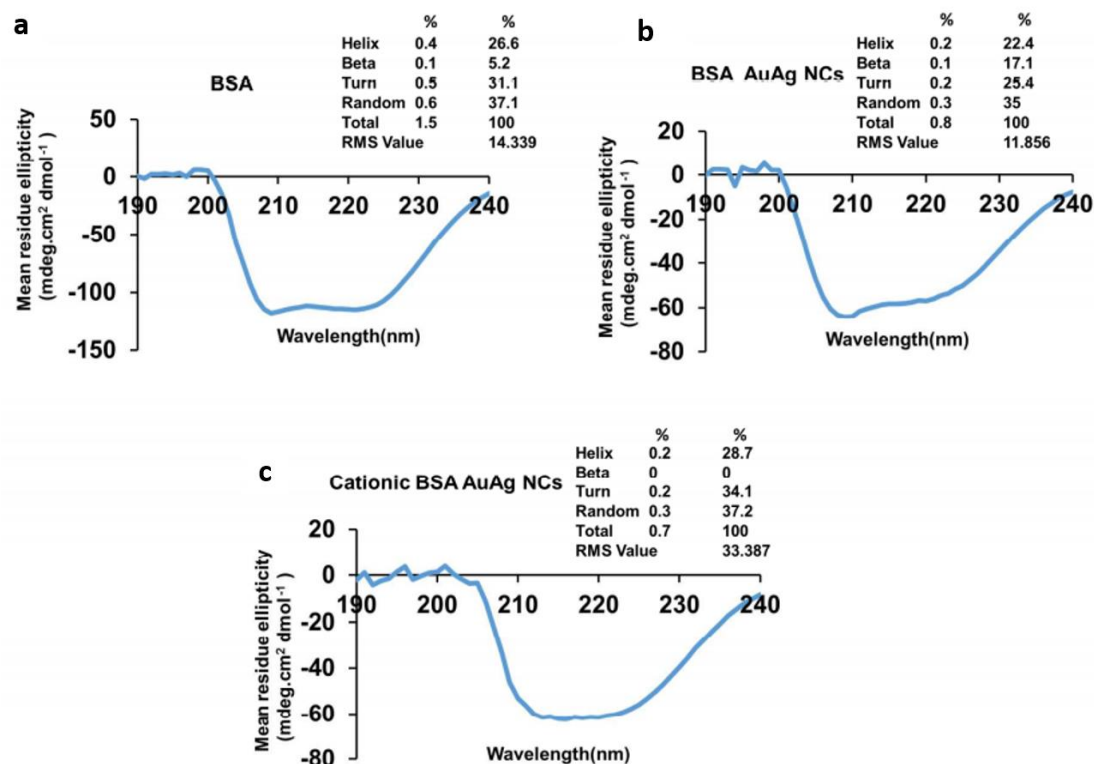


**Figure B3.3.** CD spectra of (a) BSA, (b) BSA Au-Ag NCs and (c) cationic BSA Au-Ag NCs.

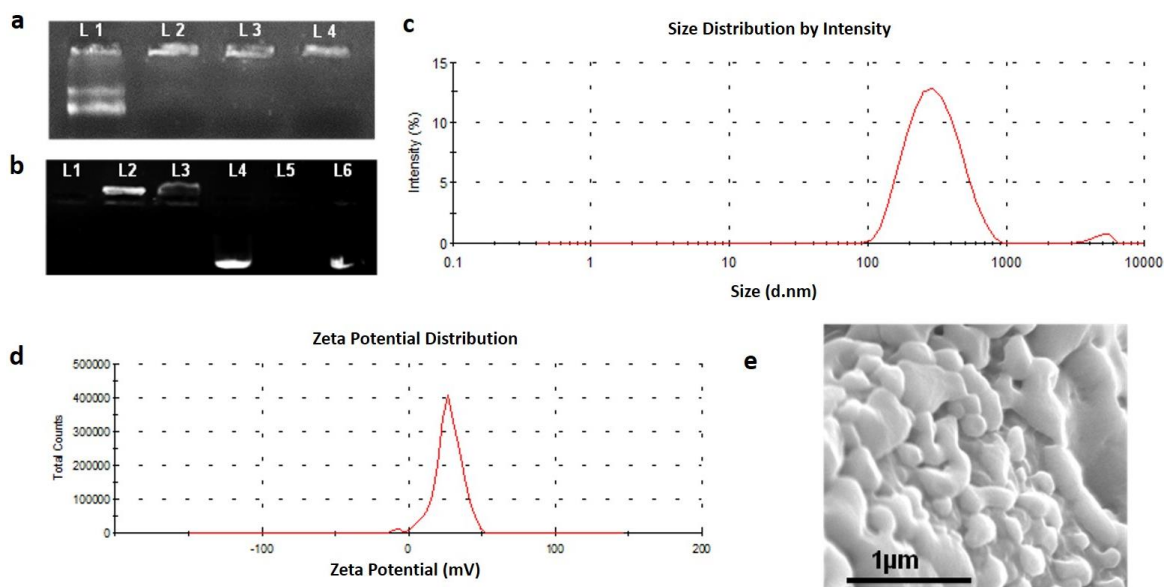


**Figure B3.4.** (a) Ethidium bromide stained agarose gel showing DNA loading in composite NPs depicted by retardation of DNA into the wells in lane 2, 3, 4 with increasing amounts of composite NPs in comparison to control without composite NPs (lane 1). (b) Ethidium bromide stained agarose gel showing protection of pDNA loaded into composite NPs (Lane 2, 3) treated with DNase I (1U/mL for Lane 2, 2U/mL for Lane 3) when compared to unbound pDNA (Lane 5, 6) treated with DNase I (2U/mL for Lane 5, 1U/ml for Lane 6), control pDNA(Lane 4), composite NPs alone (lane 1). (c) Hydrodynamic particle size distribution, (d) zeta potential and (e) FESEM image of pDNA loaded composite NPs.

| Size distribution with varying pH                 |              |                       |
|---|--------------|-----------------------|
| pH  | Without pDNA | With pDNA (0.5 μg/mL) |
| 5   | 270±19nm     | 294±20nm              |
| 7   | 223±12nm     | 266±6nm               |
| 11  | 297±33nm     | 317±32nm              |
| Size distribution with varying pDNA concentration |              |                       |
| pDNA (0.5 μg/mL)                                  |              | 266±6nm               |
| pDNA (1 μg/mL)                                    |              | 283±7nm               |

**Table B3.1.** Size distribution with varying pH and varying pDNA concentrations.

| Zeta potential with varying pH                    |              |                       |
|---|--------------|-----------------------|
| pH  | Without pDNA | With pDNA (0.5 µg/mL) |
| 5   | 26.7±0.75nm  | 25.7±0.6nm            |
| 7   | 21±3.6nm     | 19±2.3nm              |
| 11  | -12.8±4.3nm  | -18.2±4.9nm           |
| Size distribution with varying pDNA concentration |              |                       |
| pDNA (0.5 µg/mL)                                  |              | 19±2.3nm              |
| pDNA (1 µg/mL)                                    |              | 15.4±2.4nm            |

**Table B3.2:** Zeta potential with varying pH and varying pDNA concentrations.

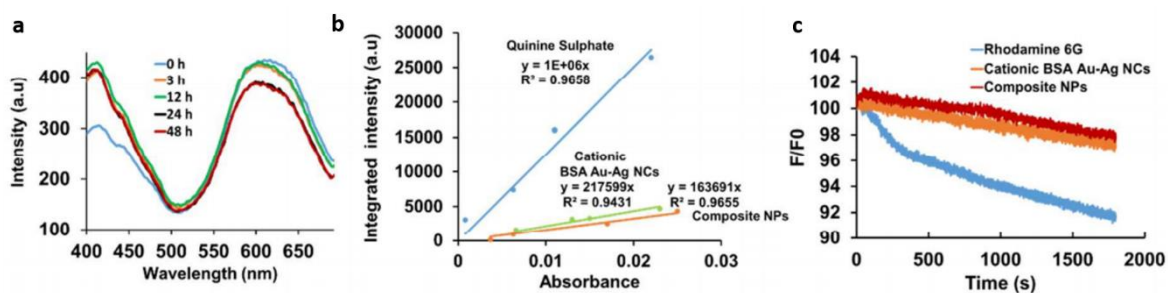


**Figure B3.5.** (a) Time dependent fluorescent spectra of pDNA loaded composite NPs, (b) quantum yield and (c) photostability of cationic BSA Au-Ag NCs and pDNA loaded composite NPs.

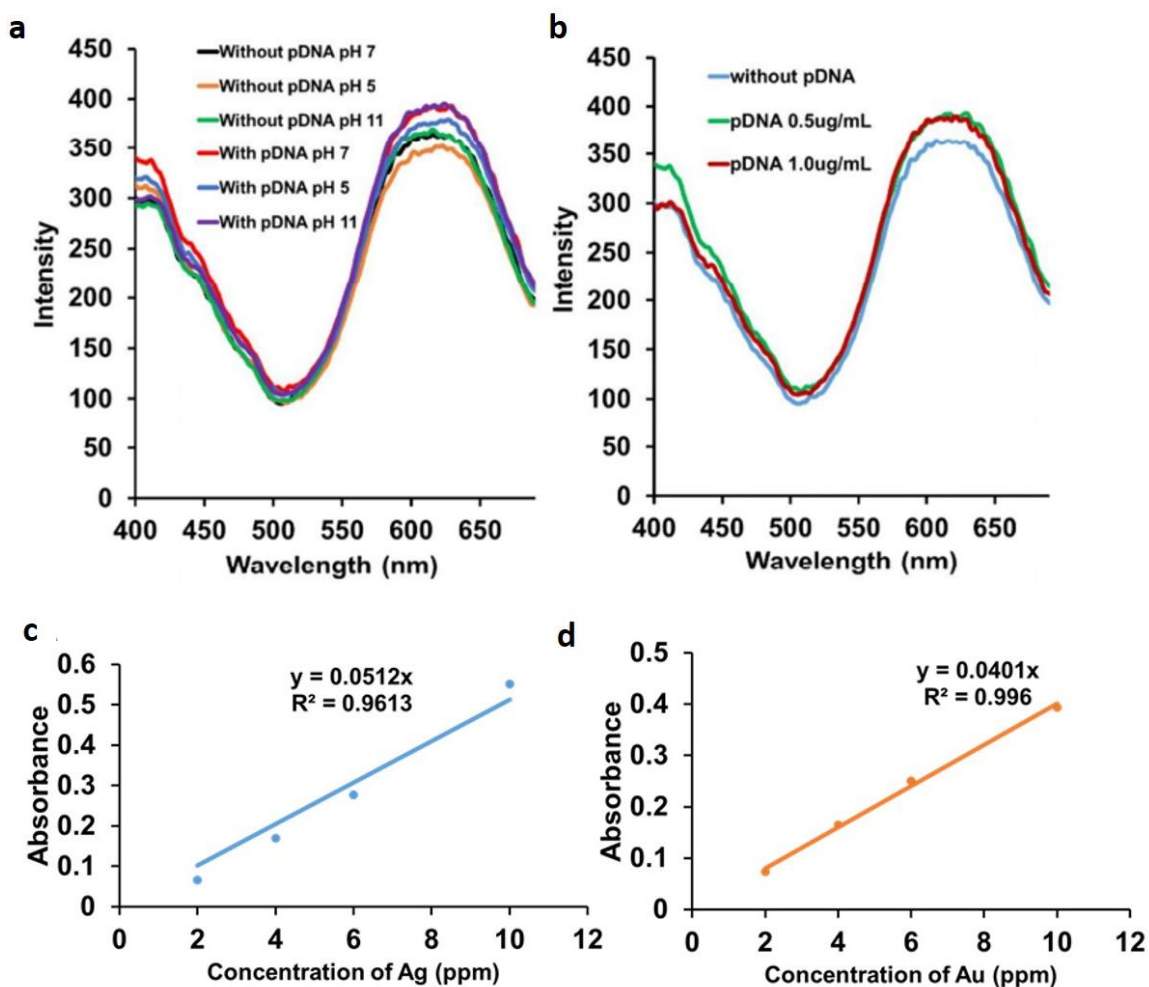


**Figure B3.6.** Luminescence intensity of composite NPs at (a) varying pH and (b) at varying pDNA concentrations. Standard calibration curve of (c) Ag and (d) Au for AAS (atomic absorption spectroscopy).

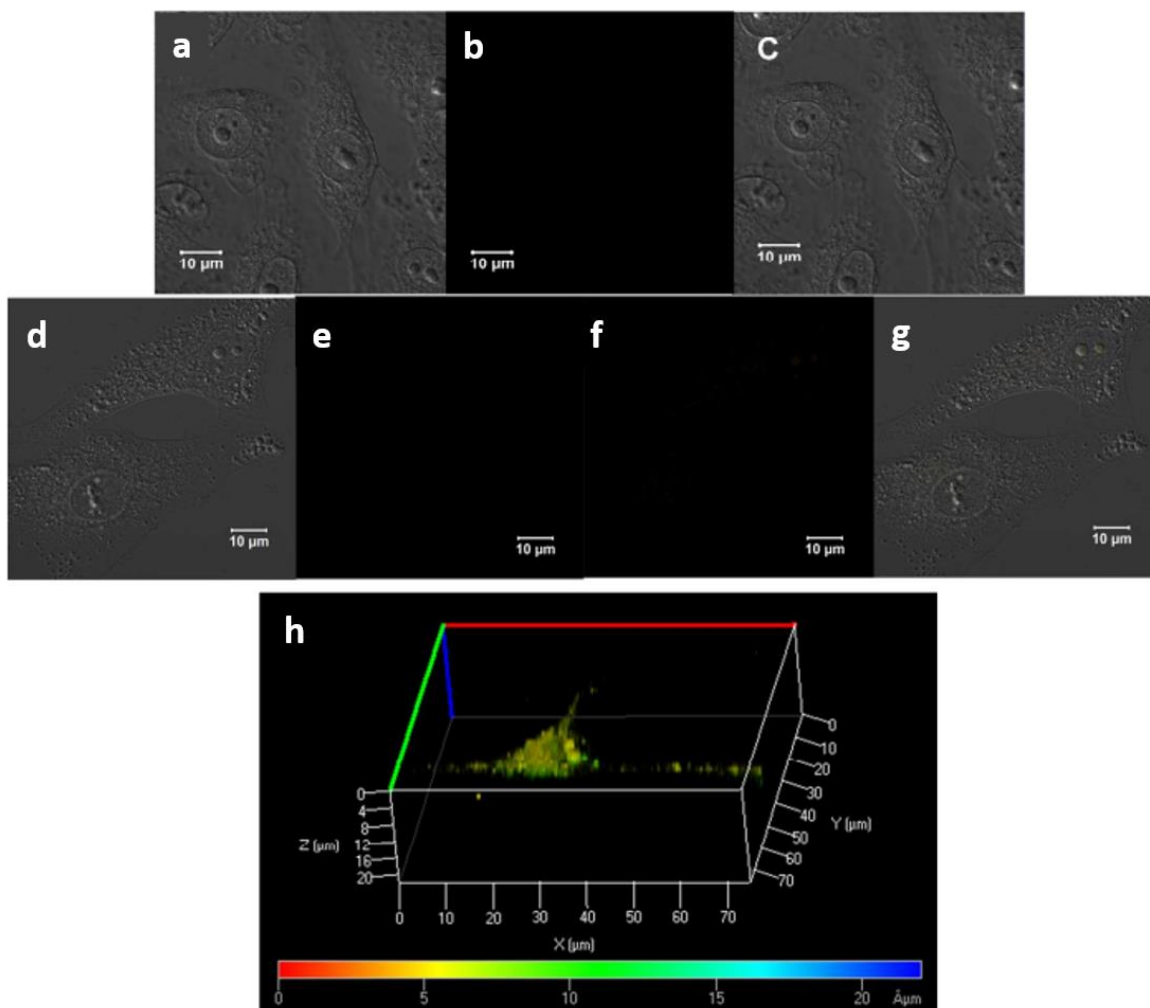


**Figure B3.7.** Confocal microscopic images of HeLa cells. (a) Bright field image, (b) fluorescence image and (c) merged fluorescent image of control HeLa cells. (d) Bright field image of untreated (control) HeLa cells, (e) fluorescence image showing no fluorescence of cytopainter green lysosome staining dye in untreated (control) HeLa cells, (f) fluorescence image showing no fluorescence of pDNA loaded composite NPs in untreated (control) HeLa cells, (g) merged fluorescent image of control HeLa cells at scale bar 10 μm. (h) Depth projection of confocal microscopy image of pDNA loaded composite NPs treated HeLa cells showing internalization of pDNA loaded composite NPs inside the cells.

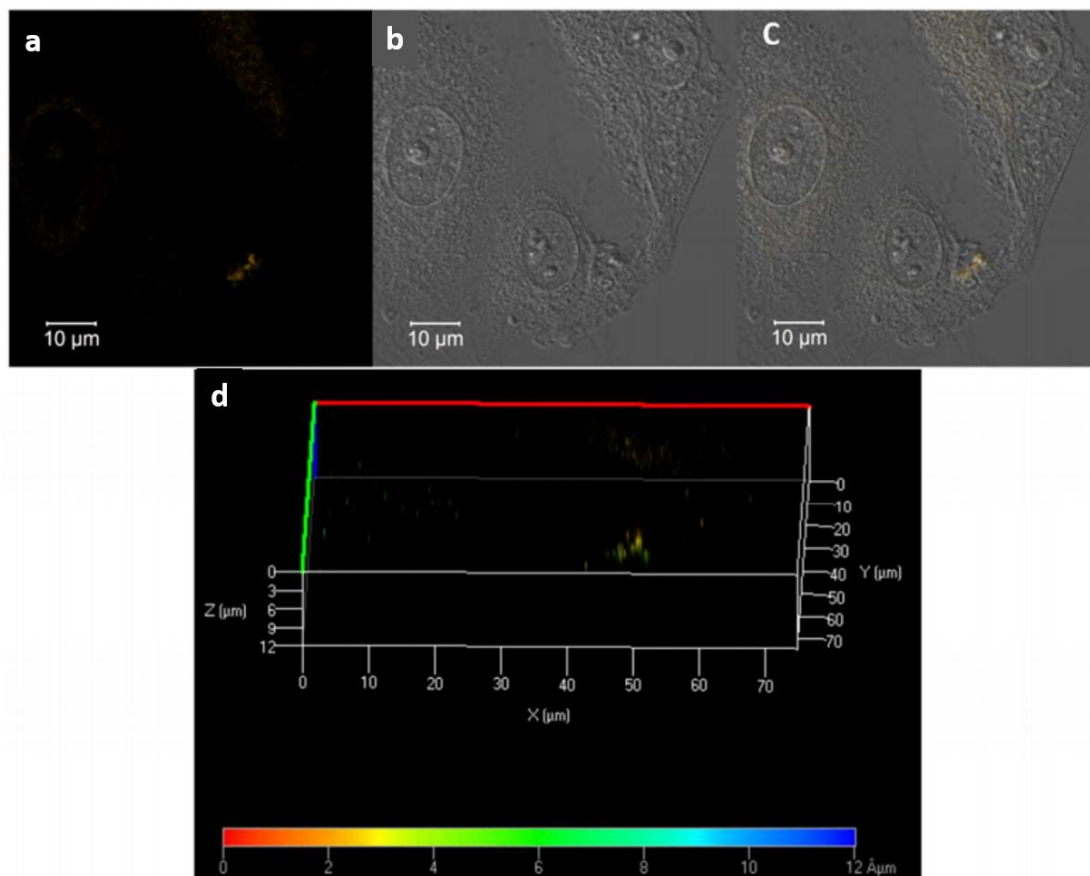


**Figure B3.8.** Confocal microscopic images of HeLa cells. (a) Fluorescence image, (b) bright field and (c) merged fluorescent image of HeLa cells treated with cationic BSA AuAg NCs (d) Depth projection of confocal microscopy image of HeLa cells treated with cationic BSA Au-Ag NCs.

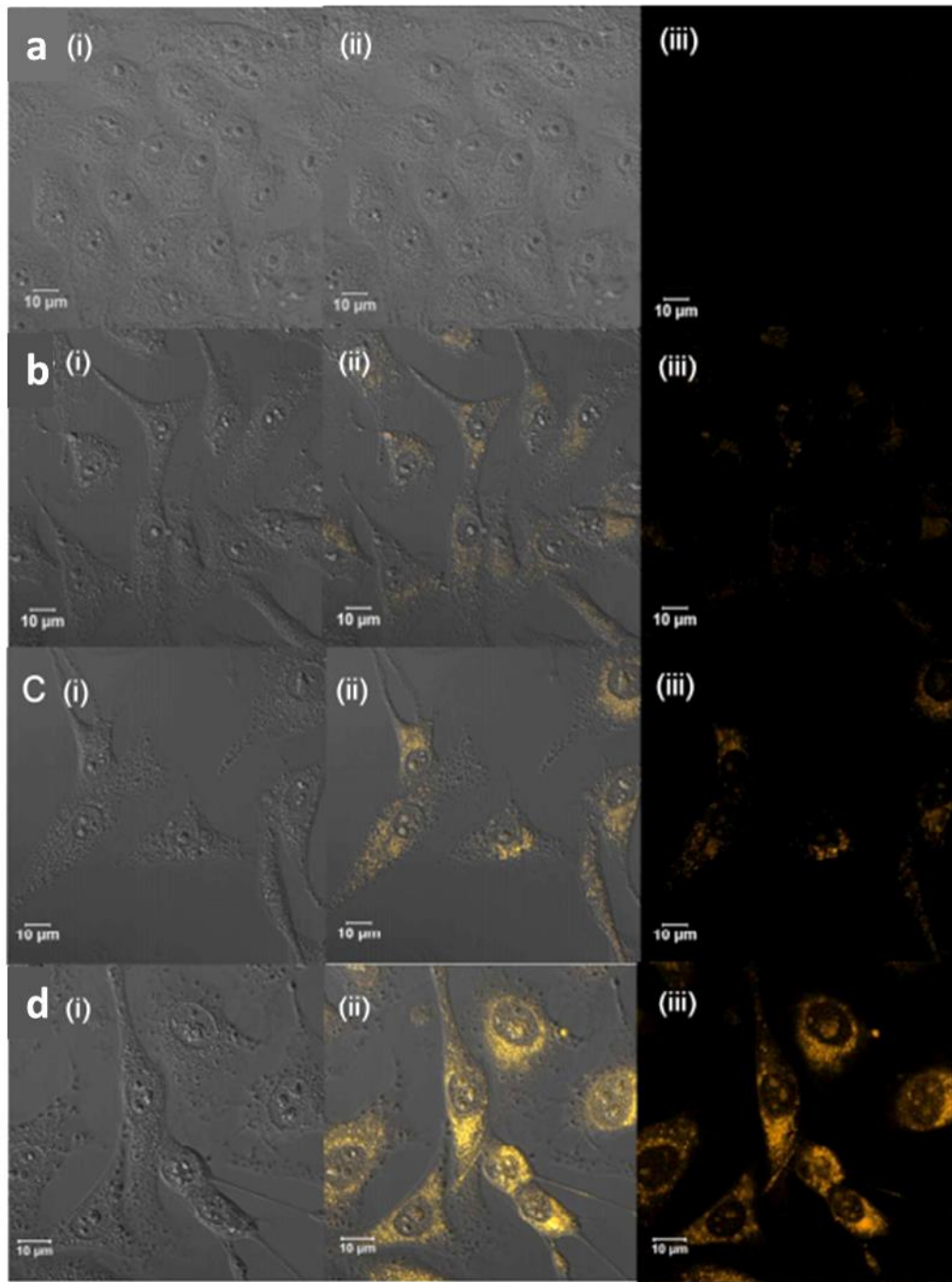


**Figure B3.9.** Time dependent confocal microscopic images of HeLa cells. (a-d) (i) Bright field image, (ii) merged fluorescent image and (iii) fluorescence image of HeLa cells treated with pDNA loaded composite NPs for (0 h, 1 h, 2 h, 4 h) Scale bar 10  $\mu\text{m}$ .

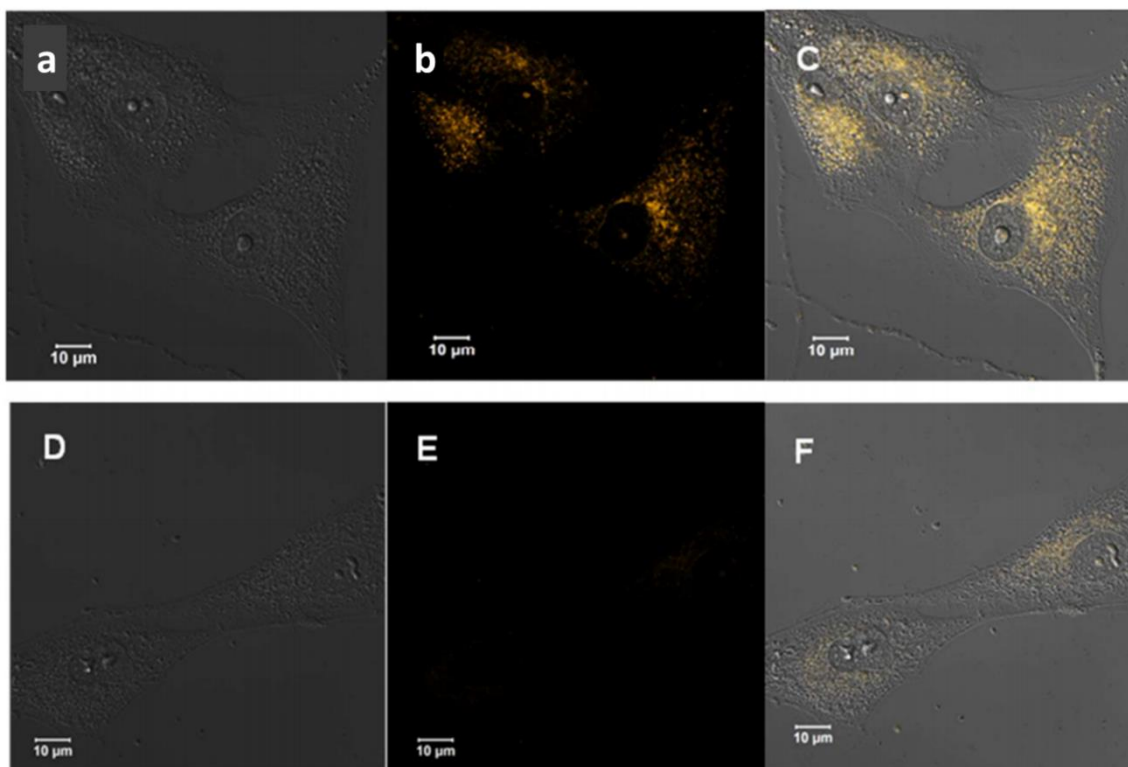


**Figure B3.10.** Confocal microscopic images of HeLa cells. (a) bright field image, (b) fluorescence image and (c) merged fluorescence image of HeLa cells treated with pDNA loaded composite NPs for 4 h; (d) bright field image, (e) fluorescence image and (f) merged fluorescent image of HeLa cells treated with 0.1% sodium azide for 10 min with subsequent treatment with pDNA loaded composite NPs for 4 h. Scale bar 10  $\mu\text{m}$ .

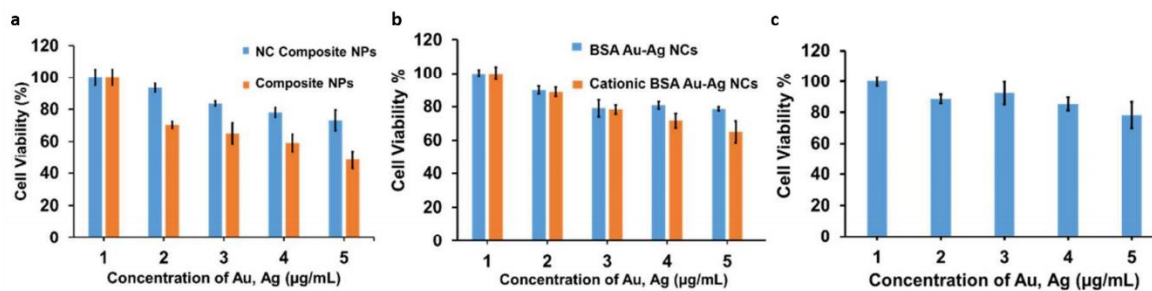


**Figure B3.11.** (a) The MTT assay representing cell viability of HeLa cells treated with negatively charged composite NPs (without pDNA) and composite NPs (without pDNA) with respect to control, (b) MTT assay representing cell viability of HeLa cells treated with BSA Au-Ag NCs and Cationic BSA Au-Ag NCs with respect to control, (c) MTT assay representing cell viability of HEK 293 cells treated with composite NPs (without pDNA) with respect to control.

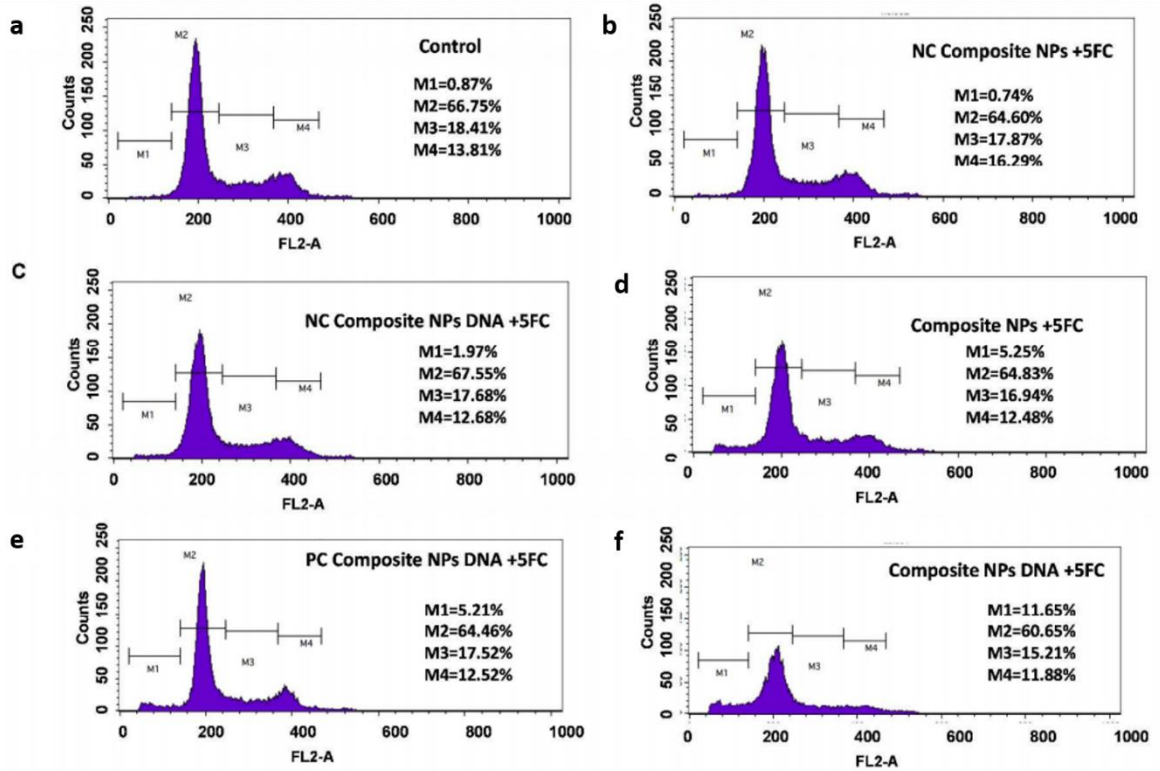


**Figure B3.12.** Cell cycle analysis of (a) control HeLa cells, HeLa cells treated with (b) negatively charged composite NPs, (c) negatively charged, (d) composite NPs, (e) positively charged composite NPs DNA without Au-Ag NCs and (f) composite NPs DNA in presence of 5-FC.

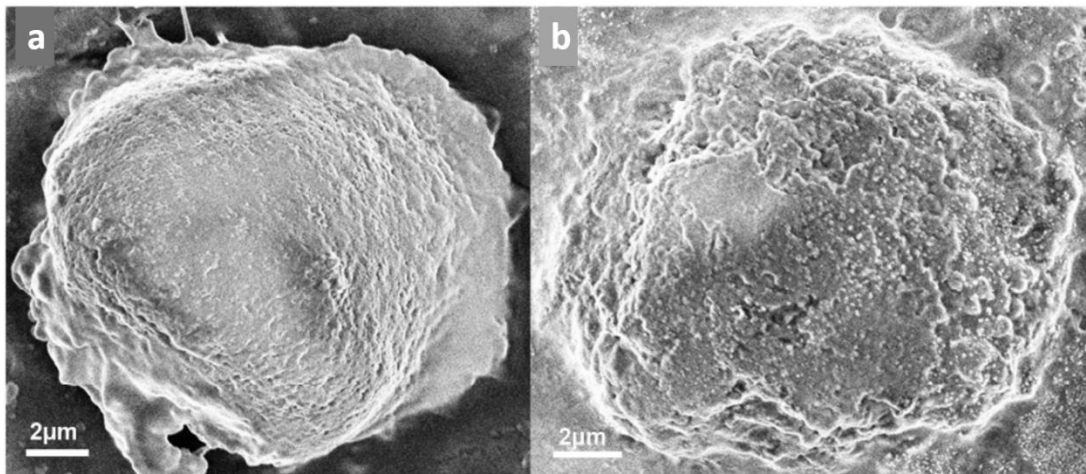
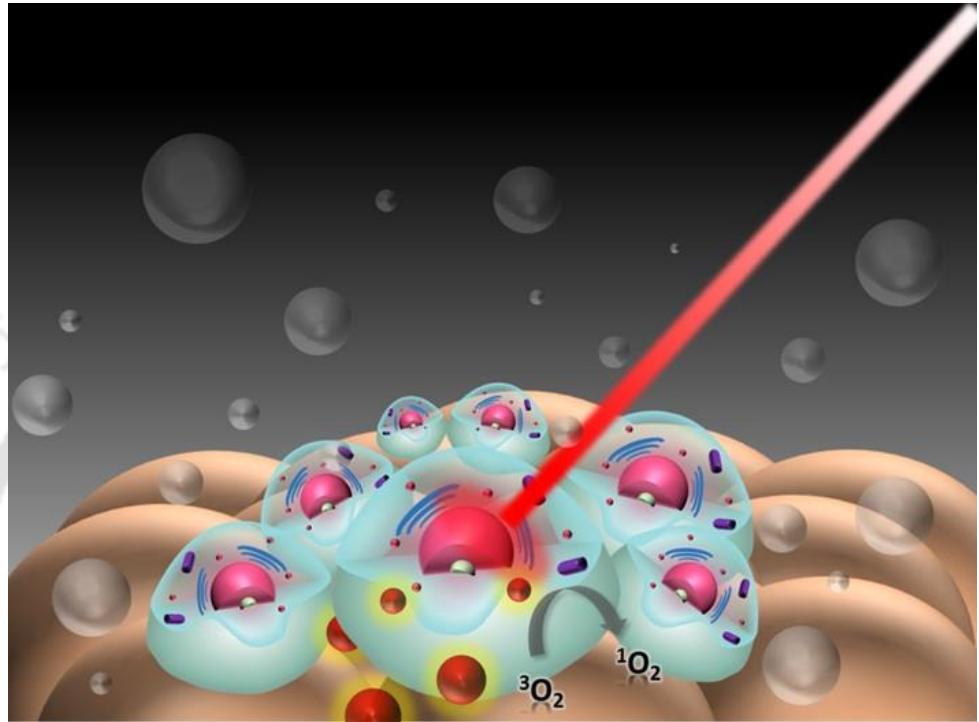


**Figure B3.13.** FESEM images of (a) control and (b) treated HeLa cells with composite NPs+DNA in presence of 5-FC.



## Chapter 4



**Gold Nanoclusters Embedded Mucin  
Nanoparticles for Photodynamic Therapy  
and Bioimaging**



## Chapter 4

# Gold Nanoclusters Embedded Mucin Nanoparticles for Photodynamic Therapy and Bioimaging

### Abstract

Gold nanocluster (Au NCs) embedded mucin nanoparticles were synthesized by a rapid synthetic procedure for application as a nanocarrier in photodynamic therapy. The photosensitizer methylene blue was loaded onto the Au NC-mucin nanoparticles. The mucin based nanocarrier exhibited excellent biocompatibility towards normal cells (HEK 293T). HeLa cancer cells were treated with methylene blue (MB) loaded Au NC-mucin nanoparticles under irradiation of 640 nm light. The cell viability assay revealed that the viability of HeLa cells was reduced after treatment with MB loaded Au NC-mucin nanoparticles kept under 640 nm irradiation. The luminescence of the Au NCs was applied for tracking the delivery of the MB by Au NC-mucin nanoparticles inside HeLa cells using confocal microscopy. The pathway of cell death was elucidated by flow cytometry based assays.

### 4.1. Introduction

Photodynamic therapy (PDT) has become an apparent non-invasive therapeutic modality where photosensitizers (PS) are activated upon light irradiation, thereby resulting in the transformation of surrounding molecular oxygen into cytotoxic singlet oxygen (SO) and reactive oxygen species (ROS) for the effective treatment of various diseases including cancer.<sup>(1)</sup>

Photosensitizers of various types have been synthesized in the last few decades, among which a few have been given the regulatory approval by Food and Drug administration (FDA) for clinical application. However, some of the notable issues with the current PSs, include nonspecific selectivity for tumor tissue versus normal tissue and compromised photophysical characteristics.<sup>(2)</sup> The efficacy in administration and delivery to target sites due to their low solubility in physiological media is to be improved which otherwise renders such PSs underutilized for clinical purpose. Another set of pervasive issues that limit the usage of most PSs are prolonged cutaneous photosensitivity, poor hydrophilicity and inadequate selectivity.<sup>(3)</sup> The inherent hydrophobic nature of most PSs leads to its pronounced self-aggregation in aqueous environment. Such a property of self-aggregation lowers their photodynamic efficacy significantly unlike monomeric species which are markedly noted for its photoactivity.<sup>(4)</sup> Hence, an interest to develop improved delivery systems for PSs have been accelerated. An ideal delivery system should entrap the PS without its activity being lost or altered. At the same time the PSs delivered by the carrier should selectively accumulate within the target tissues with negligible or no uptake by non-target cells. Various types of nanocarriers, such as liposomes, polymeric nanoparticles, proteins, ceramic nanoparticles, carbon nanomaterials, gold

nanoparticles, quantum dots (QDs), magnetic nanoparticles (MNPs) and upconversion nanoparticles (UCNPs) have been formulated to attain stable dispersions of photosensitizers in aqueous media for their effective delivery. Entrapment of drugs/ sensing elements into nanoparticles possess several advantages, which primarily include the role of particle matrix as a barrier preventing the interference of intracellular environment with loaded cargo which by interaction could potentially alter the functional characteristics of the loaded cargo.<sup>(5)</sup> Moreover, nanocarriers adequately improvise the solubility of sparingly aqueous soluble drugs, rendering extended half-life during circulation in the blood.<sup>(6)</sup> These nanosystems efficiently modulate the drug pharmacokinetics leading to avid uptake by the target tissues followed by their accumulation in uptaken regions. They are beneficial in terms of reduced side effects, increased bioavailability, and further improve susceptibility of target region to the mode of action of the loaded drug. However, while developing nanocarriers, the penetrability into tumor tissues is a challenge to be addressed and it is also important to design nanocarriers with biocompatible and biodegradable characteristics.<sup>(7)</sup> Designing a putative drug delivery nanoparticle, requires that the nanoparticle possess the ability to traverse through mucus barrier without experiencing the resistance due to interactions with the mucin. Further, the rate of penetration of nanoparticles through mucus should exceed its characteristic clearance rate.<sup>(8)</sup> Mucus is a viscous fluid that shields all wet epithelial arena, including nasal cavity, oral cavity, gastrointestinal tract, lungs and female genital tract.<sup>(9)</sup> The major component of mucus is mucin which is either bound to cell membrane or secreted externally. The term “mucin” comprises a family of high molecular weight glycosylated proteins. It took an evolutionary period of millions of years to have mucin bestowed with the ability to interact with wide range of molecules for providing protection against pathogenic viruses, bacteria and minute particles.<sup>(10)</sup> Being highly complex in structure, mucin molecules are predominantly equipped with an optimized and manifold chemistry. Their protein backbone possesses large amount of thiol groups and hydrophobic/charged domains are prevalent within the highly entangled network of mucin. Additionally, the attachment of oligosaccharides to mucin protein backbone is majorly responsible for enhancement of intramolecular and intermolecular hydrogen bonding characteristics, excellent hydration and hydrophilic nature. Moreover, the net negative charge mucin at neutral pH is conferred by sialic acid, carboxyl and sulfate groups adherent to it.<sup>(11)</sup> Thus, the unique chemistry and the intricate composition of mucus leads to binding and retention of the therapeutic molecules within the complex matrix and this makes mucus play an important role as biophysical barrier to most of the uptaken drugs.

Until recent times, it was established that mucus acts as protective layer against harmful foreign entities like pathogenic bacteria, enzymes and chemicals. However, the research advances have revealed the possible multiple interactions of mucins or mucus glycoproteins with many biologically important entities such as enzymes, drugs, polymers, cations viruses, cell surfaces molecules and bacteria in numerous ways.<sup>(12)</sup> Though mucosal barrier creates a critical problem for drug delivery, an interesting approach can be brought using this tenacious nature of mucin by exploiting the possible

mucin–drug interactions for encapsulation and delivery of drug molecules. The ultimate goal is to develop mucin-based biomaterials to retain and release drugs over long periods of time. The complexation efficiency of mucin with hydrophobic molecules is interesting to note, which in fact enhances its solubility in aqueous environment. Novel mucin-complexed molecules depicts potency in terms of long term bioavailability and high membrane-penetration capability. The ability of bovine submaxillary mucin to stabilize hydrophobic nanocolloid dispersions such as C60 fullerene and multi-walled carbon nanotubes (MWNT) in aqueous medium was demonstrated in a study.<sup>(13)</sup> The intriguing mucin-protein interactions have inspired to further advance the research in demonstrating development of highly versatile multilayered structures/scaffolds using layer-by-layer (LBL) approach for applications in drug delivery and regenerative medicine. The reduced opsonization effect with promising haemo- and cyto-compatibility are marked qualities of mucylated nanocarriers (e.g., polylactic-*co*-glycolic acid).<sup>(14)</sup> The coating of mucin on biomaterials can considerably minimize adherence of protein and neutrophil onto biomaterial substrate like polyethylene terephthalate, which effectively aid in the reduction of host immune response resulted from biomaterials.<sup>(15)</sup> The drug encapsulated mucin coated micro- or nanotubes can be employed for targeted payload delivery and longer resident time.

The primary method to harness the properties of mucin for drug delivery is to assemble them into biomaterials with its intact biophysical characteristics. To develop mucin based biomaterial, a layer-by-layer assembling can be implemented where mucin is complexed with biomaterials such as lysozymes, chitosan, or lectins.<sup>(16,17)</sup> Another strategical development has been evolved where mucin–alginate<sup>(18)</sup> or mucin–gelatin<sup>(19)</sup> complexes have been synthesized to design microparticles. A robust macroscopic covalently cross-linked mucin hydrogel developed via assembly of methacrylated mucin have been reported to investigate the drug binding and release efficacy of mucin molecule.<sup>(20)</sup> Recently a report suggested the formation of a mucin particle for enzyme encapsulation and release.<sup>(21)</sup> These mucin-based scaffolds with its elaborate inherent chemical nature (hydrophilicity) and its mucoadhesive interactions (e.g., hydrophobic, electrostatic forces), are suggested to be capable of loading both hydrophilic and hydrophobic drugs, offering sustained drug release. Majority of the previous reports involved time consuming protocols, multiple precursors for synthesis of mucin based nanocarriers. However, no previous investigation has been carried out to exploit the potency of solely mucin-based biomaterials assembled into nanocarriers via facile one pot synthetic route in retention and release of drug molecules.

It is to be noted that one of the major setbacks in photodynamic therapy arises from the inability to trace the photosensitizers under conventional tracking techniques.<sup>(22)</sup> The putative behaviour of PS in getting accumulated at cancer site and the lack of successive follow-up of therapy leads to limited use of such therapeutic practices. Nanoparticles can act as a multimodal platform with imaging property equipped within it thereby qualifying these drug delivery system into theranostic systems. Theranostic nanocarriers have improved the outcome of photodynamic-based processes and several

multifunctional systems have been realised for image-guided photosensitizer delivery.<sup>(22,23)</sup> The prompt diagnosis and treatment initiation made possible with this technique significantly increases the chances of cure. A wide variety of luminescent materials including QDs, and UCNPs (upconversion nanoparticles) have been developed as multifunctional platform for both optical imaging and drug/gene delivery. However, most conventionally existing QDs are composed of heavy metal elements (such as  $\text{Cd}^{2+}$ ,  $\text{Pb}^{2+}$ , etc.). The cytotoxic nature of heavy metal ions released into biological systems and their deleterious environmental causes results in limited application of QDs in the field of theranostics<sup>(24)</sup> In case of UCNPs, the lanthanide complexes exhibit poor thermal stability and mechanical stability which reduces its applications.<sup>(25)</sup> On the other hand, recently noble metal nanoclusters such as gold nanoclusters (AuNCs) have gained wide attraction because of their high fluorescence, excellent photostability, negligible toxicity, high biocompatibility and aqueous solubility.<sup>(26,27)</sup> Therefore, photosensitizing agents, conjugated with fluorescent metal nanoclusters, can offer significant advantages for efficient image guided photodynamic cancer treatment.

Here, in a fast and easy synthesis of a mucin based nanocarrier embedded with luminescent Au NCs is reported. The cationic photosensitizer MB was loaded onto the Au NCs-mucin nanoparticles for photodynamic ablation of HeLa cancer cells and simultaneous bioimaging application. The role of singlet oxygen generation and subsequent cell death pathway was elucidated by flow cytometry based assays.

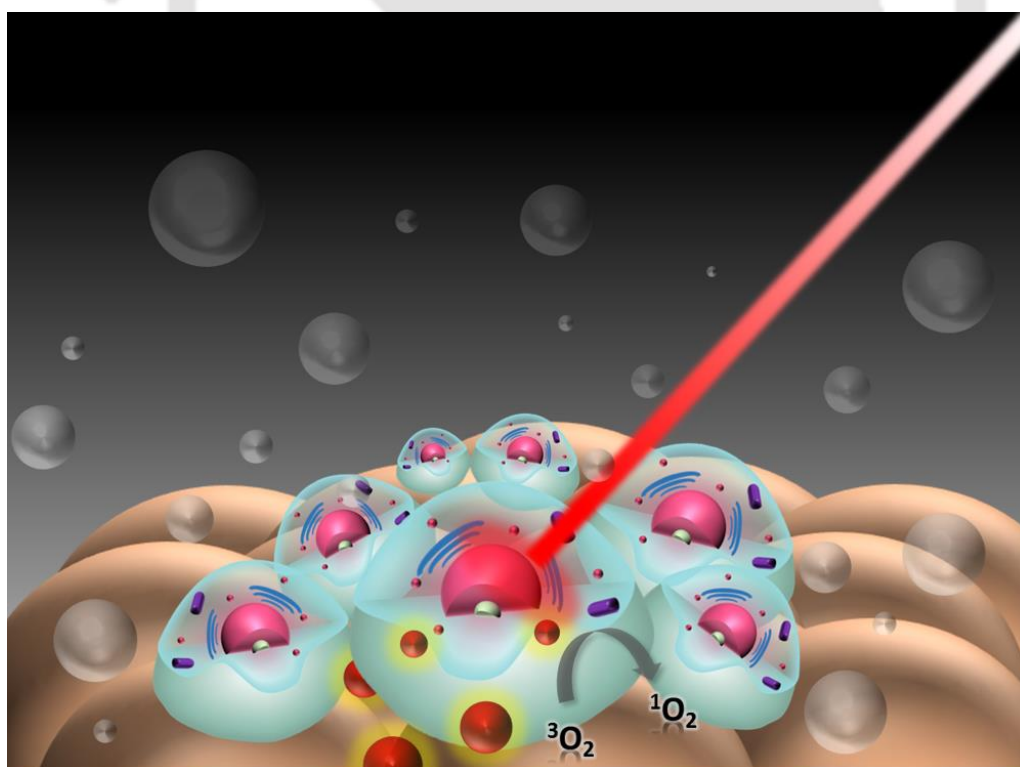


**Figure 4.1.** Schematic representation of MB Loaded Au NC-mucin NPs mediated photodynamic therapy

## 4.2. Synthesis and Characterisation

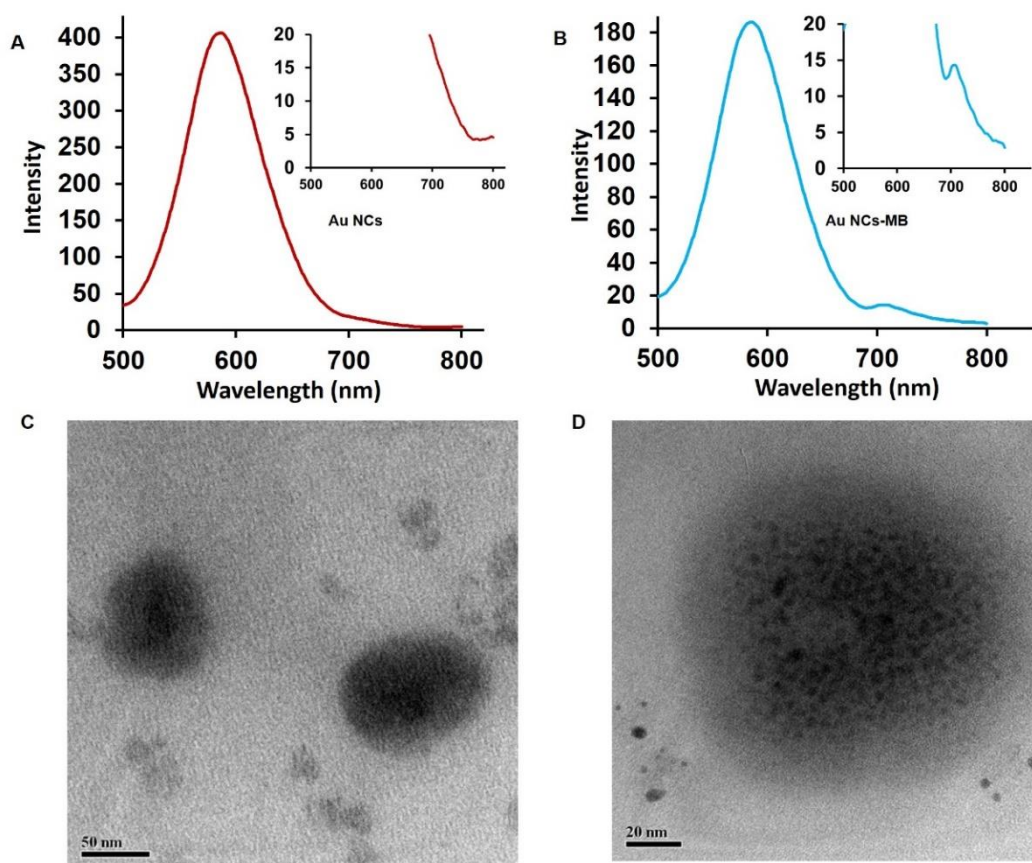


**Figure 4.2.** (A) Emission spectra of Au NC-mucin NPs ( $\lambda_{em} = 580$  nm) when excited at 300 nm. (B) Emission spectra of MB loaded Au NC-mucin NPs ( $\lambda_{em} = 580$  nm, 700nm) when excited at 300 nm. (C) TEM image of Au NC-mucin NPs with 50 nm scale bar. (D) Magnified TEM image of Au NC-mucin NPs with 20 nm scale bar.

The Au NCs embedded mucin nanoparticles (Au NC-mucin NPs) appeared as a colourless dispersion with a strong emission peak at 620 upon excitation at 300 nm which indicated the formation of Au NCs (**Figure 4.2A**). The MB loaded Au NC-mucin NPs exhibited an additional fluorescence peak at around 700 nm which confirmed the binding of MB (**Figure 4.2B**). The UV-Vis absorbance at 280 nm is due to the tryptophan residues of the protein in case of Au NC-mucin NPs as well as MB loaded Au NC-mucin NPs. MB loaded Au NC-mucin NPs in addition exhibited a peak at 660 nm due to the presence of MB which corresponds to maximum absorption peak of only MB. The absence of plasmonic signature in case of Au NC-mucin NPs at 520 nm indicates that Au NPs were not present (**Appendix C, Figure C4.1a-c**). TEM investigation showed the formation of MB loaded Au NC-mucin NPs with an average size of  $139 \pm 47$  nm. Magnified TEM investigation revealed the presence of Au NCs with an average size of  $1.9 \pm 0.34$  nm inside the mucin nanoparticles (**Figure 4.2C,D**). The loading efficiency of cationic photosensitizer methylene blue loaded on the Au NC-mucin NPs was found to be 70% (**Appendix C, Figure C4.1d**). After loading of MB, luminescence of Au NC-mucin NPs were quenched in comparison to the as synthesised Au NC-mucin NPs due to possible photo-

induced charge transfer between MB and Au NCs.<sup>(28)</sup> The zeta potential of mucin(-17.3±2.3), Au NC-mucin NPs (-5.5±0.2), MB loaded Au NC-mucin NPs (-2.8±0.1) indicated the binding of MB to the Au NC-mucin NPs (**Appendix C, Figure C4.2a-c**). The photostability studies of emission intensity of the Au NC- mucin nanoparticles revealed that the NCs were stable compared to standard rhodamine 6G. The luminescence intensity decrease rate ( $F/F_0$ ) of the NCs was 0.27% per min, whereas in the case of commonly used fluorescent dye rhodamine 6G, the rate was found to be 0.80% per min. The quantum yield of MB loaded Au NC-mucin NPs was measured to be 3.5% using quinine sulphate as standard and was deemed suitable for imaging applications (**Appendix C, Figure C4.3a,b**). The CD spectra of native mucin represented lack of well-defined secondary structure, characteristic of mucins due to heavy glycosylation.<sup>(29)</sup> Also, CD spectra of the Au NC-mucin NPs when compared to native mucin showed decrease in the percentage of turns with nominal increase in  $\alpha$ -helix percentage. (**Appendix C, Figure C4.4a,b**). The release profile of the MB from the Au NC-mucin NPs was studied at pH 4.5 and 7.5. It was revealed that about 55% of the drug was released at the end of 24 h at pH 4.5 and release of 26% was exhibited at pH 7.5 at the end of 24 h. The sustained release profile followed by initial burst release helps in retention of the photosensitizer for its optimum activity (**Appendix C, Figure C4.5**).

### 4.3. Detection of Singlet Oxygen Generation

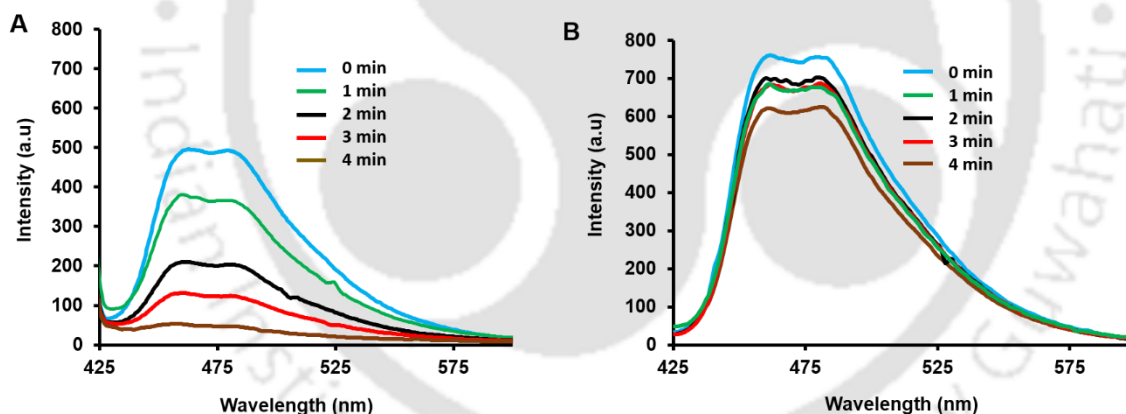


**Figure 4.3.** Luminescence spectra of (A) DPBF and MB loaded Au NC-mucin NPs, and (B) only DPBF irradiated with 640 nm light.

The potential of the MB loaded Au NC-mucin NPs in generation of singlet oxygen was determined by DPBF based singlet oxygen detection. The luminescence spectra of DPBF in presence of MB loaded Au NC-mucin NPs and only DPBF (irradiated with 640 nm light) were analysed. In the presence of MB loaded Au NC-mucin NPs, the luminescence of DPBF quenched gradually with time possibly due to the breakdown of DPBF in presence of the singlet oxygen generated by the MB loaded Au NC-mucin NPs. On the other hand, in the absence of MB loaded Au NC-mucin NPs significant decay in luminescence was not observed (**Figure 4.3A**). These results indicated the potential of the MB loaded Au NC-mucin NPs in singlet oxygen generation.

#### 4.4. Uptake and Delivery of MB Loaded Au NC-mucin NPs

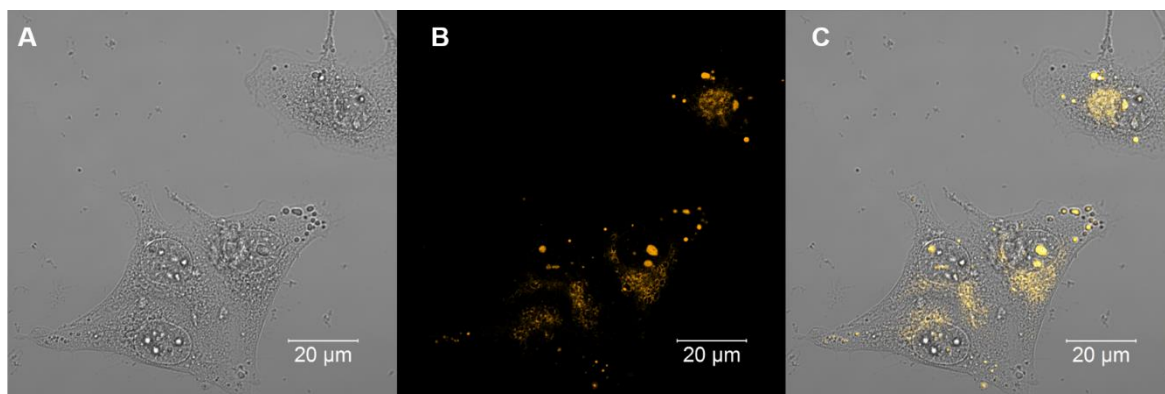


**Figure 4.4.** Confocal microscopic images of HeLa cells. (A) Bright field image, (B) fluorescence image and (C) merged fluorescent image of HeLa cells treated with MB loaded Au NC-mucin NPs.

For the application of the MB loaded Au NC-mucin NPs in bio-imaging and tracking the delivery of MB through the luminescence of Au NCs, HeLa cancer cells were kept under treatment with MB loaded Au NC-mucin NPs for 4 h and then were visualized under a confocal microscope. The confocal microscopic images showed the uptake of the MB loaded Au NC-mucin NPs into cancer cells (**Figure 4.4A-C**) as indicated by the luminescence of Au NCs. The images of control cells without treatment did not exhibit any luminescence (**Appendix C, Figure C4.6a-c**). The z-stack of the confocal microscopic images demonstrated internalization of MB loaded Au NC-mucin NPs into cancer cells (**Appendix C, Figure C4.7a-d**). The confocal microscopic images of cancer cells treated with Au NC-mucin NPs and MB only are shown in (**Appendix C, Figure C4.8a,b**). This showed the potential use of luminescent MB loaded Au NC-mucin NPs in imaging cancer cells as well as tracking the delivery of therapeutic photosensitizer MB.

## 4.5. Photodynamic Therapy and Mechanism of Cell Death

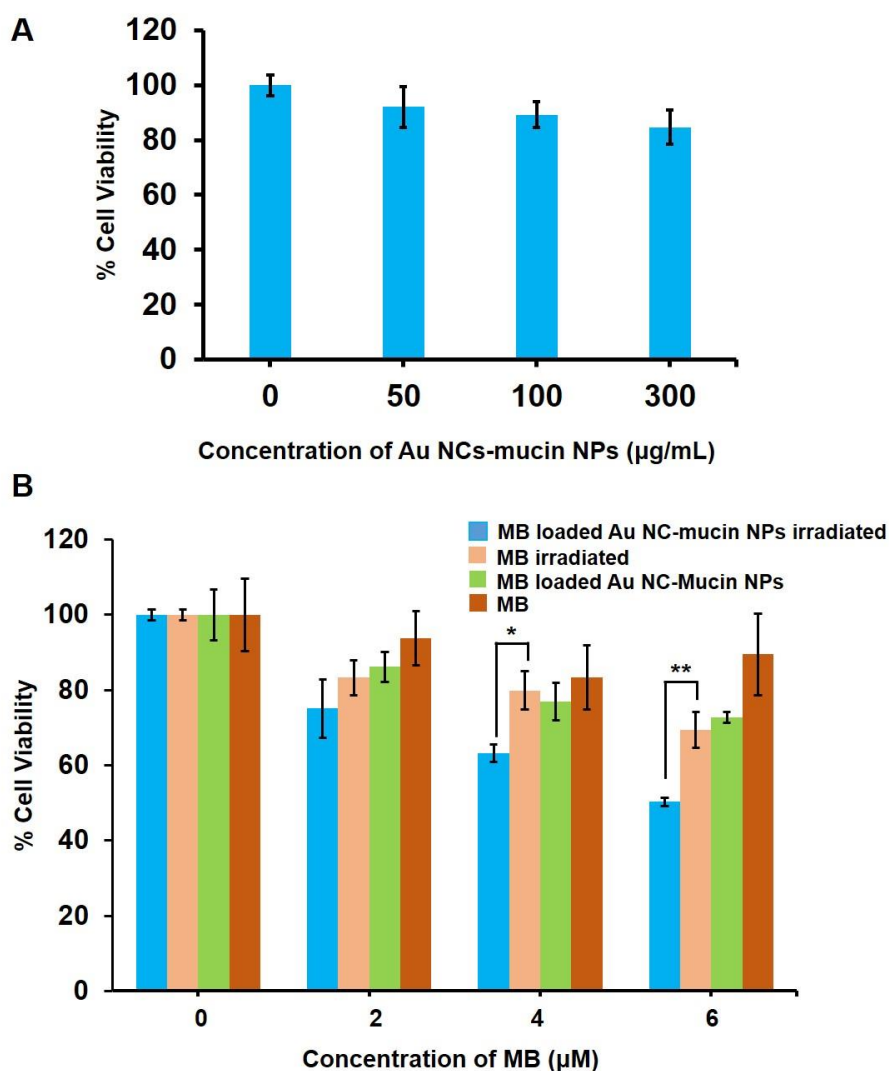


**Figure 4.5.** (A) MTT assay of HEK 293T cells, (B) MTT assay of HeLa cells treated with MB, MB loaded Au NC-mucin NPs in dark, MB under irradiation, and MB loaded Au NC-mucin NPs under irradiation. The values are represented as mean  $\pm$  SD of three individual experiments.

The biocompatibility of the Au NC-mucin NPs was determined by treating the HEK 293T human embryonic kidney cell lines with Au NC-mucin NPs for 24 h. The MTT assay revealed that more than 80% of the cells were viable after 24 h of treatment (**Figure 4.5A**). In order to establish the potential of MB loaded Au NC-mucin NPs in photodynamic therapy, the HeLa cancer cells were treated with MB, Au NC-mucin NPs, MB loaded Au NC-mucin NPs in dark as well as under irradiation at 640 nm light for 30 min by using a custom LED array device at low irradiation doses<sup>31</sup> (as mentioned in the Experimental Section) compared to high power lasers. After the exposure the cells were further incubated for 24 h. The MTT assay revealed that in case of the MB loaded Au NC-mucin NPs irradiated samples, 50% of the cells were viable at MB concentration of 6  $\mu\text{M}$  whereas 69 % cells were viable in case of only MB. Minimum level of dark toxicity was observed in case of

both only MB, MB loaded Au NC-mucin NPs (**Figure 4.5B**). Hence, an optimum level of photodynamic effect was achieved by MB, MB loaded Au NC-mucin NPs at low concentrations of drug which resulted in cancer cell death.

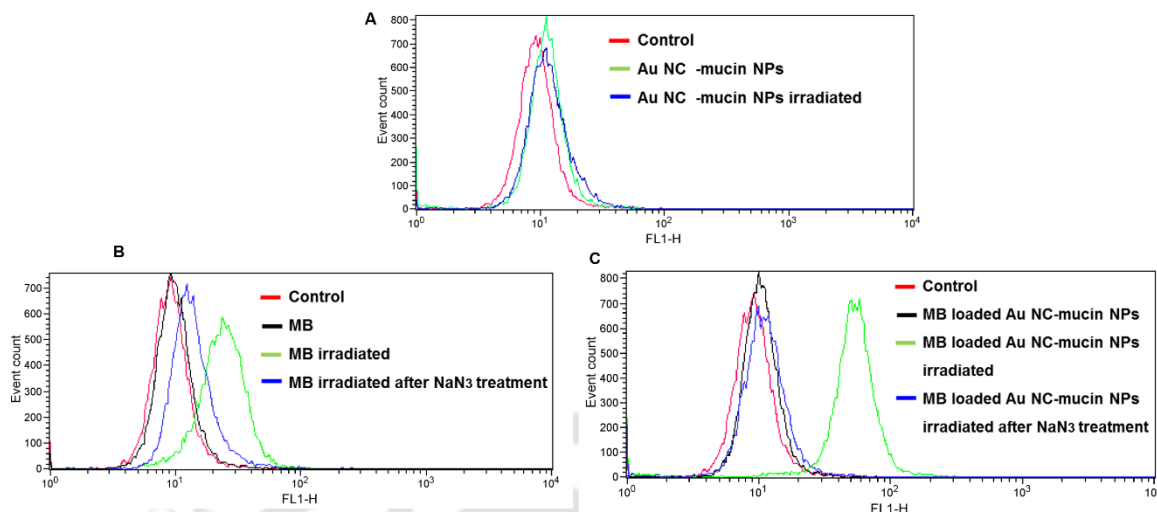


**Figure 4.6.** ROS generation profile of (A) HeLa cells treated with Au NC-mucin NPs, (B) MB, (C) MB loaded Au NC-mucin NPs under different conditions.

To establish that the mechanism of cell death is initiated by the generation of singlet oxygen, intracellular ROS levels were monitored in HeLa cells treated with MB, MB loaded Au NC-mucin NPs under irradiation with 640 nm light and in dark. Increased levels of ROS was found in case of irradiated samples in comparison to control and samples in dark. Further, to ascertain that the behavior exhibited is due to the generation of singlet oxygen, the intracellular ROS levels were monitored in HeLa cells with pretreatment of sodium azide (specific singlet oxygen quencher)<sup>31</sup> before MB, MB loaded Au NC-mucin NPs treatment under irradiation with 640 nm light and in dark. The results indicated that in case of sodium azide pretreated samples, the ROS levels were sufficiently quenched in the cells treated with MB, MB loaded Au NC-mucin NPs under irradiation (**Figure 4.6A-C**). The enhanced quenching of ROS levels in case sodium azide pretreated samples under irradiation indicated that the cell death initiated under irradiation was possibly due to MB, MB loaded Au NC-mucin NPs mediated PDT via generation of singlet oxygen.

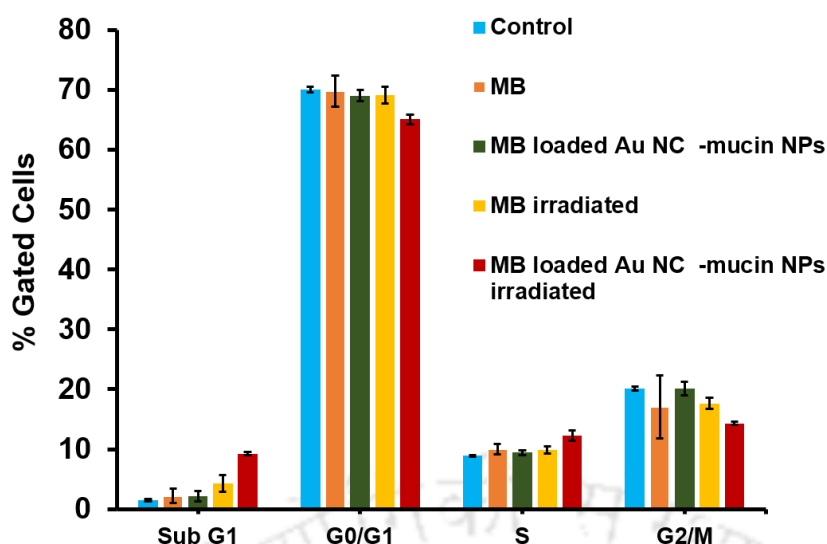


**Figure 4.7.** Cell cycle analysis of control HeLa cells, HeLa cells treated with MB, MB loaded Au NC-mucin NPs in dark, MB under irradiation, and MB loaded Au NC-mucin NPs under irradiation.

Also, cell cycle analysis was carried out by propidium iodide (PI) staining, which showed increase in sub G<sub>1</sub> cell population after treatment with MB, MB loaded Au NC-mucin NPs irradiated with 640 nm light as compared to other controls, along with slight changes in other phases of cell cycle (G<sub>0</sub>/G<sub>1</sub>, S, and G<sub>2</sub>/M) as shown in **Figure 4.7**. Herein, the significant increase in sub G<sub>1</sub> population gives the indication of apoptosis mode of cell death.

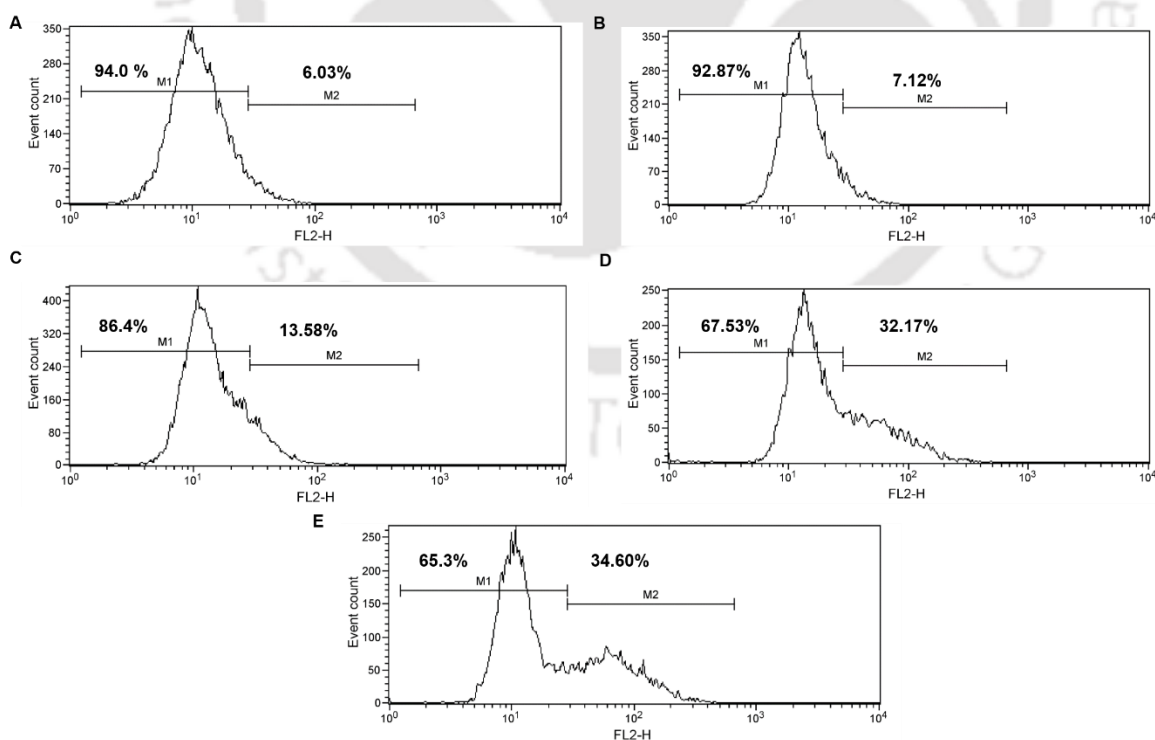


**Figure 4.8.** Caspase-3 assay of HeLa cells showing percentage of apoptosis in (A) control, treated with (B,C) MB, MB loaded Au NC-mucin NPs in dark, (D) MB under irradiation, and (E) MB loaded Au NC-mucin NPs under irradiation.

The caspase-3 assay further strengthened the claim of apoptosis mediated cell death. An anti-caspase antibody was used to label caspase-3 produced inside the cells during apoptosis. It revealed that MB, MB loaded Au NC-mucin NPs treated cells irradiated with 640 nm light showed a considerable increase in the active caspase-3 positive cell (apoptotic cells) population in comparison to other controls (**Figure 4.8A-E**). Hence, from all the above findings, it can be concluded that the MB loaded Au NC-mucin NPs effectively delivered the photosensitizer and killed the cancer cells by virtue of generation of singlet oxygen. Also, the luminescence property of the MB loaded Au NC-mucin NPs conferred biolabeling properties, thereby helping in tracking the delivery process of MB.

## 4.6. Conclusions

In brief, a mucin based luminescent biocompatible nanocarrier was developed for the delivery of photosensitizer MB into the HeLa cancer cells. The MB binding to Au NC-mucin NPs was carried out and uptake of the MB loaded Au NC-mucin NPs was analysed by confocal microscopy. The MB loaded Au NC-mucin NPs delivered the MB successfully and the cancer cells were killed through singlet oxygen generation. Also, the luminescent nature of the MB loaded Au NC-mucin NPs gave an opportunity for tracking the delivery of photosensitizer inside the cells without the need for organic fluorophores. The mode of cell death has been established by flow cytometry based assays. Thus, the present biocompatible MB loaded Au NC-mucin NPs system possesses the ability to be used for photodynamic cancer therapy with simultaneous bioimaging.

## 4.7. References

1. van Straten, D.; Mashayekhi, V.; de Bruijn, H. S.; Oliveira, S.; Robinson, D. J. Oncologic Photodynamic Therapy: Basic Principles, Current Clinical Status and Future Directions. *Cancers (Basel)* **2017**, *9* (2).
2. Staneloudi, C.; Smith, K. A.; Hudson, R.; Malatesti, N.; Savoie, H.; Boyle, R. W.; Greenman, J. Development and Characterization of Novel Photosensitizer : ScFv Conjugates for Use in Photodynamic Therapy of Cancer. *Immunology* **2007**, *120* (4), 512–517.
3. Huang, P.; Xu, C.; Lin, J.; Wang, C.; Wang, X.; Zhang, C.; Zhou, X.; Guo, S.; Cui, D. Folic Acid-Conjugated Graphene Oxide Loaded with Photosensitizers for Targeting Photodynamic Therapy. *Theranostics* **2011**, *1*, 240–250.
4. Liang, X.; Li, X.; Yue, X.; Dai, Z. Conjugation of Porphyrin to Nanohybrid Cerasomes for Photodynamic Diagnosis and Therapy of Cancer. *Angew. Chem. Int. Ed. Engl.* **2011**, *50* (49), 11622–11627.
5. Jawahar, N.; Meyyanathan, S. N. Polymeric Nanoparticles for Drug Delivery and Targeting: A Comprehensive Review. *International Journal of Health & Allied Sciences* **2012**, *1* (4), 217.

6. Narvekar, M.; Xue, H. Y.; Eoh, J. Y.; Wong, H. L. Nanocarrier for Poorly Water-Soluble Anticancer Drugs—Barriers of Translation and Solutions. *AAPS PharmSciTech* **2014**, *15* (4), 822–833.
7. Barua, S.; Mitragotri, S. Challenges Associated with Penetration of Nanoparticles across Cell and Tissue Barriers: A Review of Current Status and Future Prospects. *Nano Today* **2014**, *9* (2), 223–243.
8. Lai, S. K.; Wang, Y.-Y.; Hanes, J. Mucus-Penetrating Nanoparticles for Drug and Gene Delivery to Mucosal Tissues. *Adv Drug Deliv Rev* **2009**, *61* (2), 158–171.
9. Boegh, M.; Nielsen, H. M. Mucus as a Barrier to Drug Delivery – Understanding and Mimicking the Barrier Properties. *Basic Clin Pharmacol Toxicol* **2015**, *116* (3), 179–186.
10. Zanin, M.; Baviskar, P.; Webster, R.; Webby, R. The Interaction between Respiratory Pathogens and Mucus. *Cell Host & Microbe* **2016**, *19* (2), 159–168.
11. Wong, P. T.; Wang, S. H.; Ciotti, S.; Makidon, P. E.; Smith, D. M.; Fan, Y.; Schuler, C. F.; Baker, J. R. Formulation and Characterization of Nanoemulsion Intranasal Adjuvants: Effects of Surfactant Composition on Mucoadhesion and Immunogenicity. *Mol Pharm* **2014**, *11* (2), 531–544.
12. Adikwu, M. U. *Biopolymers in Drug Delivery: Recent Advances and Challenges*, Chapter 2, 27-38; Bentham Science Publishers, 2010.
13. Belgorodsky, B.; Drug, E.; Fadeev, L.; Hendler, N.; Mentovich, E.; Gozin, M. Mucin Complexes of Nanomaterials: First Biochemical Encounter. *Small* **2010**, *6* (2), 262–269.
14. Thasneem, Y. M.; Rekha, M. R.; Sajeesh, S.; Sharma, C. P. Biomimetic Mucin Modified PLGA Nanoparticles for Enhanced Blood Compatibility. *Journal of Colloid and Interface Science* **2013**, *409*, 237–244.
15. Sandberg, T.; Karlsson Ott, M.; Carlsson, J.; Feiler, A.; Caldwell, K. D. Potential Use of Mucins as Biomaterial Coatings. II. Mucin Coatings Affect the Conformation and Neutrophil-Activating Properties of Adsorbed Host Proteins--toward a Mucosal Mimic. *J Biomed Mater Res A* **2009**, *91* (3), 773–785.
16. Ahn, J.; Crouzier, T.; Ribbeck, K.; Rubner, M. F.; Cohen, R. E. Tuning the Properties of Mucin via Layer-by-Layer Assembly. *Biomacromolecules* **2015**, *16* (1), 228–235.
17. Borges, J.; Mano, J. F. Molecular Interactions Driving the Layer-by-Layer Assembly of Multilayers. *Chem. Rev.* **2014**, *114* (18), 8883–8942.
18. Builders, P. F.; Kunle, O. O.; Okpaku, L. C.; Builders, M. I.; Attama, A. A.; Adikwu, M. U. Preparation and Evaluation of Mucinated Sodium Alginate Microparticles for Oral Delivery of Insulin. *European Journal of Pharmaceutics and Biopharmaceutics* **2008**, *70* (3), 777–783.
19. Ofokansi, K. C.; Adikwu, M. U.; Okore, V. C. Preparation and Evaluation of Mucin-Gelatin Mucoadhesive Microspheres for Rectal Delivery of Ceftriaxone Sodium. *Drug Development and Industrial Pharmacy* **2007**, *33* (6), 691–700.

20. Duffy, C. V.; David, L.; Crouzier, T. Covalently-Crosslinked Mucin Biopolymer Hydrogels for Sustained Drug Delivery. *Acta Biomaterialia* **2015**, *20*, 51–59.
21. Fukui, Y.; Fukuda, M.; Fujimoto, K. Generation of Mucin Gel Particles with Self-Degradable and -Releasable Properties. *Journal of Materials Chemistry B* **2018**, *6* (5), 781–788.
22. Nair, L. V.; Nazeer, S. S.; Jayasree, R. S.; Ajayaghosh, A. Fluorescence Imaging Assisted Photodynamic Therapy Using Photosensitizer-Linked Gold Quantum Clusters. *ACS Nano* **2015**, *9* (6), 5825–5832.
23. Huang, P.; Lin, J.; Wang, S.; Zhou, Z.; Li, Z.; Wang, Z.; Zhang, C.; Yue, X.; Niu, G.; Yang, M.; et al. Photosensitizer-Conjugated Silica-Coated Gold Nanoclusters for Fluorescence Imaging-Guided Photodynamic Therapy. *Biomaterials* **2013**, *34* (19), 4643–4654.
24. Stan, M. S.; Memet, I.; Sima, C.; Popescu, T.; Teodorescu, V. S.; Hermenean, A.; Dinischiotu, A. Si/SiO<sub>2</sub> Quantum Dots Cause Cytotoxicity in Lung Cells through Redox Homeostasis Imbalance. *Chemico-Biological Interactions* **2014**, *220*, 102–115.
25. Chu, Y.; Hao, H.; Xie, H.; Chen, C.; Cai, P.; Seo, H. J. Preparation of Lanthanide (Eu<sup>3+</sup>, Tb<sup>3+</sup>)-Complex-Grafted Copolymer of Methyl Methacrylate and Maleic Anhydride Films and the Promising Application as LED Luminous Layers. *J Mater Sci: Mater Electron* **2017**, *28* (7), 5615–5622.
26. Sailapu, S. K.; Dutta, D.; Sahoo, A. K.; Ghosh, S. S.; Chattopadhyay, A. Single Platform for Gene and Protein Expression Analyses Using Luminescent Gold Nanoclusters. *ACS Omega* **2018**, *3* (2), 2119–2129.
27. Dutta, D.; Sahoo, A. K.; Chattopadhyay, A.; Ghosh, S. S. Bimetallic Silver Nanoparticle–gold Nanocluster Embedded Composite Nanoparticles for Cancer Theranostics. *J. Mater. Chem. B* **2016**.
28. Rakovich, A.; Savateeva, D.; Rakovich, T.; Donegan, J. F.; Rakovich, Y. P.; Kelly, V.; Lesnyak, V.; Eychmüller, A. CdTe Quantum Dot/Dye Hybrid System as Photosensitizer for Photodynamic Therapy. *Nanoscale Res Lett* **2010**, *5* (4), 753.
29. Perez-Vilar, J.; Hill, R. L. The Structure and Assembly of Secreted Mucins. *J. Biol. Chem.* **1999**, *274* (45), 31751–31754.
30. Lerche, C. M.; Heerfordt, I. M.; Heydenreich, J.; Wulf, H. C. Alternatives to Outdoor Daylight Illumination for Photodynamic Therapy--Use of Greenhouses and Artificial Light Sources. *Int J Mol Sci* **2016**, *17* (3), 309.
31. Bancirova, M. Sodium Azide as a Specific Quencher of Singlet Oxygen during Chemiluminescent Detection by Luminol and Cypridina Luciferin Analogues. *Luminescence* **2011**, *26* (6), 685–688.

# Appendix C

## C.1 Experimental Section

### Materials and methods

#### Chemicals

HAuCl<sub>4</sub> (Au, 17 wt % in dilute HCl; 99.99%, Sigma-Aldrich), Mucin Type III from porcine stomach (Sigma-Aldrich), mercaptopropionic acid (MPA; Sigma-Aldrich), methylene blue (Merck) and Milli-Q-grade water (>18 MΩ/cm; Millipore) were used without any alterations.

#### Synthesis of Au NCs-mucin nanoparticles

The synthesis of luminescent Au NCs on mucin was achieved by slight modification of our previously reported method.<sup>(26)</sup> A total of 1 mL of 1mg/mL mucin was taken, and 8 μL of 0.11 M MPA and 20 μL of 10 mM HAuCl<sub>4</sub> were added to it. The solution was heated to 95 °C for 2 min and rapidly cooled to 4 °C. The sample was then centrifuged at 6000 rpm for 5 min, and pellet was redispersed in water for further use.

#### UV–visible spectroscopy and luminescence measurements

A UV–visible spectrophotometer (Jasco V-630) was used to record the absorbance of all samples. All luminescence-based measurements were carried out using a fluorescence spectrophotometer (PerkinElmer LS55).

#### Transmission electron microscopy (TEM)

For TEM analysis, 7 μL of the synthesized sample was drop-cast onto the TEM grid and air-dried. The TEM grid was observed under a transmission electron microscope operating at a maximum accelerating voltage of 200 keV (JEM 2100; JEOL, Peabody, MA).

#### Quantum yield (QY) measurements

The QY measurement was done using reference quinine sulfate in a 0.10 M H<sub>2</sub>SO<sub>4</sub> solution. The equation used for calculation of the QY is as follows:

$$QY = QY_r \frac{m}{m_r} \frac{n^2}{n_r^2}$$

Here,  $m$  is the slope of integrated luminescence intensity versus absorbance plot,  $n$  is the refractive index, and subscript  $r$  indicates the reference solution quinine sulfate. The absorbance and luminescence intensity measurements were carried out consecutively one after the other using the same solution. The QY of the standard ( $QY_r$ ) is 0.54, and the refractive index of water (solvent) is 1.33.

**1, 3 - diphenylizobenzofuran (DPBF) singlet oxygen detection experiment:**

For this, 100  $\mu\text{L}$  of MB loaded Au NC-mucin NPs were mixed with 100  $\mu\text{L}$  of DPBF (0.08 mM) in dimethyl sulfoxide (DMSO) under dark conditions. Another set containing only DPBF was kept as control. The samples were irradiated for 0 to 4 min in steps of 1 min using LED array with peak emission around 640 nm (2000 lux). The luminescence of DPBF was recorded using Perkin Elmer LS 55 fluorescence spectrophotometer.

**Cell culture**

HeLa (human cervical carcinoma), HEK 293T (human embryonic kidney) cells for cell culture experiments were acquired from the National Centre for Cell Sciences, Pune, India. For culturing cells in a 5%  $\text{CO}_2$  humidified incubator at 37  $^\circ\text{C}$ , Dulbecco's modified Eagle's medium, supplemented with l-glutamine (4 mM), penicillin (50 units/mL), streptomycin (50 mg/mL, Sigma-Aldrich), and 10% (v/v) fetal bovine serum (FBS; PAA Laboratories, Austria), was used.

**Confocal microscopy**

For experiments in confocal microscopy,  $1 \times 10^5$  HeLa cells were seeded on coverslips in 35 mm culture dishes and grown in a 5%  $\text{CO}_2$  humidified incubator (37  $^\circ\text{C}$  for 24 h). Thereafter, the cells were treated with MB, Au NC-mucin NPs and MB loaded Au NC-mucin NPs for 3 h. The treated cells were fixed using 0.1% formaldehyde and 70% chilled ethanol. The coverslips were mounted on glass slides, and the ends were sealed. Control samples without treatment were prepared in a similar manner. The samples were observed (at excitation 405 nm) under a Zeiss LSM 880 microscope.

**MTT Assay**

For assessment of the cell viability,  $1 \times 10^4$  HeLa and HEK cells/well were seeded in a 96-well plate and cultured overnight (37  $^\circ\text{C}$  for 24 h) in a 5%  $\text{CO}_2$  humidified incubator. The cells were treated with MB, Au NC-mucin NPs and MB loaded Au NC-mucin NPs for 3 h and then irradiated with 640 nm light for 30 min using a custom made (red) LED array device at an irradiation dose of 2000 lux and thereafter incubated for 24 h. Control experiments were carried out by treating the cells with MB and MB loaded Au NC-mucin NPs without irradiation (in dark). Thereafter, MTT [3-(4,5-dimethylthiazol-2-yl)-2,5-diphenyltetrazolium bromide] assay was carried out. MTT is reduced by mitochondria in living cells into colored formazan. Thus, absorbance at 570 nm reveals the amount of formazan product, which directly relates to the number of live cells. The absorbance at 690 nm was subtracted (background interference). The percent of cell viability was calculated as

$$\% \text{ viable cells} = \frac{(A_{570} - A_{690}) \text{ of treated cells}}{(A_{570} - A_{690}) \text{ of control cells}} \times 100$$

### Determination of reactive oxygen species (ROS)

For ROS generation studies, HeLa cells were seeded at a density of  $1 \times 10^5$  cells/well in a 6-well plate, grown for 24 h, and then treated for 3 h with MB and MB loaded Au NC-mucin NPs. Thereafter the cells were irradiated in a similar manner as described in MTT assay to induce ROS generation. In order to confirm the role of singlet oxygen towards increased ROS levels the cells were pretreated with 50 mM sodium azide ( $\text{NaN}_3$ ) for 1 h before irradiation. Control experiments were carried out by treating the cells with MB and MB loaded Au NC-mucin NPs without irradiation (in dark). After the treatment, the cells were incubated for 10 min in 1 mM 2,7-dichlorofluorescein diacetate (DCFH-DA; 5  $\mu\text{L}$ /well; Sigma-Aldrich). The media was discarded, and the cells were harvested and redispersed in fresh media. DCFH-DA, which is a nonfluorescent dye, converts to DCFH through hydrolysis inside live cells. The hence-formed DCFH on oxidation by ROS converts to green fluorescent dichlorofluorescein (DCF). The samples were analyzed in FL1-H channel in a flow cytometer (FacsCalibur, BD Biosciences, NJ) at an excitation wavelength of 488 nm and emission wavelength of 530 nm for DCF fluorescence. The fluorescence data for 15000 cells in each sample were recorded with the Cell Quest program (BD Biosciences).

### Cell cycle analysis

A propidium iodide (PI)-based staining method was adopted for cell cycle analysis. HeLa cells at a density of  $1 \times 10^5$  cells/well were seeded in 6-well plates, grown, and then treated with MB and MB loaded Au NC-mucin NPs in a similar manner as in case of MTT assay. At the end of 24 h incubation the media and PBS were collected separately for both the treated and control cell samples. The cells were then harvested by trypsinization, and all of the samples were centrifuged (650 rcf, 6 min). Following this, the cells were fixed under constant vortexing by the slow addition of 1 mL of 70% chilled ethanol and stored at 4 °C. The cells were then centrifuged, washed in ice-cold PBS, and treated with RNase for 1 h at 55 °C. Then 10  $\mu\text{L}$  of PI (1 mg/mL) was added to all of the samples, and incubation was carried out in the dark at 37 °C for 30 min. The samples were analyzed in a flow cytometer (BD). PI fluorescence data were recorded for 15000 cells in each sample with the Cell Quest program (BD) for further analysis.

### Caspase-3 assay

For caspase-3 assay, HeLa cells ( $1 \times 10^5$  cells/well; 6-well plates) were grown for 24 h, followed by treatment with ~~with~~ MB and MB loaded Au NC-mucin NPs in a similar manner as in case of MTT assay. At the end of 24 h incubation both the treated and control cells after trypsinization were fixed in 0.1% formaldehyde for 15 min. The samples were centrifuged at 650 rcf for 6 min, and the pellet was redispersed in PBS. Thereafter, 0.5% Tween 20 was added to the samples and incubated in the dark for 20 min. The cells were washed three times with PBS, and 10  $\mu\text{L}$  of PE-conjugated anticaspase-3 antibody was added. After incubation for 0.5 h at 37 °C, the samples were analyzed

for PE fluorescence in a flow cytometer (BD). Fluorescence data for 15000 cells were recorded with the Cell Quest program (BD) in each sample for further analysis.

## C.2 Figures

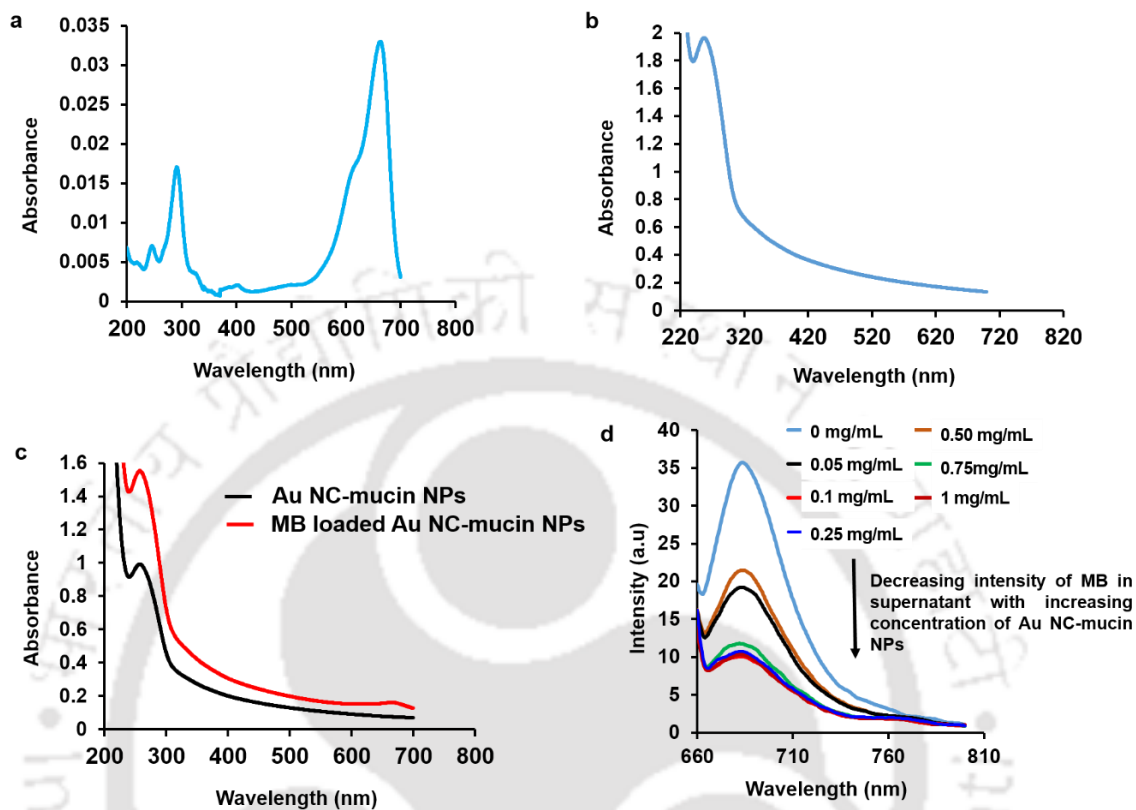


**Figure C4.1.** (a) UV-Visible spectrum of MB. (b) UV-Visible spectrum of mucin. (c) UV-Visible spectrum of Au NC-mucin NPs, MB loaded Au NC-mucin NPs. (d) Loading efficiency of MB onto Au NC-mucin NPs.

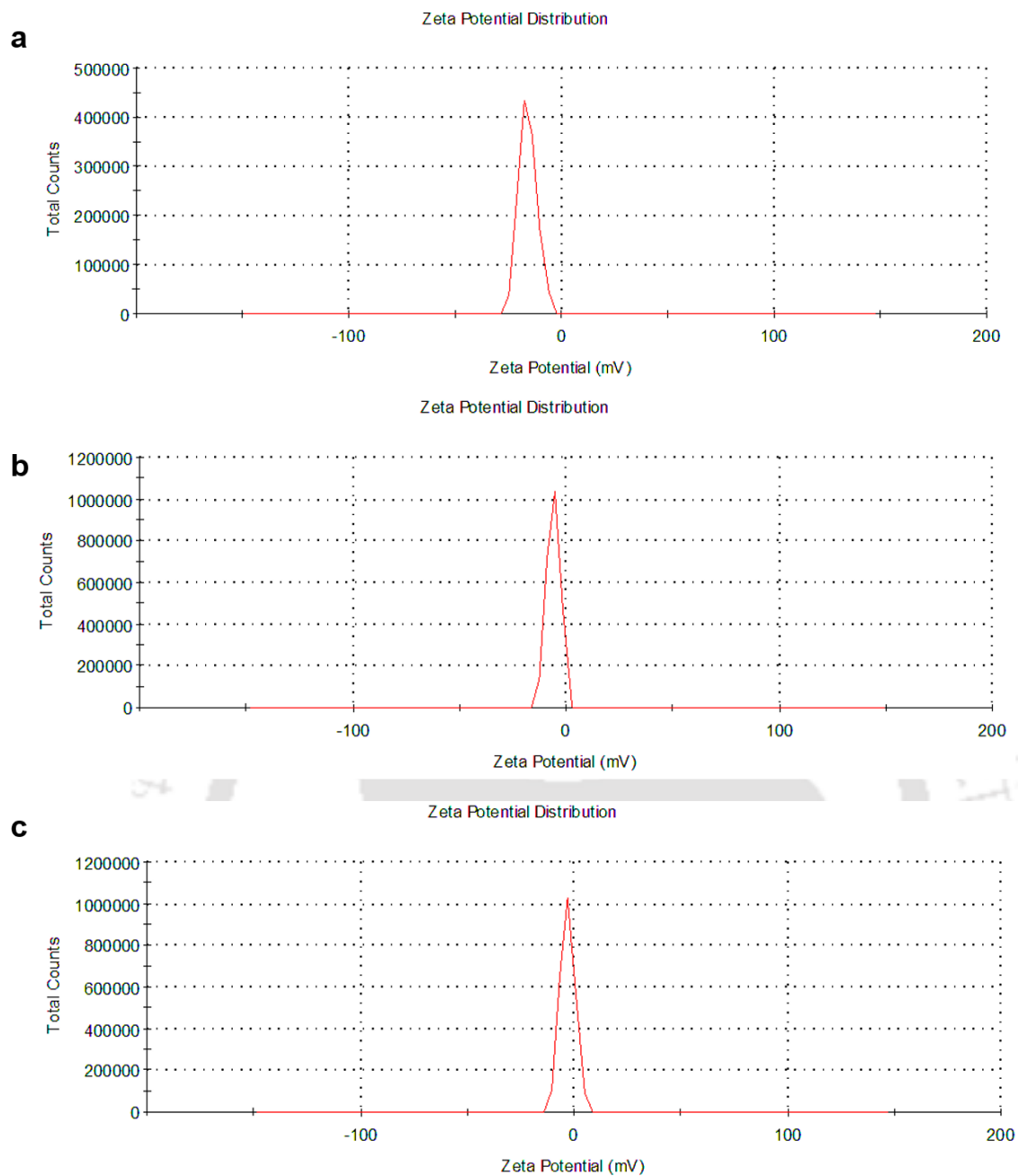


**Figure C4.2.** (a-c) Zeta potential of mucin, Au NC-mucin NPs, MB loaded Au NC-mucin NPs.

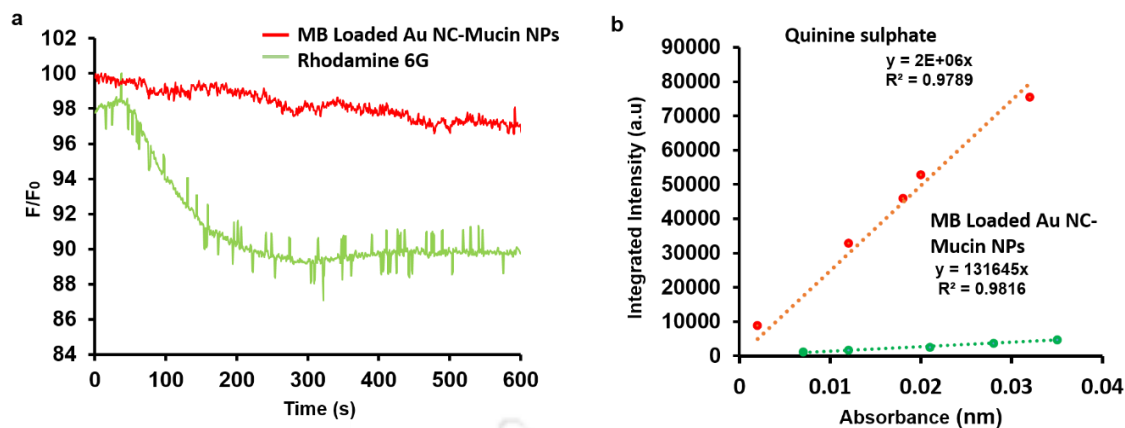


**Figure C4.3.** (a) Photo stability of MB loaded Au NC-mucin NPs. (b) Quantum yield of MB loaded Au NC-mucin NPs.

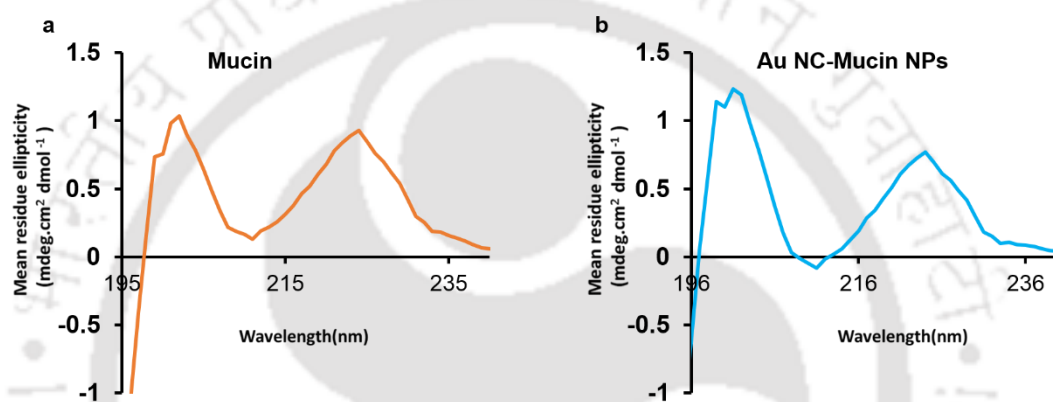


**Figure C4.4.** (a,b) CD spectra of the mucin, Au NC-mucin NPs.

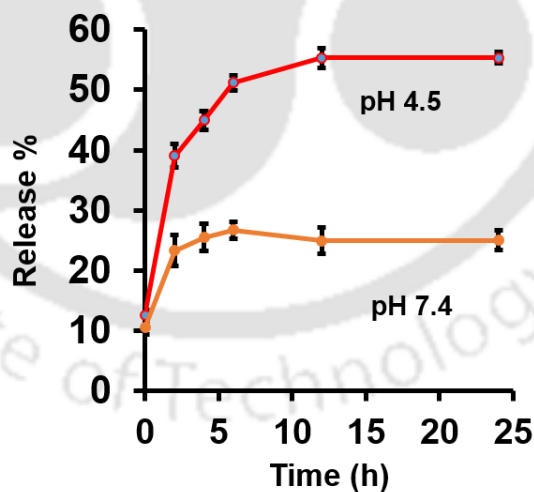


**Figure C4.5.** Release profile of MB from Au NC-mucin NPs at pH 7.4 and 4.5.

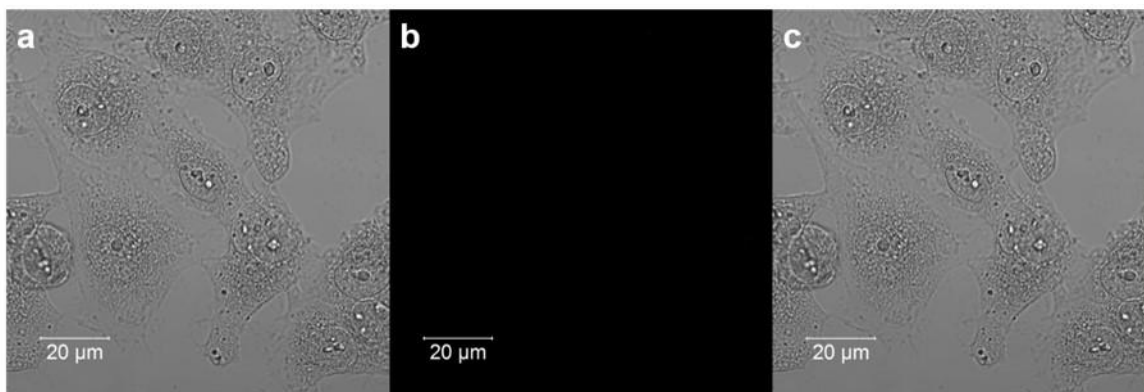


**Figure C4.6.** (a-c) Bright-field, fluorescence, and merged images of control HeLa cells.

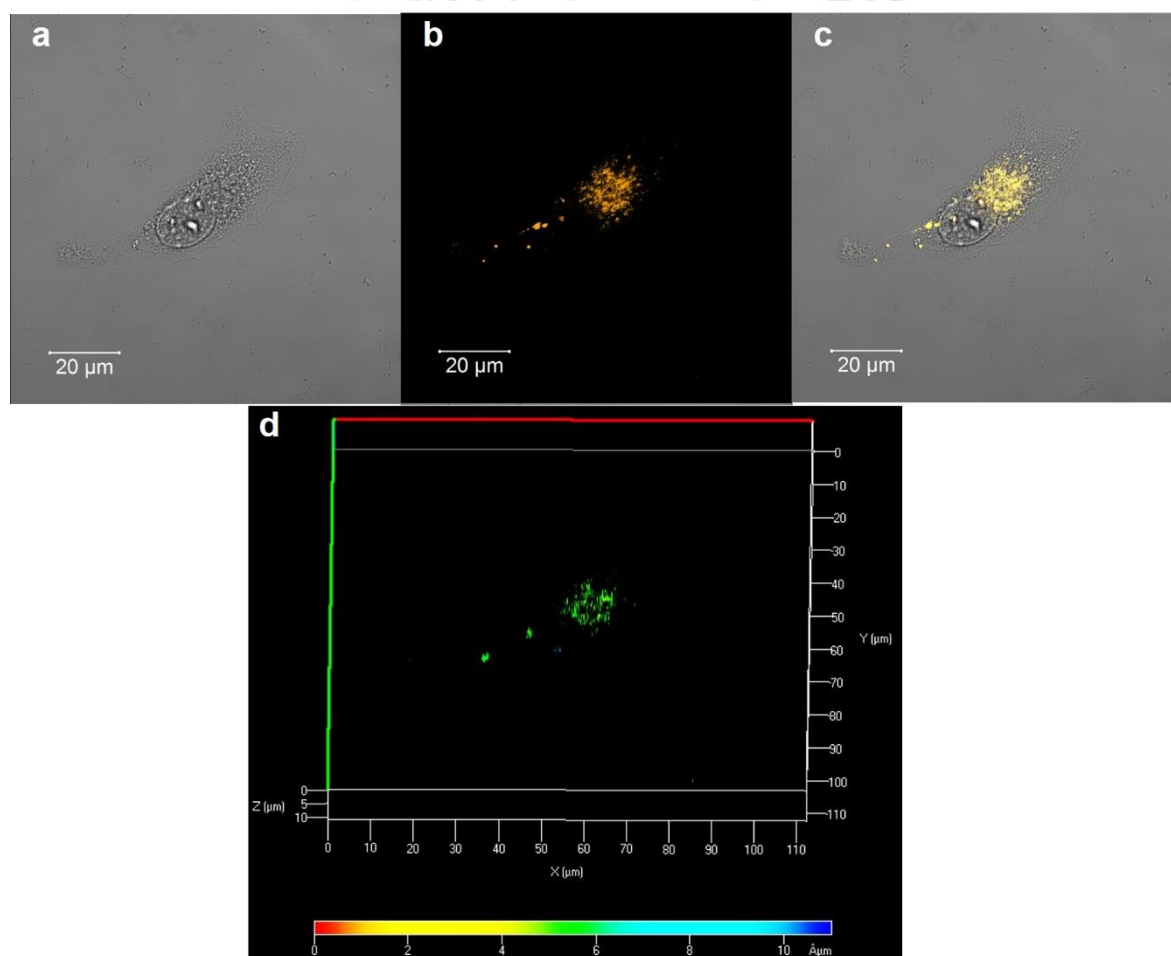


**Figure C4.7.** (a-c) Bright field image, fluorescence image and merged image of HeLa cells treated with MB loaded Au NC-mucin NPs. (d) Depth projection of confocal microscopy image showing internalization of MB loaded Au NC-mucin NPs inside HeLa cell.

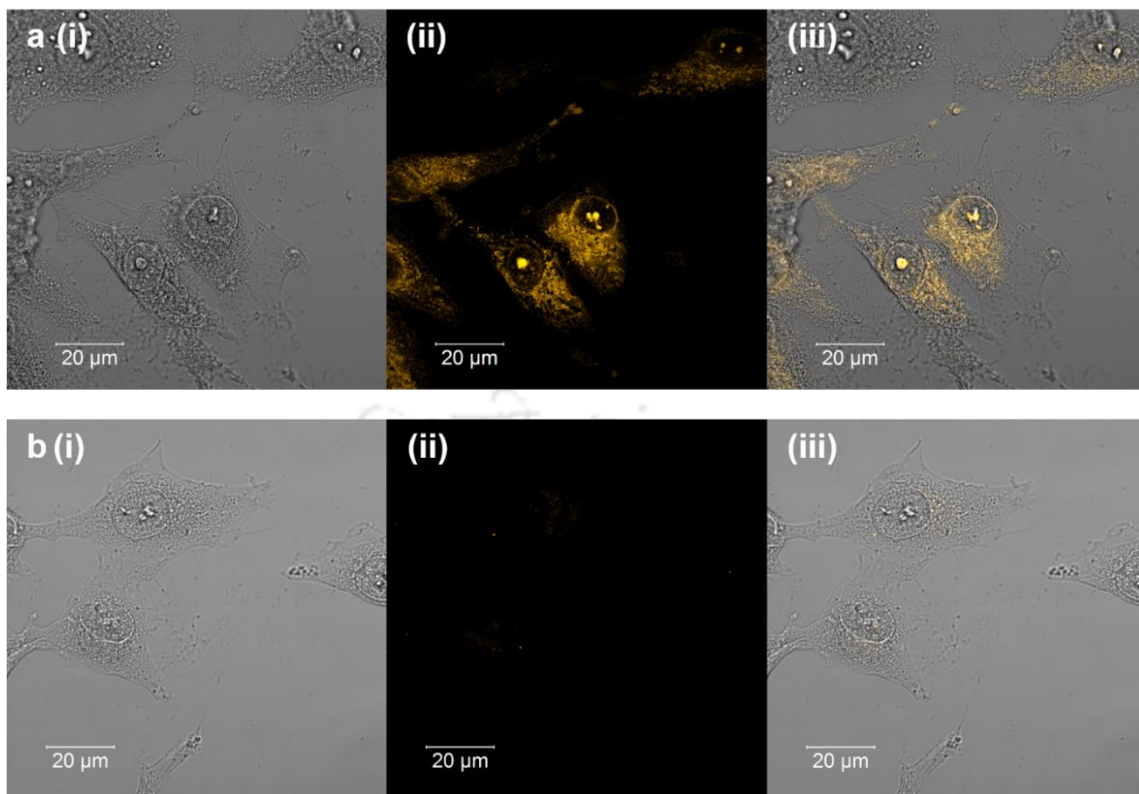


**Figure C4.8.** (a) (i–iii) Bright-field, fluorescence, and merged images of HeLa cells treated with Au NC-mucin NPs. (b) (i–iii) Bright-field, fluorescent, and merged images of HeLa cells treated with MB.



## Chapter 5



### Phenylboronic Acid Templated Gold Nanoclusters for Mucin Detection Using a Smartphone-Based Device and Targeted Cancer Cell Theranostics

D. Dutta, S.K. Sailapu, A. Chattopadhyay and S. S. Ghosh, *ACS Appl. Mater. Interfaces* 10, 4, 3210-3218



## Chapter 5

# Phenylboronic Acid Templated Gold Nanoclusters for Mucin Detection Using a Smartphone-Based Device and Targeted Cancer Cell Theranostics

---

### Abstract

A phenylboronic acid templated gold nanocluster probe was developed to detect biomarker mucin by a noninvasive luminescence based method using a point-of-care smartphone-based fluorescence detection device. The gold nanocluster probe is able to detect mucin specifically. The same probe was applied for *in vitro* targeted bioimaging of HeLa and Hep G2 cancer cells, and it demonstrated specific therapeutic effects toward cancer cells as well as multicellular tumor spheroids imparting theranostic properties. The module is found to be more effective toward HeLa cells, and a pathway of cell death was established using flow-cytometry-based assays.

### 5.1. Introduction

Biological molecules like protein receptors, aptamers, peptides, antigens, and antibodies are widely accepted in cancer research for sensing, recognition, assay of biomarkers, and delivery of therapeutic solutions.<sup>(1)</sup> However, they lack stability when subjected to changes in the pH and heat and are more susceptible to degradation during surface modifications, which is highly desirable to link other moieties such as fluorophores for detection purposes.<sup>(1)</sup> Alternatively, the use of small synthetic molecules for the recognition of a specific analyte provides a suitable platform, which is by far more stable and can be easily modified for enhancing activity. Akin to biological interactions, these chemical molecules make use of the functional groups present on them and bind to the analyte with high specificity and affinity. In this regard, phenylboronic acid has been accredited with targeting sialic acid residues with high specificity at physiological pH.<sup>(2)</sup> A wealth of nanoparticle-based delivery vehicles have been developed in the recent past targeting sialic acids on cancer cell surfaces.<sup>(3-5)</sup> Overexpression of sialic acid residues or altered glycosylation play a pivotal role in the manifestation of many diseases including various cancers like prostate, liver, breast, cervical, and stomach among many others. Further, hypoxic regions of solid tumors are also known to overexpress sialic acids.<sup>(6, 7)</sup> In addition to targeting, boronic acids have also gained interest in anticancer therapy as potential proteasome inhibitors, enzyme inhibitors, boron neutron therapy agents, etc. Drug testing has been carried out using boron-containing drugs as a new class of pharmaceuticals for various diseases including cancer.<sup>(8-14)</sup> As a consequence, besides the successful detection of cancer markers,

boronic acids hold the potential to act as anticancer agents. However, for the application of boronic acids as anticancer agents, it is essential to track their distribution inside the cells, and this can be achieved via tagging of the therapeutic boron-based compounds with imaging probes. Rapid sensing methods based on specific targeting of sialic acid could be also useful for the development of point-of-care (POC) diagnostic devices and is of importance in targeted delivery and therapeutics. An important secretory glycoprotein, mucin, contains sialic acid moieties and is found to be associated with pathways in cancer progression, invasion, and metastasis. Also, mucins constitute a major portion of the tumor area/volume in many cases.<sup>(15)</sup> However, the rapid detection of mucin is challenging because current standard methods, like histochemical analysis of tumor tissues through PAS/Alcain blue staining,<sup>(16,17)</sup> are invasive and time-consuming and alternative approaches, such as enzyme-linked immunosorbent assays, antibody-mediated field-effect-transistor devices, and aptamer-based fluorometric assays,<sup>(18-22)</sup> require expensive antibody-mediated reactions and complicated labeling steps for signal generation. Thereby, the development of a rapid “one-step” assay for analysis of mucins present in body fluids, tumor biopsy, etc., could enable integration to POC platforms for *in vitro* diagnostics. A key element would be its specific recognition using labeling molecules for adequate signal generation using minimal precursors in order to keep the operation of the device simple, accurate, and specific.

Therefore, an important factor to either use boronic acid template systems for the development of rapid *in vitro* POC assays to detect mucin or track intracellular distribution during therapeutic regime inside cells is to achieve effective tagging with reporter molecules. In this regard, fluorometric markers are promising because of their fast response and sensitivity and, hence, are widely used in the detection of biomolecular analytes and bioimaging. Although fluorescence labeling is a daunting challenge with respect to small molecules like phenylboronic acid, it is mostly favored and considered to be advantageous because of its applications in theranostics.

Among fluorescence reporters, organic dyes had been a choice for decades in fluorescence-based studies, but their applications in biological experiments are limited because of their low photostability, toxicity (in certain cases), and poor solubility in water.<sup>(23)</sup> Nanomaterials like quantum dots, C dots, etc., although a viable option, often require either high-temperature conditions or purification steps and take a long time, and related toxicity concerns arising from the use of heavy metals in the synthesis of quantum dots hinder their extensive usage.<sup>(24-27)</sup> Recently, noble-metal nanoclusters of gold, silver, and copper have emerged as promising candidates for sensing assays and biological applications because of their biocompatibility, photostability, and large Stokes shift.<sup>(28)</sup> However, the majority of available techniques involve the presynthesis of nanomaterials and then require functionalization to achieve effective conjugation with receptors for recognition purposes. This not only introduces an extra step but also increases the possibility of the loss of properties of the nanomaterial or the biological component involved. Instead, the direct use of an as-

synthesized luminescent nanomaterial is preferred, particularly for POC assays, in order to reduce time, cost, and resources and to avoid extra steps. However, such approaches toward developing luminescence-based assays using nanoclusters on small molecules, produced through rapid synthetic routes to detect important cancer biomarker mucins, have not been pursued so far. In addition, the application of the same luminescent probe on small molecules for the specific labelling of cancer cells as well as tumor spheroids along with anticancer activity has not been explored.

In this chapter, a rapid synthetic route of luminescent phenylboronic acid templated gold nanoclusters (PB-Au NCs) to elucidate targeted anticancer therapeutic effects with simultaneous bioimaging and for application in *in vitro* POC diagnostics is reported. For theranostic applications, the PB-Au NCs probe was applied to specifically label (imaging) cancer cells by virtue of luminescence from Au NCs and simultaneously induce therapeutic effects toward cancer cells, resulting from the contribution of a boron component. The penetration and therapeutic efficacy of PB-Au NCs was also studied in the case of multicellular spheroids of HeLa cells to better mimic the tumor environment. The uptake and detailed mechanism of cell death induced by PB-Au NCs were evaluated. Further, the antibacterial potential of PB-Au NCs was explored in order to assess its potential in combating secondary bacterial infections in cancer. Toward diagnostics, we discovered a rapid “one-step” luminescent assay for mucin detection based on its interaction with an indigenously developed PB-Au NC probe and further developed a mobile-phone-based POC device with software for integration of the assay and readout. The specificity of the probe toward mucin resulted in the enhancement of luminescence upon its addition and thereby allowed one to develop a rapid assay to be integrated into a POC device. The overall work is illustrated in **Figure 5.1** which depicts multiple applications of the as-synthesized PB-Au NC probe for mucin detection using a smartphone-based platform, targeted bioimaging, therapeutic activity toward cancer cells, and multicellular spheroids.

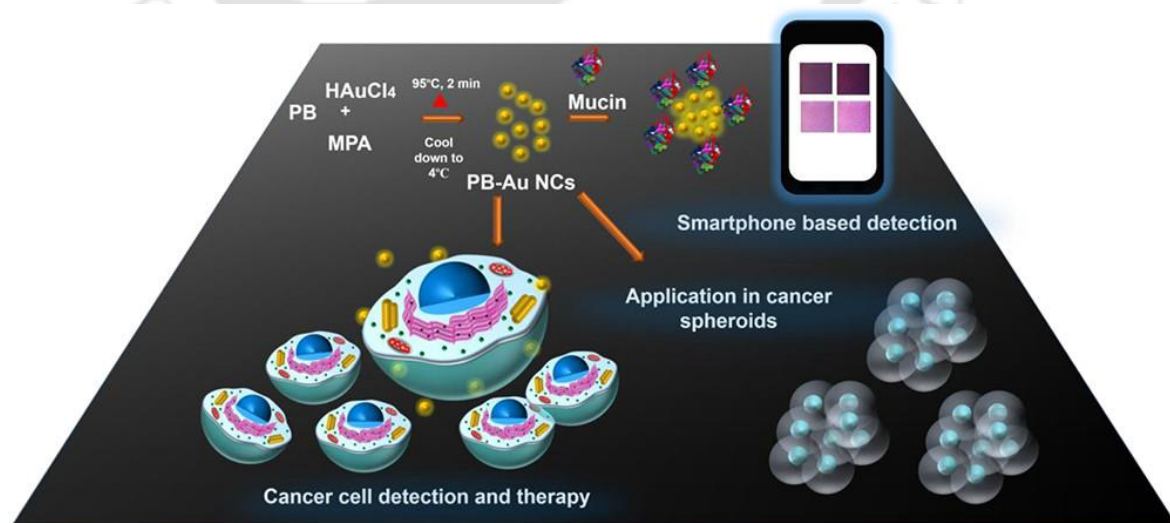


**Figure 5.1.** Schematic representation of the rapid synthesis procedure of PB-Au NCs and their application in targeted cancer cell imaging and therapy as well as smartphone-based mucin detection.

## 5.2. Synthesis and Characterisation of PB-Au NCs

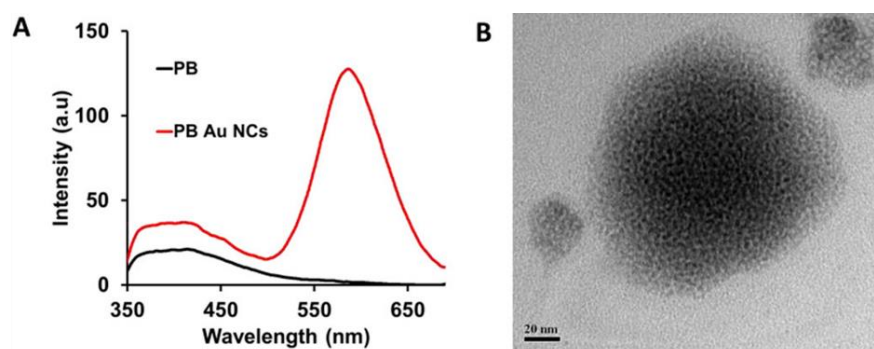


**Figure 5.2.** (A) Luminescence spectra of PB and PB-Au NCs. (B) TEM image of PB-Au NCs at 20 nm scale bar.

The Au NCs synthesized on phenylboronic acid appeared as a colorless suspension. The formation of Au NCs was suggested by the exhibition of luminescence with a peak emission at 580 nm when excited by 300 nm light (**Figure 5.2A**). In addition, SPR signatures corresponding to Au nanoparticles were not observed, indicating no possible contamination or formation of Au nanoparticles (**Appendix D, Figure D5.1a**). The excitation spectrum of PB-Au NCs revealed excitation maxima at around 300 nm (**Appendix D, Figure D5.1b**). TEM images revealed the formation of nanoclusters with an average size of  $2.0 \pm 0.5$  nm (**Figure 5.2B** and **Appendix D, Figure D5.1c**). The QY of the Au NCs was found to be 3.1% with respect to quinine sulfate as the standard. The luminescence decrease rate in the case of PB-Au NCs was found to be 0.73% per min compared to 4.0% per min in the case of standard organic dye rhodamine 6G. This indicated that the hence-prepared PB-Au NCs were more photostable than rhodamine 6G. The matrix-assisted laser desorption/ionization time-of-flight (MALDI-TOF) results revealed a peak at  $m/z$  4764 in the case of PB-Au NCs, which corresponds to  $[\text{Au}_{18}(\text{MPA}_{11}) + 3\text{Na}^+ - 3\text{H}^+]^{3-}$ , suggesting the presence of 18 Au atoms in the core of the metal nanocluster (**Appendix D, Figure D5.2a-d**).

### 5.3. Uptake and Targeting of Cancer Cells by PB-Au NCs

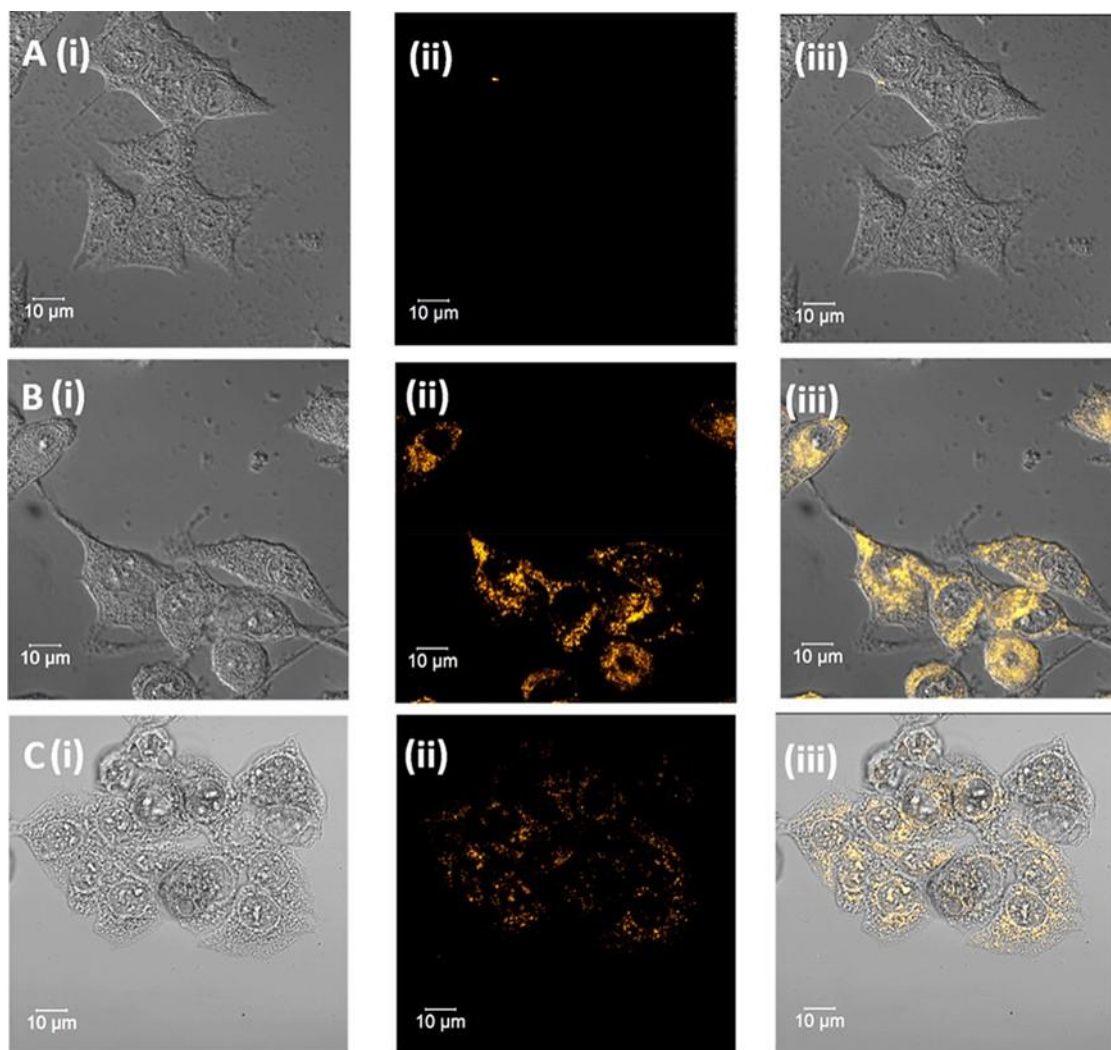


**Figure 5.3.** (A) (i–iii) Bright-field, fluorescent, and merged images of HEK cells treated with PB-Au NCs. (B) (i–iii) Bright-field, fluorescent, and merged images of HeLa cells treated with PB-Au NCs. (C) (i–iii) Bright-field, fluorescent, and merged images of Hep G2 cells treated with PB-Au NCs.

Further, to analyze the potential of PB-Au NCs in targeting cancer cells, HEK, HeLa, and Hep G2 cells were treated with PB-Au NCs. The intracellular uptake of PB-Au NCs was confirmed using confocal microscopy and flow cytometry by monitoring the luminescence of Au NCs present in PB-Au NCs. The results obtained from both of these techniques revealed that the uptake was found to be negligible for the normal cell line HEK and a maximum in the case of HeLa cells and was closely followed by Hep G2 cells (**Figure 5.3A-C** and **Appendix D, Figure D5.3a-c**). The control cells without treatment of PB-Au NCs did not exhibit any fluorescence (**Appendix D, Figure D5.4a-e**). A depth projection of confocal microscopy images of HeLa cells showed internalization of PB-Au NCs in the cells (**Appendix D, Figure D5.5a-d**). To further confirm that PB-Au NCs interact with sialic acid residues on the cancer cell surface, an inhibition assay was performed, where cancer cells

were first reacted with PB alone to block the binding sites and thereafter were treated with PB-Au NCs. The results revealed that, in the case of cells treated with free PB, the uptake was reduced. Thereby, the inhibition assay indicated that the uptake of PB-Au NCs was mediated through the interaction of PB and sialic acid residues on the cancer cell surface (**Appendix D, Figure D5.6a-c**). The semi quantitative real-time polymerase chain reaction of sialyl transferase genes also revealed the overexpression of ST3GALIII (in HeLa and Hep G2) and ST6GALI (in HeLa) compared to the normal cell line HEK, which, in turn, effects the sialic acid expression on the cancer cell surface (**Appendix D, Figure D5.7**).

#### 5.4. Cell Viability and Mechanism of Cell Death

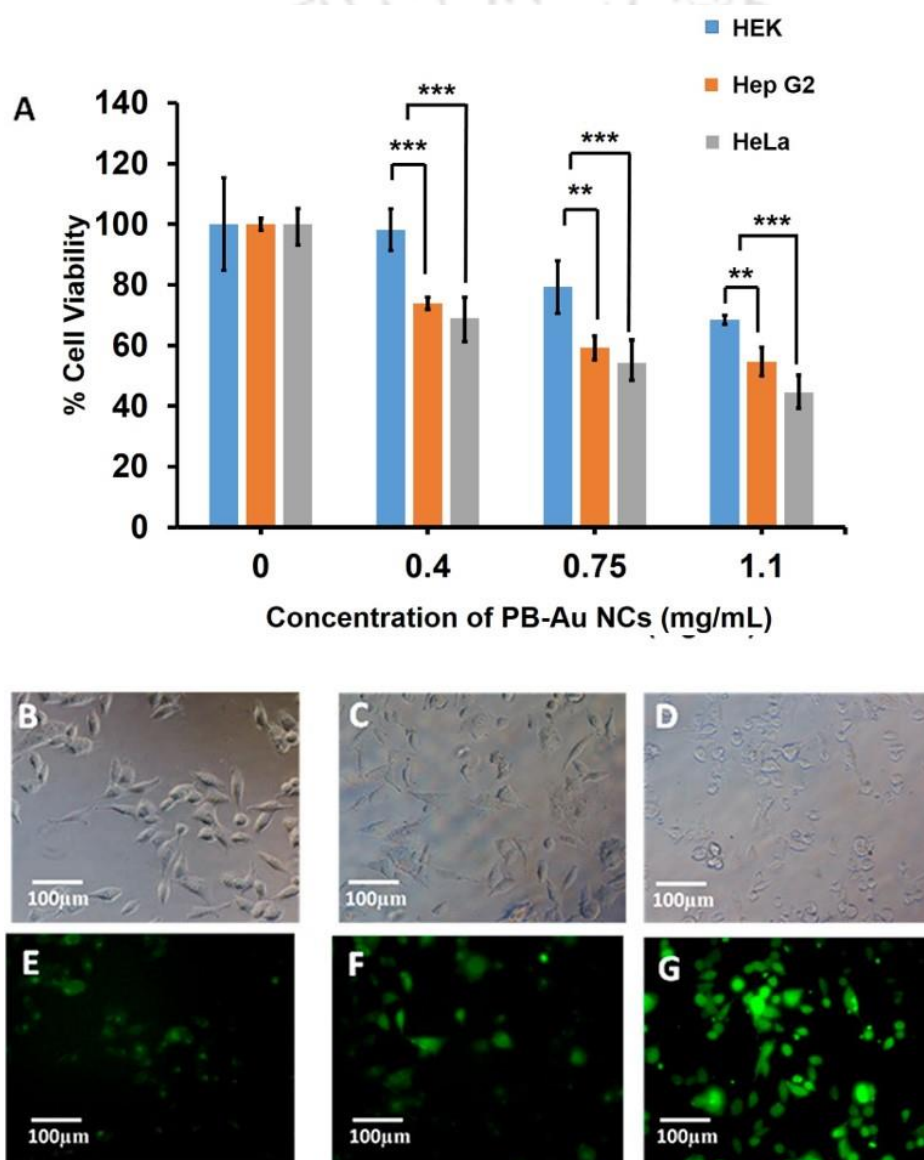


**Figure 5.4.** (A) Cell viability assay of HeLa, HEK, and Hep G2 cells treated with PB-Au NCs. (B–D) Bright-field images of control HeLa cells and HeLa cells treated with PB-Au NCs. (E–G) Fluorescent images of control HeLa cells and HeLa cells treated with PB-Au NCs exhibiting DCF fluorescence. The values are represented as mean  $\pm$  SD of three individual experiments.

Following uptake studies, the therapeutic potential of PB-Au NCs was assessed by MTT assay in all three cell lines. As anticipated, the *in vitro* antiproliferative activity was found to be maximum for the HeLa cells, followed by Hep G2 and HEK. The IC<sub>50</sub> dose was found to be 1.1 mg/mL for HeLa, and the viabilities of the Hep G2 and HEK cells were around 54% and 70%, respectively, at this dose. These results indicated that PB-Au NCs specifically showed therapeutic effects toward cancer cells (HeLa and Hep G2) over normal cells (HEK; **Figure 5.4A**). In addition, the results of MTT assay with free PB treatment alone confirmed that the activity of PB was not significantly affected after the formation of Au NCs (**Appendix D, Figure D5.8a**). For elucidating the mechanism of cell death, further experiments were carried out on HeLa cells because the therapeutic effect of PB-Au NCs was found to be maximum in this case. The generation of high levels of ROS has been identified as an early marker of progression toward apoptosis in most of the cell death pathways, followed by anticancer agents. In this regard, DCFH-DA-based ROS assay was carried out to determine the intracellular ROS levels. The results revealed a higher amount of ROS generation in the case of PB-Au NC-treated cells. This was indicated by the fluorescence intensity (measured at 530 nm emission for DCF fluorescence), which was found to be high in the case of PB-Au NC-treated cells with respect to control cells (**Appendix D, Figure D5.8b**). This was supported by the fluorescence microscopic images of the cells treated with PB-Au NCs, where the intensity was higher in comparison to control cells. The changes in the morphology of the cells were also observed in the corresponding bright-field images of the PB-Au NC-treated cells with respect to control cells (**Figure 5.4B-G**).

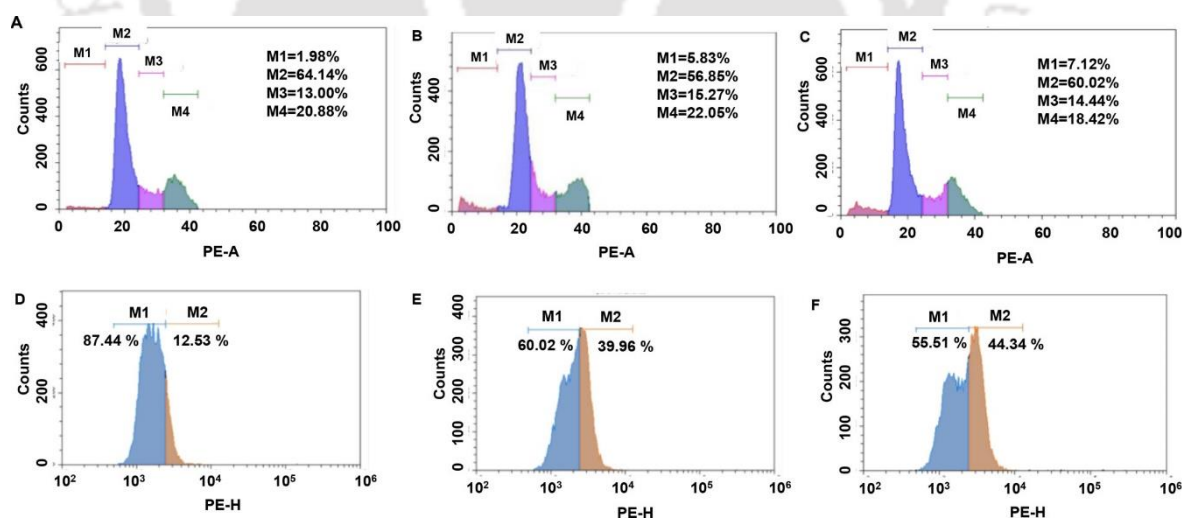


**Figure 5.5.** Cell cycle analysis of (A) control HeLa cells and HeLa cells (B) treated with PB and (C) treated with PB-AuNCs, where M1 = sub G<sub>1</sub>, M2 = G<sub>0</sub>/G<sub>1</sub>, M3 = S, and M4 = G<sub>2</sub>/M. Caspase-3 assay of (D) control HeLa cells and HeLa cells (E) treated with PB and (F) treated with PB-AuNCs, where M1 = active caspase-3 negative and M2 = active caspase-3 positive.

Subsequently, to unravel the effects of PB-Au NC treatment on the cell cycle distribution, cell cycle analysis was carried out using flow-cytometry-based PI assay. This provides vital information related

to the cell death mechanism. The population of cells in the sub-G1 phase, which represents the apoptotic cell population, was found to be more in the case of both PB (5.83%) and PB-Au NC (7.12%) treated cells in comparison to control cells (1.98%; **Figure 5.5A-C**). This indicated a possible apoptosis mode of cell death. This was then confirmed via analysis of the activation of caspase-3, which plays a pivotal role in the downstream of the apoptotic pathway. In caspase-3 assay, an antiCaspase-antibody was used to label caspase-3 produced inside the cells during apoptosis. This assay confirmed a substantial increase in the active caspase-3 positive cells (apoptotic cells) in the case of both PB- and PB-Au NC-treated cells in comparison to control cells (**Figure 5.5D-F**). Hence, all of the above results revealed the targeted theranostic potential of PB-Au NCs (delivering both imaging capabilities and therapy) and can be used for the anticancer treatment regime.

### 5.5. 3D Multicellular Spheroids Culture and Anticancer Activity

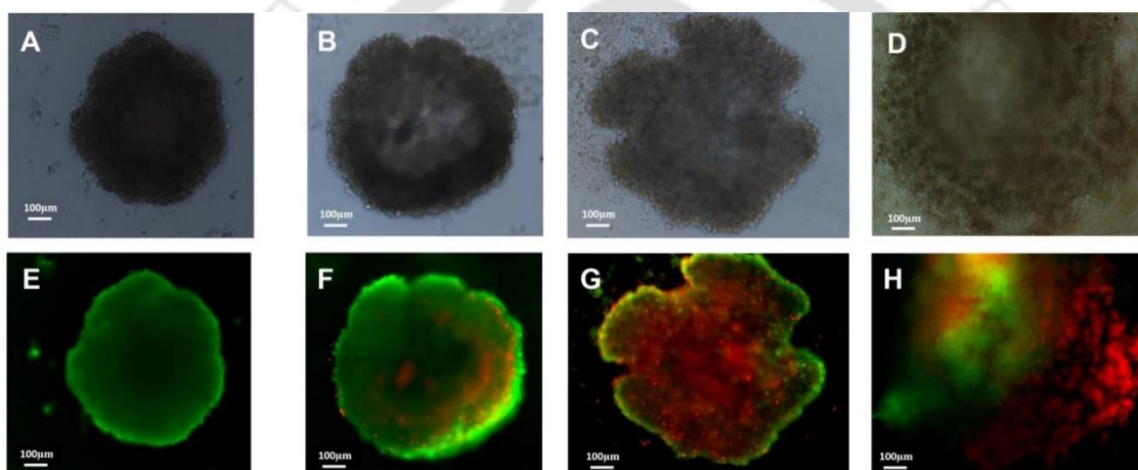


**Figure 5.6** (A–D) Bright-field images of control HeLa spheroids and HeLa spheroids treated with increasing doses of PB-Au NCs (0, 1, 3, and 6 mg/mL) for 24 h and stained with AO–EtBr. (E–H) Fluorescent images of control HeLa spheroids and HeLa spheroids treated with PB-Au NCs (0, 1, 3, and 6 mg/mL) for 24 h and stained with AO–EtBr.

In an attempt to establish the potential application of these nanoclusters in a more realistic solid tumor environment, the penetration capacity and therapeutic activity of the PB-Au NCs were determined using 3D multicellular HeLa spheroids. The *in vitro* spheroid culture of the HeLa cells was established using agarose-coated wells in a 96-well plate, where, with an increase in the number of cells, the sphere diameter was found to increase (**Appendix D, Figure D5.9a-d**). The spheres (before treatment with PB-Au NCs) were stained with AO live cell staining dye, and the depth projection of confocal images revealed the morphology of the stained 3D multicellular spheroid (**Appendix D, Figure D5.10a,b**). Thereafter, the spheres were treated with PB-Au NCs, and the successful delivery of PB-Au NCs into the spheroids was essentially established using confocal microscopy (through luminescence of Au NCs; **Appendix D, Figure D5.11a-c**). The depth projection of the confocal image exhibited uptake of PB-Au NCs inside the spheroids (**Appendix D,**

**Figure D5.11d).** Confocal images of control HeLa spheroids without PB-Au NC treatment did not exhibit any fluorescence (**Appendix D, Figure D5.12a-c**). For evaluation of the therapeutic potential, the spheroids were treated with different concentrations of PB-Au NCs and were analyzed by AO–EtBr (live and dead) assay to identify living (green) and dead (red) cells. At 6 mg/mL PB-Au NCs, the bright-field images showed disintegration of the tumor spheres and the amount of dead cells (represented by red in the double-staining assay) was also found to be maximum at this dose (**Figure 5.6A-H**). These results indicated the successful application of a PB-Au NC probe for labeling and therapeutic response toward multicellular spheroids.

## 5.6. Antibacterial Activity

One of the major causes of death in several cancer patients is the secondary bacterial infection.<sup>(29, 30)</sup> In this context, we evaluated the potential of PB-Au NCs as antibacterial agents. It was found that, for Gram-negative antibiotic-resistant *E. coli*, the MIC was at 0.5 mg/mL and the MBC was at 0.7 mg/mL. For Gram-positive *S. aureus*, the MIC was at 0.8 mg/mL and the MBC was at 1 mg/mL. Further, the growth characteristics of treated and control bacteria were monitored for up to 12 h. The growth was found to be minimum for the MBC and MIC in the case of both Gram positive and Gram negative bacteria (**Appendix D, Figure D5.13a-d**). Hence, it was revealed that PB-Au NCs could show antibacterial properties, which would potentially help in the reduction of secondary bacterial infections in cancer.

## 5.7. Detection of Mucin using Smartphone Based Platform

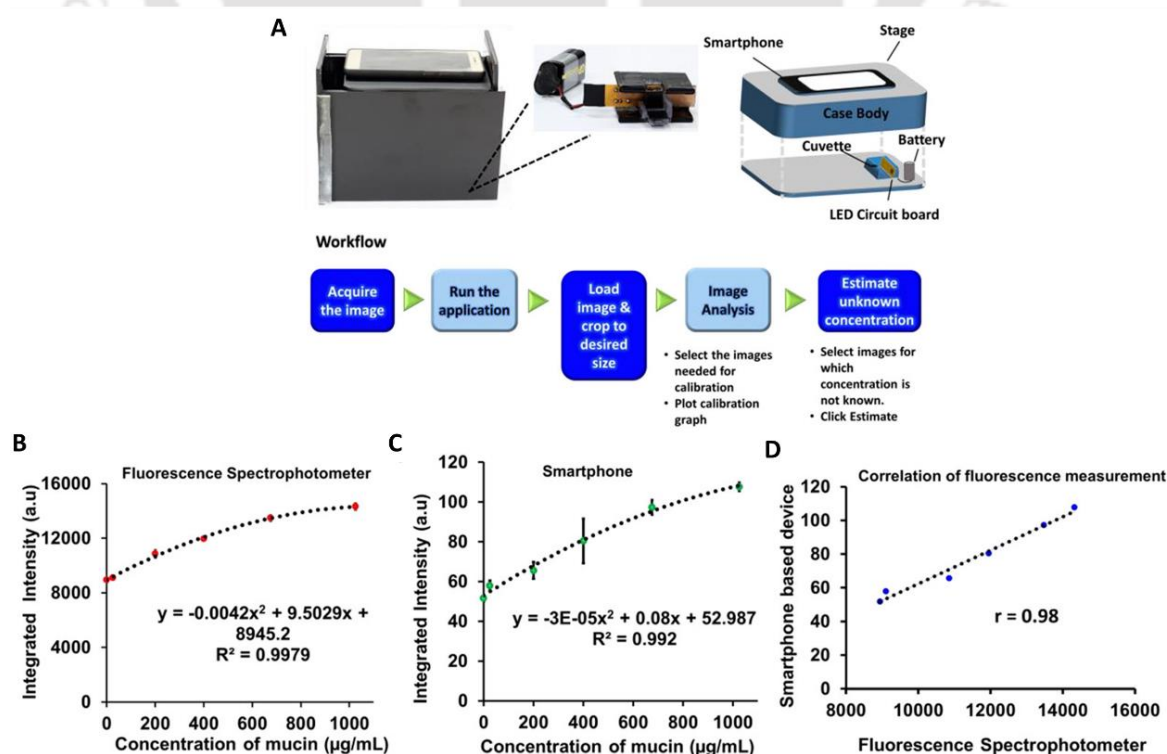


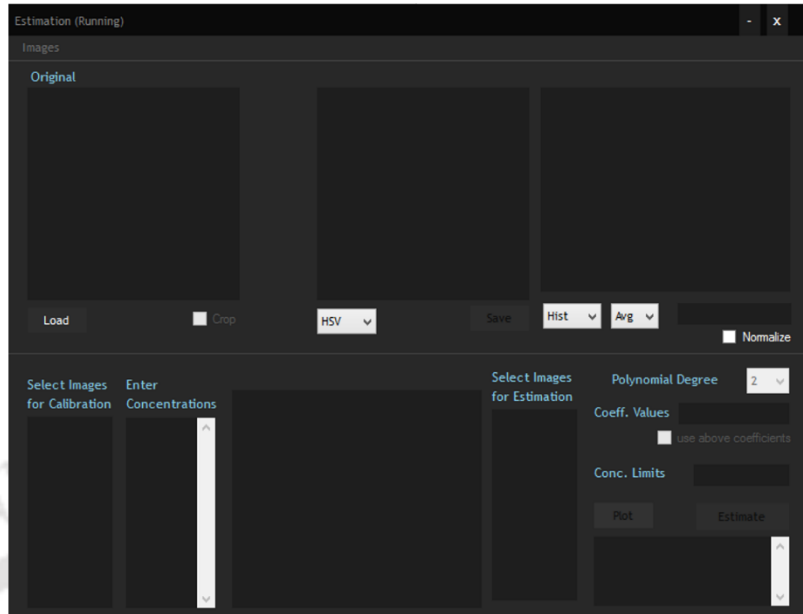
**Figure 5.7.** (A) Smartphone-based device and workflow of the procedure. (B and C) Response of PB-Au NCs with increasing

concentrations of mucin recorded with a fluorescence spectrophotometer and a smartphone-based device. The values are represented as the mean  $\pm$  standard deviation of three individual experiments. (D) Correlation of fluorescence measurement between a fluorescence spectrophotometer and a smartphone-based device.

Interestingly, when the PB-Au NCs were allowed to interact with mucin type III from porcine stomach (examined as a model system for human mucin glycoprotein), it was observed that their interaction could enhance the luminescence intensity. Upon the addition of increasing amounts of mucin to the PB-Au NC probe, the luminescence increased proportionately (**Appendix D, Figure D5.14a**). Also, the increase in the mucin concentration could be detected in terms of the luminescence enhancement of PB-Au NCs when measured in the presence of FBS spiked with mucin (**Appendix D, Figure D5.15a**). Subsequently, the detection of mucin was also carried out in human plasma. The increase in the mucin concentration in terms of the luminescence enhancement was observed in human plasma spiked with mucin. This indicates the potential of using the probe in clinical samples (**Appendix D, Figure D5.15b**). The stability of the PB-Au NC probe was studied in human plasma for up to 24 h. The results revealed the stability of PB-Au NCs in human plasma, and no loss of luminescence was observed for up to 24 h (**Appendix D, Figure D5.15c**). In addition, hemolysis assay indicated the blood compatibility of the PB-Au NC probe because no significant percentage of hemolysis was observed (**Appendix D, Figure D5.15d**). For ascertaining the specificity of these PB-Au NCs toward mucin, other possible interfering analytes such as glucose, trypsin, lipase, HSA, and  $\alpha$ -amyloglucosidase were tested. The luminescence intensity of PB-Au NCs was found to specifically increase with respect to mucin (**Appendix D, Figure D5.14b**). This behavior was possibly due to the interaction between sialic acid moieties on the mucin surface, with the boronic acid template leading to a favorable reduction in the intraparticulate distance between Au NCs, causing an enhanced luminescence effect. This was supported by OD measurements where the interaction between mucin and PB-Au NCs<sup>(31)</sup> marked an increase in the turbidity of the PB-Au NC suspension in comparison to other controls (**Appendix D, Figure D5.15e**). Also, the TEM image after the addition of mucin revealed the presence of aggregation. The possibility of electrostatic interaction was negligible because the  $\zeta$  potentials of both PB-Au NCs and mucin at physiological pH were negative ( $-6.1 \pm 0.16$  and  $-18 \pm 1.4$ , respectively; **Figure D5.16a-d**).

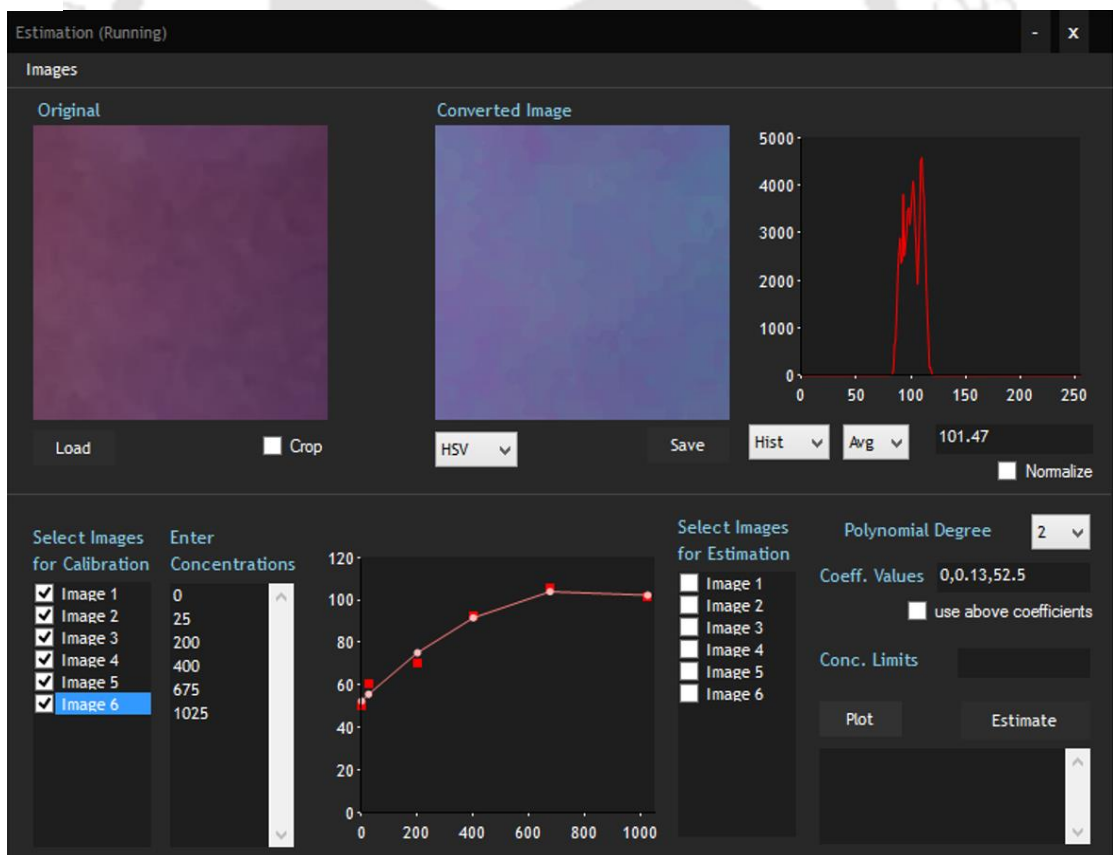
**A**

Single image view with cropping options, represented in different color spaces with related information



Calibration and estimation of samples from images

**B**



C

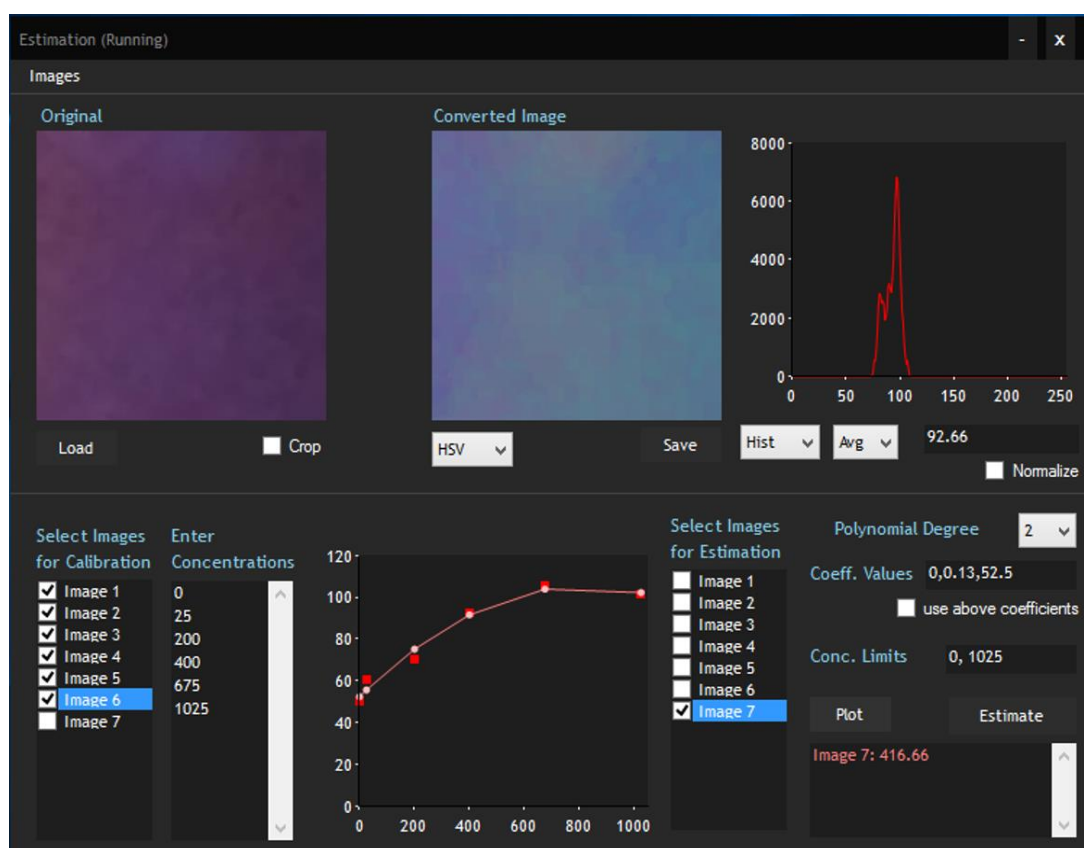


**Figure 5.8.** (A-C) Snapshots of the work flow of the custom designed application.

Upon identification that the simple addition of mucin on the synthesized PB-Au NCs would allow its immediate and specific detection as a virtue of an increase in the luminescence signal, we worked toward the development of a POC platform based on a mobile phone to integrate this assay for the rapid estimation of mucin using the luminescence of Au NCs. Here, the system offers two advantages that are of primary interest for the development of POC assays. First, the synthesis of Au NCs on PB is rapid, involving a simple procedure. Second, changes in the luminescence can be achieved immediately after the addition of mucin. These significantly reduce the time and being a “one-step” procedure requires no additional functionalization steps. The compact device consists of a UV-LED (300 nm) for excitation of the sample in a custom-designed cuvette. The device has a height-adjustable platform to mount the mobile phone at the desired working distance, and its camera is used to acquire images of the emitted light from the sample (in a perpendicular direction to the excitation light source) through the emission filter and lens. A user-friendly software application was developed to obtain intensities of the emitted light and estimate the concentration of the samples through image analysis (Figure 5.7A). Parts A–C of Figure 5.8 shows screen shots of the application developed for performing the fluorometric quantification and the detailed approach followed in this process. To employ the device for mucin quantification, calibration was initially carried out by

acquiring images of luminescent samples of PB-Au NCs after interacting with known concentrations of mucin and analyzing the image intensities by the custom-designed software application. It was found that the obtained intensities and concentrations of mucin (in the range of 0–1000  $\mu\text{g/mL}$ ) were to be best fit with a second-order polynomial. The obtained relation was then compared to that obtained by the standard spectrofluorometer to evaluate its performance. The fluorescence intensity from the standard spectrofluorometer and the concentration of mucin were also found to best fit with a second-order polynomial similar to that obtained by the device. A good correlation was observed between fluorescence measurements with the spectrofluorometer and smartphone-based device with a correlation coefficient ( $r$ ) equal to 0.98. On the basis of the experiments, the detection limit was found to be 25  $\mu\text{g/mL}$ . Alternatively, using the obtained second-order relationships, the limit of detection determined by adding 3 times the standard deviation to the mean of the control sample (with no mucin) was found to be 42.8  $\mu\text{g/mL}$  for the device and 42.7  $\mu\text{g/mL}$  for the standard fluorescence spectrophotometer, which is suitable for detecting mucin concentrations present in body fluids<sup>(32-35)</sup> (**Figure 5.7B–D**). These results demonstrate that the performance of the POC device toward mucin detection is comparable to those of standard fluorescence spectrophotometric techniques. To the best of our knowledge, the time taken for probe development and mucin detection in the present work is the shortest among previously reported methods, which enables it to be a rapid POC assay. In this context, the earlier works report time-consuming probe development techniques, functionalization, and, thereafter, long incubation periods on the sensor surface for reactions to occur.<sup>(36)</sup>

## 5.8. Conclusions

In brief, the work presented a rapid method to develop luminescent Au NCs using a small-molecule phenylboronic acid for simultaneous imaging and therapy of cancer cells (theranostic applications) and to achieve mucin detection. It was demonstrated that the PB-Au NC probe possesses the ability to deliver the simultaneous targeted imaging and therapy of HeLa and Hep G2 cancer cells. This helped in the assessment of the distribution of phenylboronic acid as an anticancer agent inside cancer cells as well as multicellular spheroids. The pathway and mechanism of cell death initiated by PB-Au NCs was studied using flow-cytometry-based assays. Also, the potential antibacterial nature of the PB-Au NCs expands its application in combating possible secondary bacterial infections in some cancers. In addition, the luminescence of PB-Au NC probe enhanced upon its interaction with mucin. This phenomenon led to the development of a fast luminescent assay for mucin detection suitable for integration to POC platforms. Further a cost-effective, portable POC device to detect the luminescence of PB-Au NC probe and estimate mucin was developed. The smartphone-based POC device functions through image-analysis-based methods to carry out the detection of mucin involving a “one-step” procedure. The above findings in the case of cancer cells and multicellular spheroids, along with the blood compatibility and stability of the PB-Au NC probe in human plasma, indicate

the potential applicability of the PB-Au NCs for *in vivo* models and opens up a new paradigm for future work.

## 5.9. References

1. Whyte, G. F.; Vilar, R.; Woscholski, R. Molecular recognition with boronic acids—applications in chemical biology *Journal of Chemical Biology* **2013**, 6 (4) 161–174.
2. Geninatti Crich, S.; Alberti, D.; Szabo, I.; Aime, S.; Djanashvili, K. MRI visualization of melanoma cells by targeting overexpressed sialic acid with a Gd(III)-dota-en-pba imaging reporter *Angew. Chem., Int. Ed.* **2013**, 52 (4) 1161–1164.
3. Matsumoto, A.; Kataoka, K.; Miyahara, Y. New directions in the design of phenylboronate-functionalized polymers for diagnostic and therapeutic applications *Polym. J.* **2014**, 46 (8) 483–491.
4. Deshayes, S.; Cabral, H.; Ishii, T.; Miura, Y.; Kobayashi, S.; Yamashita, T.; Matsumoto, A.; Miyahara, Y.; Nishiyama, N.; Kataoka, K. Phenylboronic acid-installed polymeric micelles for targeting sialylated epitopes in solid tumors *J. Am. Chem. Soc.* **2013**, 135 (41) 15501–15507.
5. Chen, W.; Ji, S.; Qian, X.; Zhang, Y.; Li, C.; Wu, W.; Wang, F.; Jiang, X. Phenylboronic acid-incorporated elastin-like polypeptide nanoparticle drug delivery systems *Polym. Chem.* **2017**, 8 (13) 2105–2114.
6. Liang, Y.; Hua, Q.; Pan, P.; Yang, J.; Zhang, Q. Development of a novel method to evaluate sialylation of glycoproteins and analysis of gp96 sialylation in HeLa, SW1990 and A549 cell lines *Biol. Res.* **2015**, 48, 52.
7. Kannagi, R.; Sakuma, K.; Miyazaki, K.; Lim, K. T.; Yusa, A.; Yin, J.; Izawa, M. Altered expression of glycan genes in cancers induced by epigenetic silencing and tumor hypoxia: clues in the ongoing search for new tumor markers *Cancer Sci.* **2010**, 101 (3) 586–593.
8. Momose, I.; Abe, H.; Watanabe, T.; Ohba, S.; Yamazaki, K.; Dan, S.; Yamori, T.; Masuda, T.; Nomoto, A. Antitumor effects of tyropeptin-boronic acid derivatives: New proteasome inhibitors *Cancer Sci.* **2014**, 105(12) 1609–1615
9. Hattori, Y.; Ishimura, M.; Ohta, Y.; Takenaka, H.; Kirihaata, M. Visualization of Boronic Acid Containing Pharmaceuticals in Live Tumor Cells Using a Fluorescent Boronic Acid Sensor *ACS Sensors* **2016**, 1 (12)1394–1397.
10. Finch, J.; Jinna, S. Spotlight on tavaborole for the treatment of onychomycosis *Drug Des., Dev. Ther.* **2015**, 9, 6185–6190.

11. Trippier, P. C.; McGuigan, C. Boronic acids in medicinal chemistry: anticancer, antibacterial and antiviral applications *MedChemComm* **2010**, 1 (3) 183–198
12. Bradke, T. M.; Hall, C.; Carper, S. W.; Plopper, G. E. Phenylboronic acid selectively inhibits human prostate and breast cancer cell migration and decreases viability *Cell Adhesion & Migration* **2008**, 2 (3) 153–160.
13. Yang, W.; Gao, X.; Wang, B. Boronic acid compounds as potential pharmaceutical agents *Med. Res. Rev.* **2003**, 23 (3) 346–368.
14. Hanaoka, K.; Watabe, T.; Naka, S.; Kanai, Y.; Ikeda, H.; Horitsugi, G.; Kato, H.; Isohashi, K.; Shimosegawa, E.; Hatazawa, J. FBPA PET in boron neutron capture therapy for cancer: prediction of  $^{10}\text{B}$  concentration in the tumor and normal tissue in a rat xenograft model *EJNMMI Res.* **2014**, 4 (70) 1–8.
15. Kufe, D. W. Mucins in Cancer: Function, Prognosis and Therapy *Nat. Rev. Cancer* **2009**, 9 (12) 874–885.
16. Byrne, J. P.; Bhatnagar, S.; Hamid, B.; Armstrong, G. R.; Attwood, S. E. A Comparative Study of Intestinal Metaplasia and Mucin Staining at the Cardia and Esophagogastric Junction in 225 Symptomatic Patients Presenting for Diagnostic Open-Access Gastroscopy *Am. J. Gastroenterol.* **1999**, 94 (1) 98–103.
17. Ullah, E. Mucin Histochemistry in Tumours of Colon, Ovaries and Lung *J. Cytol. Histol.* **2012**, 03 (07) 1–4.
18. Ma, N.; Jiang, W.; Li, T.; Zhang, Z.; Qi, H.; Yang, M. Fluorescence aggregation assay for the protein biomarker mucin 1 using carbon dot-labeled antibodies and aptamers *Microchim. Acta* **2015**, 182 (1) 443–447.
19. He, Y.; Lin, Y.; Tang, H.; Pang, D. A graphene oxide-based fluorescent aptasensor for the turn-on detection of epithelial tumor marker mucin 1 *Nanoscale* **2012**, 4 (6) 2054–2059.
20. Cheng, A. K. H.; Su, H.; Wang, Y. A.; Yu, H.-Z. Aptamer-Based Detection of Epithelial Tumor Marker Mucin 1 with Quantum Dot-Based Fluorescence Readout *Anal. Chem.* **2009**, 81 (15) 6130–6139.
21. Zheng, G.; Patolsky, F.; Cui, Y.; Wang, W. U.; Lieber, C. M. Multiplexed electrical detection of cancer markers with nanowire sensor arrays *Nat. Biotechnol.* **2005**, 23 (10) 1294–1301.
22. Shen, P.; Xia, Y. Synthesis-modification integration: one-step fabrication of boronic acid functionalized carbon dots for fluorescent blood sugar sensing *Anal. Chem.* **2014**, 86 (11) 5323–5329.

23. Zourob, M.; Elwary, S.; Turner, A. P. F. *Principles of Bacterial Detection: Biosensors, Recognition Receptors and Microsystems*; Springer Science & Business Media, **2008**; pp 436– 437.
24. Hardman, R. A Toxicologic Review of Quantum Dots: Toxicity Depends on Physicochemical and Environmental Factors *Environ. Health Perspect* **2006**, 114 (2) 165– 172
25. Zhang, Y.; He, Y. H.; Cui, P. P.; Feng, X. T.; Chen, L.; Yang, Y. Z.; Liu, X. G. Water-Soluble, Nitrogen-Doped Fluorescent Carbon Dots for Highly Sensitive and Selective Detection of Hg<sup>2+</sup> in Aqueous Solution *RSC Adv.* **2015**, 5 (50) 40393– 40401
26. Li, Z.; Yao, W.; Kong, L.; Zhao, Y.; Li, L. General Method for the Synthesis of Ultrastable Core/Shell Quantum Dots by Aluminum Doping *J. Am. Chem. Soc.* **2015**, 137 (39) 12430– 12433.
27. Qu, K.; Wang, J.; Ren, J.; Qu, X. Carbon Dots Prepared by Hydrothermal Treatment of Dopamine as an Effective Fluorescent Sensing Platform for the Label-Free Detection of Iron(III) Ions and Dopamine *Chem. - Eur. J.* **2013**, 19 (22) 7243– 7249.
28. Sahoo, A. K.; Banerjee, S.; Ghosh, S. S.; Chattopadhyay, A. Simultaneous RGB emitting Au nanoclusters in chitosan nanoparticles for anticancer gene theranostics *ACS Appl. Mater. Interfaces* **2014**, 6 (1) 712– 724.
29. Cummins, J.; Tangney, M. Bacteria and Tumours: Causative Agents or Opportunistic Inhabitants? *Infect. Agents Cancer* **2013**, 8, 11.
30. Vento, S.; Cainelli, F.; Temesgen, Z. Lung Infections after Cancer Chemotherapy *Lancet Oncol.* **2008**, 9 (10)982– 992.
31. Li, C.; Liu, Z.; Yan, X.; Lu, W.; Liu, Y. Mucin-Controlled Drug Release from Mucoadhesive Phenylboronic Acid-Rich Nanoparticles *Int. J. Pharm.* **2015**, 479 (1) 261– 264.
32. Ehre, C.; Worthington, E. N.; Liesman, R. M.; Grubb, B. R.; Barbier, D.; O’Neal, W. K.; Sallenave, J.-M.; Pickles, R. J.; Boucher, R. C. Overexpressing mouse model demonstrates the protective role of Muc5ac in the lungs *Proc. Natl. Acad. Sci. U. S. A.* **2012**, 109 (41) 16528– 16533.
33. Zhao, H.; Jumblatt, J. E.; Wood, T. O.; Jumblatt, M. M. Quantification of MUC5AC protein in human tears *Cornea* **2001**, 20 (8) 873– 877.
34. Jinnai, M.; Niimi, A.; Ueda, T.; Matsuoka, H.; Takemura, M.; Yamaguchi, M.; Otsuka, K.; Oguma, T.; Takeda, T.; Ito, I.; Matsumoto, H.; Mishima, M. Induced sputum concentrations of mucin in patients with asthma and chronic cough *Chest* **2010**, 137 (5) 1122– 1129.

35. Raynal, B. D. E.; Hardingham, T. E.; Thornton, D. J.; Sheehan, J. K. Concentrated solutions of salivary MUC5B mucin do not replicate the gel-forming properties of saliva *Biochem. J.* **2002**, 362 (2) 289– 296.
36. Wei, W.; Li, D. F.; Pan, X. H.; Liu, S. Q. Electrochemiluminescent Detection of Mucin 1 Protein and MCF-7 Cancer Cells Based on the Resonance Energy Transfer *Analyst* **2012**, 137 (9) 2101– 2106.

Content of the chapter has been reproduced with permission from American Chemical Society (D. Dutta, S.K. Sailapu, A. Chattopadhyay and S. S. Ghosh, ACS Appl. Mater. Interfaces 10, 4, 3210-3218).

## Appendix D

### D.1 Experimental Section

#### Materials and methods

##### Chemicals

HAuCl<sub>4</sub> (Au, 17 wt % in dilute HCl; 99.99%, Sigma-Aldrich), phenylboronic acid (Sigma-Aldrich), mercaptopropionic acid (MPA; Sigma-Aldrich), mucin from porcine stomach type III, bound sialic acid 0.5–1.5%, partially purified powder (Sigma-Aldrich), human serum albumin (HSA; Sigma-Aldrich), trypsin (Sigma-Aldrich), lipase (Sigma-Aldrich),  $\alpha$ -amyloglucosidase (Merck), glucose (Merck), Luria–Bertani broth, brain–heart infusion media, and Milli-Q-grade water (>18 M $\Omega$ /cm; Millipore) were used without any alterations.

##### Synthesis of PB-Au NCs

The synthesis of luminescent Au NCs on phenylboronic acid was a modification of our previously reported method.<sup>(18)</sup> A total of 1 mL of a 12 mg/mL phenylboronic acid solution was taken, and 10  $\mu$ L of 0.11 M MPA and 30  $\mu$ L of 10 mM HAuCl<sub>4</sub> were added to it. The solution was heated to 95 °C for 2 min and rapidly cooled to 4 °C. The sample was then centrifuged at 10000 rpm for 3 min, and pellets were redispersed in water for further use.

##### UV–visible spectroscopy and luminescence measurements

A UV–visible spectrophotometer (Jasco V-630) was used to record the absorbance of all samples. All luminescence-based measurements were carried out using a fluorescence spectrophotometer (PerkinElmer LS55).

### Transmission electron microscopy (TEM)

For TEM analysis, 7  $\mu\text{L}$  of the synthesized sample was drop-cast onto the TEM grid and air-dried. The TEM grid was observed under a transmission electron microscope operating at a maximum accelerating voltage of 200 keV (JEM 2100; JEOL, Peabody, MA).

### Zeta potential measurements

A Malvern Zetasizer Nano ZS was employed for  $\zeta$ -potential measurement.

### Quantum yield (QY) measurements

The QY measurement was done using reference quinine sulfate in a 0.10 M  $\text{H}_2\text{SO}_4$  solution. The equation used for calculation of the QY is as follows:

$$\text{QY} = \text{QY}_r \frac{m}{m_r} \frac{n_r^2}{n^2}$$

Here,  $m$  is the slope of integrated luminescence intensity versus absorbance plot,  $n$  is the refractive index, and subscript  $r$  indicates the reference solution quinine sulfate. The absorbance and luminescence intensity measurements were carried out consecutively one after the other using the same solution. The QY of the standard ( $\text{QY}_r$ ) is 0.54, and the refractive index of water (solvent) is 1.33.

### Cell culture

HeLa (human cervical carcinoma), HEK 293T (human embryonic kidney), and Hep G2 (human hepatocellular carcinoma) cells for cell culture experiments were acquired from the National Centre for Cell Sciences, Pune, India. For culturing cells in a 5%  $\text{CO}_2$  humidified incubator at 37  $^\circ\text{C}$ , Dulbecco's modified Eagle's medium, supplemented with L-glutamine (4 mM), penicillin (50 units/mL), streptomycin (50 mg/mL, Sigma-Aldrich), and 10% (v/v) fetal bovine serum (FBS; PAA Laboratories, Austria), was used.

### Confocal microscopy

For experiments in confocal microscopy,  $1 \times 10^5$  HeLa, Hep G2, and HEK cells were seeded on coverslips in 35 mm culture dishes and grown in a 5%  $\text{CO}_2$  humidified incubator (37  $^\circ\text{C}$  for 24 h). Thereafter, the cells were treated with PB-Au NCs for 4 h. The treated cells were fixed using 0.1% formaldehyde and 70% chilled ethanol. The coverslips were mounted on glass slides, and the ends were sealed. Control samples without treatment with PB-Au NCs were prepared in a similar manner. The samples were observed (at excitation 405 nm) under a Zeiss LSM 880 microscope. For a sialic acid inhibition experiment, the cells were treated with free phenylboronic acid (7 mg/mL) prior to treatment with PB-Au NCs.

### MTT assay

For assessment of the cell viability,  $1 \times 10^4$  HeLa, Hep G2, and HEK cells/well were seeded in a 96-well plate and cultured overnight (37 °C for 24 h) in a 5% CO<sub>2</sub> humidified incubator. The cells were treated with PB and PB-Au NCs for 24 h, and thereafter MTT assay was carried out. MTT is reduced by mitochondria in living cells into colored formazan. Thus, absorbance at 570 nm reveals the amount of formazan product, which directly relates to the number of live cells. The absorbance at 690 nm was subtracted (background interference). The percent of cell viability was calculated as

$$\% \text{ viable cells} = \frac{(A570 - A690) \text{ of treated cells}}{(A570 - A690) \text{ of control cells}} \times 100$$

### Uptake and activity in 3D multicellular spheroids

Multicellular spheroids of HeLa cells were formed by seeding cells into low attachment wells of a 96-well plate. The low attachment was achieved by casting a layer of 0.8% agarose onto the wells. The spheroids were then subjected to treatment with PB-Au NCs and analyzed by confocal microscopy to observe internalization of PB-Au NCs. The acridine orange–ethidium bromide (AO–EtBr) double staining was carried out at different doses for analyzing the therapeutic ability of PB-Au NCs.

### Determination of reactive oxygen species (ROS)

For ROS generation studies, HeLa cells were seeded at a density of  $1 \times 10^4$  cells/well in a 96-well plate, grown for 24 h, and then treated for 3 h with PB-Au NCs. After the treatment, the cells were incubated for 10 min in 1 mM 2,7-dichlorofluorescein diacetate (DCFH-DA; 5 μL/well; Sigma-Aldrich). The media was discarded, and the cells were harvested and redispersed in fresh media. DCFH-DA, which is a nonfluorescent dye, converts to DCFH through hydrolysis inside live cells. The hence-formed DCFH on oxidation by ROS converts to green fluorescent dichlorofluorescein (DCF). The samples were analyzed using an epifluorescence microscope (Nikon ECLIPSE TS100, Tokyo, Japan) at an excitation wavelength of 488 nm for DCF fluorescence. Also, the fluorescence intensity was measured in a TECAN microplate reader.

### Cell cycle analysis

A propidium iodide (PI)-based staining method was adopted for cell cycle analysis. HeLa cells at a density of  $1 \times 10^5$  cells/well were seeded in 6-well plates, grown, and then treated with PB and PB-Au NCs for 24 h. The media and PBS were collected separately for both the treated and control cell samples. The cells were then harvested by trypsinization, and all of the samples were centrifuged (650 rcf, 6 min). Following this, the cells were fixed under constant vortexing by the slow addition of 1 mL of 70% chilled ethanol and stored at 4 °C. The cells were then centrifuged, washed in ice-cold PBS, and treated with RNase for 1 h at 55 °C. Then 10 μL of PI (1 mg/mL) was added to all of

the samples, and incubation was carried out in the dark at 37 °C for 30 min. The samples were analyzed in a CytoFLEX flow cytometer (Beckman Coulter). PI fluorescence data were recorded for 15000 cells in each sample with the *CytExpert* program (Beckman Coulter) for further analysis.

### **Caspase-3 assay**

For caspase-3 assay, HeLa cells ( $1 \times 10^5$  cells/well; 6-well plates) were grown for 24 h, followed by treatment with PB and PB-Au NCs for 24 h. Both the treated and control cells after trypsinization were fixed in 0.1% formaldehyde for 15 min. The samples were centrifuged at 650 rcf for 6 min, and the pellet was redispersed in PBS. Thereafter, 0.5% Tween 20 was added to the samples and incubated in the dark for 20 min. The cells were washed three times with PBS, and 10  $\mu$ L of PE-conjugated anticaspase-3 antibody was added. After incubation for 0.5 h at 37 °C, the samples were analyzed for PE fluorescence in a CytoFLEX flow cytometer (Beckman Coulter). Fluorescence data for 15000 cells were recorded with the *CytExpert* program (Beckman Coulter) in each sample for further analysis.

### **Antibacterial activity**

For an antibacterial activity test, ampicillin-resistant *E. coli* and *Staphylococcus aureus* were selected as representatives of Gram-negative and Gram-positive bacteria, respectively. Different concentrations of PB-Au NCs were used to determine the minimum inhibitory concentration (MIC) and minimum bactericidal concentration (MBC). The bacteria ( $10^8$  CFUs/mL) were grown in media in the presence of different concentrations of PB-Au NCs for 12 h. The lowest concentration at which there was no visual turbidity was taken as the MIC value of PB-Au NCs. The cultures that lacked turbidity were reinoculated in fresh media to determine the MBC. The lowest concentration of the composite that was bactericidal was taken as the MBC. Bacterial growth was monitored by measuring the optical density (OD) at 595 nm using a UV–visible spectrophotometer.

### **Smartphone/mobile-phone-based system for luminescence measurements**

The mobile-phone-based system for luminescence measurements featured a custom-designed dismountable portable mechanical case with smartphone mounting capability. The case contained a dedicated compartment to accommodate a custom-designed cuvette, a commercially obtained ultraviolet light-emitting-diode (UV-LED) source (300 nm), an optical filter, and a lens. The cuvette ( $1 \times 1 \times 1.5$  cm) holds liquid samples and was properly shielded in such a way as to obstruct the passage of light (except on one side of the lateral wall required for incident light). A battery-powered UV-LED (310 nm) was placed facing the lateral wall of the cuvette to provide a source of excitation for the Au NCs. A stage to mount the mobile phone was set perpendicular to the excitation light source, as shown in **Figure 5.7A**. The emitted light passed through the emission filter (cutoff  $\sim$ 400 nm) and an additional lens (placed between the cuvette and camera) and was imaged with the camera of the mobile phone.

### Software Application for Luminescence Measurements

To analyze the captured images, a software application has been developed using open-source software and image processing libraries, which perform the tasks of image processing, calibration, and estimation of the concentrations of the unknown samples. The working process of the application is as illustrated in the workflow (**Figure 5.7**). In the first step, desired images were selected using the application images for analysis. During this step, selective cropping of the image can be done. In the second step, at least three images (the more, the better) were selected with known concentrations to establish the calibration equation needed for the estimation of unknown samples. After this, estimated concentration values of the selected unknown images are displayed based on the best-fit equation.

The application allows the transformation and display of selected images in different color models with histogram- and intensity-related data of the desired channels. Scatter plots and calibration values along with the fitted graph are displayed in the application with the option to export.

#### Luminescence quantification

With the hand-held POC platform, 24-bit images (ARGB) of the emitted luminescence from various samples were acquired using the mobile-phone camera. A representative  $300 \times 300$  pixel square area in each image was selected and converted to single V-channel image (HSV model). Thereafter, the average intensities of the converted images were acquired. To acquire calibration values, the intensities of the images (whose concentrations are known) were plotted against their concentration values. Thereafter, these values were fit to a second-order polynomial equation. The equation was further used to obtain the concentrations of the unknown samples based on the intensity acquired from the image of the emitted luminescence.

#### Hemolysis assay

To obtain red blood cells (RBCs), 2.0 mL of human blood was centrifuged at 3000 rpm for 10 min. The supernatant was removed, and the RBCs were washed three times with phosphate-buffered saline (PBS). The RBCs were then resuspended in PBS. A total of 20  $\mu$ L of this RBC suspension was added to 80  $\mu$ L of PB-Au NCs (0.4, 0.75, 1.1, and 10 mg/mL). Water and PBS were taken as positive and negative controls, respectively. The samples were incubated at 37 °C for 3 h and thereafter centrifuged at 3000 rpm for 10 min. The supernatant was collected, and the absorbance was measured at 570 nm with the reference as 655 nm. The percentage of hemolysis was calculated by

$$\% \text{ hemolysis} = \frac{(\text{Absorbance of sample} - \text{Absorbance of negative control})}{(\text{Absorbance of positive control} - \text{Absorbance of negative control})} \times 100$$

## D.2 Figures

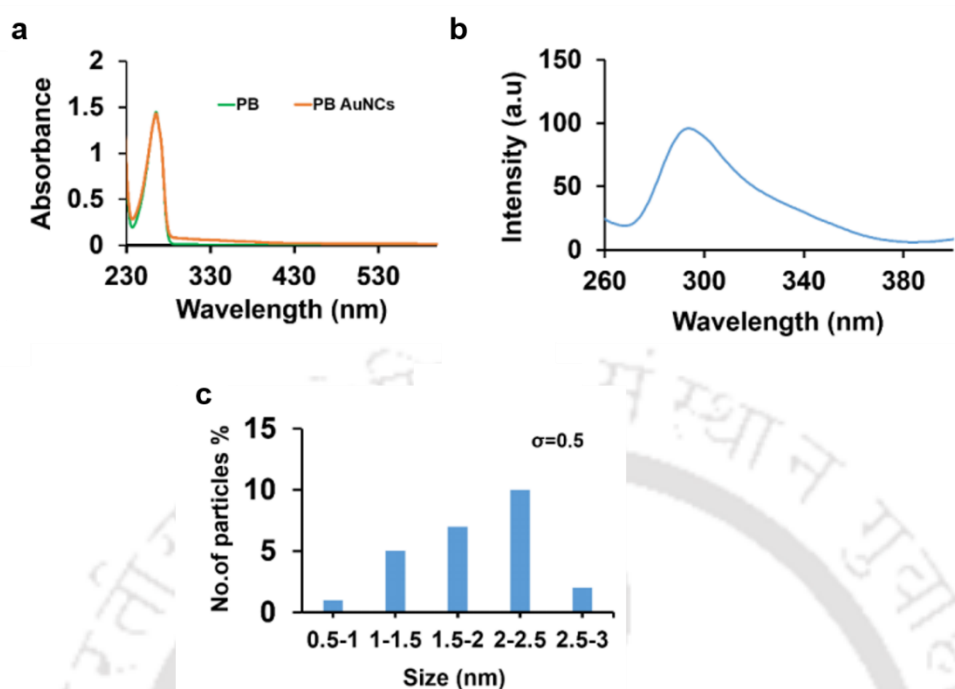


**Figure D5.1.** (a) UV-Visible spectrum of PB, PB-Au NCs. (b) Excitation spectrum of PB-Au NCs. (c) Particle size distribution of PB-Au NCs.

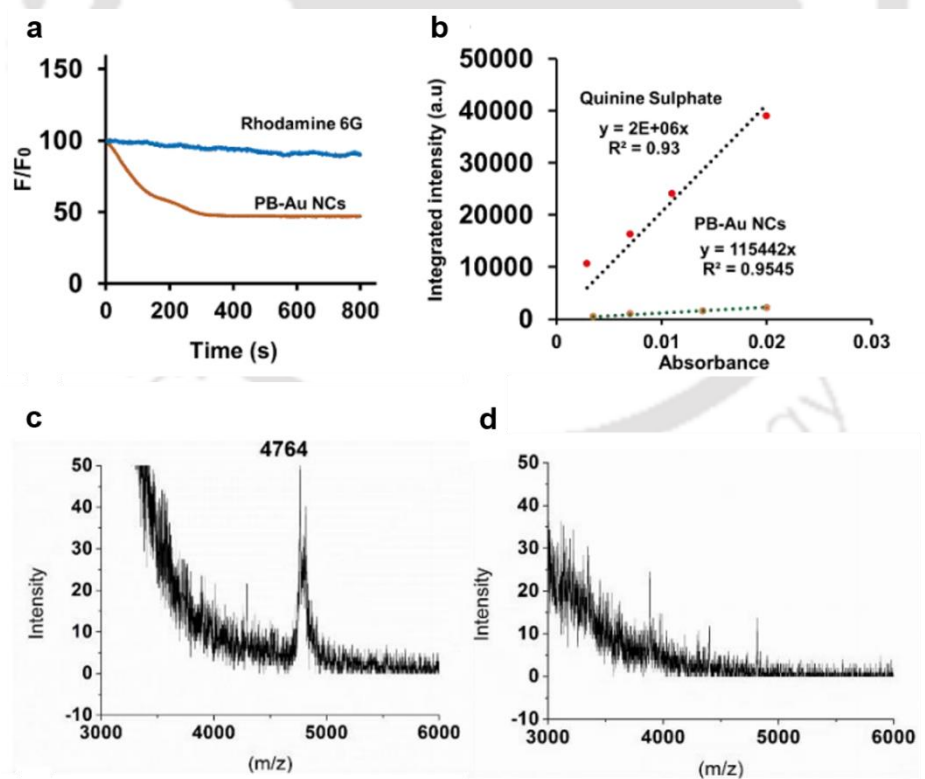


**Figure D5.2.** (a-d) Photo stability, quantum yield, MALDI-TOF of PB-Au NCs, MALDI-TOF of PB.

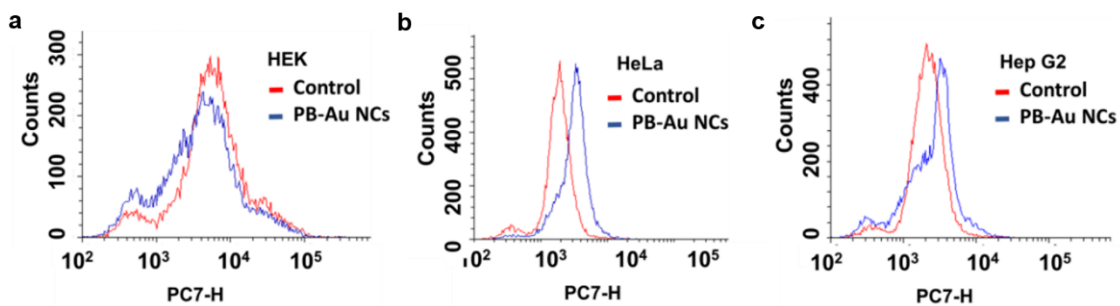


**Figure D5.3.** (a-c) Uptake of PB-Au NCs by HEK, HeLa, Hep G2 cells studied using FACS by tracking the fluorescence of PB-Au NCs.

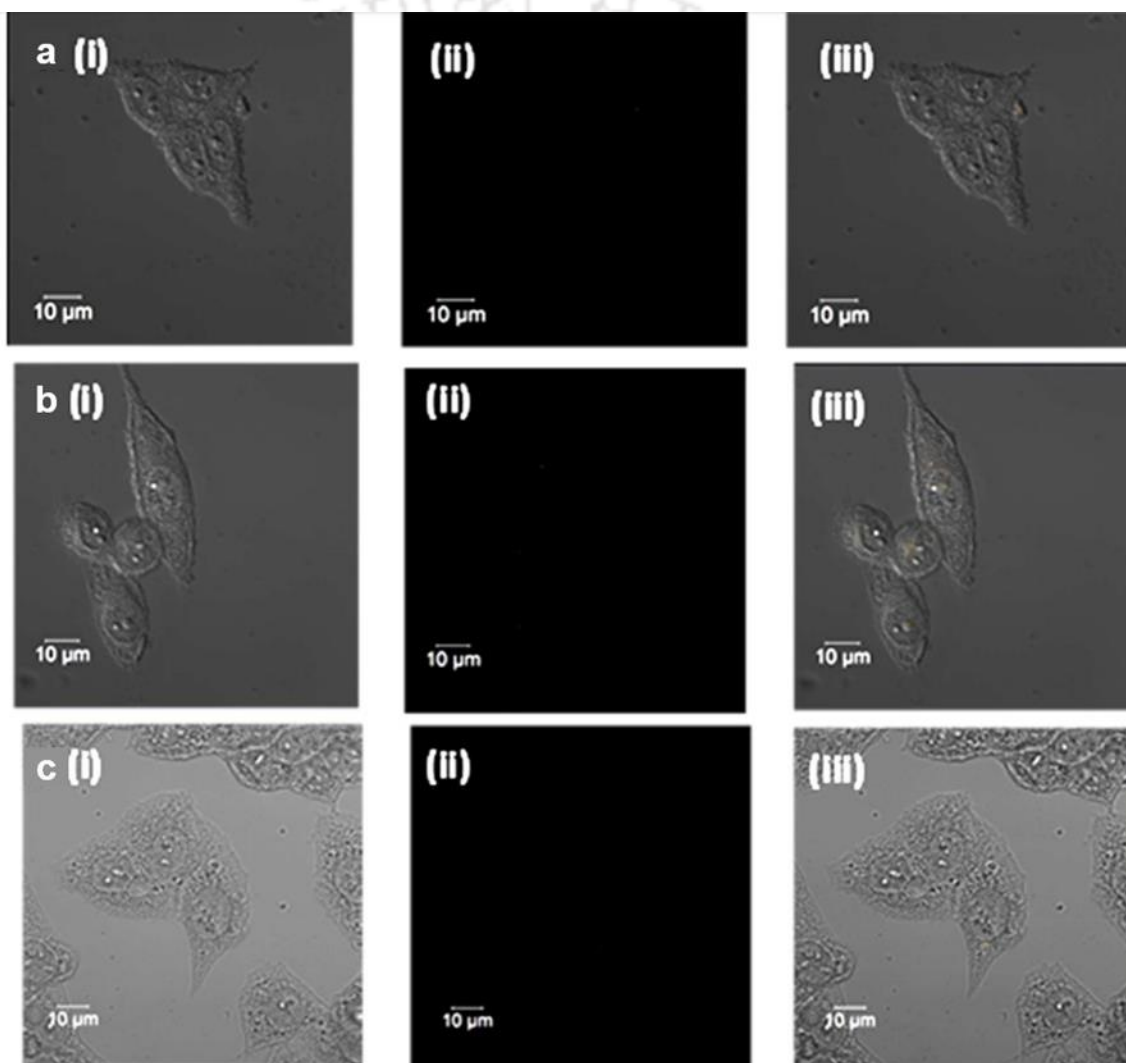


**Figure D5.4.** (a) (i-iii) Bright field image, fluorescent image and merged image of control HEK cells. (b) (i-iii) Bright field image, fluorescent image and merged image of control HeLa cells. (c) (i-iii) Bright field image, fluorescent image and merged image of control Hep G2 cells.

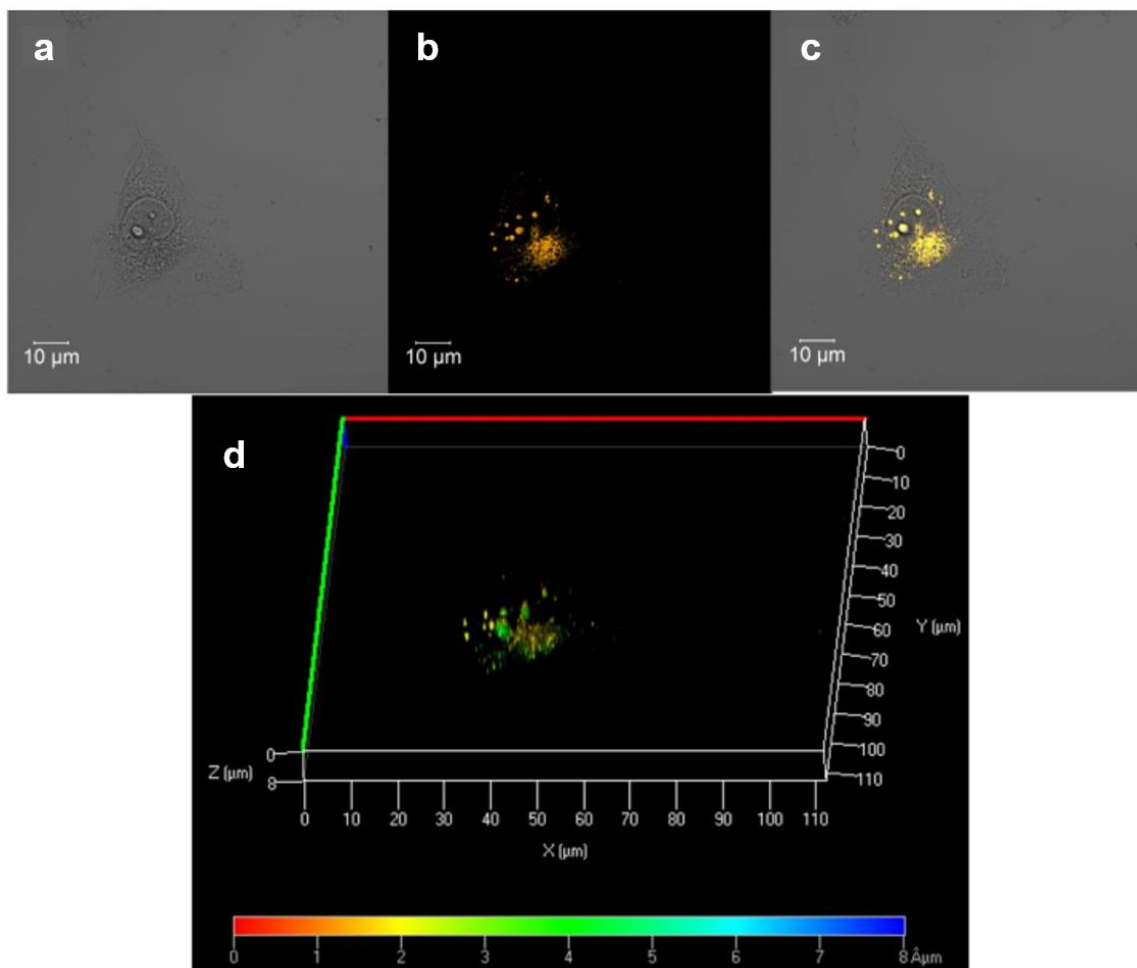


**Figure D5.5.** (a-c) Bright field image, fluorescent image and merged image of HeLa cells treated with PB-Au NCs. (d) Depth projection of confocal microscopy image showing internalization of PB-Au NCs inside HeLa cell.

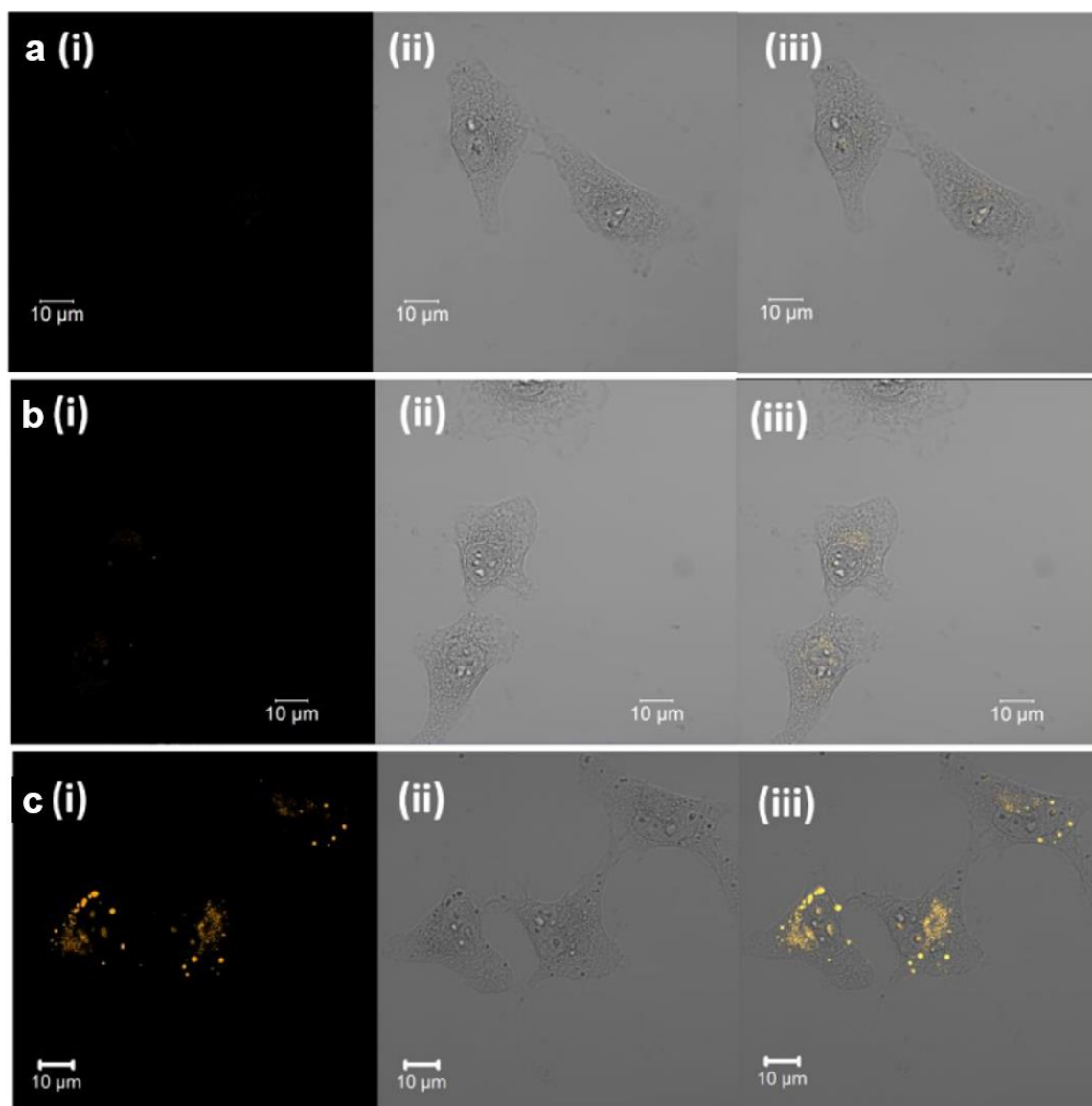


**Figure D5.6.** (a) (i-iii) Fluorescent image, bright field image and merged image of control HeLa cells. (b) (i-iii) Fluorescent image, bright field image and merged image of HeLa cells that were first exposed to free PB and then treated with PB-Au NCs. (c) (i-iii) Fluorescent image, bright field image and merged image of HeLa cells treated with PB-Au NCs.

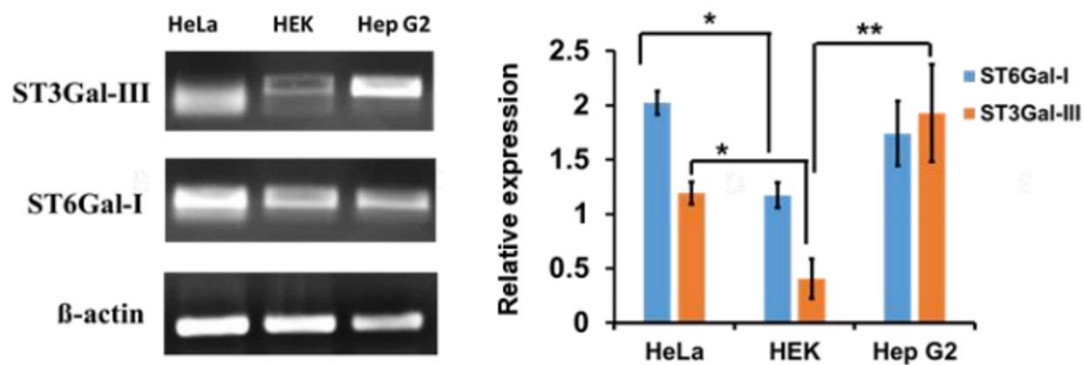


**Figure D5.7.** Semi quantitative RT-PCR of genes ST3GAL-III, ST6GAL-I,  $\beta$ -actin expressed in HeLa, HEK, Hep G2 cell lines.

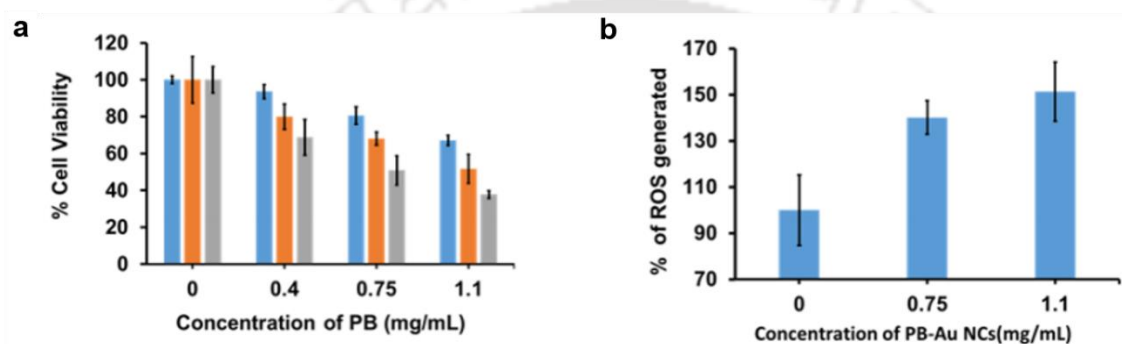


**Figure D5.8.** (a) Cell viability assay of HeLa cells treated with free PB. (b) ROS generation profile of DCFH-DA stained HeLa cells treated with PB-Au NCs in comparison to control HeLa cells.

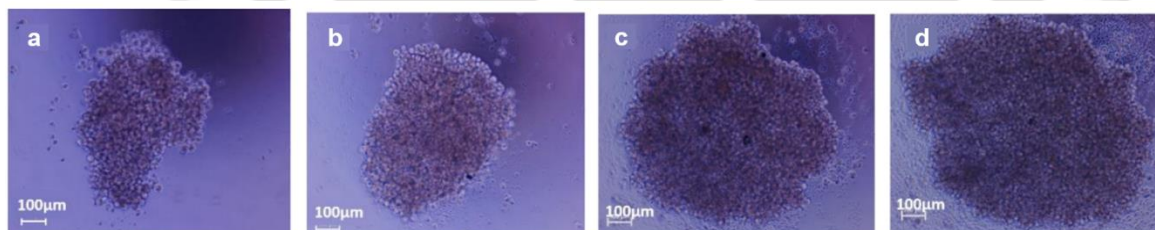


**Figure D5.9.** (a-d) Increasing diameter of HeLa spheroids generated by seeding of increasing number of cells (2000 cells/well, 5000 cells/well, 10000 cells/well, 20000 cells/well).

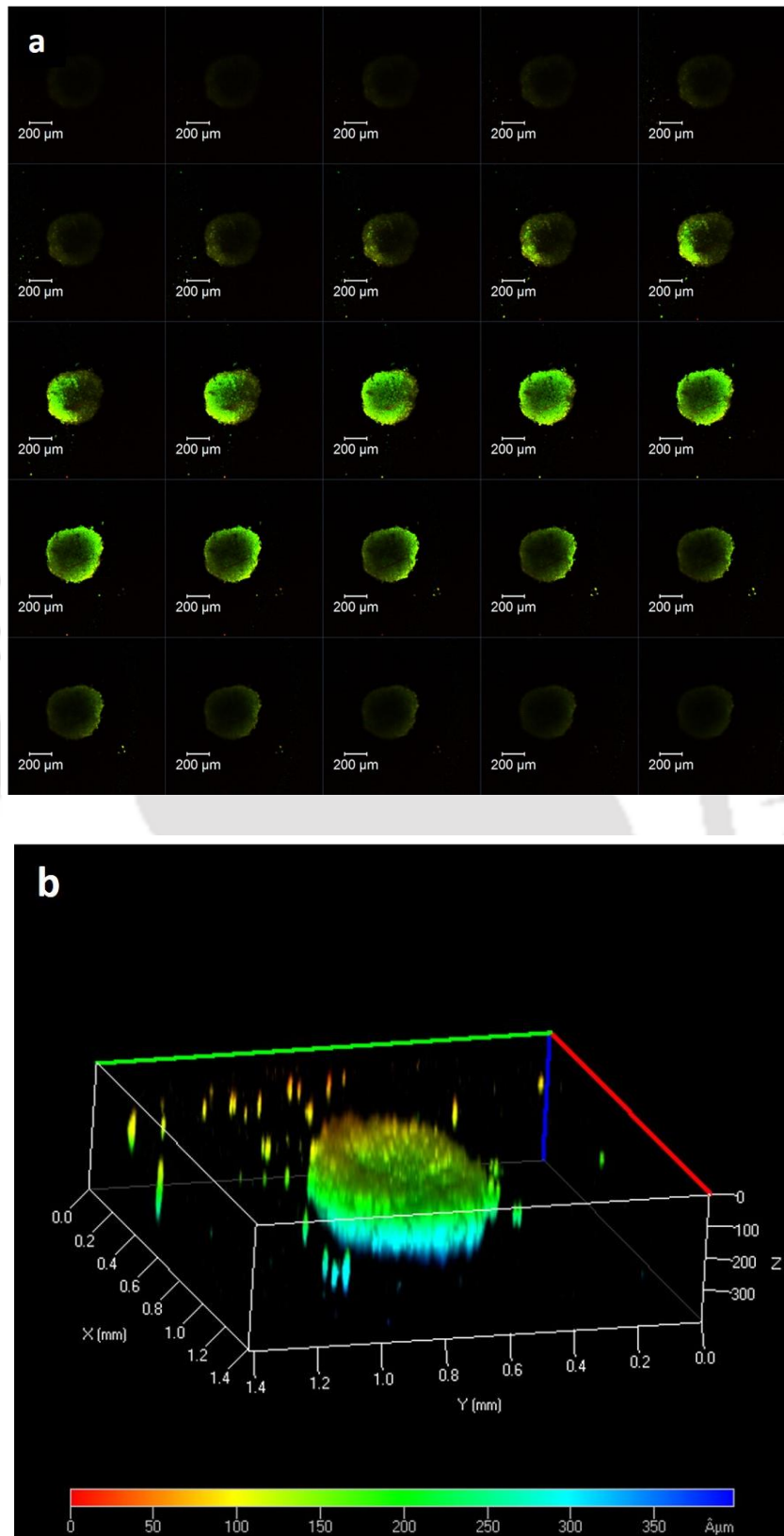


**Figure D5.10.** (a) Z-stack of confocal microscopy image of HeLa spheroid stained with acridine orange. (b) Depth projection of confocal microscopy image.

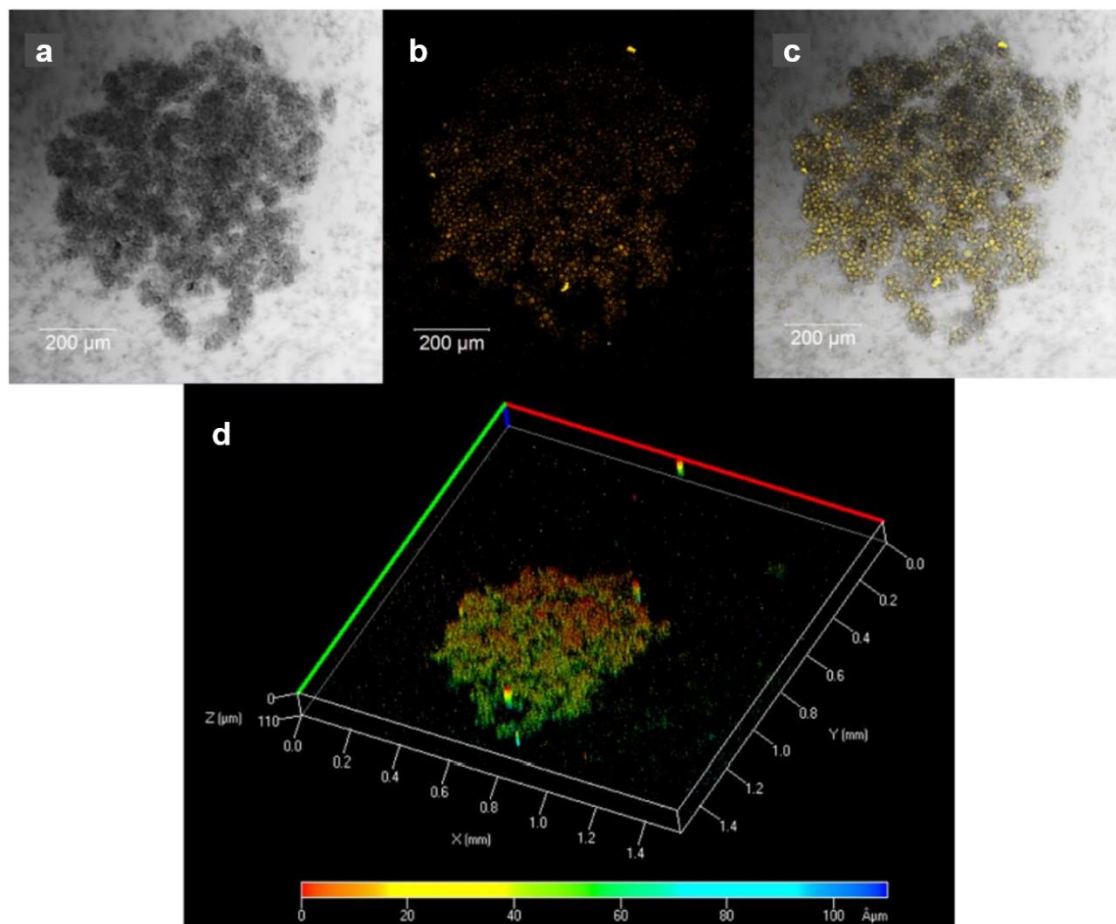


**Figure D5.11.** (a-c) Bright field image, fluorescent image, and merged image of HeLa spheroid treated with PB-Au NCs (6 mg/mL for 4 h). (d) Depth projection of confocal microscopy image of HeLa spheroid treated with PB-Au NCs (6 mg/mL for 4 h).

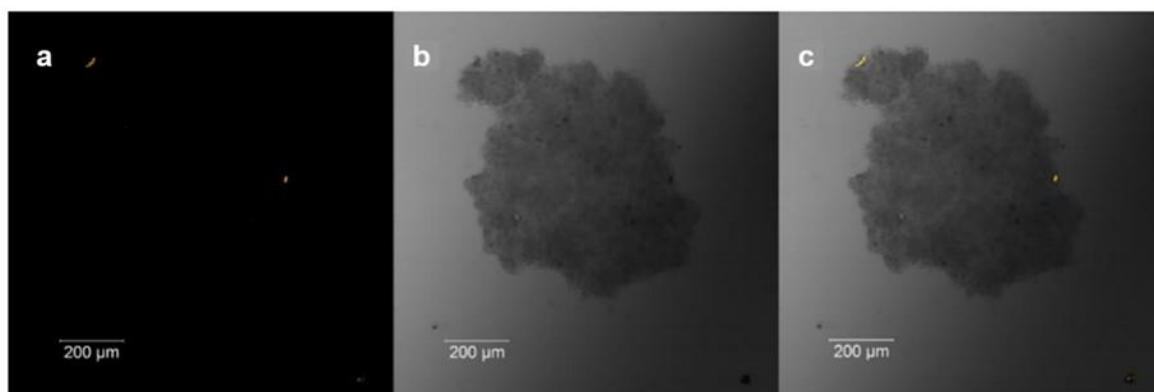


**Figure D5.12.** (a-c) Bright field image, fluorescent image, and merged image of control HeLa spheroid.

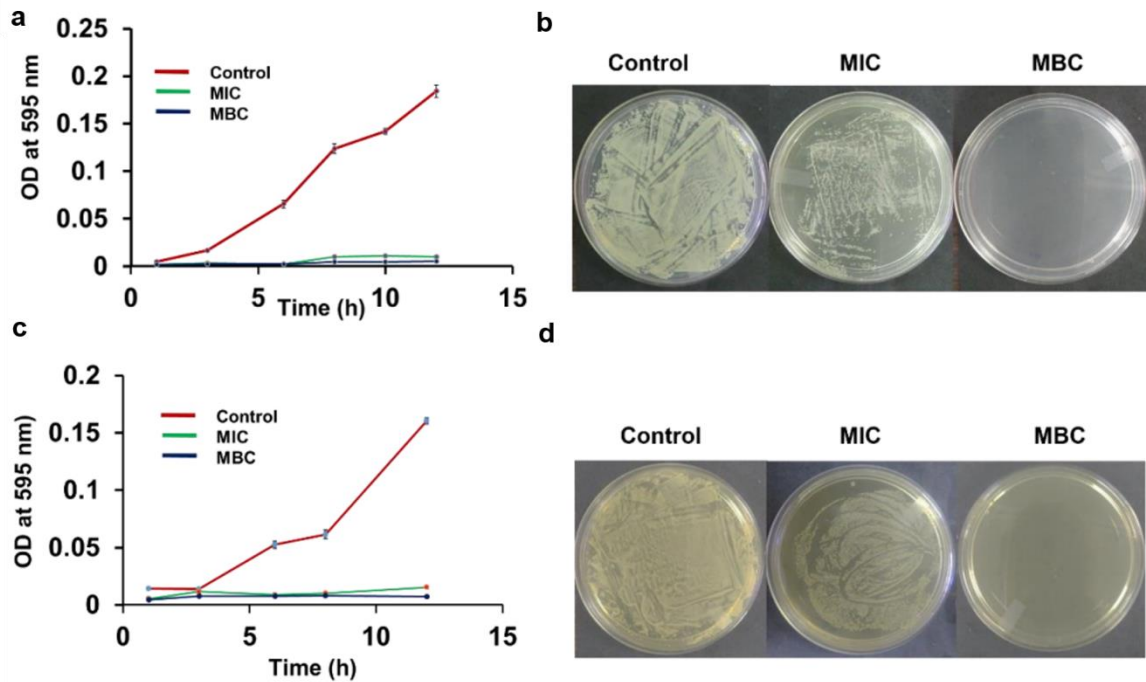


**Figure D5.13.** (a) Growth profile of control *E. coli*, *E. coli* after treatment with PB-Au NCs with MIC and MBC doses. (b) Respective plating images of control *E. coli*, *E. coli* after treatment with PB-Au NCs with MIC and MBC doses. (c) Growth profile of control *Staphylococcus aureus*, *Staphylococcus aureus* after treatment with PB-Au NCs with MIC and MBC doses. (d) Respective plating images of control *Staphylococcus aureus*, *Staphylococcus aureus* after treatment with PB-Au NCs with MIC and MBC doses.

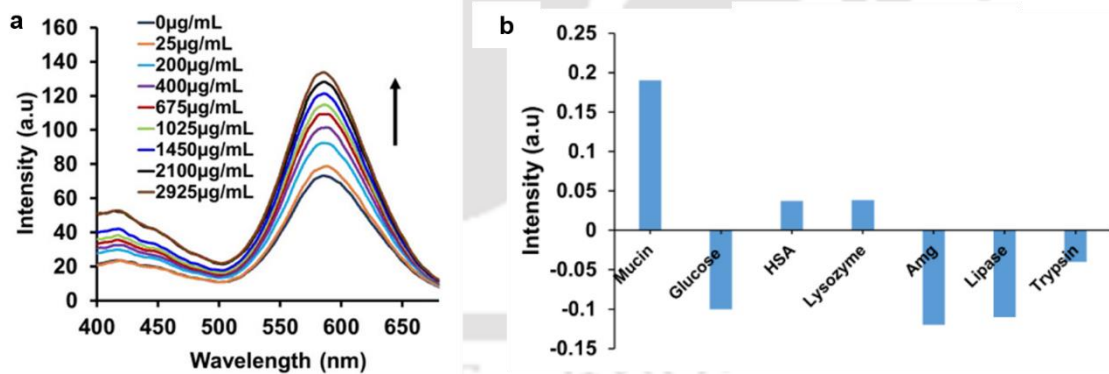


**Figure D5.14.** (a) Luminescence spectra of PB-Au NCs with increasing mucin concentrations. (b) Comparison of effect of various interfering analytes with respect to mucin towards fluorescence of PB-Au NCs.

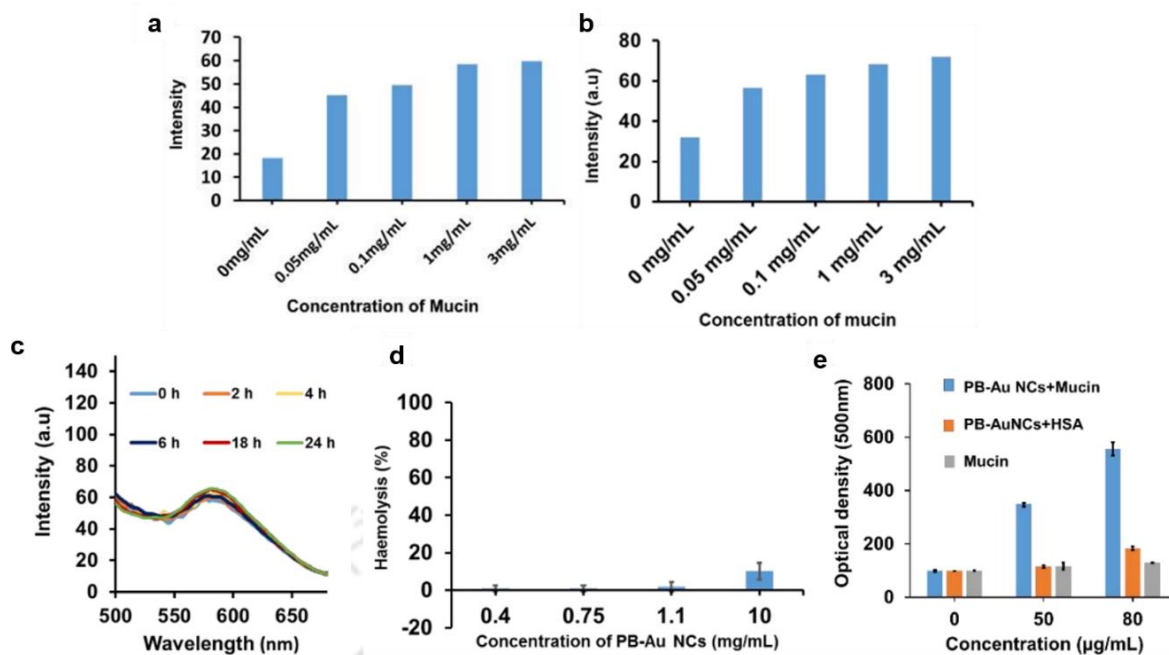


**Figure D5.15.** (a,b) Luminescence intensity of PB-Au NCs in presence of mucin in FBS, luminescence intensity of PB-Au NCs in presence of mucin in human plasma. (c) Stability of PB-Au NCs in human plasma. (d) Hemolysis assay of PB-Au NCs. (e) Change in optical density of PB-Au NCs suspension caused by addition of mucin or HSA.

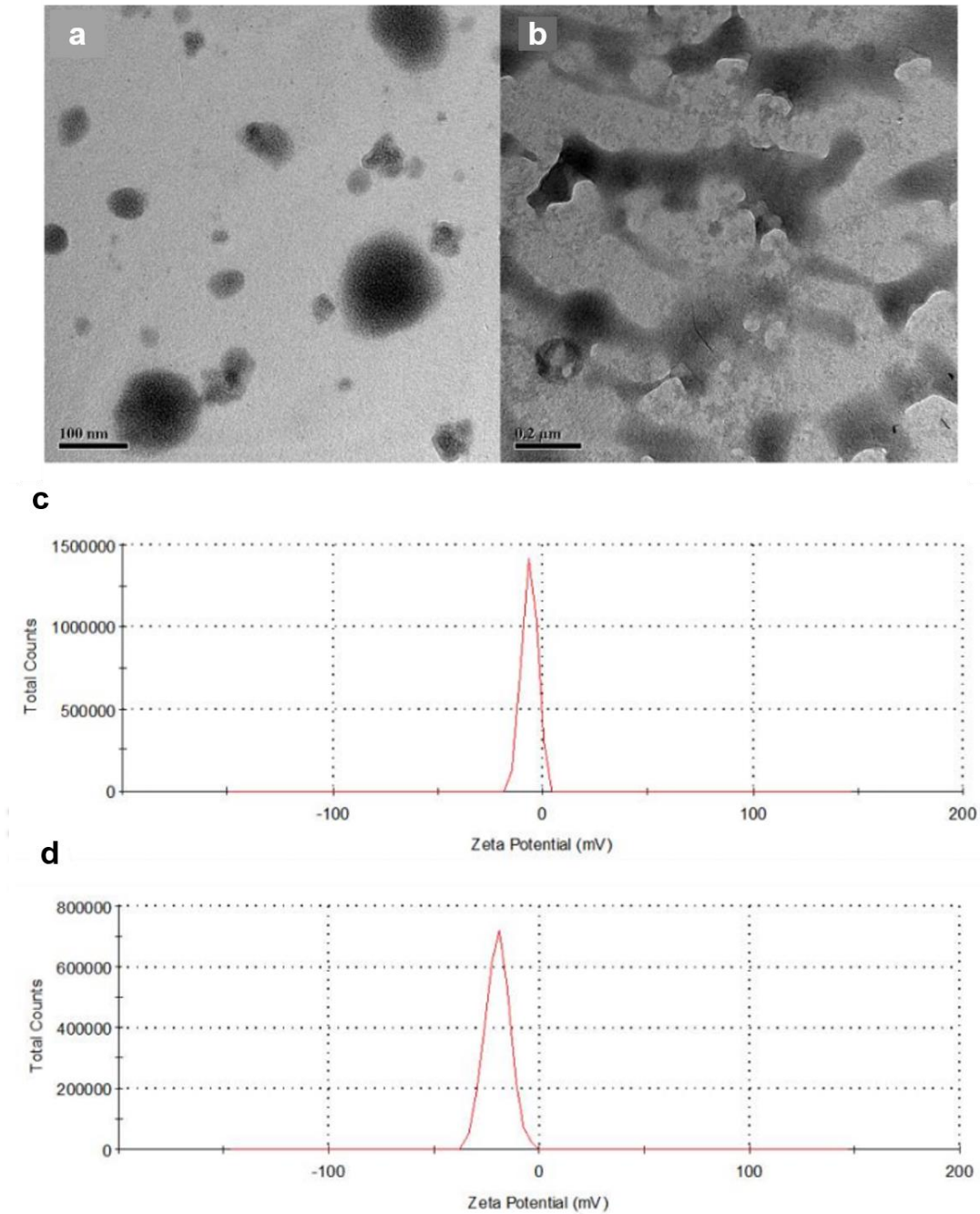
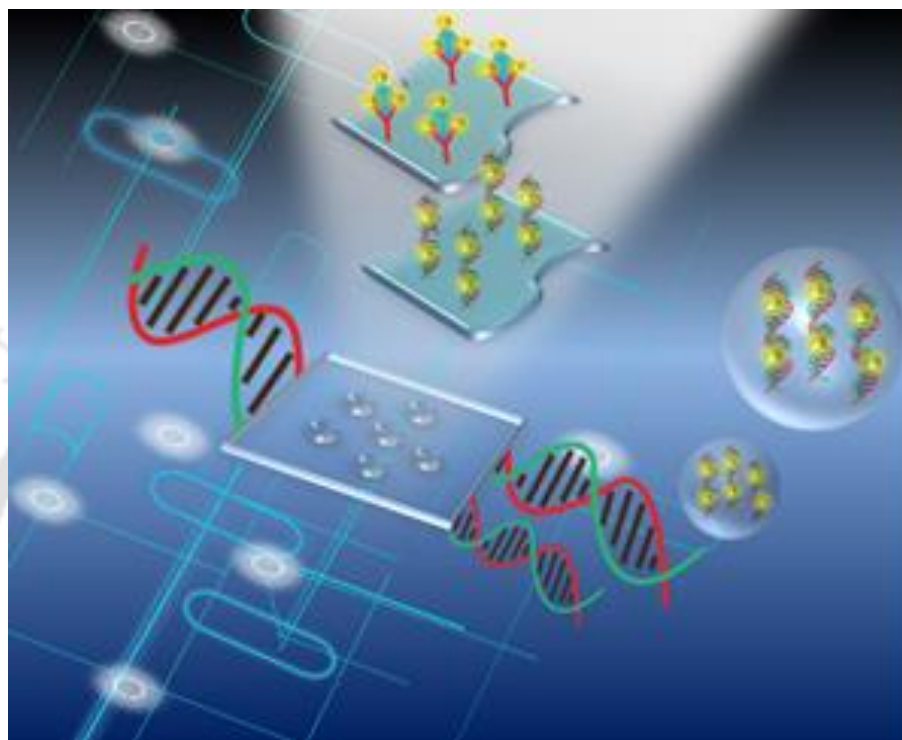


**Figure D5.16.** (A, B) TEM of PB-Au NCs before and after addition of mucin (showing aggregation) respectively. (C, D) Zeta potential of PB-Au NCs and mucin, respectively.



## Chapter 6



### Protein Expression Analyses Using Luminescent Gold Nanoclusters

S.K. Sailapu, D. Dutta, A. Chattopadhyay and S. S. Ghosh, *ACS Omega*  
3, 2, 2119-2129



## Chapter 6

# Protein Expression Analyses Using Luminescent Gold Nanoclusters

**Note:** This work was carried out in collaboration with Dr. Sunil Kumar Sailapu and a portion of the work (gene expression analyses) is a part of his thesis. The custom made bench top device and the principle of synthesis of gold nanoclusters in both the works are the same (or an alternate form of this). The synthesis, characterisation of gold nanoclusters on protein and the protein expression studies is a part of the current thesis.

---

### Abstract

Luminescent gold nanoclusters were employed to carry out protein expression studies using a bench top device. A rapid and easy method to synthesize gold (Au) nanoclusters on protein template was developed. The method of synthesis is versatile and can be applied to different classes of protein. Employing luminescent gold nanoclusters (Au NCs) as the signal generating agents, array-based protein analysis with custom designed user friendly graphical user interfaces is implemented. As proof of concept, the device and methods were applied to further to analyse the expressions of glutathione-S-transferase (GST) and GST tagged human granulocyte macrophage colony stimulating factor (hGMCSF) recombinant proteins purified from bacterial strain of *Escherichia coli* (*E. coli*) BL21(DE3). The rapid diagnosis using luminescence of Au nanoclusters offer potential use in disease diagnostics with a vision to extend health care facilities especially to remote geographical locations.

### 6.1. Introduction

The analysis of proteins can be considered as one of the key elements towards unravelling the molecular basis of human health. Development of new methods and devices for the analyses is important, not only for encouraging faster and sensitive detection techniques but also a broad spectrum of the global populace should be able to benefit from such developments. This can possibly be realised by interdisciplinary research through a combination of conventional molecular biology methods and currently developing fields like nanophotonics. Recent developments, in the field of proteomics, have helped to decode vital information from DNA in terms of expressed proteins in order to predict possible disease markers and mutations, personalised disease susceptibility and discovery of novel therapeutic moieties.<sup>(1,2)</sup> The analysis of protein expression have been an inevitable part of the above mentioned achievements.<sup>(3,4)</sup> However, the success of these developments have been associated with sophisticated instrumentation and fabrication techniques, complex and multistep analysis, functionalization of the molecules in order to achieve high sensitivity and selectivity.<sup>(5-8)</sup> One of the important techniques that is usually applied for diagnostics is fluorescence based probes for detection of target proteins. Due to high sensitivity fluorometric techniques are

preferred over colorimetric assays, which are avoided essentially due to background. However, use of conventional organic dyes and radioactive isotopes have been limited due to their several drawbacks.<sup>(9)</sup> The conventional organic fluorophores are susceptible to photo-bleaching, photo-blinking and often displays carcinogenicity. Though quantum dots have been used as fluorometric tags in expression studies as better materials, their toxicity is a concern.<sup>(10-12)</sup> Thus, there is a genuine need to develop new fluorescence probes that would address point-of-care diagnosis for easy access by a large population at an affordable cost. It is also worth noting here that most of the diagnostic techniques (for protein detection) adopt initial synthesis of nanomaterial followed by specific functionalization for conjugation with the capture proteins. This particular approach demands extra labor (such as isolation of the probe), processing and thus is time consuming making them not suitable for fast detection. Also, since interaction with biomolecules occurs post nanomaterial synthesis, there lies a possibility that their complete conjugation may be difficult to achieve due to potential of loss of functionality of the capture proteins to some extent. Validation in every step is necessary to certify the functionality, which is vital for subsequent interactions to occur. Few atom luminescent metal nanoclusters are an exciting option as fluorophore due to their salient features including small size, high photostability, low toxicity with respect to other fluorophores, and low photo-blinking.<sup>(10)</sup> Recently, these metal nanoclusters have been applied as luminescent probe for various applications.<sup>(13-17)</sup> Biomolecules such as DNA and proteins have been reported to be capable of directing the synthesis of fluorescent metal nanoclusters. Gold nanoclusters were also reported to be less cytotoxic and have good renal clearance as suggested by in vivo studies. However, extensive applications of these nanoclusters have so far been limited in rapid detection assays involving proteins, due to the requirement of large amount of precursors, longer time period of synthesis, and extensive purification steps.<sup>(18,19)</sup> In addition, in earlier works they report formation of larger sized Au nanoparticles alongside Au nanoclusters which is undesirable in case of luminescence based detection.<sup>20,21</sup>

In the current context, to employ them as signal generating agents for array based protein expression analysis, the synthesis should be rapid, applicable for protein (as direct template) in liquid as well as solid phase. The use of paper based methods for array based analysis avoid the sophisticated and complex fabrication procedure. This makes the whole process simple, less expensive, flexible and disposable, that is favourable for adopting it as an diagnostic assay in remote locations.<sup>(22,23)</sup> The traditional dot blot assays are useful for analysis of small number of samples and are viable alternatives to highly sophisticated micro-array platforms especially in case of first principle analysis. Herein, the synthesis of protein templated luminescent Au nanoclusters (signal generating probe) by a rapid single-step method for array based analysis of multiple proteins is reported as illustrated in Scheme 1. This synthesis of Au nanoclusters can be implemented on protein in solution or purified protein bound to an antibody attached to polyvinylidene difluoride (PVDF) membrane. The method proposed had been applied to evaluate protein expression, clinically important protein glutathione-

S-transferase (GST) and GST tagged human granulocyte macrophage colony stimulating factor (GST-hGMCSF) expressed in *Escherichia Coli* (*E. coli*) BL21 (DE3) was used. The expressions were studied using array based methods on a PVDF membrane as shown in **Figure 6.1A-C**, following purification and capture by an immobilized anti-GST antibody. The results corroborated with conventional sodium dodecyl sulfate polyacrylamide gel electrophoresis (SDS-PAGE).

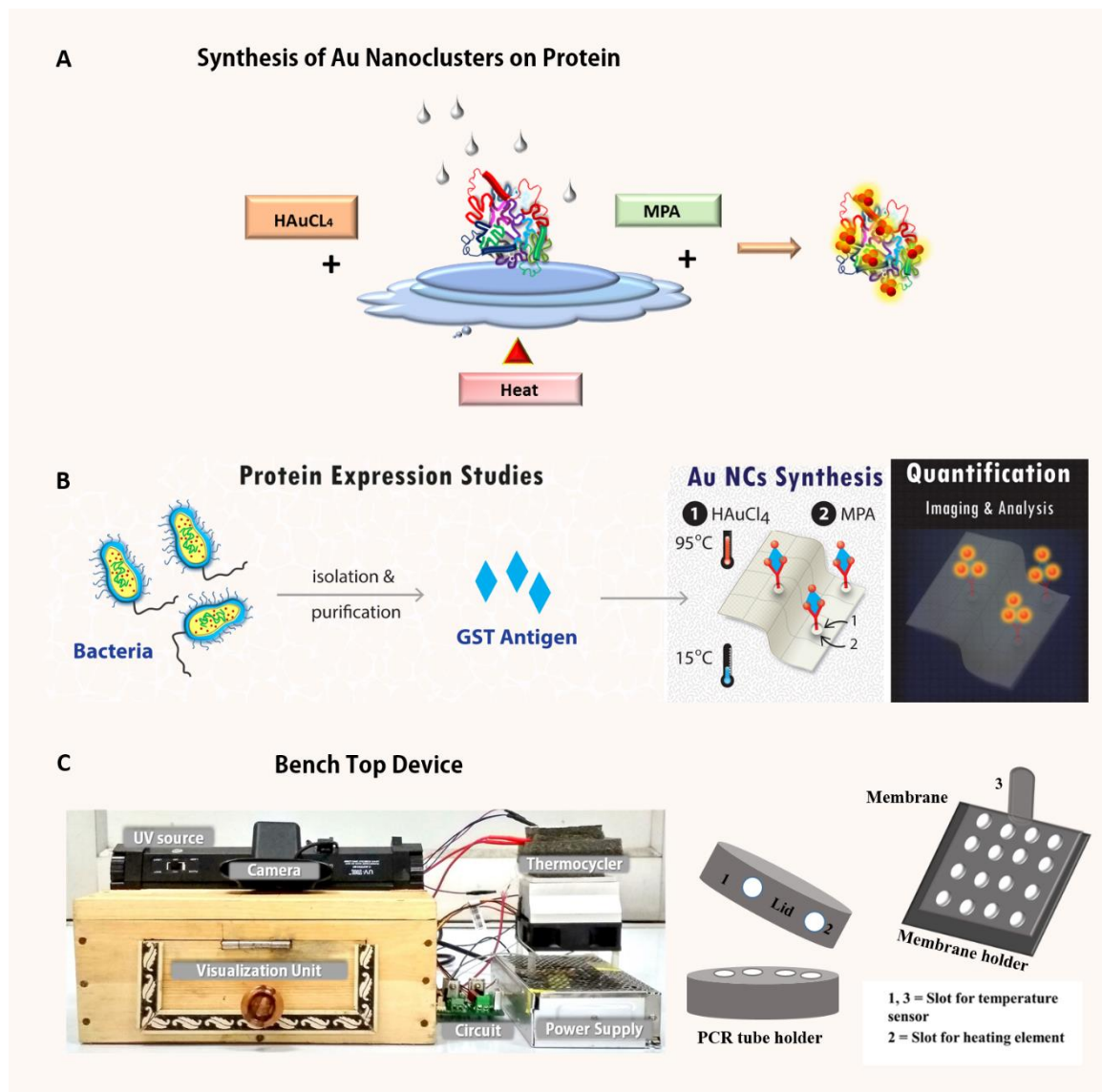


**Figure 6.1.** (A) Synthesis of Au nanoclusters on protein template, (B) Protein Expression Studies: Glutathione-S-transferase (GST) antigens were extracted and purified from *E. coli* BL21 (DE3) bacteria and were spotted on polyvinylidene difluoride (PVDF) membrane containing preimmobilized GST antibodies. Synthesis of Au nanoclusters was carried out on these spots using a single temperature cycle and the membrane was imaged and analysed using a bench top device, (C) Bench top device.

## 6.2. Rapid Synthesis of Au Nanoclusters with Proteins

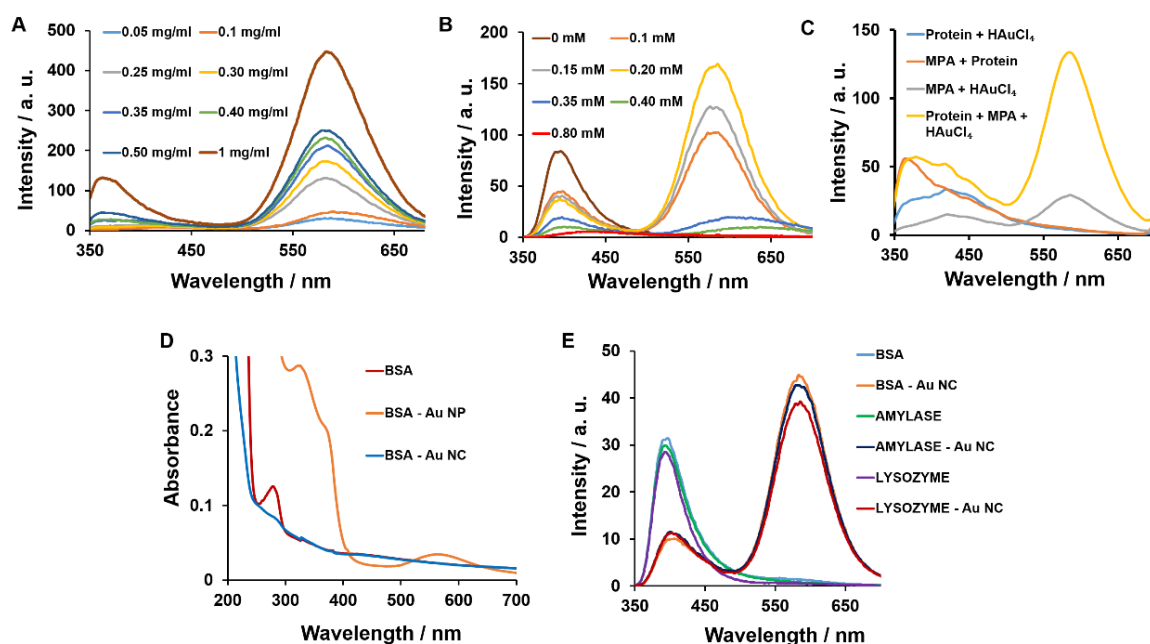


**Figure 6.2.** (A) Luminescence spectra of Au nanoclusters synthesized using different concentrations of BSA with fixed concentration of  $\text{HAuCl}_4$ . (B) Luminescence spectra of Au nanoclusters synthesized with different concentrations of  $\text{HAuCl}_4$  and fixed BSA concentration. (C) Luminescence spectrum of the as-synthesized composite (Au nanoclusters in protein showing the peak emission at 585 nm when excited by 320 nm UV light) and respective controls. (D) UV-Vis spectra corresponding to formation of Au nanoclusters and Au nanoparticles. (E) Luminescence spectra of Au nanoclusters synthesized using various proteins as templates. Excitation wavelength: 300 nm. In the figure, NP stands for nanoparticle; NC for nanocluster.

A novel method of synthesizing Au nanoclusters on protein templates was developed. The synthesis in the presence of proteins involved a single step heating and cooling cycle with precursors. Au nanoclusters were synthesized on bovine serum albumin (BSA) as the template – using  $\text{HAuCl}_4$  and MPA as the precursor reagents - by heating to 95 °C for 2 min and cooling to 15 °C for 3 min in the custom made bench top device (thermal cycler) (**Figure 6.1C**). Au nanoclusters, thus formed emitted luminescence at 580 nm, when excited by 300 nm light. The formation of the nanoclusters was found to be dependent on the amount of protein. Also, the nanocluster synthesis is not specific to particular protein sequence and this has been demonstrated using different classes of proteins. For various proteins the luminescence intensity obtained was not significantly different from one another. The versatility makes this assay applicable to wide range of proteins, which is necessary for diagnostic applications (**Figure 6.2A,E**). With gradual increase in amount of  $\text{HAuCl}_4$  however, the intensity decreases at high concentrations of  $\text{HAuCl}_4$  as there is a formation of Au NPs instead of Au nanoclusters. This was inferred by the decrease in luminescence intensity and the appearance of SPR peak at 580 nm at high  $\text{HAuCl}_4$  concentrations (**Figure 6.2B,D**). The luminescence profile of the

Au nanoclusters for a range of concentrations of protein (BSA) and  $\text{HAuCl}_4$  is shown in **Appendix E, Figure E6.1a,b**. The surface intensity plot (**Appendix E, Figure E6.1a,b**) indicated that the luminescence intensity increased with the amount of  $\text{HAuCl}_4$  (or protein) for a range of concentration of either protein (or  $\text{HAuCl}_4$ ), followed by decrease in the luminescence after a certain concentration. Proteins are a well-known template for nanoclusters synthesis. Herein, they act as a stabilizer by providing steric protection along with MPA (auxiliary small molecule stabilizer) which passivates the Au nanoclusters through  $-\text{S}-\text{Au}$  bond linkages. It could be possible that the clusters were stabilized by both protein and  $-\text{COO}-$  groups of MPA. In addition, MPA also contributed in reduction of  $\text{AuCl}_4^-$  to produce the nanoclusters.<sup>24,25</sup> The fluorescence spectrum of only MPA and  $\text{HAuCl}_4$  showed formation of extremely low intensity Au nanoclusters, while no formation of Au nanoclusters was found in case of only protein and  $\text{HAuCl}_4$ . However, in presence of protein along with MPA and  $\text{HAuCl}_4$ , the intensity of the formed Au nanoclusters were significantly high and also were found to be stable in nature (**Figure 6.2C**).

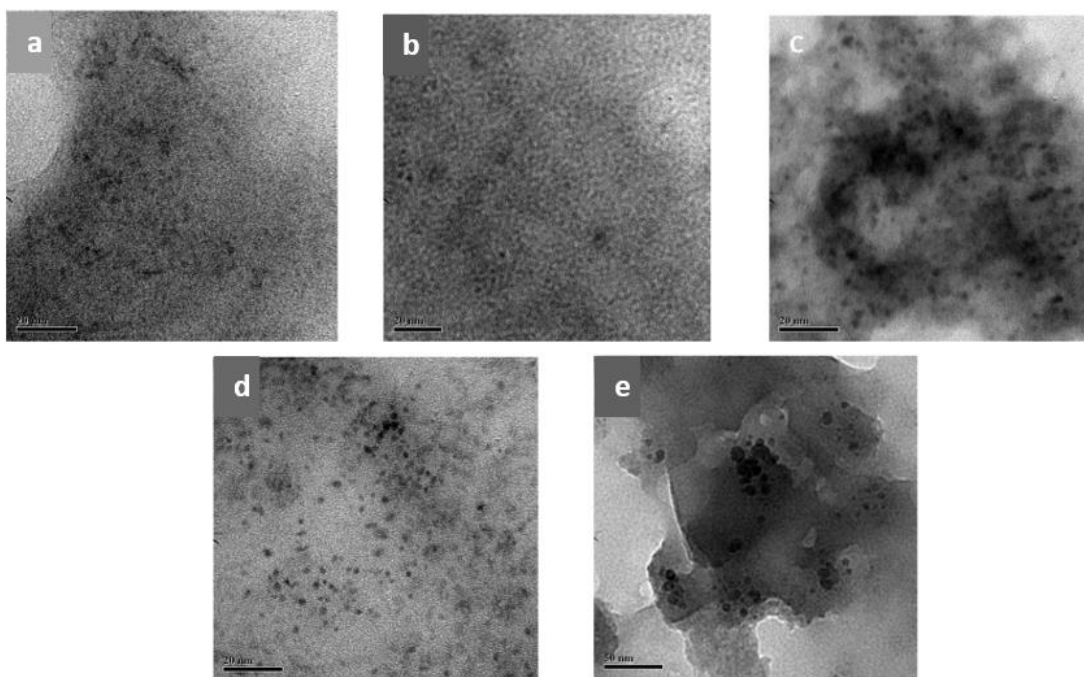


**Figure 6.3.** TEM images of Au nanoclusters synthesized using BSA as template. At lower concentrations of  $\text{HAuCl}_4$ , i.e., at (A) 0.1 mM, (B) 0.15 mM, (C) 0.20 mM, (D) 0.30 mM, Au nanoclusters were formed while use of the higher concentration, (E) 0.80 mM, resulted in the formation of Au nanoparticles.

Transmission electron microscopy (TEM) showed the formation of small particles owing to Au nanoclusters and also indicated an increase in the particle size from  $0.75 \pm 0.27$  nm to  $5.81 \pm 2.05$  nm, with increasing concentrations of  $\text{HAuCl}_4$  (**Figure 6.3A-E**), which corroborated with the luminescence profile and UV-visible analysis discussed above (**Figure 6.2B,D**).

At lower concentrations of  $\text{HAuCl}_4$ , Au nanoclusters were formed with particle size gradually increasing with concentration of  $\text{HAuCl}_4$ . The particle size obtained from TEM analysis was  $0.75 \pm 0.27$  nm,  $1.20 \pm 0.33$  nm,  $1.46 \pm 0.35$  nm for 0.1 mM, 0.15 mM, 0.20 mM of  $\text{HAuCl}_4$  respectively. However, at 0.30 mM, the particle size was about  $1.95 \pm 0.53$  nm and with further increase in  $\text{HAuCl}_4$  concentration led to plasmonic Au nanoparticles with particle size  $5.81 \pm 2.05$  nm at 0.80 mM. Also, circular dichroism (CD) spectroscopy revealed that the formation of Au nanoclusters did not alter the 3D structure of BSA significantly. The CD spectrum of BSA-Au nanoclusters exhibited ( $\alpha$ -helix: 27.8,  $\beta$ -sheet: 15.2; turn 25.1; random coil: 31.8; RMS value: 10.54) with respect to control ( $\alpha$ -helix: 29,  $\beta$ -sheet: 21.5; turn: 19.9; random coil: 29.6; RMS value: 8.14). But in case of Au nanoparticle formation ( $\alpha$ -helix: 0,  $\beta$ -sheet: 55.5; turn: 0; random coil: 44.5; RMS value: 36.63), there was an increase in  $\beta$ -sheet percentage, which generally results when the protein is exposed to harsh conditions (high temperature and the presence of high  $\text{HAuCl}_4$  concentrations in the present case) (**Appendix E, Figure E6.2a-c**). The photoluminescence quantum yield of Au nanoclusters on proteins was found to be 4.5 %, thus making them suitable for sensing applications. Also, when compared to an organic dye rhodamine 6G with luminescence decrease rate of 2.7 % per min, the Au nanoclusters showed a luminescence decrease rate of 0.26 % per min, indicating higher photostability (**Appendix E, Figure E6.3a,b**). The matrix-assisted laser desorption/ionization time-of-flight (MALDI-TOF) analysis (**Appendix E, Figure E6.4a,b**) showed a distinct peak at 71171 (m/z). The m/z difference between BSA and Au nanoclusters is 4350.8 (m/z) favoring possible formation of  $(\text{Au}_{16}(\text{MPA})_{11} + 2\text{Na}^+ - \text{H}^+)^{-1}$  corresponding to a metal cluster with 16 Au atoms.

### 6.3. Application of Au Nanoclusters for Protein Expression Studies

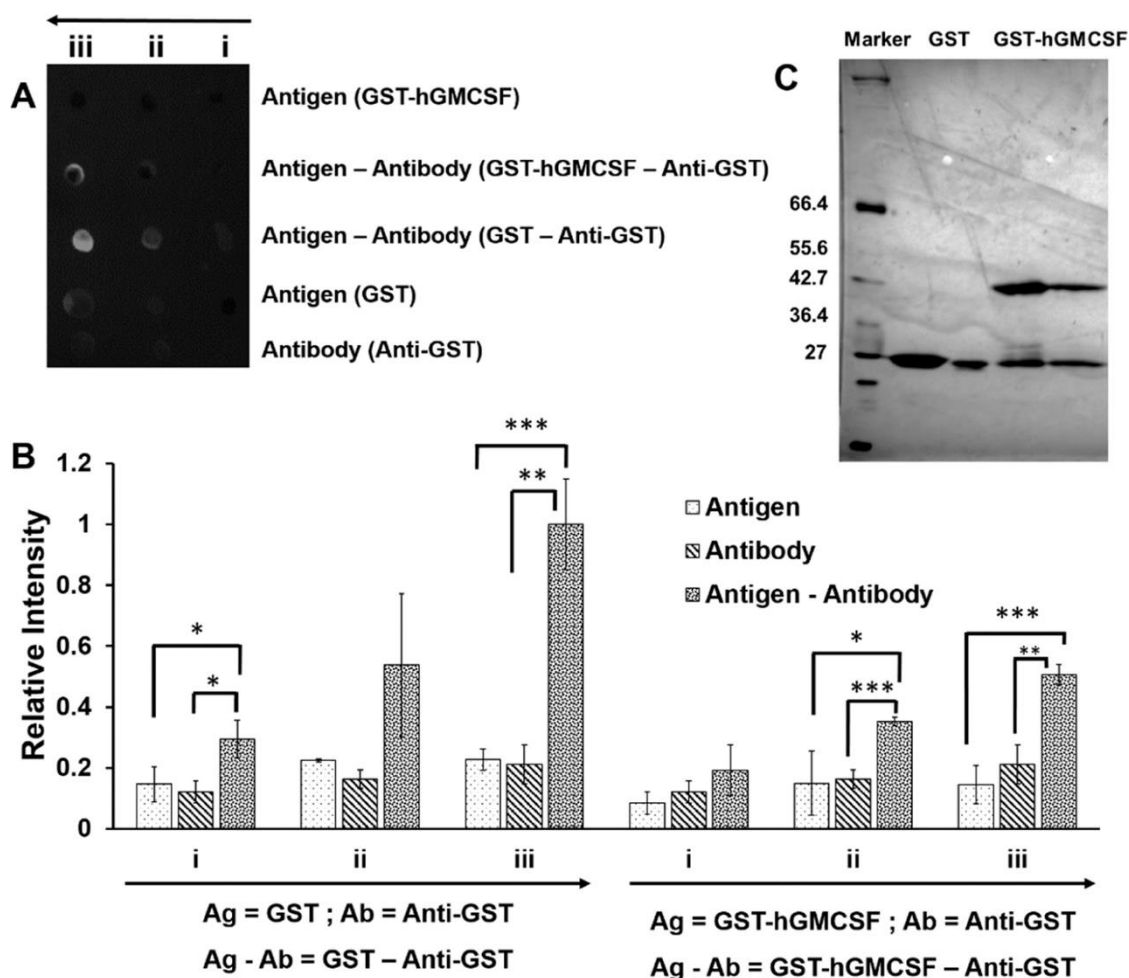


**Figure 6.4.** Study of expression of multiple proteins isolated from *E. coli* BL21. (A) Grayscale images under UV illumination (254 nm) of Au nanoclusters synthesized on various proteins (spots). First, increasing concentrations ((i) 0.1  $\mu\text{g}$ , (ii) 0.2  $\mu\text{g}$  and (iii) 0.4  $\mu\text{g}$ ) of anti-GST antibody were immobilized on to the PVDF membrane in two rows and interacted with increasing concentrations ((i) 0.08  $\mu\text{g}$ , (ii) 0.16  $\mu\text{g}$  and (iii) 0.32  $\mu\text{g}$ ) of GST-hGMCSF in one row and with ((i) 0.1  $\mu\text{g}$ , (ii) 0.2  $\mu\text{g}$  and (iii) 0.4  $\mu\text{g}$ ) of pure GST in another row. Only GST-hGMCSF, pure GST and Ab (Anti-GST) were also immobilized in separate rows on the PVDF membrane in increasing amounts for comparison and analysis. (B) Relative luminescence intensities (with respect to the maximum mean intensity in the entire data) of Au nanoclusters synthesized on spotted proteins as mentioned above. The graph depicts the averaged intensity of data from three separate experiments with their standard deviation. (C) SDS-PAGE analysis of pure GST and GST-hGMCSF. Experiments were done in triplicates, \* $P < 0.05$  with respect to Ag or Ab, \*\* $P < 0.01$  with respect to Ag or Ab, \*\*\* $P < 0.001$  with respect to Ag or Ab.

For the application of these Au nanoclusters in protein expression studies, the expression profiling of GST and GST-hGMCSF in *E. coli* BL 21 DE3 cells was performed after their isolation and purification. The integrity and functionality of the isolated proteins (GST, GST-hGMCSF) were analyzed by using standard SDS-PAGE, circular dichroism (CD) spectroscopy, Bradford

assay, 1-chloro-2,4-dinitrobenzene (CDNB) assay (**Appendix E, Figure E6.5 and Figure E6.6**). In SDS-PAGE, bands corresponding to GST and GST-hGMCSF were observed at 26 kDa and 42 kDa, respectively, and concentrations of the proteins obtained from Bradford assay were 239  $\mu\text{g/mL}$  and 96  $\mu\text{g/mL}$  for GST, GST-hGMCSF, respectively.

CD spectroscopy confirmed that 3D conformation of GST<sup>26</sup> as well as GST-hGMCSF<sup>27</sup> was intact for functionality. Also, CNDB assay specific for determination of GST enzyme activity confirmed that the GST was functional for both the cases of GST and GST-hGMCSF. After obtaining the proteins (GST and GST-hGMCSF) in their functional forms, they were allowed to interact with their respective anti-GST antibodies previously immobilized on the PVDF membrane along with their GST, GST-hGMCSF and anti GST antibody controls. Then, Au nanoclusters were synthesized on the respective spots using the thermocycler in a single cycle of heating and cooling. Thereafter, the membrane was imaged using the visualization unit of the bench top device and the luminescence intensity of the Au nanoclusters was found to be the highest in case of GST – anti-GST antibody conjugate followed by GST-hGMCSF– anti-GST antibody conjugate, when compared to only GST, GST-hGMCSF, anti-GST antibody as shown in **Figure 6.4**. These results corroborated the standard SDS-PAGE and Bradford assay results obtained previously. As the formation of the nanoclusters was found to be dependent on the amount of protein, it was observed that in the case of immobilized antibodies, or only GST protein on the membrane, there was no visible formation of nanocluster as adequate amount of protein was absent in both these cases. Whereas, when both the immobilized antibody along with the GST protein were present together, the increase in amount of protein content led to the formation of nanoclusters. Hence, in absence of the analyte, which can be either the antibody or the antigen depending on the assay, the luminescence will not be generated or will be always less compared to the antigen-antibody conjugate. As a control experiment, specific GST protein and a nonspecific BSA protein was interacted with anti-GST antibody and it was found that the luminescence did not get enhanced in the case of BSA as it did with increasing concentrations of GST, possibly due to washing away of the nonspecific BSA antigen (**Appendix E, Figure E6.7**). Hence, it can be concluded that the luminescent Au nanoclusters, synthesized *in situ*, were efficient probes for the protein expression studies. The short time and minimum precursor requirement compared to earlier reports<sup>20,21</sup> make the Au nanocluster probe reported herein ideal for point-of-care (POC) detection. In addition, the current method did not form any larger sized Au nanoparticles alongside Au nanoclusters, which was generally observed in previously reported works.<sup>20,21</sup> The rapid method of synthesis directly proteins with minimum precursor concentrations, biocompatibility, concentration dependent luminescence makes the current study an important addition in the analysis of protein expression.

## 6.4. Enhancement of Sensitivity with Zinc Ions

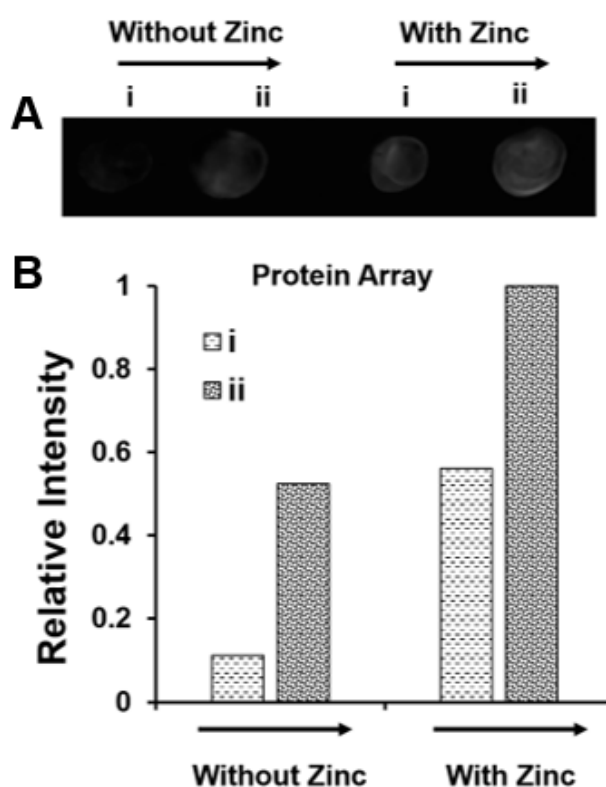


**Figure 6.5.** (A) Luminescence intensities of Au nanoclusters before and after addition of zinc ions on proteins in nitrocellulose and PVDF membrane. (B) Relative luminescence intensities (with respect to the maximum intensity in the entire data) of spots as obtained from the image analysis for proteins respectively. Here, the arrows denote increasing concentrations of proteins.

It may further be mentioned here that in array based analysis, involving protein, addition of zinc ions during the synthesis of Au nanoclusters enhanced the luminescence intensity of the Au nanoclusters. As shown in **Figure 6.5A,B**, in one of the rows, zinc ions were added during the synthesis of Au nanoclusters. As is evident from the image analysis, the luminescence intensity increased in the case where zinc ions were added to the reaction mixture. The reason for the increase in luminescence may be attributed to the aggregation of Au nanoclusters caused by zinc ions.<sup>28</sup> Thus, this technique can be used for enhancement of luminescence in case of lower signal intensity.

## 6.5. Conclusions

A rapid method for protein expression assay based on luminescent bio-friendly Au nanoclusters is established. The facile and rapid synthesis of signal generating Au nanoclusters on protein allowed semi-quantitative and qualitative analyses. Further, it provided a method of synthesis of Au nanoclusters for protein analyses in liquid as well as samples on membrane. Importantly, the

techniques, methods and materials employed are bio and environmentally friendly. Taken in account all these sublime features, the method may add a new dimension to the existing techniques with the amalgamation of nanotechnology and fundamentals of proteomics. This may create motivation to converge various techniques and develop methods in a view to make rapid diagnostics available across the globe.

## 6.6. References

1. Lockhart, D. J.; Winzeler, E. A. Genomics, Gene Expression and DNA Arrays. *Nature* **2000**, *405*, 827-836.
2. Tyers, M.; Mann, M. From Genomics to Proteomics. *Nature* **2003**, *422*, 193-197.
3. Gaj, S.; Eijssen, L.; Mensink, R. P.; Evelo, C. T. Validating Nutrient-Related Gene Expression Changes from Microarrays Using  $Rt^2$  PCR-Arrays. *Genes Nutr.* **2008**, *3*, 153-157.
4. Brandt, S.; Kloska, S.; Altmann, T.; Kehr, J. Using Array Hybridization to Monitor Gene Expression at the Single Cell Level. *J. Exp. Bot.* **2002**, *53*, 2315-2323.
5. Quijada, L.; Soto, M.; Requena, J. M. Genomic DNA Macroarrays as a Tool for Analysis of Gene Expression in Leishmania. *Exp. Parasitol.* **2005**, *111*, 64-70.
6. Randolph, J. B.; Waggoner, A. S. Stability, Specificity and Fluorescence Brightness of Multiply-Labeled Fluorescent DNA Probes. *Nucleic Acids Res.* **1997**, *25*, 2923-2929.
7. Moreira, B. G.; You, Y.; Owczarzy, R. Cy3 and Cy5 Dyes Attached to Oligonucleotide Terminus Stabilize DNA Duplexes: Predictive Thermodynamic Model. *Biophys. Chem.* **2015**, *198*, 36-44.
8. Toutchkine, A.; Nalbant, P.; Hahn, K. M. Facile Synthesis of Thiol-Reactive Cy3 and Cy5 Derivatives with Enhanced Water Solubility. *Bioconj. Chem.* **2002**, *13*, 387-391.
9. Ahrberg, C. D.; Ilic, B. R.; Manz, A.; Neužil, P. Handheld real-time PCR device. *Lab Chip* **2016**, *16*, 586-592.
10. Yuan, X.; Luo, Z.; Zhang, Q.; Zhang, X.; Zheng, Y.; Lee, J. Y.; Xie, J. Synthesis of Highly Fluorescent Metal (Ag, Au, Pt, and Cu) Nanoclusters by Electrostatically Induced Reversible Phase Transfer. *ACS Nano* **2011**, *5*, 8800-8808.

11. Tsoi, K. M.; Dai, Q.; Alman, B. A.; Chan, W. C. W. Are Quantum Dots Toxic? Exploring the Discrepancy between Cell Culture and Animal Studies. *Acc. Chem. Res.* **2013**, *46*, 662-671.
12. Yong, K.-T.; Law, W.-C.; Hu, R.; Ye, L.; Liu, L.; Swihart, M. T.; Prasad, P. N. Nanotoxicity Assessment of Quantum Dots: From Cellular to Primate Studies. *Chem. Soc. Rev.* **2013**, *42*, 1236-1250.
13. Zhang, Z.; Liu, Y.; Liu, P.; Yang, L.; Jiang, X.; Luo, D.; Yang, D. Non-invasive detection of gastric cancer relevant d -amino acids with luminescent DNA/silver nanoclusters. *Nanoscale* **2017**, *9*, 19367–19373.
14. Govindaraju, S.; Ankireddy, S. R.; Viswanath, B.; Kim, J.; Yun, K. Fluorescent Gold Nanoclusters for Selective Detection of Dopamine in Cerebrospinal fluid. *Sci. Rep.* **2017**, *7*, 40298.
15. Meng, L.; Zhu, Q.; Yin, J.-H.; Xu, N. Polyethyleneimine protected silver nanoclusters luminescence probe for sensitive detection of cobalt (II) in living cells. *J. Photochem. Photobiol. B* **2017**, *173*, 508–513.
16. Pyo, K.; Ly, N. H.; Yoon, S. Y.; Shen, Y.; Choi, S. Y.; Lee, S. Y.; Joo, S.-W.; Lee, D. Highly Luminescent Folate-Functionalized Au<sub>22</sub> Nanoclusters for Bioimaging. *Adv. Healthcare Mater.* **2017**, *6*, DOI: 10.1002/adhm.201700203.
17. Shen, D.; Henry, M.; Trouillet, V.; Comby-Zerbino, C.; Bertorelle, F.; Sancey, L.; Antoine, R.; Coll, J.-L.; Jossierand, V.; Le Guével, X. Zwitterion functionalized gold nanoclusters for multimodal near infrared fluorescence and photoacoustic imaging. *APL Materials* **2017**, *5*, 053404.
18. Lin, C.-A. J.; Yang, T.-Y.; Lee, C.-H.; Huang, S. H.; Sperling, R. A.; Zanella, M.; Li, J. K.; Shen, J.-L.; Wang, H.-H.; Yeh, H.-I.; Parak, W. J.; Chang, W. H. Synthesis, Characterization, and Bioconjugation of Fluorescent Gold Nanoclusters toward Biological Labeling Applications. *ACS Nano* **2009**, *3*, 395-401.
19. Lu, Y.; Chen, W. Progress in the Synthesis and Characterization of Gold Nanoclusters. In *Gold Clusters, Colloids and Nanoparticles I*, Mingos, D. M. P., Ed. Springer International Publishing: Cham, 2014; pp 117-153.
20. Chakraborty, S.; Babanova, S.; Rocha, R. C.; Desireddy, A.; Artyushkova, K.; Boncella, A. E.; Atanassov, P.; Martinez, J. S. A Hybrid DNA-Templated Gold Nanocluster For Enhanced Enzymatic Reduction of Oxygen. *J. Am. Chem. Soc.* **2015**, *137*, 11678–11687.

21. Kennedy, T. A. C.; MacLean, J. L.; Liu, J. Blue emitting gold nanoclusters templated by poly-cytosine DNA at low pH and poly-adenine DNA at neutral pH. *Chem. Commun.* **2012**, *48*, 6845–6847.
22. Costa, M. N.; Veigas, B.; Jacob, J. M.; Santos, D. S.; Gomes, J.; Baptista, P. V.; Martins, R.; Inacio, J.; Fortunato, E. A Low Cost, Safe, Disposable, Rapid and Self-Sustainable Paper-Based Platform for Diagnostic Testing: Lab-on-Paper. *Nanotechnology* **2014**, *25*, 094006.
23. Liana, D. D.; Raguse, B.; Gooding, J. J.; Chow, E. Recent Advances in Paper-Based Sensors. *Sensors (Basel)* **2012**, *12*, 11505-11526.
24. Dutta D.; Sahoo A. K.; Chattopadhyay A.; Ghosh S. S. Bimetallic silver nanoparticle–gold nanocluster embedded composite nanoparticles for cancer theranostics *J. Mater. Chem. B*, **2016**, *4*, 793-800.
25. Sahoo A. K.; Banerjee S.; Ghosh S. S.; Chattopadhyay A. Simultaneous RGB Emitting Au Nanoclusters in Chitosan Nanoparticles for Anticancer Gene Theranostics *ACS Appl Mater Interfaces*, **2014**, *6*, 712-724.
26. Ishii, M.; Fujita, S.; Yamada, M.; Hosaka, Y.; Kurachi, Y. Phosphatidylinositol 3,4,5-trisphosphate and Ca<sup>2+</sup>/Calmodulin Competitively Bind to the Regulators of G-Protein-Signalling (RGS) Domain of RGS4 and Reciprocally Regulate Its Action. *Biochem. J.* **2005**, *385*, 65-73.
27. Chaubey, N.; Ghosh, S. S. Molecular Cloning, Purification and Functional Implications of Recombinant GST Tagged hGMCSF Cytokine. *Appl. Biochem. Biotechnol.* **2013**, *169*, 1713-1726.
28. Yao, Q.; Luo, Z.; Yuan, X.; Yu, Y.; Zhang, C.; Xie, J.; Lee, J. Y. Assembly of Nanoions via Electrostatic Interactions: Ion-Like Behavior of Charged Noble Metal Nanoclusters. *Sci. Rep.* **2014**, *4*, 3848.
29. Vanitha, S.; Goswami, U.; Chaubey, N.; Ghosh, S. S.; Sanpui, P. Functional Characterization of Recombinant Human Granulocyte Colony Stimulating Factor (hGMCSF) Immobilized onto Silica Nanoparticles. *Biotechnol. Lett.* **2016**, *38*, 243-249.

(Content of the chapter has been reproduced with permission from American Chemical Society (S.K. Sailapu, D. Dutta, A. Chattopadhyay and S. S. Ghosh, ACS Omega 3, 2, 2119-2129)

# Appendix E

## E.1 Experimental Section

### Materials and Methods

#### Chemicals

HAuCl<sub>4</sub> (Au, 17 wt % in dilute HCl; 99.99%, Sigma-Aldrich), mercaptopropionic acid (MPA; Sigma-Aldrich), bovine serum albumin (BSA; Himedia), amylase (Merck), lysozyme (Sigma-Aldrich) were used without any alterations.

#### Characterization Studies

##### Analytical measurements

UV-visible spectrophotometer (JASCO V-630) was used to record UV-Vis spectra. Luminescence measurements were carried out at room temperature using Perkin-Elmer fluorescence spectrophotometer (model: LS 55).

##### Quantum Yield Measurements

For quantum yield (QY) measurements of Au nanoclusters, quinine sulphate in 0.10 M H<sub>2</sub>SO<sub>4</sub> solution was used as reference. The QY was calculated on the basis of the following equation:

$$QY = QY_r \frac{m}{m_r} \frac{n_r^2}{n^2}$$

Here, 'm' is the slope of integrated luminescence intensity vs. absorbance plot, 'n' is the refractive index and suffix, 'r' indicates reference quinine sulphate solution. Measurements of absorbance and luminescence were done simultaneously using the same solutions. The quantum yield of the standard (QY<sub>r</sub>) is 0.54 and refractive index of solvent (water) is 1.33.

##### Transmission electron microscopy (TEM)

For TEM analysis, 7 μL of Au nanocluster sample was drop cast onto a carbon coated copper grid and was allowed to air dry. The sample was imaged using JEM 2100; Jeol, Peabody, MA, USA at 200 keV.

##### Circular dichroism spectroscopy

CD spectroscopy samples were analysed using JASCO-815 spectrometer (Jasco, Japan). For measurements, a cuvette of 0.2 cm path length was used at 25 °C under constant nitrogen gas purging at a flow rate of 5 L/min. Spectra were recorded from 240 nm to 190 nm wavelength with four accumulations. In all the samples, subtraction of background spectrum of corresponding solvent was done.

**Matrix-assisted laser desorption ionization time-of-flight mass spectrometry (MALDI-TOF MS) analysis**

Samples were mixed with R-cyano-4-hydroxycinnamic acid (CHCA) matrix and analysis was performed using a MALDI TOF/TOF Analyzer (Applied Biosystems 4800 Plus MALDI).

**Synthesis of the Au nanoclusters using BSA as template**

For synthesis, 20  $\mu\text{L}$  of (0.05 mg/mL – 1.0 mg/mL) BSA (Himedia) was taken and to that 0.4  $\mu\text{L}$  of 10 mM  $\text{HAuCl}_4$  and 0.16  $\mu\text{L}$  of 0.11 M of MPA were added and the mixture was heated at 95  $^\circ\text{C}$  for 2 min and then cooled at 15  $^\circ\text{C}$  for 3 min.

**Protein Expression Studies**

- a) Expression and Purification of GST and GST-hGMCSF in *Escherichia coli* BL21 DE3: For primary culture, 20  $\mu\text{L}$  of *E. coli* BL21 DE3 stock harbouring pGEX4t2 vector was inoculated in 3 mL of LB (Luria-Bertani) media with 3  $\mu\text{L}$  of 100 mg/mL ampicillin and was incubated overnight at 37  $^\circ\text{C}$  (180 rpm). 2 mL of the grown primary culture was inoculated into 200 mL LB media with 200  $\mu\text{L}$  of 100 mg/mL ampicillin and was incubated at 37  $^\circ\text{C}$  (180 rpm) until an optical density (O.D.) of 0.6 was obtained. Following this, induction was given by 1 mL of IPTG (isopropyl  $\beta$ -D-1-thiogalactopyranoside, 24 mg/mL) at 24  $^\circ\text{C}$  (180 rpm, 6 h). The cells were then centrifuged at 6000 rpm (4  $^\circ\text{C}$ , 7 min) and the pellet hence obtained was stored at -20  $^\circ\text{C}$ . For the preparation of lysis buffer (7 mL), 100  $\mu\text{L}$  of 1 mM EDTA (ethylenediaminetetraacetic acid) and 100  $\mu\text{L}$  of 1 mM PMSF (phenylmethane sulfonyl fluoride) were added to 1X PBS (phosphate buffer saline). The cell pellet was then re-suspended in lysis buffer homogenously and was sonicated with a probe sonicator for 5 min. Centrifugation was carried out at 12000 rpm (4  $^\circ\text{C}$ , 20 min) and the supernatant was collected. The supernatant obtained in the previous step contained solubilised protein. It was first filtered through a 0.45  $\mu\text{m}$  syringe filter and then was put into glutathione agarose beads column (prepared previously by standard method) for half an hour. The flow through fractions were collected, followed by washing of the column for eight times with PBS. For elution buffer preparation, 20 mg of reduced glutathione was added to 5 mL of 50 mM Tris (pH 8). Recombinant GST bound to the affinity column was eluted with the elution buffer after 20 min. Multiple flow through fractions were collected and analysed using 12 % SDS PAGE. A similar protocol was adopted for isolation and purification of GST-hGMCSF.<sup>29</sup>
- b) Estimation of protein by Bradford assay: The concentration of the purified recombinant GST proteins was estimated using Bradford assay. The standard solution was prepared using bovine serum albumin of concentration 0.5, 1, 2, 4, 10  $\mu\text{g}/\text{mL}$  and 10  $\mu\text{L}$  of the protein sample (recombinant GST proteins) was used for analysis along with 90  $\mu\text{L}$  of Bradford reagent solution (Sigma-Aldrich). It was allowed to react at room temperature, for 10 min in dark and the optical density at 595 nm was measured using TECAN Elisa plate reader.

- c) Enzyme activity: GST activity was determined using CDNB assay: Increasing amount of protein solutions with 1X PBS buffer (pH 7.5), 1.0 mM GSH, 1.0 mM CDNB, amounting to total volume of 100  $\mu\text{L}$  were taken in a 96 well plate. The control wells contained PBS, CDNB and glutathione. After 10 min, the change in absorbance with respect to control was measured at 340 nm using TECAN Elisa plate reader. One unit of activity is defined as the formation of 1  $\mu\text{M}$  product per min at 25  $^{\circ}\text{C}$  ( $\epsilon_{\text{mM}}$  is the extinction coefficient at 340 nm in a 96-well plate is 5.3 for CDNB, D is the dilution factor).

$$\text{Change in absorbance } (\Delta A_{340}) / \text{min} = \frac{A_{340 \text{ final}} - A_{340 \text{ initial}}}{\text{reaction time}}$$

$$\text{GST Activity } (\mu\text{mol} / \text{mL} / \text{min}) = \frac{(\Delta A_{340} / \text{min}) \times V (\text{mL}) \times D}{V_{\text{enz}} (\text{mL}) \times \epsilon_{\text{mM}}}$$

- d) Immobilization of primary antibody on PVDF membrane in an array pattern: The primary antibody specific to GST antigen was immobilized on the PVDF membrane (IMMOBILON P 0.45 $\mu\text{m}$  membrane) by spotting different dilutions of primary antibody after activating the membrane of suitable dimensions (with maximum dimensions of 40 mm x 40 mm) in methanol. After spotting, the membrane was allowed to air dry for 15-20 min.
- e) Interaction of antigens with antibodies on PVDF membrane: The membrane was blocked using blocking solution (as mentioned above) for 30 min to avoid unspecific binding after that the membrane was incubated with respective GST antigens for 30 min and was washed with PBST (phosphate buffered saline with Tween 20) buffer for reducing non specificity.
- f) Synthesis of Au nanoclusters on PVDF membrane: After antigen-antibody interactions, Au nanoclusters were synthesized on the spots, by adding 1.5  $\mu\text{L}$  of 0.7 mM  $\text{HAuCl}_4$  and 0.5  $\mu\text{L}$  of 0.01 M MPA followed by heating the membrane using thermocycler at 95  $^{\circ}\text{C}$  for 2 min and then cooling at 15  $^{\circ}\text{C}$  for 3 min.
- g) Image acquisition & analysis: The membrane with synthesized Au nanoclusters was imaged and analysed using the visualization unit using custom developed software under UV illumination (254 nm).

**Statistical analysis:** Data were expressed as mean value  $\pm$  standard deviation (SD). Students t-test was employed to test significant differences between the experimental groups. (\*P <0.05, \*\*P<0.01, \*\*\*P<0.001).

## E.2 Figures

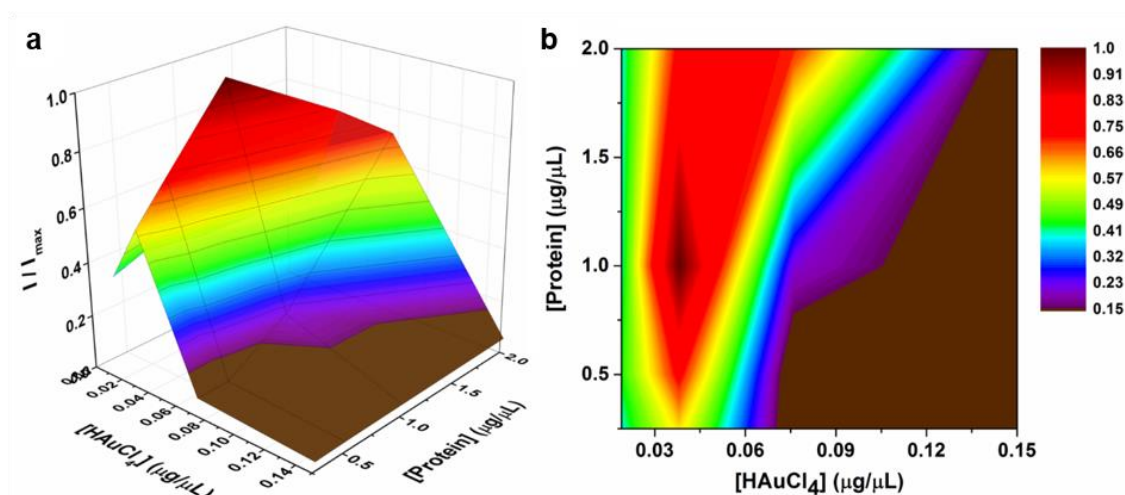


**Figure E6.1.** Luminescence plot of Au nanoclusters for various concentrations of the protein (BSA) and  $HAuCl_4$ . (a) Surface plot of relative emission intensity ( $I / I_{max}$ ) of Au nanoclusters for different concentrations of protein and  $HAuCl_4$ . Here intensity  $I$  is the luminescence due to protein - Au nanoclusters at 580 nm (when excited by 300 nm light), the maximum luminescence due to protein - Au nanoclusters is represented by  $I_{max}$ . (b) Contour plot showing the behaviour of luminescence of Au nanoclusters with varying precursor concentration.

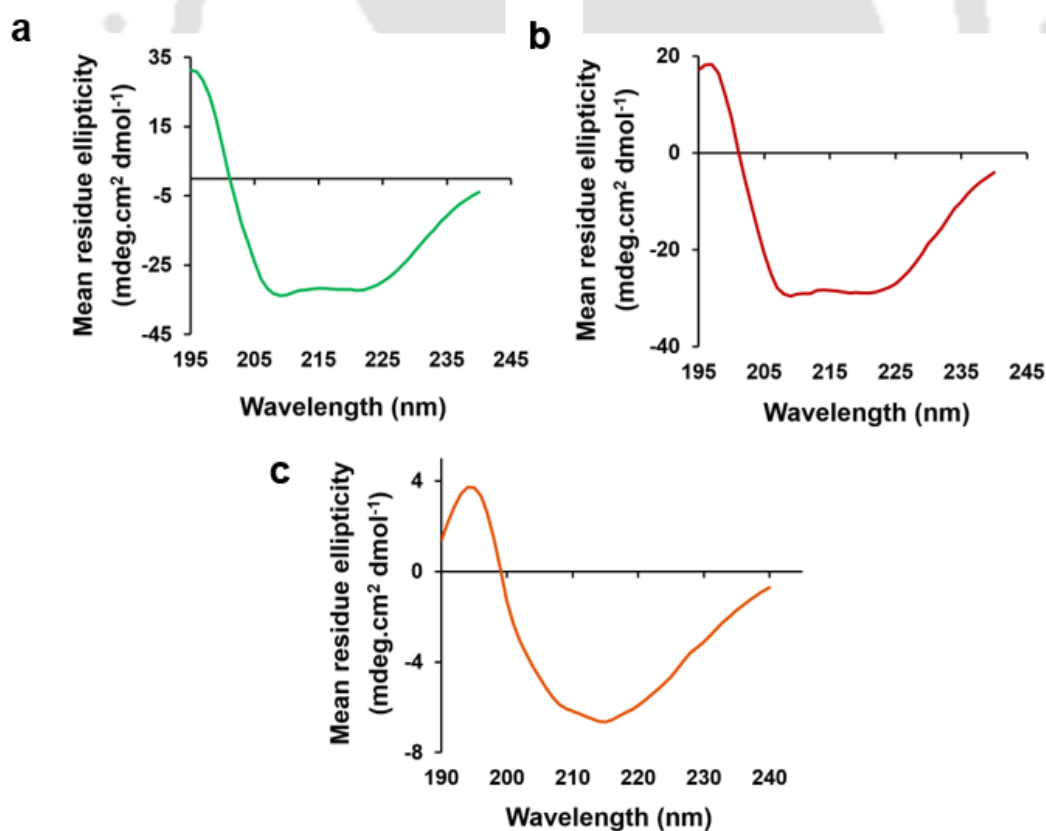


**Figure E6.2.** CD spectra of (a) BSA, (b) BSA - Au nanoclusters and (c) BSA - Au nanoparticles.

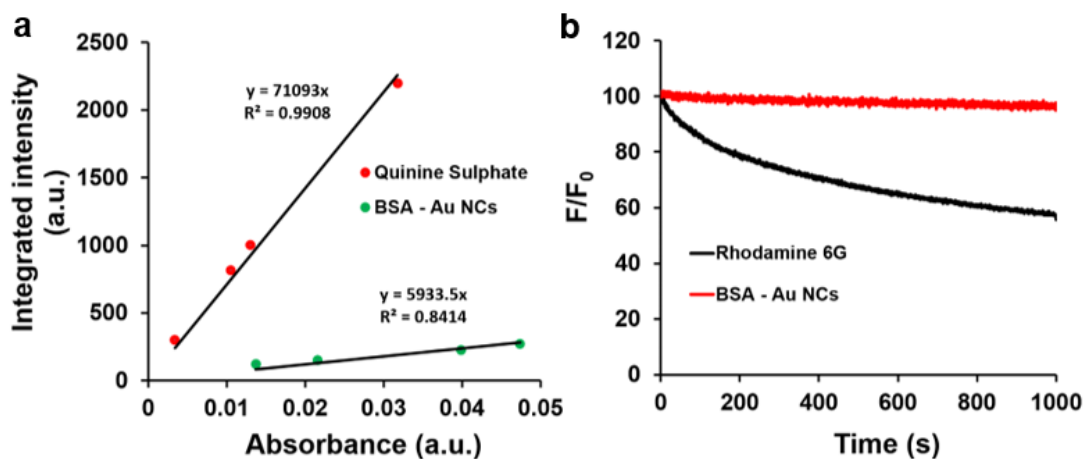


**Figure E6.3.** (a) Photoluminescence quantum yield of BSA – Au nanoclusters measured with respect to quinine sulphate as the reference. (b) Photostability of BSA – Au nanoclusters with respect to rhodamine 6G. In the figure, NC stands for nanocluster.

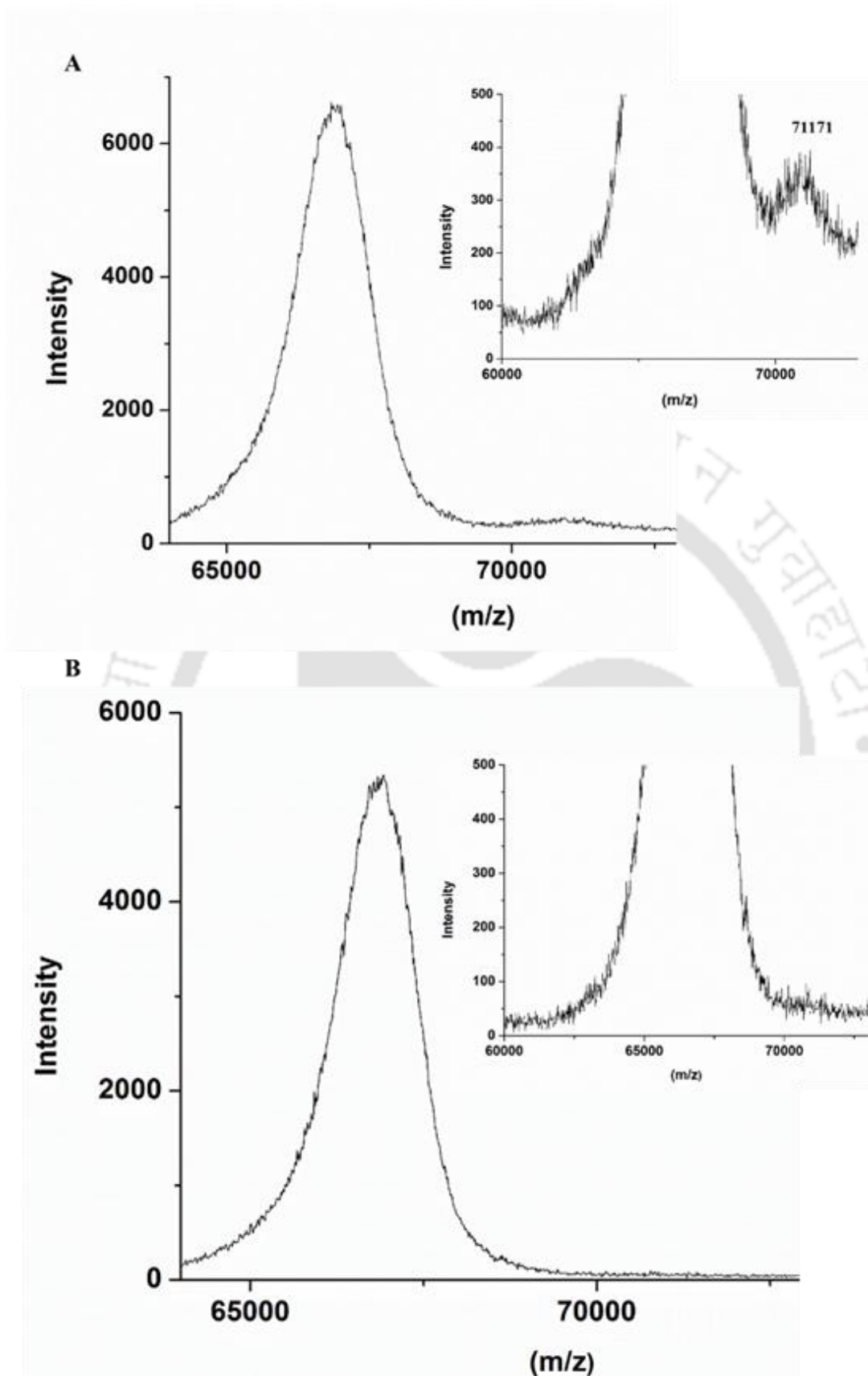
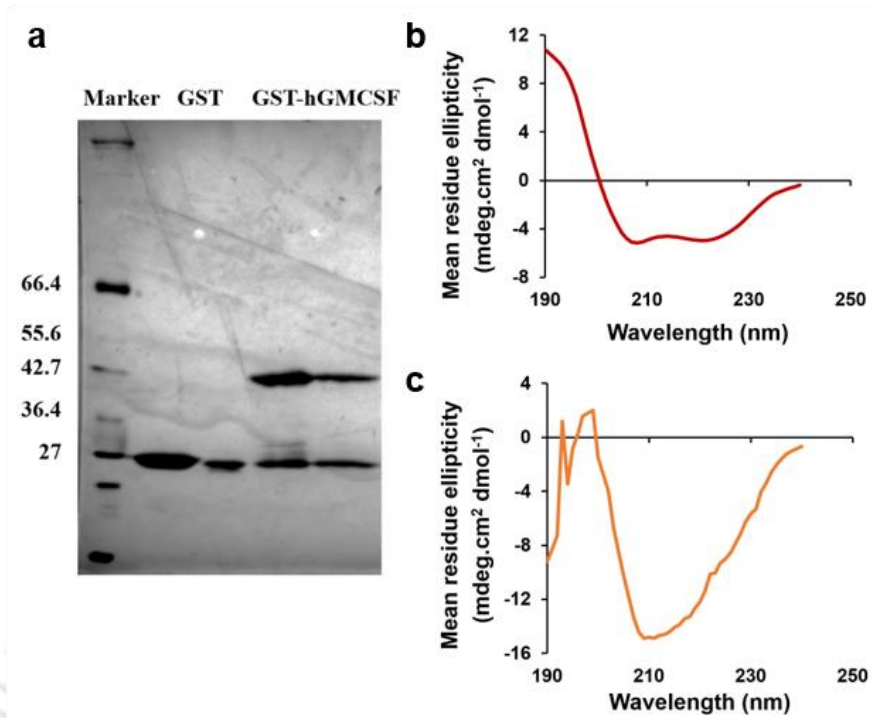
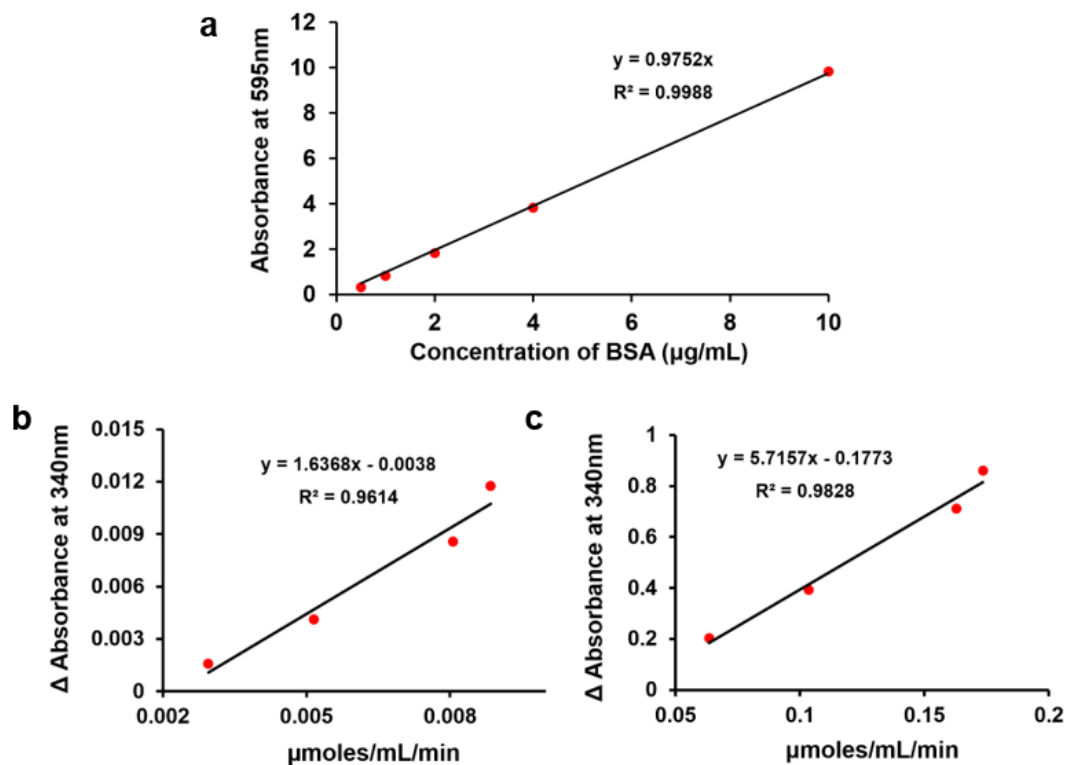


Figure E6.4. MALDI-TOF results of (a) BSA-templated Au nanoclusters and (b) BSA only.



**Figure E6.5.** (a) SDS PAGE of purified GST and GST-hGMCSF showing bands at 26 kDa and 42 kDa, respectively. (b, c) CD spectra of GST and GST-hGMCSF.



**Figure E6.6.** (a) Standard absorbance plot of BSA for estimation of protein concentration. (b) Enzyme activity assay of purified GST. (c) Enzyme activity assay of purified GST-hGMCSF.

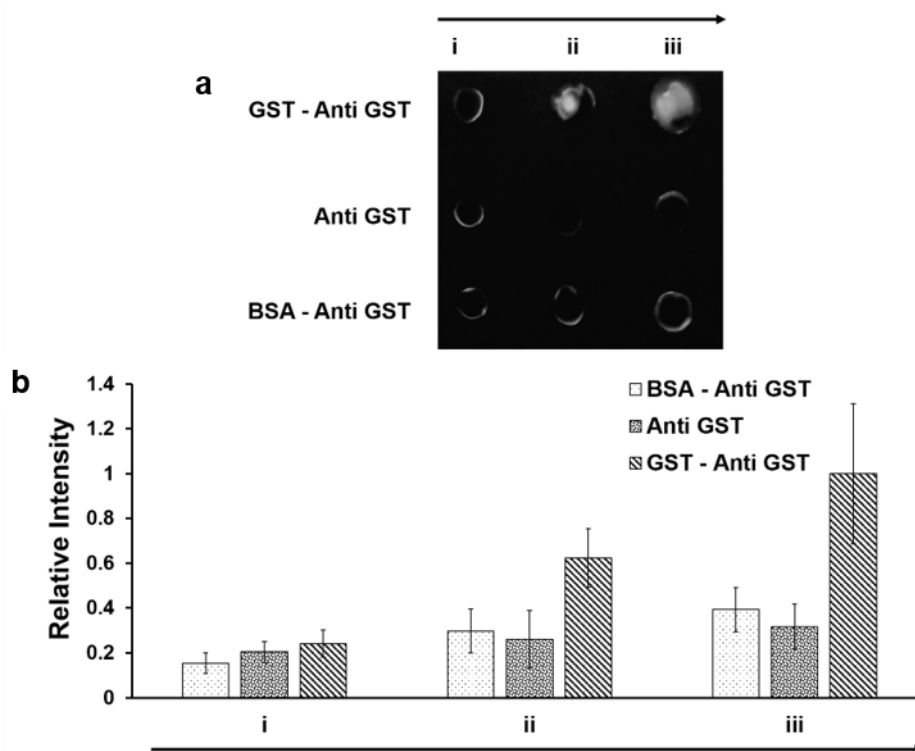


**Figure E6.7.** Luminescence profile of Au nanoclusters synthesized on anti-GST, GST – antiGST and BSA – anti-GST. (a) Grayscale image under UV illumination (254 nm) of Au nanoclusters synthesized using GST – anti-GST antibody, anti-GST antibody, non-specific antigen BSA – anti-GST antibody, on PVDF membrane, in increasing amounts (indicated by the arrow). (b) Relative luminescence intensities (with respect to the maximum intensity in the entire data) of Au nanoclusters synthesized on all spots (as obtained from image analysis). The values are represented as mean  $\pm$  SD of three individual experiments.

**Description of Figure E6.7.**

Anti-GST antibody was immobilized on to the PVDF membrane in three rows in increasing concentrations ((i) 0.1  $\mu$ g, (ii) 0.2  $\mu$ g and (iii) 0.4  $\mu$ g). Pure GST was interacted with immobilized anti-GST in the first row in increasing concentrations ((i) 0.1  $\mu$ g, (ii) 0.2  $\mu$ g and (iii) 0.4  $\mu$ g). BSA was interacted with immobilized anti-GST in the third row in increasing concentrations (i) 0.1  $\mu$ g, (ii) 0.2  $\mu$ g and (iii) 0.4  $\mu$ g). The second row was kept as control for only anti-GST. Au nanoclusters were then synthesized on all the spots of the membrane using the thermocycler unit of the bench top device. The membrane was then imaged (**Figure E6.7a**) in the visualization unit of the bench top device and was analysed using the custom developed software. The intensity analysis (**Figure E6.7b**) showed that the luminescence didn't get enhanced in the case of BSA as it did with increasing concentrations of GST, possibly due to washing away of the nonspecific BSA antigen.

## Conclusions and Future Perspectives

This dissertation cumulates synthesis and applications of multifunctional nanomaterials towards the achievement of *in vitro* therapy and diagnostics. Biopolymer chitosan based bimetallic silver nanoparticle-gold nanocluster were synthesized for application in cancer cell bioimaging and simultaneous induction of apoptosis. The pathway of uptake was elucidated by TEM investigations as well as flow cytometry without the use of organic fluorophores and the mechanism of cell death was also confirmed by flow cytometry based assays.

Thereafter, an attempt was made towards development of a suicide gene (CD-UPRT) carrier based on cationic serum albumin embedded with luminescent bimetallic gold-silver nanoclusters. The luminescence of the nanoclusters helped in tracking the delivery of suicide gene as well as contributed to ROS generation due to their ultrasmall nature. The suicide gene in presence of the prodrug 5 FU, triggered apoptosis in HeLa cancer cells. The combinatorial module in presence of both nanoclusters and suicide gene was found to have pronounced effect compared to other controls in reducing the viability of the cancer cells. Moreover,

Another aspect of generation of ROS and subsequent cell death supplemented by luminescence tracking was explored by developing a luminescent gold nanocluster embedded mucin based nanocarrier for photosensitizer drug (MB) delivery. The delivery of the photosensitizer was monitored by gold nanoclusters luminescence and HeLa cancer cells were rendered towards cell death via singlet oxygen generation under irradiation of 640 nm light. The uptake as well as mechanism of cell death was elucidated.

Phenylboronic acid templated gold nanoclusters were explored towards *in vitro* targeted bioimaging and therapy of HeLa and HepG2 cancer cells. The activity of the gold nanoclusters were also studied in a more realistic tumor like environment by employing *in vitro* 3D multicellular spheroids. The same nanoclusters were also applied for development of a smartphone based device for biomarker mucin detection (*in vitro*). The interaction between the phenylboronic acid templated gold nanoclusters with the mucin led to an increase in luminescence of gold nanoclusters which was exploited for detection of mucin.

A simple, rapid and biofriendly synthesis method of formation of gold nanoclusters on proteins was developed for application in *in vitro* diagnostics. Particularly the gold nanoclusters were employed in assaying recombinant GST and GST-tagged proteins. The gold nanocluster probe was found to be efficient in comparison to traditional methods.

Overall the dissertation presents a variety of approaches employing multifunctional nanomaterials for theranostic application. Based on the findings of *in vitro* cell culture and studies on multicellular spheroid cultures the hence synthesised nanomaterials could be further explored in *in vivo* systems. The use of a natural polymer chitosan as a stabilizer offers biocompatibility and biodegradability rather than those involving the use of organic moieties, with enhanced permeation and mucoadhesive properties suitable for systemic nanocarrier based applications. Also, serum albumin based materials had been applied in various drug delivery systems like Abraxane, an FDA-approved albumin-based nanoparticle system successfully implemented for breast cancer therapy. Also, cationic albumin has been reported for delivery of therapeutic moieties both *in vitro* as well as *in vivo* with minimal toxicity and good biocompatibility. In a similar line, mucin and other types of protein based metal nanocluster systems open up a new paradigm in terms of the development of drug carriers as well as signal generating agents that can have potential applications *in vivo* with good biodegradability and minimal toxicity. Boronic acids apart from being successful targeting agents, have also gained attention in anticancer therapy. Bortezomib, a boronic acid based drug have been approved by FDA for use in multiple myeloma treatment. Also, drug testing is being carried out using boron-containing drugs as a new class of pharmaceuticals for various diseases. Hence, the above mentioned systems combined with the numerous advantages of metal nanoclusters as biological probes like low toxicity, high photo stability, good renal clearance, water solubility, ultrasmall size enabling deeper tissue penetration compared to quantum dots and organic dyes offers a potential possibility of implementing these systems in clinical as well as *in vivo* applications. Nanotoxicity evaluation of the synthesized nanomaterials in embryonic development of zebra fish model systems can also be pursued. Moreover, the results of the diagnostic assays obtained *in vitro* open up possibilities of implementing the diagnostic approaches in clinical samples.

## Publication and Patents

### Publications from Thesis

1. **Dutta, D.;** Sahoo, A. K.; Chattopadhyay, A.; Ghosh, S. S. Bimetallic Silver Nanoparticle–gold Nanocluster Embedded Composite Nanoparticles for Cancer Theranostics. *J. Mater. Chem. B* **2016**, *4* (4), 793–800.
2. **Dutta, D.;** Chattopadhyay, A.; Ghosh, S. S. Cationic BSA Templated Au–Ag Bimetallic Nanoclusters As a Theranostic Gene Delivery Vector for HeLa Cancer Cells. *ACS Biomater. Sci. Eng.* **2016**, *2* (11), 2090–2098.
3. **Dutta, D.;** Sailapu, S. K.; Chattopadhyay, A.; Ghosh, S. S. Gold Nanoclusters embedded Mucin nanoparticles for Photodynamic Therapy and Bioimaging. (**Manuscript under preparation**)
4. **Dutta, D.;** Sailapu, S. K.; Chattopadhyay, A.; Ghosh, S. S. Phenylboronic Acid Templated Gold Nanoclusters for Mucin Detection Using a Smartphone-Based Device and Targeted Cancer Cell Theranostics. *ACS Appl. Mater. Interfaces* **2018**, *10* (4), 3210–3218.
5. Sailapu, S. K.; **Dutta, D.;** Sahoo, A. K.; Ghosh, S. S.; Chattopadhyay, A. Single Platform for Gene and Protein Expression Analyses Using Luminescent Gold Nanoclusters. *ACS Omega* **2018**, *3* (2), 2119–2129.

### Publications from Collaborations

6. Sahoo, A. K.; Goswami, U.; **Dutta, D.;** Banerjee, S.; Chattopadhyay, A.; Ghosh, S. S. Silver Nanocluster Embedded Composite Nanoparticles for Targeted Prodrug Delivery in Cancer Theranostics. *ACS Biomater. Sci. Eng.* **2016**, *2* (8), 1395–1402.
7. Dutta, A.; **Dutta, D.;** Sanpui, P.; Chattopadhyay, A. Biomimetically Crystallized Protease Resistant Zinc Phosphate Decorated with Gold Atomic Clusters for Bioimaging. *Chem. Commun.* **2017**, *53* (7), 1277–1280.
8. Bhuyan, T.; Singh, A. K.; **Dutta, D.;** Unal, A.; Ghosh, S. S.; Bandyopadhyay, D. Magnetic Field Guided Chemotaxis of IMushbots for Targeted Anticancer Therapeutics. *ACS Biomater. Sci. Eng.* **2017**, *3* (8), 1627–1640.

9. Narayanan, S.; **Dutta, D.**; Arora, N.; Sahoo, L.; Ghosh, S. S. Phytaspase-Loaded, Mn-Doped ZnS Quantum Dots When Embedded into Chitosan Nanoparticles Leads to Improved Chemotherapy of HeLa Cells Using in Cisplatin. *Biotechnol. Lett.* **2017**, *39* (10), 1591–1598.
10. Sahoo, A. K.; Sailapu, S. K.; **Dutta, D.**; Banerjee, S.; Ghosh, S. S.; Chattopadhyay, A. DNA-Templated Single Thermal Cycle Based Synthesis of Highly Luminescent Au Nanoclusters for Probing Gene Expression. *ACS Sustainable Chem. Eng.* **2018**, *6* (2), 2142–2151.
11. Zehra, N; **Dutta, D**; Akhtar H.M; Ghosh,S.S; Iyer, P.K. Fluorescence Resonance Energy Transfer Based Wash-Free Bacterial Imaging and Antibacterial Application Using Cationic Conjugated Polyelectrolyte. *ACS Appl. Mater. Interfaces* **2018**, 10.1021/acsami.8b07516.
12. Sailapu S. K.; **Dutta D.**; Simon A. T.; Ghosh S. S.and Chattopadhyay A. Smartphone based portable LED device for photodynamic therapy and colorimetric assays. (**Manuscript Under Preparation**).

#### Patents from Thesis

1. Arun Chattopadhyay, Sunil Kumar Sailapu, **Deepanjalee Dutta**, Amaresh Kumar Sahoo, Siddhartha Sankar Ghosh. A device with integrated methods for reverse transcription polymerase chain reaction (RT-PCR) and/or DNA/protein array based analyses (**2015**). Indian Patent Application No.**1259/KOL/2015 A**.
2. Arun Chattopadhyay, Sunil Kumar Sailapu, **Deepanjalee Dutta**, Amaresh Kumar Sahoo, Siddhartha Sankar Ghosh. A device with integrated methods for reverse transcription polymerase chain reaction (RT-PCR) and/or DNA/protein array based analyses (**2016**). International Patent Application No.**PCT/IN2016/000141**.

#### Patents from Collaborations

1. Arun Chattopadhyay, Sunil Kumar Sailapu, **Deepanjalee Dutta**, Siddhartha Sankar Ghosh, Anitha T Simon. Wirelessly Operated LED Device For Photodynamic Therapy And Subsequent Monitoring Of Therapeutic Success (**2017**). Indian Patent Application No.201731031603.
2. Parameswar Krishnan Iyer, Anamika Dey, Ashish Singh, **Deepanjalee Dutta**, Siddhartha Sankar Ghosh. An ultra-low voltage operated organic field effect transistor (OFET) based bio-sensing system and a method for fabricating the same (**2018**). Indian Patent Application No. 201831000478.

## Conference and Workshop attended

1. Poster presentation 8<sup>th</sup> Bangalore India Nano, Bangalore , March 3-4, 2016 (Silver nanoparticle-gold nanocluster embedded chitosan nanocarrier for cancer theranostic application)
2. Poster presentation in International Conference on Functional Materials, IIT Kharagpur, India, December 12-14, 2016 (Silver nanoparticle-gold nanocluster impregnated chitosan nanocarrier for cancer theranostic application).
3. **Best model presentation**, Reflux 2016, IIT Guwahati, (A bench top device for genomics and proteomics).
4. **Shortlisted within top 15 proposals**, Assam Biotech conclave, Guwahati Biotech Park , January 5-6, 2017, (A bench top device and integrated methods for gene and protein analysis).
5. Model presentation, TechExpo 2017, Technique IIT Guwahati, August 31 – September 3, 2017 (A bench top device for genomics and proteomics).
6. Oral presentation in National Seminar on Advances in Materials Science, Guwahati University, March 24-25, 2017, (Au–Ag Bimetallic Nanoclusters embedded Cationic BSA nanocarrier for Suicide gene therapy and Bioimaging of HeLa cancer cells).
7. **Best poster presentation**, Nanobiotech'17, KTDC Samudra, Trivandrum, December 6-8, 2017 (Bimetallic Au–Ag Nanoclusters embedded Cationic BSA nanocarrier for Bioimaging and Suicide gene therapy of HeLa cancer cells)..
8. **Best poster presentation**, ICANN 2017, IIT Guwahati , December 18-21, 2017, (Bimetallic Au–Ag nanoclusters embedded nanocarrier for Bioimaging and Suicide gene therapy of HeLa cancer cells).
9. **Best research proposal ( 2<sup>nd</sup> position )**, North East Biostart, Guwahati Biotech Park, April 3-5, 2018, (Portable smartphone based device for photodynamic therapy and colorimetric assays).
10. Model presentation, Research Conclave 2018, IIT Guwahati, March 8-11, 2018, (Portable smartphone based device for photodynamic therapy and colorimetric assays).
11. 1st-3rd National Workshop on NEMS/MEMS and Theranostics Devices, Centre for Nanotechnology, Indian Institute of Technology Guwahati.
12. One day workshop on “Biomedical Device Technology”, ICANN 2017, IIT Guwahati , December 18, 2017.
13. Workshop on Advanced techniques in cell and molecular biology, IIT Guwahati, June 24- 26, 2014.
14. Dissemination Program of National Ethical Guidelines for Biomedical and Health Research Involving Human Participants and National Ethical Guidelines for Biomedical Research Involving Children 2017, Gauhati Medical College, Assam, March 08, 2018.

# Permissions

Figure 1.1

| <b>SPRINGER NATURE LICENSE<br/>TERMS AND CONDITIONS</b>  |  |
|--|--|
|  | Apr 26, 2018   |
| This Agreement between deepanjalee dutta ("You") and Springer Nature ("Springer Nature") consists of your license details and the terms and conditions provided by Springer Nature and Copyright Clearance Center. |  |
| License Number   | 4336351063252  |
| License date   | Apr 26, 2018   |
| Licensed Content Publisher   | Springer Nature  |
| Licensed Content Publication   | Applied Microbiology and Biotechnology   |
| Licensed Content Title   | Current state and prospects of the phytosynthesized colloidal gold nanoparticles and their applications in cancer theranostics |
| Licensed Content Author  | Muhammad Ovais, Abida Raza, Shagufta Naz et al   |
| Licensed Content Date  | Jan 1, 2017  |
| Licensed Content Volume  | 101  |
| Licensed Content Issue   | 9  |
| Type of Use  | Thesis/Dissertation  |
| Requestor type   | academic/university or research institute  |
| Format   | print and electronic   |
| Portion  | figures/tables/illustrations   |
| Number of figures/tables/illustrations   | 1  |
| Will you be translating?   | no   |
| Circulation/distribution   | <501   |
| Author of this Springer Nature content   | no   |
| Title  | Multifunctional Nanomaterials for Theranostic Applications   |
| Instructor name  | Prof. Siddhartha Sankar Ghosh and Prof. Arun Chattopadhyay   |
| Institution name   | IIT Guwahati   |
| Expected presentation date   | May 2018   |
| Portions   | Fig. 1   |
| Requestor Location   | deepanjalee dutta<br>A 003 Subansiri hostel IIT Guwahati<br><br>Guwahati, 781039<br>India<br>Attn: deepanjalee dutta           |
| Billing Type   | Invoice  |
| Billing Address  | deepanjalee dutta<br>A 003 Subansiri hostel IIT Guwahati<br><br>Guwahati, India 781039<br>Attn: deepanjalee dutta              |
| Total  | 0.00 USD   |
| Terms and Conditions   |  |

Figure 1.2

26/04/2018

RightsLink Printable License

**JOHN WILEY AND SONS LICENSE  
TERMS AND CONDITIONS**

Apr 26, 2018

This Agreement between deepanjalee dutta ("You") and John Wiley and Sons ("John Wiley and Sons") consists of your license details and the terms and conditions provided by John Wiley and Sons and Copyright Clearance Center.

|                                       |  |
|---------------------------------------|--|
| License Number                        | 4336360831119  |
| License date                          | Apr 26, 2018   |
| Licensed Content Publisher            | John Wiley and Sons  |
| Licensed Content Publication          | Wiley Interdisciplinary Reviews - Nanomedicine and Nanobiotechnology   |
| Licensed Content Title                | Engineering multifunctional nanoparticles: all-in-one versus one-for-all   |
| Licensed Content Author               | Elizabeth Huynh, Gang Zheng  |
| Licensed Content Date                 | Feb 28, 2013   |
| Licensed Content Volume               | 5  |
| Licensed Content Issue                | 3  |
| Licensed Content Pages                | 16   |
| Type of use                           | Dissertation/Thesis  |
| Requestor type                        | University/Academic  |
| Format                                | Print and electronic   |
| Portion                               | Figure/table   |
| Number of figures/tables              | 1  |
| Original Wiley figure/table number(s) | Figure 1   |
| Will you be translating?              | No   |
| Title of your thesis / dissertation   | Multifunctional Nanomaterials for Theranostic Applications   |
| Expected completion date              | May 2018   |
| Expected size (number of pages)       | 160  |
| Requestor Location                    | deepanjalee dutta<br>A 003 Subansiri hostel IIT Guwahati<br><br>Guwahati, 781039<br>India<br>Attn: deepanjalee dutta |
| Publisher Tax ID                      | EU826007151  |
| Total                                 | 0.00 USD   |

Figure 1.3

26/04/2018

RightsLink Printable License

**ROYAL SOCIETY OF CHEMISTRY LICENSE  
TERMS AND CONDITIONS**

Apr 26, 2018

This Agreement between deepanjalee dutta ("You") and Royal Society of Chemistry ("Royal Society of Chemistry") consists of your license details and the terms and conditions provided by Royal Society of Chemistry and Copyright Clearance Center.

|                                  |   |
|----------------------------------|---|
| License Number                   | 4336361081052   |
| License date                     | Apr 26, 2018  |
| Licensed Content Publisher       | Royal Society of Chemistry  |
| Licensed Content Publication     | Nanoscale   |
| Licensed Content Title           | High photostability and enhanced fluorescence of gold nanoclusters by silver doping                                       |
| Licensed Content Author          | Xavier Le Guével, Vanessa Trouillet, Christian Spies, Ke Li, Timo Laaksonen, Dagmar Auerbach, Gregor Jung, Marc Schneider |
| Licensed Content Date            | Sep 13, 2012  |
| Licensed Content Volume          | 4   |
| Licensed Content Issue           | 24  |
| Type of Use                      | Thesis/Dissertation   |
| Requestor type                   | academic/educational  |
| Portion                          | figures/tables/images   |
| Number of figures/tables/images  | 1   |
| Format                           | print and electronic  |
| Distribution quantity            | 10  |
| Will you be translating?         | no  |
| Order reference number           |   |
| Title of the thesis/dissertation | Multifunctional Nanomaterials for Theranostic Applications  |
| Expected completion date         | May 2018  |
| Estimated size                   | 160   |
| Requestor Location               | deepanjalee dutta<br>A 003 Subansiri hostel IIT Guwahati<br><br>Guwahati, 781039<br>India<br>Attn: deepanjalee dutta      |
| Billing Type                     | Invoice   |
| Billing Address                  | deepanjalee dutta<br>A 003 Subansiri hostel IIT Guwahati<br><br>Guwahati, India 781039<br>Attn: deepanjalee dutta         |
| Total                            | 0.00 USD  |

Figure 1.4

26/04/2018

RightsLink Printable License

**ROYAL SOCIETY OF CHEMISTRY LICENSE  
TERMS AND CONDITIONS**

Apr 26, 2018

This Agreement between deepanjalee dutta ("You") and Royal Society of Chemistry ("Royal Society of Chemistry") consists of your license details and the terms and conditions provided by Royal Society of Chemistry and Copyright Clearance Center.

|                                  |   |
|----------------------------------|---|
| License Number                   | 4336360939929   |
| License date                     | Apr 26, 2018  |
| Licensed Content Publisher       | Royal Society of Chemistry  |
| Licensed Content Publication     | Nanoscale   |
| Licensed Content Title           | Polycations-functionalized water-soluble gold nanoclusters: a potential platform for simultaneous enhanced gene delivery and cell imaging |
| Licensed Content Author          | Yu Tao,Zhenhua Li,Enguo Ju,Jinsong Ren,Xiaogang Qu  |
| Licensed Content Date            | May 7, 2013   |
| Licensed Content Volume          | 5   |
| Licensed Content Issue           | 13  |
| Type of Use                      | Thesis/Dissertation   |
| Requestor type                   | academic/educational  |
| Portion                          | figures/tables/images   |
| Number of figures/tables/images  | 1   |
| Format                           | print and electronic  |
| Distribution quantity            | 10  |
| Will you be translating?         | no  |
| Order reference number           |   |
| Title of the thesis/dissertation | Multifunctional Nanomaterials for Theranostic Applications  |
| Expected completion date         | May 2018  |
| Estimated size                   | 160   |
| Requestor Location               | deepanjalee dutta<br>A 003 Subansiri hostel IIT Guwahati<br><br>Guwahati, 781039<br>India<br>Attn: deepanjalee dutta                      |
| Billing Type                     | Invoice   |
| Billing Address                  | deepanjalee dutta<br>A 003 Subansiri hostel IIT Guwahati<br><br>Guwahati, India 781039<br>Attn: deepanjalee dutta                         |
| Total                            | 0.00 USD  |

Figure 1.5

26/04/2018

RightsLink Printable License

**ELSEVIER LICENSE  
TERMS AND CONDITIONS**

Apr 26, 2018

This Agreement between deepanjalee dutta ("You") and Elsevier ("Elsevier") consists of your license details and the terms and conditions provided by Elsevier and Copyright Clearance Center.

|  |   |
|--|---|
| License Number                               | 4336370649302   |
| License date                                 | Apr 26, 2018  |
| Licensed Content Publisher                   | Elsevier  |
| Licensed Content Publication                 | Biomaterials  |
| Licensed Content Title                       | Photosensitizer-conjugated silica-coated gold nanoclusters for fluorescence imaging-guided photodynamic therapy                               |
| Licensed Content Author                      | Peng Huang, Jing Lin, Shouju Wang, Zhijun Zhou, Zhiming Li, Zhe Wang, Chunlei Zhang, Xuyi Yue, Gang Niu, Min Yang, Daxiang Cui, Xiaoyuan Chen |
| Licensed Content Date                        | Jun 1, 2013   |
| Licensed Content Volume                      | 34  |
| Licensed Content Issue                       | 19  |
| Licensed Content Pages                       | 12  |
| Start Page                                   | 4643  |
| End Page                                     | 4654  |
| Type of Use                                  | reuse in a thesis/dissertation  |
| Intended publisher of new work               | other   |
| Portion                                      | figures/tables/illustrations  |
| Number of figures/tables/illustrations       | 1   |
| Format                                       | both print and electronic   |
| Are you the author of this Elsevier article? | No  |
| Will you be translating?                     | No  |
| Original figure numbers                      | Fig. 1  |
| Title of your thesis/dissertation            | Multifunctional Nanomaterials for Theranostic Applications  |
| Expected completion date                     | May 2018  |
| Estimated size (number of pages)             | 160   |
| Requestor Location                           | deepanjalee dutta<br>A 003 Subansiri hostel IIT Guwahati<br><br>Guwahati, 781039<br>India<br>Attn: deepanjalee dutta                          |
| Publisher Tax ID                             | GB 494 6272 12  |
| Total  | 0.00 USD  |

Figure 1.6

26/04/2018

RightsLink Printable License

**ELSEVIER LICENSE  
TERMS AND CONDITIONS**

Apr 26, 2018

This Agreement between deepanjalee dutta ("You") and Elsevier ("Elsevier") consists of your license details and the terms and conditions provided by Elsevier and Copyright Clearance Center.

|  |  |
|--|--|
| License Number                               | 4336370512613  |
| License date                                 | Apr 26, 2018   |
| Licensed Content Publisher                   | Elsevier   |
| Licensed Content Publication                 | TrAC Trends in Analytical Chemistry  |
| Licensed Content Title                       | Synthesis, optical properties and applications of ultra-small luminescent gold nanoclusters                          |
| Licensed Content Author                      | Malin Cui, Yuan Zhao, Qijun Song   |
| Licensed Content Date                        | May 1, 2014  |
| Licensed Content Volume                      | 57   |
| Licensed Content Issue                       | n/a  |
| Licensed Content Pages                       | 10   |
| Start Page                                   | 73   |
| End Page                                     | 82   |
| Type of Use                                  | reuse in a thesis/dissertation   |
| Portion                                      | figures/tables/illustrations   |
| Number of figures/tables/illustrations       | 1  |
| Format                                       | both print and electronic  |
| Are you the author of this Elsevier article? | No   |
| Will you be translating?                     | No   |
| Original figure numbers                      | Fig. 6   |
| Title of your thesis/dissertation            | Multifunctional Nanomaterials for Theranostic Applications   |
| Expected completion date                     | May 2018   |
| Estimated size (number of pages)             | 160  |
| Requestor Location                           | deepanjalee dutta<br>A 003 Subansiri hostel IIT Guwahati<br><br>Guwahati, 781039<br>India<br>Attn: deepanjalee dutta |
| Publisher Tax ID                             | GB 494 6272 12   |
| Total  | 0.00 USD   |
| Terms and Conditions                         |  |

## Chapter 3

11/04/2018

Rightslink® by Copyright Clearance Center



RightsLink®

Home

Account Info

Help

ACS Publications Title:  
Most Trusted. Most Cited. Most Read.Cationic BSA Templated Au-Ag  
Bimetallic Nanoclusters As a  
Theranostic Gene Delivery  
Vector for HeLa Cancer CellsLogged in as:  
deepanjalee dutta  
Account #:  
3001057958**Author:** Deepanjalee Dutta, Arun  
Chattopadhyay, Siddhartha  
Sankar Ghosh

LOGOUT

**Publication:** ACS Biomaterials Science &  
Engineering**Publisher:** American Chemical Society**Date:** Nov 1, 2016

Copyright © 2016, American Chemical Society

**PERMISSION/LICENSE IS GRANTED FOR YOUR ORDER AT NO CHARGE**

This type of permission/license, instead of the standard Terms & Conditions, is sent to you because no fee is being charged for your order. Please note the following:

- Permission is granted for your request in both print and electronic formats, and translations.
- If figures and/or tables were requested, they may be adapted or used in part.
- Please print this page for your records and send a copy of it to your publisher/graduate school.
- Appropriate credit for the requested material should be given as follows: "Reprinted (adapted) with permission from (COMPLETE REFERENCE CITATION). Copyright (YEAR) American Chemical Society." Insert appropriate information in place of the capitalized words.
- One-time permission is granted only for the use specified in your request. No additional uses are granted (such as derivative works or other editions). For any other uses, please submit a new request.

BACK

CLOSE WINDOW

Copyright © 2018 Copyright Clearance Center, Inc. All Rights Reserved. [Privacy statement](#). [Terms and Conditions](#).  
Comments? We would like to hear from you. E-mail us at [customer-care@copyright.com](mailto:customer-care@copyright.com)

## Chapter 5

11/04/2018

Rightslink® by Copyright Clearance Center



RightsLink®

Home

Account Info

Help

ACS Publications Title:  
Most Trusted. Most Cited. Most Read.Phenylboronic Acid Templated  
Gold Nanoclusters for Mucin  
Detection Using a Smartphone-  
Based Device and Targeted  
Cancer Cell TheranosticsLogged in as:  
deepanjalee dutta  
Account #:  
3001057958**Author:** Deepanjalee Dutta, Sunil Kumar  
Sallapu, Arun Chattopadhyay, et  
al

LOGOUT

**Publication:** Applied Materials**Publisher:** American Chemical Society**Date:** Jan 1, 2018

Copyright © 2018, American Chemical Society

**PERMISSION/LICENSE IS GRANTED FOR YOUR ORDER AT NO CHARGE**

This type of permission/license, instead of the standard Terms & Conditions, is sent to you because no fee is being charged for your order. Please note the following:

- Permission is granted for your request in both print and electronic formats, and translations.
- If figures and/or tables were requested, they may be adapted or used in part.
- Please print this page for your records and send a copy of it to your publisher/graduate school.
- Appropriate credit for the requested material should be given as follows: "Reprinted (adapted) with permission from (COMPLETE REFERENCE CITATION). Copyright (YEAR) American Chemical Society." Insert appropriate information in place of the capitalized words.
- One-time permission is granted only for the use specified in your request. No additional uses are granted (such as derivative works or other editions). For any other uses, please submit a new request.

BACK

CLOSE WINDOW

Copyright © 2018 Copyright Clearance Center, Inc. All Rights Reserved. [Privacy statement](#). [Terms and Conditions](#).  
Comments? We would like to hear from you. E-mail us at [customer-care@copyright.com](mailto:customer-care@copyright.com)

## Chapter 6

Thank you for contacting ACS Publications Support.

Your permission request is granted and there is no fee for this reuse. In your planned reuse, you must cite the ACS article as the source, add this direct link <https://pubs.acs.org/doi/abs/10.1021/acsomega.7b01739> and include a notice to readers that further permissions related to the material excerpted should be directed to the ACS.

I hope this is helpful and if you need further assistance, please feel free to contact me.

Sincerely,

Ashley Gibson  
ACS Publications  
Customer Services & Information  
Website: <https://help.acs.org>

### Incident Information:

Incident: 1484948  
Incident Created: 2018-04-23T09:08:17  
Short Description: Permission for use of the article in thesis  
Description: Dear Sir/Mam

I am the original author of the below mentioned publication. Kindly grant me the permission for use of the full article in my thesis.

<https://pubs.acs.org/doi/abs/10.1021/acsomega.7b01739>

For reuse of entire article in thesis.

Thesis Title: Multi functional Nanomaterials for Theranostic Applications

Regards  
Deepanjalee

Institute of Technology G.